Università degli Studi di Padova

Administrative unit: **University of Padova**

Department: **Land, Environment, Agriculture and Forestry (TESAF)**

PhD Program: **Land, Environment, Resources and Health (LERH)**

Batch: XXXV

THE DILEMMA OF **ROADS I**NDUCED LAND **DE**GRADATION (***ROADSIDE***)

PhD Program Coordinator: Prof. Marco Borga

Supervisor: Prof. Paolo Tarolli

Co-Supervisor: Prof. Stefano Grigolato

External evaluators:

Dr. Alessio Cislaghi

Prof. Manuel López-Vicente

PhD candidate: Luca Mauri

Università degli Studi di Padova

Sede Amministrativa: **Università degli Studi di Padova**

Dipartimento Territorio e Sistemi Agro-Forestali (TESAF)

Corso di dottorato di ricerca: **Land, Environment, Resources, Health (LERH)**

Ciclo: XXXV

IL DILEMMA DEL DEGRADO DEL SUOLO INDOTTO DALLA PRESENZA DI STRADE (*ROADSIDE*)

Coordinatore: Prof. Marco Borga

Supervisore: Prof. Paolo Tarolli

Co-Supervisore: Prof. Stefano Grigolato

Valutatori esterni:

Dr. Alessio Cislaghi

Prof. Manuel López-Vicente

Dottorando: Luca Mauri

TABLE OF CONTENTS

SUMMARY……1

SOMMARIO……3

Chapter 1

1 INTRODUCTION 5

1.1 Research background 5

1.2 State of science 8

1.2.1 Land degradation processes in agricultural and forested ecosystems 8

1.2.2 Road networks, erosion and landslides 10

1.2.3 Roads induced land degradation processes: research open points 15

1.3 Object of the research 17

1.4 General organization 18

Chapter 2

2 UAV-SFM 4D MAPPING OF LANDSLIDES ACTIVATED IN A STEEP TERRACED AGRICULTURAL AREA[1] 19

2.1 Abstract 20

2.2 Introduction 21

2.3 Study area 23

2.4 Material and methods 25

2.4.1 Data collection and processing 25

2.4.2 Morphometric analysis of landslides 28

2.5 Results 33

2.5.1 Structure from Motion error assessment 33

2.5.2 Relative Path Impact Index 33

2.5.3 Digital elevation models of Difference 35

2.5.4 Multi-temporal comparison of geomorphometric indicators 36

2.5.5 Multi-temporal feature extraction 39

2.6 Discussion 41

2.7 Conclusions 43

2.8 References 44

Chapter 3

3 MULTI-TEMPORAL MODELING OF ROAD-INDUCED OVERLAND FLOW ALTERATIONS IN A TERRACED LANDSCAPE CHARACTERIZED BY SHALLOW LANDSLIDES[2] 47

3.1 Abstract 48
3.2 Introduction 49
3.3 Study area 51
3.4 Material and methods 53
3.4.1 SIMulated Water Erosion (SIMWE) model 53
3.4.2 Data acquisition and elaboration 54
3.4.3 SIMWE simulations on different scenarios 57
3.5 Results 61
3.5.1 Multi-temporal hydrological simulations 61
3.5.2 Water depth comparison and statistical validation 67
3.6 Discussion 71
3.7 Conclusions 73
3.8 Supplementary material 74
3.8.1 Supplementary figures 74
3.8.2 Supplementary tables 76
3.9 References 79

Chapter 4

4 EVALUATING THE INTERACTION BETWEEN SNOWMELT RUNOFF AND ROAD IN THE OCCURRENCE OF HILLSLOPE INSTABILITIES AFFECTING A LANDSLIDE-PRONE MOUNTAIN BASIN: A MULTI-MODELING APPROACH[3] 85

4.1 Abstract 86
4.2 Introduction 87
4.3 Study area 89
4.4 Material and methods 91
4.4.1 Data acquisition and elaboration 91
4.4.2 Statistical validation of instability susceptibility mapping 101
4.5 Results 103
4.5.1 Snowmelt runoff computation 103

4.5.2 Slope stability analysis 104
4.5.3 SIMWE simulations 108
4.5.4 Statistical analysis 110
4.6 Discussion 113
4.6.1 Limitations 114
4.7 Conclusions 115
4.8 Supplementary material 116
4.8.1 Supplementary figures 116
4.8.2 Supplementary tables 117
4.8.3 Supplementary documentation 119
4.9 References of Chapter 4 126

Chapter 5

5 MODELLING WINDTHROW EFFECTS ON WATER RUNOFF AND HILLSLOPE STABILITY IN A MOUNTAIN CATCHMENT AFFECTED BY THE VAIA STORM4 135

5.1 Abstract 136
5.2 Introduction 137
5.3 Study area 139
5.4 Material and methods 141
5.4.1 Input acquisition and data elaboration 141
5.4.2 Statistical analysis 146
5.5 Results 149
5.5.1 ALS-point clouds elaboration 149
5.5.2 HEC-HMS model 152
5.5.3 RESS model 159
5.5.4 Statistical analysis 160
5.6 Discussion 163
5.6.1 Limits 164
5.7 Conclusion 165
5.8 References 166
5.9 Supplementary material 176
5.9.1 Graphical abstract 176

5.9.2 Supplementary figures 177
5.9.3 Supplementary tables 181

Chapter 6

6.1 Final remarks 186
6.2 References (Introduction and Final remarks) 190

Chapter 7

7.1 Figure index 210
7.2 Table index 218

ABBREVIATIONS AND TERMS CITATIONS 221

SUMMARY

In the last decades, the growing anthropization occurring worldwide translated into the increasing construction of roads and trails, useful for support agricultural and forested systems productivity, encourage goods movement and generally promote the development of our societies. At the same time, the presence of road networks frequently represents a critical issue in hydrological and geomorphological terms, critically interacting with natural hydrological dynamics and similarly promoting land degradation processes such as erosive phenomena, landslides and terrain instabilities. In this regard, the scientific progress led the possibility to apply softwares, tools and technologies able to perform high-resolution topographic analysis, detailed terrain reconstructions and therefore increasing the opportunity to compute hydrological and geomorphological analysis at local and wider scales. In this regard, photogrammetric techniques (e.g. Structure from Motion -SfM), combined with Uncrewed Aerial Vehicles (UAV) and Light Detection and Ranging (LiDAR)-based Airborne Laser Scanning (ALS) technology further allowed to obtain detailed spatial information for scientific purposes.

This thesis arises in light of the above issues, aiming to overcame specific gaps in the scientific knowledge regarding the role of roads in the occurrence of land degradation processes such as shallow landslides and local erosive dynamics. This work is basically structured around four researches, based on data collection in the field, application of mathematical models and Geographic Information Systems (GIS). Starting from agricultural context and therefore moving to mountain and forested systems, the thesis proposes advances for science regarding the dilemma of roads-induced land degradation processes through four scientific articles. New methodologies are proposed in this regard, potentially applicable in other contexts and study areas in order to support stakeholders and local communities in promoting specific interventions and decisions able to mitigate and prevent the occurrence of similar issues in the future.

SOMMARIO

Negli ultimi decenni, la crescente antropizzazione che si è verificata su scala globale si è tradotta in un generale aumento nella pianificazione e costruzione di reti viarie, al fine di incrementare la produttività dei sistemi agricoli e forestali, favorire la circolazione delle merci e promuovere in generale lo sviluppo delle nostre società. Nonostante tali vantaggi, la presenza di reti stradali può essere particolarmente critica sia in termini idrologici che geomorfologici, alterando le naturali dinamiche dei processi idrologici delle aree in cui le reti viarie vengono costruite e favorendo allo stesso tempo l'attivazione di processi di degrado del suolo come fenomeni erosivi, frane e problemi di instabilità del terreno. A questo proposito, il progresso scientifico degli ultimi tempi si è tradotto nella possibilità di applicare software, strumenti e tecnologie grazie alle quali effettuare analisi topografiche ad alta risoluzione, ricostruzioni dettagliate del terreno e quindi realizzare dettagliate analisi idrologiche e geomorfologiche a scale spaziali differenti. Le tecniche fotogrammetriche (e.g. la tecnica Structure from Motion -SfM), combinate con l'utilizzo di droni (Uncrewed Aerial Vehicles-UAV) e tecnologie di telerilevamento (e.g. sistemi Light Detection and Ranging -LiDAR), hanno consentito di ottenere informazioni spaziali ad altissima risoluzione e a basso costo ripetute nel tempo. Alla luce di questi aspetti, questa tesi nasce con l'obiettivo di colmare specifiche lacune scientifiche relativamente il ruolo svolto dalle reti viarie nell'attivazione di processi di degrado del suolo quali per esempio frane superficiali e dinamiche erosive del terreno, specialmente in condizioni di forte pendenza. Questo lavoro si articola pertanto in quattro differenti ricerche, basate sulla raccolta di dati in campo e sulla conseguente applicazione di modelli matematici e Sistemi Informativi Geografici (GIS). Partendo quindi dal contesto agricolo e passando ai sistemi montani e forestali, la tesi propone diversi studi innovativi riguardo il dilemma del degrado del suolo indotto dalla presenza di strade, attraverso la redazione di quattro articoli scientifici proposti in diverse riviste internazionali. A questo proposito, vengono suggerite nuove metodologie potenzialmente applicabili in altri contesti e aree di studio differenti, al fine di supportare gli stakeholders e le comunità locali nell'attuare specifici interventi sul territorio in grado di mitigare e soprattutto prevenire il verificarsi di simili problematiche in futuro.

CHAPTER 1

INTRODUCTION

1.1 Research background

The extension of road networks is worldwide recognized as one of the main issues affecting both agricultural and forested areas. Factor such as (i) demographic changes, (ii) growing urbanization, (iii) increasing productivity of agricultural and forested areas, (iv) local policies and (v) economic strategies are mainly responsible for the increasing planning and construction of road networks in many areas of the world (Vickerman *et al*., 1999; Antrop, 2004; Asher and Novosad, 2020; Pašakarnis and Maliene, 2010; Sidle, 2020). In this regard, roads expansion is strictly linked with the increasing occurrence of land degradation processes affecting agricultural zones and forest ecosystems, as underlined in several researches (Tarolli *et al*., 2015; Navarro-Hevia *et al*., 2016; Shirvani *et al*., 2020; Tarolli *et al*., 2020; Dalantai *et al*., 2021).

Roads induced land degradation affecting agricultural and forested landscapes are driven by several factors, e.g. (i) the increasing of their usage, (ii) the expansion of roads and trails systems and (iii) their unsuitable planning and management (Marion and Leung, 2004; Sidle and Ziegler, 2012). Moreover, actual changes in global and local climatic conditions are directly involved in the occurrence of degradative dynamics close to roads (Poesen *et al*., 2003; Donat *et al*., 2017; Nearing *et al*., 2004). In this context, land degradation processes involving roads and trails can also derive from design and placement of drainage systems without an effective analysis of actual changes characterizing return times of extreme rainfall events (Halsnas and Trarup, 2009; Semadeni-Davies *et al*., 2008; Sikder and Xiaoying, 2014; Zhou, 2014). In fact, the hydraulic section of ditches, culverts and other drainage solutions were proven to be inefficient in managing the increasingly intense and frequent rainfall events characterizing weather regimes of many countries worldwide (Bruen and Yang, 2006; Dougherty *et al*., 2007; Ashley *et al*., 2008; Berggren *et al*., 2012; Semadeni-Davies *et al*., 2008). At the same time, land degradation phenomena occurring close to roads are closely related to several environmental factors, such as (i) climate, (ii) topography, (iii) vegetation presence and (iv) soil surface characteristics (Douglas, 2006; Abu Hammad and Tumeizi, 2012; Cao *et al*., 2015;

Dalantai *et al*., 2021; Jaafari *et al*., 2022). Climatic factors e.g. rainfall intensity and frequency, directly promote soil failures and erosion rates (Parsakhoo *et al*., 2014). Topography has a key role in agricultural and forest land degradation close to roads networks, especially in steep slope areas where surface runoff represents the main responsible for soil losses and terrain destabilization (Leung, 1992). Moreover, slope alignment angle of roads (i.e., roads orientation to the prevalent slope) influences the occurrence of degradative processes, since roads designed with a low slope alignment angle turn out to be particularly prone to degradation (Leung and Marion, 1996). Finally, soil and surface characteristics (i.e. soil properties like soil texture, soil moisture, infiltration capacity and roughness) influence erosion dynamics, especially close to inefficiently drained roads and steeper slopes (Märker *et al*., 2008; Hammad and Tumeizi, 2012; Keshavarzi *et al*., 2019). On the other hand, soil properties could be notably altered due to the presence of roads and trails (Ziegler and Giambelluca, 1997; Ziegler *et al*., 2007; Sidle and Ziegler, 2012; Sidle *et al*., 2014; Ngezahayo *et al*., 2021). Displacing of superficial soil layers and increasing terrain compaction due to their usage potentially led to with an increasing risk of critical water runoff deviation and erosive processes activation. In this regard, several factors control soil erosion, such as soil characteristics, the slope angle (Farrell and Marion, 2002; Cao *et al*., 2015), the eroding agent, the land slope and the typology of the vegetation cover (Parsakhoo *et al*., 2014). Roads are also responsible for altering water flow directions (Tarolli *et al*., 2012) and have direct interaction with water itself. In this connection, drainage difficulties and water passages are the paramount guilty for terrain failures and banks destabilization close to mountain and agricultural roads (Gucinski *et al*., 2001). Hydrological processes can also be influenced by the presence of roads in terms of rainfall interception on their surface, alteration of subsurface water dynamics downstream and flows concentration on the roadway or in nearby channels (Gucinski *et al*., 2001). In addition to this, geomorphic processes like terrain failures and sediment transport are driven by the presence of roads, especially after strong meteorological events such as intense rainstorms (Wemple *et al*., 2001; Arnaez *et al*., 2004).

Considering all these issues, emerges first of all the necessity to start researches that could further investigate the influence of factors such as rainfall intensity and variability, soil and land cover conditions, hydrological properties of the terrain and respective geomorphological properties in roads-land degradation interactions (Salesa *et al*., 2019). Moreover, little is known about the possible role of roads as sinks or sources of water, directly involved in the occurrence of terrain failures, shallow landslides and erosive processes. Another issue that needs more attention in the scientific point of view is the investigation of the roads' role in water overland flow paths alteration, both in term of rainfall and snowmelt runoff deviation in agricultural and mountain areas respectively. In

fact, water is collected from the slope that roads intersect therefore flowing on its surface, causing the structural weakening of roads' banks and slope terrain close to these last. In this regard, is essential to better detect mutual interactions between these factors at hillslope and watershed scale. Finally, low-cost and sustainable management interventions could be undertaken starting from filling the scientific gaps above, therefore aiming to propose low-cost and efficient methodology able to better control and foresee such land degradation phenomena affecting urbanized agricultural and mountain areas over time.

1.2 State of science

1.2.1 Land degradation processes in agricultural and forested ecosystems

Nowadays, one of the main factors related to the increase of land degradation phenomena affecting agricultural areas is represented by the raising of surfaces destined to crops cultivation, as underlined by several studies (Pender *et al*., 2004; Grassini *et al*., 2013; Laurance *et al*., 2014; Lindblom *et al*., 2017). In addition, together with the practice of monoculture and the parallel adoption of increasingly intensive agriculture practices, soil erosion represents the most relevant cause of degradation affecting agroecosystems worldwide. This is particularly notable in those areas where intensive agriculture is firmly established or where land conformation has imposed its own development in steep slope areas (Ghafari *et al*., 2017). According to recent FAO estimates, the hilly areas where traditional agriculture is adopted are subject to erosion processes, affecting about 15 t/hectare/year of soil (FAO and ITPS, 2015). In fact, agricultural soil losses represent a problem recognized for several decades, with a proved eroding rate of agricultural soil troublingly faster respect to the contemporary processes of pedogenesis (FAO and ITPS, 2015). Water-induced erosion processes are strictly responsible for deterioration processes of agricultural soil, especially in relation with actual changes affecting extreme rainfall events (Anderson *et al*., 2021; Yakupoglu *et al*., 2021). In Europe in particular, about 68% of total soil losses driven by water erosion affects agricultural areas, which together cover about 50% of the entire European surface (Panagos *et al*., 2015; Panagos *et al*., 2021). In Italy, water erosion represents an issue of primary interest especially in terraced wine-growing areas, a land use category particularly prone to erosion issues due to water (Prosdocimi *et al*., 2015). This is essentially due to the steep slope of vineyards and the pedo-climatic characteristics of the Italian peninsula (Corti *et al*., 2011; Robinson and Philips, 2000; Tarolli *et al*., 2012). Soil compaction is responsible for land degradation involving more than 30 million hectares of agricultural areas in Europe (Akker and Canarache, 2001; Balbuena *et al*., 2000). Similar problems have also been detected and analysed in many parts of the world such as China, Russia, Australia and America (Soane and van Ouwerkerk, 1994; Nawaz *et al*., 2013) with an estimate, at a global level, of a total of about 70 million hectares of agricultural land subject to compaction (FAO and ITPS, 2015). Soil compaction induces erosion phenomena, a decrease in soil productivity and slowed down growth of root systems, directly connected with consequently economic difficulties for stakeholders involved in the production chain. Finally, among the main causes related to the occurrence of land degradation processes affecting agricultural areas, soil saturation represents an issue of primary relevance. In this connection, the reduction of croplands productivity is one of the most significant consequences

related to waterlogging dynamics (Xiaoli *et al*., 2017).

As said, one of the major issues affecting agricultural systems in many development regions of the world is represented by land degradation issues such as erosion and shallow landslides (Wallace *et al*., 2011; Bajocco *et al*., 2012; Galati *et al*., 2015; Prosdocimi *et al*., 2015). In this regard, has been estimated that about 20% of the cultivated areas of the world are involved in landslides and terrain failures, with a yearly corresponding loss of arable land of more than 5 million hectares (Hamdy and Aly, 2014). Factors influencing the incidence of land degradation dynamics in agricultural systems are (i) increasing use of agricultural machinery (Pijl *et al*., 2019), (ii) changes in land use and land cover (Hein, 2007; Sidle, 2007; Bajocco *et al*., 2012; Fagnano *et al*., 2012; Lopez-Vincente et al., 2017), (iii) intensification of agricultural land use and contemporary lack of conservation measures (Coxhead and Shively, 1995), (iv) increasing extension of agricultural lands (Chauhan *et al*., 2010), (v) land abandonment (Filho et al., 2016; Lasanta et al., 2017; Levers *et al.*, 2018; Louwagie *et al*., 2011; Saikia, 2014; Ustaoglu and Collier, 2018) and (vi) climate change (Webb *et al*., 2017), as well as (vii) increasing anthropogenic pressure (Sidle *et al*., 2014; Salvati *et al*., 2015) and (viii) diffusion of wildlife species (Mauri *et al*., 2019). This also has relevant consequences in economic terms, besides for the environment and society in general (Hamdy and Aly, 2014; Hein, 2007; Pender *et al*., 2004; Shiferaw and Holden, 2001).

In addition to agricultural realities, forested areas represent one of the most significant terrestrial biomes in terms of ecosystem benefits and services (Taye *et al*., 2021). Especially for steep-slope areas, the presence of forests implicates several advantages, such as (i) improved hillslopes stability, (ii) protective functions against rock falls and snow avalanches (iii) control of terrain desertification, (iv) reduction of erosion processes, (v) restoration of soil fertility, (vi) mitigation of microclimate conditions and (vii) increasing biodiversity (Sebald *et al*., 2019; D'Amboise *et al*., 2021; Perzl *et al*., 2021)**.** In addition, forests represent habitats for wildlife and flora and many communities over the world derive their livelihoods from provided goods and services. In this connection, over the last few decades, deforestation and land degradation of forested areas has proceeded at an alarming velocity, with serious effects on biodiversity and climate (Kelly *et al*., 2015). FAO and ITPS (2015) reported that, globally, deforestation from 1990 to 2005 has yearly involved more than 10 million hectares of forests, without significant trend decrease over time. In this connection, several forms of land degradation are detectable in forested areas, mainly deriving from human impact and activities such as (i) over-exploitation, (ii) recurring fires and (iii) presence of anthropogenic features such as roads and trails (Contreras-Hermosilla, 2000; Saikia, 2014; Yakubu *et al*., 2015; Chalise *et al*., 2019). In addition, natural disturbances such as fires, snow avalanches, windstorms and biotic hazards

frequently affect forested systems worldwide both leading to positive consequences (e.g. regarding forests ecology and natural dynamics) and negative issues like the increasing risks of land degradation phenomena (e.g. hillslope instabilities, gully erosion and shallow landslides; Berger and Rey, 2004; Hanewinkel *et al*., 2011; Getzner *et al*., 2017). Topography, soil properties, stand conditions and forest management practices also regulate such physical processes over time. Starting from the above considerations, it is also worth mentioning how the increasing of human pressure on the forested ecosystems frequently translates into several issues such as (i) land conversion, (ii) land use changes, (iii) deforestation, (iv) clear cut and harvesting practices, that are anyhow responsible for degradation dynamics commonly affecting forested areas (Ebodé *et al*., 2020; Rull and Vegas-Vilarrúbia, 2021).

1.2.2 Road networks, erosion and landslides

In light of the above, within the context of economic growth, supporting of agricultural development, forest management and easing of logging operations, roads are rapidly branching out in many developing agricultural and mountain areas worldwide (Dutton *et al*., 2005; Fannin and Lorbach, 2007; Sidle and Ziegler, 2012; Salesa *et al*., 2019). In this connection, recent researches highlighted the direct correlation between the increasing extension of land devoted to agricultural or silvicultural practices and the occurrence of terrain instabilities in many parts of the American and European continent (Romm, 2011; Bajocco *et al*., 2012). With regard to agricultural areas, roads presence and land degradation processes such as landslides and erosive phenomena are strictly correlated (Coker and Fahey, 1993; Wemple *et al*., 2001; Eker and Aydin, 2014; Lucieer *et al*., 2014). Figure 1.1 shows an example of shallow landslide occurred close to a section of a paved road in a terraced vineyard (northern Italy).

Figure 1.1 *Landslide involving a slope under a section of a paved road located in a terraced vineyard in Trentino Alto-Adige region, northern Italy (photo by Luca Mauri)*

Road networks have several functions in agriculture, i.e. (i) encourage fast communications (Gollin and Rogerson, 2010), (ii) improve farmland administration, (iii) simplify agricultural operations, (iv) support the expansion of the agriculture sector (Sidle and Ziegler, 2012), (v) improve agriculture's economy (Lokesha and Mahesha, 2016), (vi) maximize farming production (Llanto, 2012; Tunde and Adeniyi, 2012), (vii) ensure the quality of agricultural produce (Bradbury *et al*., 2017), (viii) facilitate the access in croplands (Gollin and Rogerson, 2010), (ix) simplifies agronomic operations and (x) encourages the circulation of agricultural products in the territory (Sidle and Ziegler 2012; Fungo *et al*., 2017; Kiprono and Matsumoto, 2018). At the same time, notwithstanding its benefits, the presence of roads within cultivated areas can induce the activation of instabilities, especially in terms of environmental and geomorphological issues (Loeffler *et al*., 2009; Daigle, 2010; Penna *et al*., 2014). In fact, jointly with road presence, factors like rain intensity, vegetation presence, surface topography and the concentration of shallow water flows (Borga *et al*., 2002b; Penna *et al*., 2014) play a primary role in agricultural land degradation. In this connection, Sidle *et al*. (2006) highlighted how soil erosion and landslides incidence can seriously increase due to specific dynamics such as sediment discharging from roads during rainfall events. In this context, the alteration of water overland flow directions occurs through (i) the interception of superficial and subsurface water fluxes, (ii) the concentration of flows on the road and (iii) the alteration of already present flow directions (Borga *et al*., 2004; Tarolli *et al*., 2013). In addition, topography has a direct role in hillslopes failures driven by roads and trails, especially in steep slopes where surface runoff is considered as one of the

main responsible for soil losses and hillslopes destabilization (Leung, 1992). The relation between degradative dynamics affecting agricultural systems and the contemporary presence of roads in terms of sediment removal and delivery over time is similarly clear (Motha *et al*., 2004). In fact, several factors are responsible for sediment generation and deposition close to rural roads e.g. (i) water runoff, (ii) raindrop impact, (iii) raindrop splash (Aksoy and Kavvas, 2005), (iv) rainfall amount and intensity, (v) characteristics of road surface, (vi) road slope, (vii) usage and (viii) maintenance (Fu *et al*., 2010; Gruszowski *et al*., 2003). Also, sediment delivery from roads is regulated by (i) the displacement of drainage structures along the road, (ii) the distance of drainage outlets to streams, (iii) the slope of the roads, (iv) the presence of concavities on roads' surface and (v) local contributing area (Megahan and Ketcheson, 1996). As underlined in Fu *et al*. (2010) and in Ramos-Scharròn and MacDonald (2017), roads-surface erosion is one of the main sediment sources related to land degradation processes, meaning "roads-surface erosion" as sediment detachment and deposition processes taking place along the road's surface (Fu *et al*., 2010). In this regard, there is a notable relation between roads-surface erosion and the role played by cut slopes, respectively in term of runoff generation and sediment production (Croke *et al*., 2006). In fact, water runoff along roads tends to be more noticeable due to the interception of subsurface water flows by cut slopes, with a consequent increase of potential erosion rates close to the roadway (MacDonald *et al*., 2001; Fu *et al*., 2010). Pore-water pressure, drainage rate, antecedent rainfall, moisture content and slope constituents (Guzzetti et al., 2007; Kim et al., 2021; Li et al., 2021; da Silva et al., 2022; Dai et al., 2022) concurrently regulates such a critical interaction between roads and hillslope destabilizations. Second, especially recently constructed paved and unpaved roads are characterized by similar issues, the former mainly due to the lack of the protection role played by vegetation and rock armoring, the latter due to low infiltration rates because of terrain compaction and inefficient vegetation cover within the affected hillslopes (Ziegler and Giambelluca, 1997; Ziegler *et al*., 2001; Gruszowski *et al*., 2003; Dimitriou *et al*., 2013). It is therefore widely recognized that rural roads play a primary role in sediment production and related transport (Liu *et al*., 2010; Cao *et al*., 2015). In addition to the above, several researches stressed out as the increasing employment of roads, together with their inefficient planning and construction strictly control the activation of slope failures close to specific sections of trail networks (Deluca *et al*., 1998; Marion and Leung, 2004; Cao *et al*., 2006; Arnáez *et al*., 2007; Liu *et al*., 2016; Salesa *et al*., 2019). Also, road's construction is notably associated with a consequent destabilizing effect respect to the undercut slope and the subsequent alteration of natural drainage systems (Sidle *et al*., 2006; Lennartz, 2013). Factors like (i) roads characteristics, (ii) intensity and type of usages and (iii) environmental conditions such as terrain characteristics (Corbane *et al*., 2008; Ruiz-Sinoga and Martínez-Murillo, 2009), land morphology (Fox and Bryan, 2000) and hydrological

properties (Comino *et al*., 2015) particularly influence landslides incidence over time (Bodoque *et al*., 2017). Finally, current changes in climate conditions (e.g. more frequent and intense rainfall events and variations in the spatial distribution of precipitations) are likewise involved in land surface instabilities close to roads (Poesen *et al*., 2003; Nearing *et al*., 2004; Pendergrass and Hartmann, 2014). In this connection, the design of most of the road networks in steep slopes agricultural and forested areas involves the presence of drainage systems oftentimes ineffective in dealing with the increasingly frequent extreme water supplies due to global climatic changes.

Similarly to agricultural context, roads have various functions for mountain and forested areas, i.e. (i) ensure rapid communications, (ii) improve environmental management (iii) simplify logging procedures, (iv) allow forestry and hydraulic interventions, (v) ease the woodland usages and (vi) facilitate defensive measures regarding preventions against natural hazards such as wild fires, windstorms and snow avalanches (Lugo and Gucinski, 2000; Demir, 2007; Gumus *et al*., 2008). At the same time, their increasing employment, not optimal planning and inefficient maintenance over time influence the consequent activation of land degradation processes like erosive dynamics and landslides downstream the roadway (Marion and Leung, 2004; Salesa *et al*., 2019), as shown in the example in Figure 1.2. In this regard, hydro-geomorphic processes are negatively influenced by the widespread diffusion of roads in mountain landscapes, both at local and watershed scale (Wemple *et al*., 2001; Sidle and Ziegler, 2012; Sosa-Pérez and MacDonald, 2017; Salesa *et al*., 2019).

Figure 1.2 *Example of shallow landslide activated above a section of a paved road located in a mountain grassland environment (Trentino Alto-Adige region, northern Italy; photo by Luca Mauri)*

The environmental impact of roads located in forested zones is globally recognised (Liu *et al*., 2016) as confirmed in numerous studies (Luce and Black, 1999; Ziegler *et al*., 2000; Wemple *et al*., 2001; Arnaez *et al*., 2004; Cao *et al*., 2006; Foltz *et al*., 2009). For example, in North-America DeLuca *et al*. (1998) and Leung and Marion (1999) underlined as the increase of attendance of mountain areas and the contemporary development of tourism activities has induced a constant deterioration of road networks, directly responsible for the occurrence of erosive dynamics. This is jointly due to the displacement of materials from the roadway and the ineffective water regulation along it, with the consequently increased risk of erosive phenomena occurring downstream the road itself (Ziegler and Giambelluca, 1997; Croke and Hairsine, 2006; Akay *et al*., 2008; Fu *et al*., 2010; Shi *et al*., 2012; Brown *et al*., 2013). This also depends on the characteristics of the road, on their intensity and type of usage, as well as on environmental conditions in which are placed (Fig.1.3); (Bodoque *et al*., 2017; Karki and Ojha, 2021). Also, Tarolli *et al*. (2013) investigated the increase of erosion susceptibility in specific Italian forest landscapes characterized by the presence of roads and trails, highlighting as their usage can be directly responsible for the activation and intensification of soil erosion processes. As a matter of fact, especially abandoned and wrongly planned roads (Tomczyk *et al*., 2016) are affected by erosive dynamics and therefore the rates of sediment production can considerably increase (Luce and Black, 1999; Surfleet and Marks, 2021; Zhao *et al*., 2022).

Figure 1.3 *Shallow landslide (black arrow) occurred in a wind-disturbed forested catchment (Veneto region, northern Italy; photo by Luca Mauri)*

1.2.3 Roads induced land degradation processes: research open points

Looking at the issues presented above, scientific knowledge is actually lacking in several unresolved aspects that need to be deeply detected in scientific terms. In this regard, researches concerning the possibility to investigate the evolution of shallow landslides occurring close to agricultural roads through the multi-temporal comparison of specific geomorphological indexes at hillslope scale is still missing in the scientific literature. Moreover, in-depth detection of roads' role in altering water overland flows depending on both roads presence and rainfall intensity is actually missing in the available scientific literature. The application of *Uncrewed Aerial Vehicle* (UAV)-based photogrammetric techniques for elaborating high-resolution multi-temporal terrain reconstruction and therefore computing the presented hydro-geomorphological analysis represents an innovative aspect to be further investigated.

In addition, it is necessary to analyse the relationship between the presence of roads and the consequent activation of shallow landslides in mountainous areas. In particular, the possibility of jointly apply hydrological and geomorphological models in the detection of the interaction between roads, snowmelt runoff and landslides occurrence close to mountain roads is an aspect that is still

largely unexplored. The deepening of these issues through a multi-modeling approach at watershed scale, starting from *Airborne Laser Scanning* (ALS)-data acquisition and elaboration, is an open point to be studied.

The scientific literature is also lacking in the analysis of how unexpected changes in land use and management of wooded areas due to natural disturbances are responsible for the activation of soil degradation events and for altering local hydrological regimes over time in close proximity to roads. Indeed, the role played by rural roads in these circumstances is still unclear, as well as the possibility to model and quantify the effect of extended land-use changes driven by such extreme events on the hydrological properties of forested catchments.

These analyses could lead to planning more efficient maintenance interventions on rural road networks in both agriculture and forested areas, focusing on specific zones affected by similar issues. In addition, innovative studies regarding the relationship between roads and land degradation processes could represent a useful starting point for preventing the occurrence of analogous dynamics over time. In this regard, the integrated application of *Geographic Information Systems* (GIS), photogrammetric and remote sensing techniques and mathematical models could represent an added value in the investigation of roads-induced land degradation dynamics at field and watershed scales.

1.3 Object of the research

The present thesis mainly aims to fill the gap in the scientific knowledge regarding the role of road networks in the occurrence of land degradation processes affecting agricultural and forested systems. In this connection, different specific objectives served as basis for four research papers proposed to the scientific community during the doctoral period. In line with the above, the thesis is first and foremost aimed at investigating the role played by rural roads in the occurrence of terrain instabilities affecting steep slopes agricultural systems. In this connection, this research firstly set one's sights on the analysis of road-induced alteration of water runoff dynamics within a terraced agricultural area affected by shallow landslides. The consequent evolution of unstable areas downstream to specific section of the road network is therefore going to be evaluated both in geomorphological and hydrological terms. The same issue is planned to be investigated respectively focusing on a mountain basin and a forested catchment affected by extended land use changes as a result of the Vaia windstorm. Regarding the former, the specific purpose translates into the possibility to improve scientific awareness regarding the interaction between water runoff resulting from melting snowpacks, roads and shallow landslides occurring in a mountain area. Concerning the latter, the specific objective is to explore the influence of *boundary conditions* (i.e., land cover, land uses and land management) on both hydrological properties and soil instabilities occurring close to a road network in a wind-disturbed forested basin. In light of the foregoing, this thesis aspires to propose new methods counting on the combined implementation of physical models, photogrammetry, remote sensing techniques and GIS. The study also wants to propose innovative, low cost and efficient methodologies that could serve as effective tool to prevent the occurrence of land degradation processes driven by roads presence, therefore supporting stakeholders and public authorities involved in the management of similar phenomena.

1.3.1 General organization

The thesis is a collection of four scientific articles, resulted from the three years of the doctoral period. In particular, three articles have been published on peer-review journals (Chapters 2, 3 and 4), while the fourth (Chapter 5) is actually under the review process. Only modifications to the original papers are minor changes to layout, figures and tables numbering for consistency and readability.

The first scientific article proposes a multi-temporal comparison of geomorphometric indicators to describe a landslide-prone terraced agricultural system, characterized by the presence of a rural road. Starting from multi-temporal UAV-based photogrammetric surveys, the research aims to propose a comparison of such indicators over time in order to monitor the dynamics of a shallow landslide occurred close to the rural road, as well as detect the role of the road in altering water runoff toward the instable hillslope. Research outcomes were presented in the research paper entitled *UAV-SfM 4D mapping of landslides activated in a steep terraced agricultural area*, published in the Journal of Agricultural Engineering in 2021 [IF: 1.727, Q3].

The contribution of rural roads in altering water overland flows in a steep slope terraced systems affected by the occurrence of shallow landslides was further detected in the second research paper entitled *Multi-temporal modeling of road-induced overland flow alterations in a terraced landscape characterized by shallow landslides*, published in the International Soil and Water Conservation Research (ISWC) journal in 2021 [IF: 6.027, Q1]. Starting from UAV-based photogrammetric surveys, hydrological modeling of water flows depth alterations due to the presence of the road were carried looking at both its presence and assumed absence within the study area.

The third scientific article focused on the investigation of the interaction between snowmelt runoff, roads and terrain instabilities affecting a steep-slope mountain grassland catchment, starting from ALS-derived point clouds elaboration and novel multi-modeling approach. Results were proposed in the research paper entitled *Evaluating the interaction between snowmelt runoff and road in the occurrence of hillslope instabilities affecting a landslide-prone mountain basin: A multi-modeling approach*, published in Journal of Hydrology in 2022 [IF: 6.708, Q1].

Finally, the effects of land use changes driven by windthrow occurrence in altering water runoff dynamics and soil stability were analysed. Starting from multi-temporal elaboration of ALS-derived point clouds, different hydrological and geomorphological models were jointly implemented looking at a wind-disturbed forested catchment characterized by road presence and shallow landslide activation below it. Research outcomes were proposed in the fourth scientific article entitled *Modelling windthrow effects on water runoff and hillslope stability in a mountain catchment affected by the Vaia storm*, currently under review.

CHAPTER 2

UAV-SFM 4D MAPPING OF LANDSLIDES ACTIVATED IN A STEEP TERRACED AGRICULTURAL AREA[1]

Luca Mauri,[1] Eugenio Straffelini,[1] Sara Cucchiaro,[1, 2] Paolo Tarolli[1]

[1]*Department of Land, Environment, Agriculture and Forestry, University of Padova, Legnaro, Italy*
[2]*Department of Agricultural, Food, Environmental and Animal Sciences, University of Udine, Udine, Italy*

Keywords: Landslides, Roads, Agricultural Systems, UAV, GIS

[1] Mauri, L., Straffelini, E., Cucchiaro, S., Tarolli, P. (2021). UAV-SfM 4D mapping of landslides activated in a steep terraced agricultural area. ***Journal of Agricultural Engineering***, LII:1130. doi:10.4081/jae.2021.1130

2.1 Abstract

The presence of roads is closely linked with the activation of land degradative phenomena such as landslides. Factors such as ineffective road management and design, local rainfall regimes, and specific geomorphological elements actively influence landslide occurrence. In this context, recent developments in digital photogrammetry (e.g., Structure from Motion; SfM) paired with Uncrewed Aerial Vehicles (UAV) systems increase our possibilities to realize low-cost and recurrent topographic surveys. This can lead to the development of multi-temporal (hereafter: 4D) and high-resolution Digital Elevation Models (DEMs), which are fundamental to analyse geomorphological features and quantify processes at the fine spatial and temporal resolutions at which they occur. This research proposes a multi-temporal comparison of the main geomorphometric indicators describing a landslide-prone terraced vineyard to assess the observed high-steep slope failures. The possibility to investigate the evolution of landslide geomorphic features in steep agricultural systems through a high-resolution and 4D comparison of such indicators is still a challenge to be explored. In this article, we considered a case study located in the central Italian Alps, where two landslides were activated below a rural road within a terraced agricultural system. The dynamics of the landslides were monitored by comparing repeated DEMs), (Digital elevation model Of Difference), which reported erosion values of about 20 m^3 and 10 m^3 for the two landslide zones and deposition values of more than 15 m^3 and 9 m^3, respectively. The road network's role in the alteration of superficial water flows was proved by the elaboration of the relative path impact index. Altered water flows were expressed by values between 2σ and 4σ close to the collapsed surfaces. The increase in profile curvature and roughness index described the landslides evolution over time. Finally, the multi-temporal comparison of feature extraction underlined the geomorphological changes affecting the study area. The accuracy of features extraction was analysed through the quality index computation, expressed in a range between 0 (low accuracy) and 1 (high accuracy), and proved to be equal to 0.22 m (L1-pre), 0.63 m (L1-post), and 0.69 m (L2). Results confirmed the usefulness of high-resolution and 4D UAV-based SfM surveys to investigate landslides triggering due to the presence of roads at hillslope scale in agricultural systems. This work could be a useful starting point for further studies of landslide-susceptible zones on a wider scale to preserve the quality and the productivity of affected agricultural areas.

2.2 Introduction

Several factors cause land degradation in agriculture, e.g., i) human pressure (Salvati *et al*., 2015); ii) land use and land cover changes (Bajocco *et al*., 2012); and iii) climate changes (Webb *et al*., 2017). In particular, hydro-erosive dynamics and their evolution into more complex phenomena, such as landslides, are typical land degradation processes and landform-shaping phenomena affecting cultivated lands with severe economic and environmental costs. Among the anthropogenic factors that significantly impact surface erosion and landslides, road construction plays an important role. Indeed, landslide activation and the presence of roads are strongly connected (Sidle and Ziegler, 2012). Road construction has a primary influence on landslide activation, especially in steep zones, for example, through the reduction of the slope terrain stability, the increase of slope on fill and cut surfaces, and the alteration of hydrological processes (Eker and Aydin, 2014). Moreover, the increase of road networks leads to significant changes in drainage system networks and sediment dynamics (Persichillo *et al*., 2018), representing a predisposing factor for greater susceptibility to landslide activation. Despite their usefulness, the negative impacts of roads on agriculture are well documented, especially in terms of environmental and geomorphological issues (Sidle and Ziegler, 2012). Human interventions through farming practices (Bordoni *et al*., 2019), specific environmental conditions, and land abandonment processes could affect the conservation of terraced cultivated zones, activating landslide phenomena. In detail, factors like surface topography, land cover and management, soil erodibility and geological characteristics, as well as rain intensity and the concentration of surface water flows along a preferential path (Lanni *et al*., 2012) are the factors that play a primary role in landslide activation. Meanwhile, sediments discharged from roads during rainfall events can seriously increase channel erosion and landslide occurrence (Sidle *et al*., 2006). Indeed, the presence of roads in agriculture alters the water flow directions through: i) the interception of superficial and sub-surface water flows; ii) the concentration of flows on the road itself; and iii) the modification of already present flow directions (Borga *et al*., 2004). Therefore, since topography plays a direct role in landslide activation, especially in steep slopes, continuous monitoring of the landscape evolution through geomorphological indicators could provide important information on the road-landslide dynamics. In this context, recent developments in digital photogrammetry (e.g., Structure from Motion; SfM) together with Uncrewed Aerial Vehicles (UAVs) have increased our possibilities to conduct low-cost and recurrent topographic surveys of the Earth surface. Compared to other techniques, such as Light Detection And Ranging (LiDAR), the SfM technique combined with multi-view stereo (MVS) algorithms (hereafter together referred to as SfM) allow us to obtain a high-quality and cost-effective 3D reconstruction of an object starting from a series of two-dimensional images,

taken from different points of view (Westoby *et al*., 2012). Furthermore, it is interesting to evaluate the use of these technologies in the continuous monitoring of landslides in agricultural contexts and investigate the interaction between the presence of infrastructures such as roads and the activation of instability phenomena. High-resolution terrain reconstruction at a detailed scale can be performed through SfM application to carry out an accurate analysis of geomorphological processes involving landslide-prone areas over time. Starting from UAV-SfM data, the multi-temporal comparison of geomorphometric indicators, such as roughness, landform curvature, and feature extraction in landslide-prone zones, can be performed. The continuous development that characterizes these technologies offers countless opportunities for future applications, launching new challenges in different fields. In light of the above, this research proposes a detailed integrated multi-temporal analysis of geomorphological changes involving a terraced vineyard affected by landslides activated near a road network. Multi-temporal (hereafter: 4D) and high-resolution Digital Elevation Models (DEMs),) were used to assess the dynamic of landslide geomorphic features after two subsequent failure events. While the multitemporal survey has already been carried out for deep-seated landslides monitoring, large-scale subsidence or mining activities, its application in high-steep agricultural context to detect the changes of shallow landslide features, activated even by roads, is absolutely novel. More in detail, the geomorphic feature extraction, based on detection of thresholds derived by statistical analysis of landform curvature variability, has been proposed considering a single survey, therefore without addressing multitemporal extraction (Tarolli *et al*., 2012). Thus, the UAV-based multi-temporal monitoring of shallow landslide features (e.g., crowns) dynamics over time represents a further novel aspect of our work. Finally, the proposed research fills the gap in scientific knowledge regarding the possibility of efficiently analysing landslide evolution in agricultural systems by comparing these geomorphometric indexes at hillslope scale, adopting a flexible, low-cost, yet accurate approach.

2.3 Study area

The study area is located in the Trento province, in the southern part of the Trentino Alto Adige region, in northern Italy (Fig. 2.1A). It has an extension of 2.2 ha, with a southwest aspect, an average slope of 27.6°, and an average elevation of 287 m a.s.l. (elevation range between a minimum of 266 m a.s.l. downstream and a maximum of 320 m a.s.l. on the top). The annual average rainfall based on 20-year average values from 10 local stations close to the study area is equal to 1088 mm, with a standard deviation of 222 mm that identifies notable inter-annual rainfall variations. The study area is characterized by terraces constructed on steep slopes (average slope equal to 27.49 degrees) using earth banks, with an inter-row grass cover on the entire cultivated surface. In the study area, three shallow landslides were detected during the two field surveys. The first (18 October 2019) identified a first landslide (L1) below a specific section of the road located in the vineyard (Fig. 2.1C) and another zone involved in older terrain failures (L3, Fig. 2.1E). During the second survey (17 December 2019), an evolution of the L1 zone was observed, with significant involvement of the L1 area. Finally, a further landslide (L2, Fig. 2.1D), about 20 m away from the first, was detected. Factors like steep slopes and high rainfall rates potentially triggered such terrain failures. In this regard, a local weather station recorded an intensity peak equal to 33.6 mm h–1 and other rain events with lower-intensity but longer duration during the weeks preceding the days when the landslides were probably activated, with average values between 0.4 and 1.3-mm h–1, and rainfall duration between 5 and 11 hours. In addition to this, the presence of the road network within the study area can be considered as an additional element, which was potentially responsible for the observed terrain failures. The road was made to reach the highest sections of the vineyard to facilitate some agricultural activities. The road's surface is partly made of concrete (Fig. 2.1B) with some unpaved sections in the whole vineyard. The total length of the road network inside the study area is about 600 m with an average width of about 2 m, on an average slope of 15.7° (slope range between a minimum of 0.03° and a maximum of 19.2°).

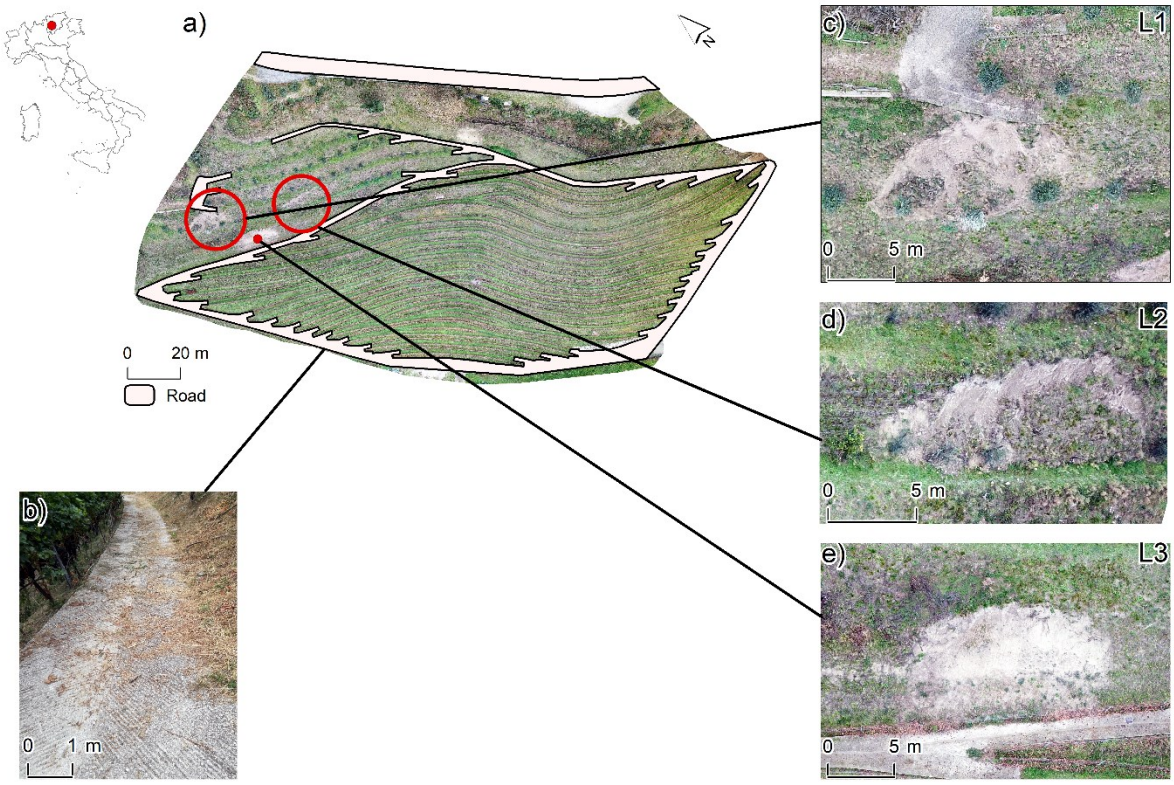

Figure 2.1. *Overview of the entire study area (A) and focus on landslides detected during Uncrewed Aerial Vehicles-Structure from Motion surveys. In particular, this figure shows the paved road surface (B), the first observed landslide (L1, C), the second landslide (L2, D), and the third observed collapsed surface (L3, E).*

2.4 Material and methods

2.4.1 Data collection and processing

2.4.1.1 Landslide overview within the study area

During field inspections, the extension and the thickness of the soil removed by the landslides were measured manually with a stick meter to have an initial overview of their characteristics. The measures taken on the field firstly underlined an increased extension of the L1 surface of more than 50 m^2 (Fig. 2.2). The measurements of the vertical distance between the top of L1 and the ground below were calculated manually during the first and the second survey and were equal to a maximum value of 0.85 m and 1.20 m, respectively. The length of the road section located at the top of L1 was 11.8 m, and L1 was characterized by an average slope of 38 degrees, covering a surface of 44 m^2 and a perimeter of above 34 m. The measurements of L2 revealed an average slope of 40.9 degrees, a surface of more than 60 m^2, a perimeter of about 40 m, and a maximum vertical distance (between its crown and the ground below) equal to 1.10 m. Finally, the characteristics of the third observed failure (L3) did not change between the first and the second UAV survey, with a corresponding surface of 98 m^2, a perimeter of about 45 m, an average slope of 43.4 degrees, and a maximum vertical distance equal to 0.90 m. Considering that, the proposed analysis investigated the land degradation dynamics affecting L1 and L2 zones over time.

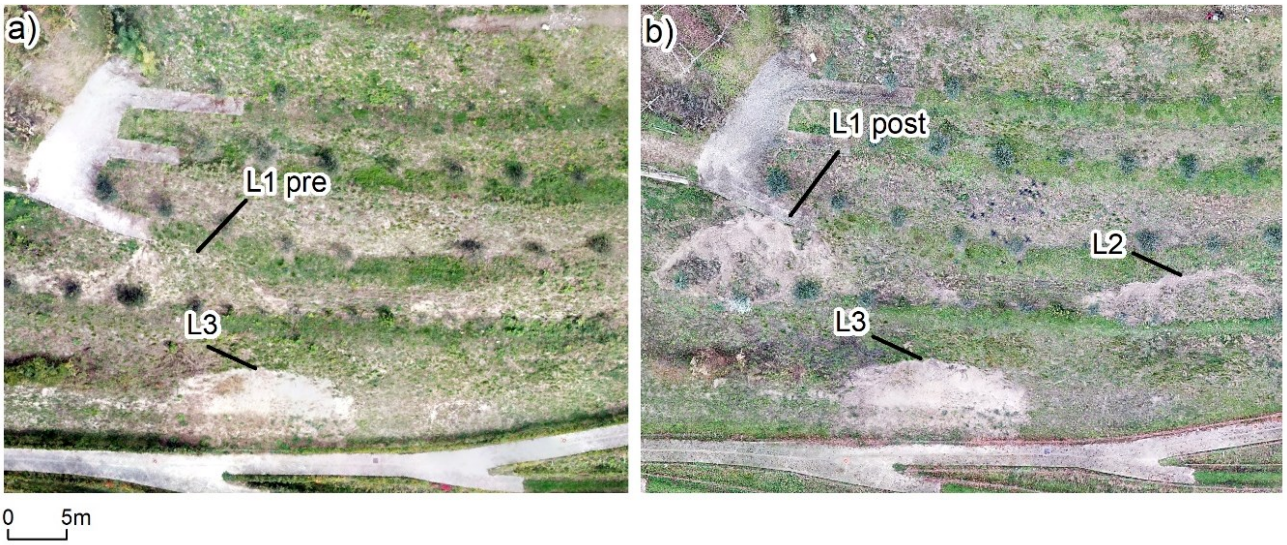

Figure 2.2. *Comparison between landslides detected during the first Uncrewed Aerial Vehicles (UAV) survey (A: 18 October 2019) and the second one (B: 17 December 2019). Both aerial photos were taken during field surveys with UAV.*

2.4.1.2 Uncrewed Aerial Vehicles-Structure from Motion data acquisition

4D UAV-SfM surveys were carried out to compare and detect the differences in topographical and geomorphological terms for the detected landslide. Ground Control Points (GCPs) and Check Points (CPs) were considered as an integral part of the process to reduce errors significantly and check the quality of the output. Particular attention was paid to the location of visible GCPs and CPs in the study area, making sure they were uniformly distributed. Two UAV-SfM surveys were conducted on 18 October 2019 and 17 December 2019, respectively, after two subsequent landslide events. Each survey was planned on days with similar weather conditions and at the same time of day to preserve the quality of the SfM survey. Photos were taken with a DJI Mavic-Pro UAV, which mounts a camera with 1/2.3" sensor (CMOS), focal length 26 mm, 12 M pixel, and a stabilized 3-axes gimbal. The GCPs and CPs were measured using the Geomax Zenith40R GNSS receiver in RTK mode (WGS 84/UTM zone 32N coordinate system; EPSG 32632). To achieve an optimal aerial image overlap and for the subsequent generation of photogrammetric outputs, a detailed flight mission planning is fundamental before image acquisition. In this way, the main parameters concerning both the flight (*e.g.*, speed and altitude of the drone) and the camera (*e.g.*, gimbal tilt and image format) were carefully set. Since the flight altitude is related to the take-off point, the survey was divided into different parts, considering the altitude differences in the entire study area. Nadiral and oblique photographs were integrated to have a complete survey of the vertical (*e.g.*, terrace walls) and horizontal (flat terrace areas) features of the study area. Finally, the surveys were integrated with pictures taken in manual flight mode. In this way, it was possible to focus on specific zones (*e.g.*, the detected landslides) and increase the quality of the outputs significantly. Regarding the first UAV-SfM survey performed, a total of 464 images were taken on a surface of 2.22 ha at a flight altitude of 46 m. The second UAV-based survey covered an equivalent surface at the same altitude, taking a total of 515 images. A total of 23 GCPs and 10 CPs were located among the study area and measured with the GNSS receiver, with an X, Y-Z accuracy between 0.03 and 0.04 m.

2.4.1.3 Structure from Motion data processing

UAV images were processed using the software Agisoft Metashape Pro® v 1.6.2., which makes it possible to reconstruct a three-dimensional model of a surface based on SfM and MVS algorithms. In particular, the procedure included the fundamental steps, *i.e.*, i) camera pre-calibration and removal of low-quality images; ii) SfM step that aligned photos and created a sparse points cloud; iii) GCPs addition for point cloud georeferencing and respective error evaluation; iv) point cloud optimization through a bundle adjustment algorithm; v) elaboration of high-density point cloud; vi) orthomosaic generation. To identify any bias and estimate the accuracy and precision of the obtained point clouds,

1/3 of GCPs were selected and considered as CPs, excluding them in the data georeferencing process (Cucchiaro *et al*., 2018). In this way, an analysis of GCPs and CPs residuals (e.g., the difference between the real coordinates of this point and the modelled values) provide a measure of uncertainty of each point cloud. The mean of the residuals indicates the accuracy of the registration process; the standard deviation of the residuals yields an indication of the precision level (Cucchiaro *et al*., 2018). Furthermore, the Root Mean Square Error (RMSE3D) was computed in x, y, and z directions to check further for potentially biased point errors (Remondino *et al*., 2017).

2.4.1.4 Structure from Motion point cloud post-processing

The obtained point clouds were processed using Cloud Compare software (http://www.danielgm.net), to approach point filtering steps. In this regard, the removal of noises and outliers preserving terrain features and details were performed on both point clouds following two phases. Firstly, manual cleaning was conducted to remove all the points outside the study area, clearly defining its boundaries. Secondly, outliers were removed through the Statistical Outlier Removal (SOR) filter, based on the point cloud library. The SOR algorithm computes the average distance between each point and its neighboring points. It rejects the points beyond a specific threshold, which is calculated based on two parameters: *k* (*i.e*., the number of points to consider in the computation of the mean distance) and *nSigma* (*i.e*., the standard deviation multiplier threshold). Subsequently, point clouds were filtered by selecting only the points belonging to the Earth's surface. This operation is crucial in DEM creation, particularly in complex areas, such as agricultural fields with dense vegetation. Despite numerous semi-automatic algorithms for extracting terrain points from clouds, manual filtering allowed us to carefully clean the point clouds. In this connection, point clouds were divided into regular sections along the line of maximum slope, creating strips and facilitating the cleaning process. Finally, a quality evaluation of the elaborated 3D point clouds was computed, looking at precision, accuracy, and registration errors through the GCPs and CPs quality assessment.

2.4.1.5 Point clouds co-registration and Digital Elevation Models elaboration

To improve the results of the multi-temporal point clouds comparison, the co-registration step was necessary to minimize the spatial difference between them, especially regarding vertical data (*i.e*., the elevation value). To identify the reference point cloud and the aligned one, the RMSE3D values of GCPs and CPs were considered (Table 2.1). Based on these values, the point cloud of December 2019 was chosen as the reference cloud, while the point cloud of the first survey was considered as the aligned one, which was moved during the co-registration procedure. Point clouds co-registration was performed in Cloud Compare, using the Point Pairs Picking tool. Manholes located along the

road network around the vineyard were considered as specific stable point pairs in both point clouds to align. An error analysis was computed by looking at the multiscale model to model cloud comparison (M3C2) distance calculation during the cloud-to-cloud comparison (Lague *et al*., 2013), considering the standard deviation of M3C2 value as precision error for stable areas. Finally, the elaboration of DEMs), was carried out considering the Natural Neighbour Interpolation technique. Based on a subset of surrounding points, it provides a value to the unknown point according to the weight assigned to each one as a function of a proportional area. Subsequently, the interpolation was performed using ArcGIS® software, setting a DEM cell size of 0.15 m to identify specific geomorphological changes and surface alterations. An analysis of DEMs), accuracy was carried out, focusing on the discrepancies between the CPs elevation measurements detected with the GNSS and the corresponding DEM values so as to calculate the RMSE for each digital elevation model.

2.4.2 Morphometric analysis of landslides

2.4.2.1 Relative Path Impact Index

Considering the aims of this research, it is fundamental to better understand if the road's presence plays a potential role in the activation of the observed landslides. To quantify the influence of the road on the alteration of surface flow directions, the Relative Path Impact Index (RPII) was applied (Tarolli *et al*., 2013), investigating the possibility of adopting this method also in a terraced agricultural area. The RPII, mathematically defined by Equation 2.1, is a morphological index that can compute the effects of specific anthropogenic elements (*e.g*., roads and trails) on the distribution of the contributing area and hence of the flow pathways. In particular, the contributing area is considered a proxy of the distribution of the flow paths. The logarithmic form of the index better underlines the zones with an increase of the drainage area due to the road presence.

$$RPII = \ln\left(\frac{A_r - A_{sm}}{A_{sm}}\right) \tag{2.1}$$

Considering the equation above, A_r stands for the contributing area evaluated in the presence of the road network, while A_{sm} represents the contributing area elaborated without any road through a specific DEM smoothing process. In this regard, the drainage areas were calculated following the methodology proposed in Tarolli *et al*. (2013) using the D-Infinity flow direction algorithm. The DEM derived from the first UAV survey was considered in order to focus on the predictive role of RPII in the detection of any alteration of road-induced flow directions. Therefore, the considered

DEM was smoothed applying the quadratic approximation introduced by Evans (1979), as underlined in the following Equation (2.2):

$$Z = ax^2 + by^2 + cxy + dx + ey + f \quad (2.2)$$

where *x*, *y,* and *Z* are local coordinates and parameters *a* to *f* stand for the quadratic coefficients, solved by applying a 91-m moving window to correctly simulate the absence of infrastructures (*i.e.*, the road network). In our case, looking at both DEM resolution and road size, this turned out to be the most appropriate value able to correctly smoothen the considered DEM and avoid excessive reductions in the extent of the terrain elevation model, as a consequence of the smoothing operations. The RPII values are directly proportional to the alteration of flow paths due to the presence of specific anthropogenic features (Tarolli *et al*., 2013).

2.4.2.2 Quantification of morphological changes through Digital elevation models of Difference computation

The geomorphological changes affecting the study area were analysed through DEMs), comparison. This is possible by DEMs subtraction and calculating the total volume of erosion, deposition, and net change through the DEM of difference (DoD) elaboration. DoD was performed with the Geomorphic Change Detection (GCD) ArcGIS ® software (Weaton *et al*., 2010). Due to the morphological complexity of the study area, it was not possible to use a uniform error and consequently apply a simple minimum level of detection (*minLoD*) for the DoD computation (Bossi *et al*., 2015) to achieve efficient results. In this regard, a spatial *minLoD* was applied to threshold correctly any significant changes (Cucchiaro *et al*., 2018) and evaluate spatial uncertainties in each DEM. The multiple error assessment method was performed based on the different types of surfaces in the study area in which the DoD was computed. The various surfaces were divided into stable areas, vegetation, landslides, and zones that were previously excluded in DoD computation (*i.e.*, No Data resulting from the presence of shadows or holes in the computed clouds, as well as zones with low point density). During the DoD elaboration, error surfaces were created for each surface type, considered a specific mask with a respective error value (*i.e.*, 0.044 m for the road network, 0.120 m for vegetation, and 0.044 m for landslides). Error values for the road network and landslides were calculated considering the road as a stable area. The *Multiscale Model to Model Cloud Comparison* (M3C2) tool of cloud compare was used to define the distance between SfM point clouds in these unchanging zones. The standard deviation of M3C2 distance was adopted as precision error for stable areas and landslides to correctly calculate erosion, deposition, and net change volumes. Finally, vegetated surfaces (*i.e.*, vineyard and grass zones located around it) were considered the last surface types with error values related to the

presence of residual vegetation (*i.e.*, low foliage and residual biomass) on the ground, especially along the rows of vines. In this connection, the error value for vegetated surfaces was chosen according to the absolute mean of vertical residual noises within both vineyard and grass zones. The computation of uncertainty values (*i.e.*, precision errors) of each surface type was performed for the two DEM to propagate them during their comparison. The spatially distributed approach was suggested for error propagation and further identification of the final *minLoD* value to analyse successfully any detected geomorphological changes. The *minLoD* value can be calculated based on Equation (2.3) proposed by Brasington *et al.* (2003):

$$minLoD = t\sqrt{(\varepsilon_{1-i})^2 + (\varepsilon_{2-i})^2} \quad (2.3)$$

where *t* stands for spatial distributed Student's *t*-values, while *ε1-I* and *ε2-i* stand for the errors of a specific *i*-pixel for each DEM. The final thresholded DoD was elaborated adopting a *t*-value equal to 1.96, corresponding to a 95% confidence interval (CI) to maintain a conservative approach for the DoD computation. Finally, the budget segregation function of GCD was applied to calculate the erosion and deposition volumes for specific regions of the study area, for which the DoD was elaborated (that is, focus the analysis on landslides zones). The raw DoD was computed, comparing the values of the thresholded DoD with the results of DoD elaborated avoiding the application of a specific minLoD.

2.4.2.3 Multi-temporal comparison of geomorphometric indicators

Land morphological changes were analysed further by the computation of specific geomorphometric indicators. First, a multi-temporal comparison of the curvature and roughness index of landslide-prone areas was computed. In this work, a multi-temporal mapping of curvature changes along the landslide profile was elaborated starting from the analysis of the profile curvature, *i.e.*, the curvature along the vertical plane in the steepest downslope direction (Krebs *et al*., 2015). The selection of specific kernel size in the profile curvature elaboration permitted us to depict the land surface curvature in detail. The profile curvature was calculated with a 9-cell moving window to precisely identify all convexity and concavity zones. In addition to the multi-temporal analysis of the profile curvature, the multi-temporal comparison of the roughness index was elaborated. As underlined by Sofia (2020), the variability of surface roughness can be associated with the occurrence of gravitational processes, such as landslides and erosive phenomena. In this connection, surface roughness can be defined as the standard deviation of residual topography (Cavalli and Tarolli, 2011). Therefore, each computed DEM was smoothed within a 9-cell moving window, looking at the size of the specific features under investigation. The corresponding grid of residual topography was then

created by calculating the cell-by-cell difference between the original DEM and the smoothed one. The standard deviation of residual topography was calculated considering the following Equation (2.4), through the application of specific codes in the GRASS GIS environment:

$$\sigma = \sqrt{\frac{\sum_{i=1}^{n}(x_i - x_m)^2}{n}} \tag{2.4}$$

where σ stands for the roughness index, n is the number of processed cells in the moving window, xi is the value of the i-cell of the residual topography within the selected moving window, and xm is the mean of the processed cells within the 9-cell moving window.

2.4.2.4 Multi-temporal feature extraction

To perform a multi-temporal feature extraction, the maximum curvature (C_{max}) was calculated to highlight local surface convexity identified in slope discontinuities and consequently related to landslide-prone surfaces (Tarolli *et al*., 2012). C_{max} was elaborated following the multi-scale parameterization proposed by Wood (1996). Accordingly, it is possible to evaluate C_{max} using the following Equations (2.5 and 2.6):

$$C_{max} = -a - b + \sqrt{(a-b)^2 + c^2} \tag{2.5}$$

$$C_{max} = k * g\left(-a - b + \sqrt{(a-b)^2 + c^2}\right) \tag{2.6}$$

where *a, b* and *c* are quadratic coefficients, *g* is the DEM grid resolution, and *k* is the size of the selected moving window. A 9-cell moving window was chosen for C_{max} computation to adequately proceed in features extraction overlooking the presence of irrelevant elements. The interquartile range (IQR) was used to define the threshold value of C_{max}. In particular, a threshold equal to 1.5 IQR of C_{max} was adopted as a suitable threshold for shallow landslide feature extraction, as already demonstrated in Tarolli *et al*. (2012), where similar shallow landslide features were considered. The following Equation (2.7) was adopted in the calculation:

$$C_{max} > m * IQR_{C_{max}} \tag{2.7}$$

where *m* is the selected multiplication factor, and *IQR* stands for the difference between the third and the first quartiles. Landserf and Matlab® software packages were used for C_{max} elaboration and its respective threshold evaluation. The accuracy of extracted features for both L1 and L2 was assessed, considering that the process of features classification is affected by statistical errors. After defining the null hypothesis, in this case corresponding to the condition in which the study area is not involved in landslides, it is necessary to define whether it was correctly discarded in favor of the alternative

one (*i.e.,* the presence of landslide features within the detected study area) through the feature extraction procedure. Therefore, type I error is shown if the null hypothesis is rejected, when indeed it is true. On the contrary, type II error occurs when the null hypothesis is accepted, when indeed it is false. Type I error stands for false-positive, and type II error for false negative (Tarolli *et al.,* 2012). To verify the accuracy of the extracted features, they were compared with the features of L1 and L2 mapped and rasterized from orthophoto and field data. Considering the landslide measures collected on the field, a buffer of 1.5 m was created on each side of the L1, and L2 reference features, respectively, to envelope convex slope breaks and to correct issues related to horizontal accuracy misstatements of each DEM. The goodness of feature extraction was analysed by calculating the quality index (Equation 2.8) proposed by Heipke *et al.* (1997):

$$Quality = \frac{TP}{TP+FP+FN} \tag{2.8}$$

where TP are true positives (*i.e*., the features which are correctly detected by the extraction method), FP are false positives (defined as the extracted features that do not correspond to the field observations), and FN are false negatives (*i.e*., zones within the buffer that are not extracted by the adopted method). The quality index ranges between 0 (for no overlap between extracted and observed features) and 1 (for perfect overlap between extracted and observed features) (Tarolli *et al.,* 2012).

2.5 Results

2.5.1 Structure from Motion error assessment

An overview of main parameters and errors computation of the SfM point clouds is presented in the following Table 2.1, which highlights the magnitude in centimetres of the overall accuracy of the SfM surveys, described by the respective GCPs and CPs errors.

Table 2.1. *Main errors in the Structure from Motion surveys point clouds.*

Point cloud	**Point cloud (number of points)**	**Point cloud accuracy (m)**			**Point cloud precision (m)**			**RMSE 3D CPs (m)**	**RMSE 3D GCPs (m)**
		x	**y**	**z**	**x**	**y**	**z**		
Survey 1 (18 October 2019)	78,940,480	0.040	0.020	0.035	0.020	0.026	0.037	0.057	0.039
Survey 2 (17 December 2019)	67,120,287	0.017	0.016	0.038	0.014	0.012	0.026	0.046	0.039

The table shows the number of points of the two computed dense point clouds, point cloud accuracy [described by the absolute mean of check points (CPs) residuals] and point cloud precision (described by standard deviation of CPs residuals) for the two Uncrewed Aerial Vehicles surveys, and root mean square error (RMSE 3D) total value observed during point cloud elaboration, respectively regarding ground control points (GCPs) and CPs.

The values of the M3C2 distance are in centimetres, further underlining the quality of the computed analysis. The uncertainty values of each detected surface type were identified by looking at each UAV-derived point cloud (Table 2.2). The co-registration process was then performed to obtain a final RMS value (*i.e.*, the co-registration error) equal to 0.045 m. Finally, DEM_{RMSE} was equal to 0.103 m and 0.058 m, respectively, for the first and the second computed digital elevation model.

2.5.2 Relative Path Impact Index

Fig. 2.3A shows the detail of the RPII index close to the L1 location. Fig. 2.3B shows that a specific section of the road is potentially involved in alterations of the water flows and consequently in the

detected geomorphological changes. Moreover, the evident alteration of the water flows located to the left of the L1 area consists of a zone that is not currently affected by land degradation. However, this could be potentially predictive of a worsening of the present situation in the future. Furthermore, concerning the RPII index near the L2 zone (Fig. 2.3C), it appears that the unpaved section of the road network located above the L2 area is potentially responsible for the alterations of the shallow water flows toward the zone affected by the landslide (Fig. 2.3D). As the figure shows, there is a marked alteration of the flow paths (identified by medium-high RPII values) starting from that section of the unpaved road upwards to intercept the L2 area and then reaching the underlying paved road. The RPII index underlines the primary role played by the presence of the road in the terraced vineyard in the alteration of the water flows, thus potentially triggering the activation of landslides.

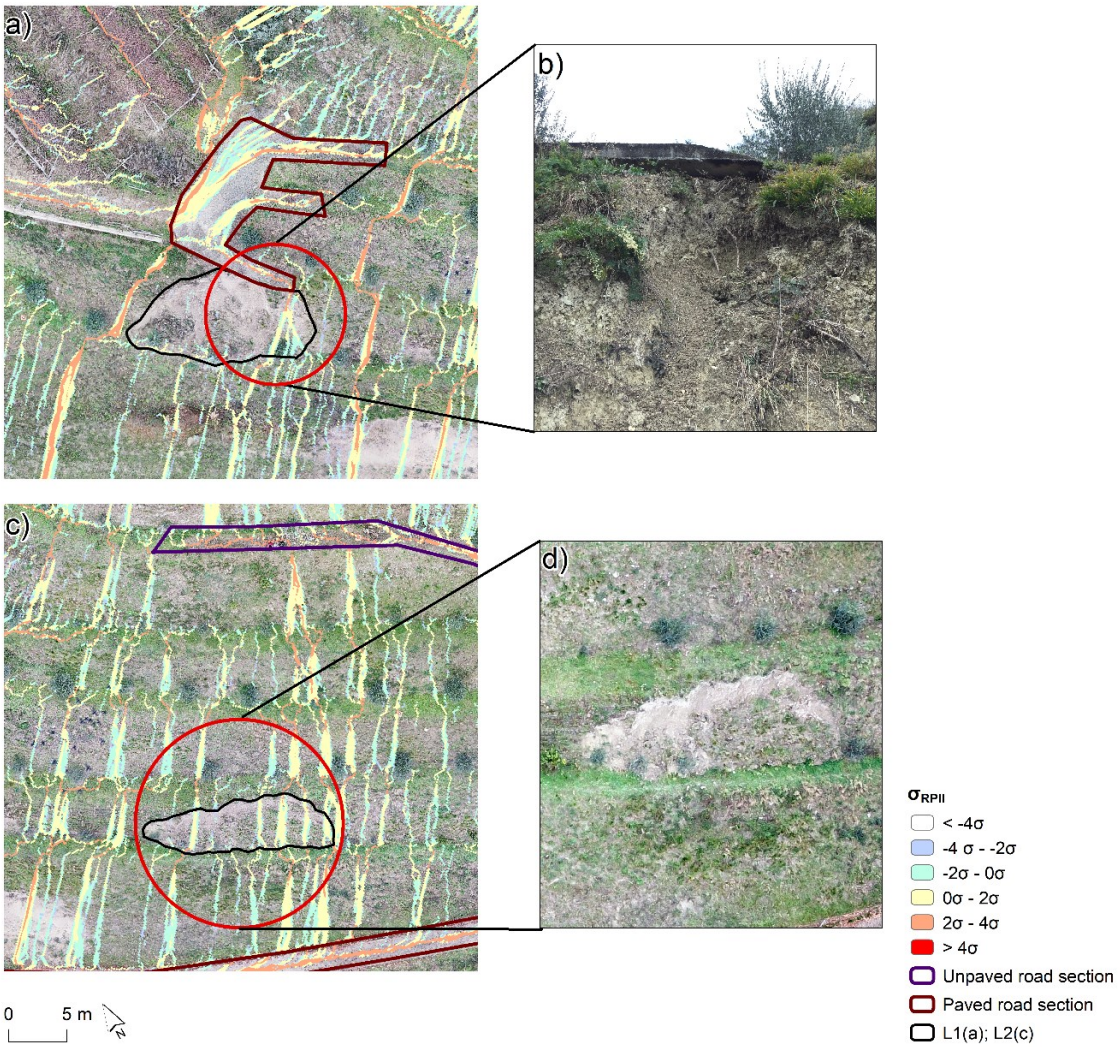

Figure 2.3. *Detail of relative path impact index (RPII) underlining the flow alterations close to the paved section of the road, located upstream to the L1 (A) and L2 (C) zones and focus on L1 (B) and L2 (D) areas under the specific road section. Critical zones, identified by the higher σRPII values (reddish colours) represent the flow concentrations due to the presence of the road. In particular, the red circles highlight such alteration close to the road segment located upstream the L1 (A) and L2 zone (C).*

2.5.3 Digital elevation models of Difference

Fig. 2.4A illustrates the thresholded DoD (95% CI) elaborated for the entire study area. Erosion and deposition surfaces for both L1 (Fig. 2.4B) and L2 zones (Fig. 2.4C) are notable, while erosion areas into the vineyard mainly derive from small residual discrepancies in the filtering processes. Results from budget segregation are reported in Table 2.2 and in the bar plots of volumetric changes (Fig. 2.4D and E). Table 2.2 highlights that differences between the raw DoD values and the thresholded DoD are in the order of a few centimetres, thus showing low uncertainties in the accuracy of the volume estimation.

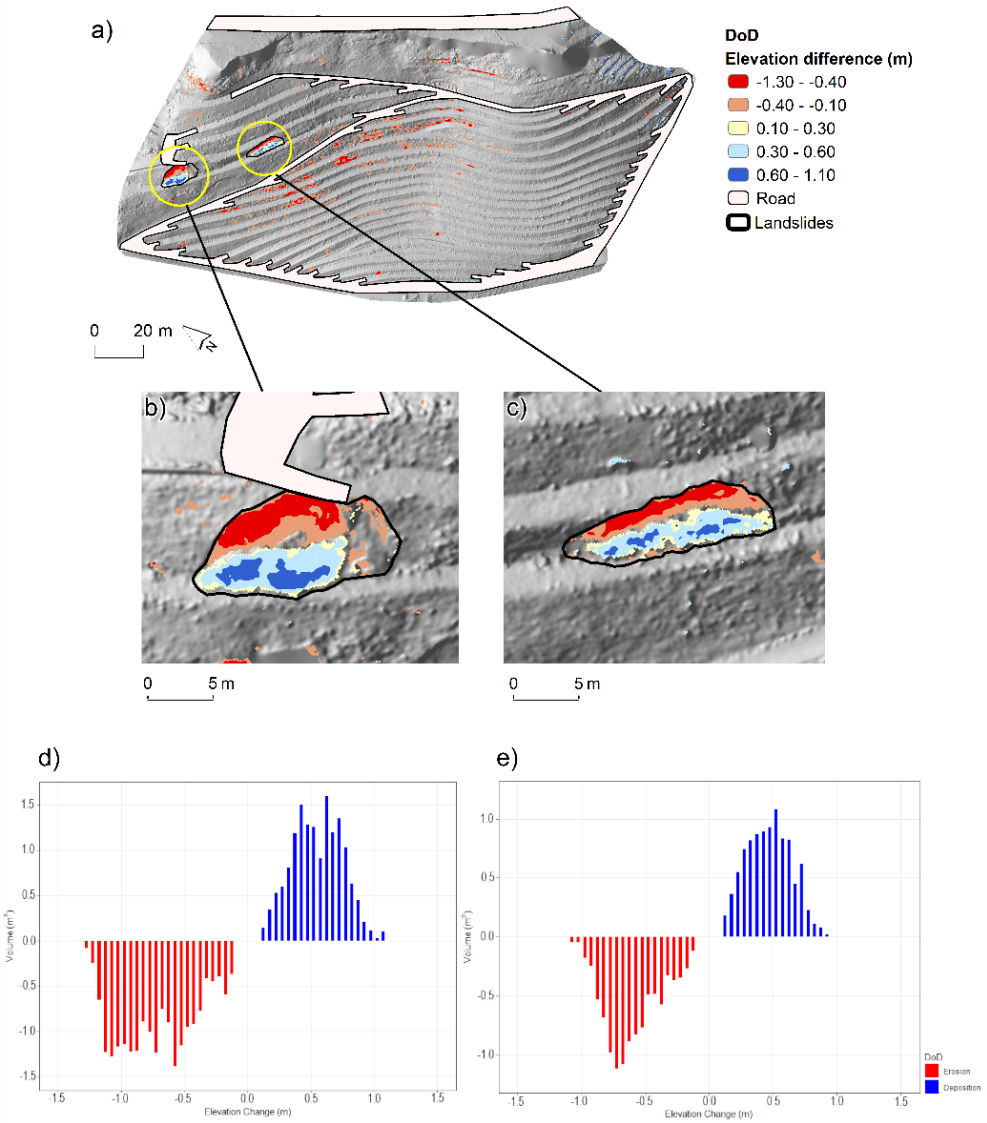

Figure 2.4. *Overview of the computed digital elevation models of difference (DoD) (95% confidence interval) (A) and focus on DoD elaborated for the L1 (B) and L2 zones (C). Erosion is shown in reddish colours, deposition in blue. The figure also shows the bar plot of elevation changes regarding volumetric erosion and deposition values derived from budget segregation results computed for the L1 (D) and L2 zones (E) respectively.*

Table 2.2. *Detail of budget segregation results for the digital elevation models of difference (DoD) computed for L1 and L2. The table shows the results of thresholded DoD and their respective raw DoD results for each detected landslide.*

DoD	**Thresholded DoD (95% IC)**			**Raw DoD**		
December 2019-October 2019	**Erosion (m^3)**	**Deposition (m^3)**	**Net volume difference (m^3)**	**Erosion (m^3)**	**Deposition (m^3)**	**Net volume difference (m^3)**
L1	20.49 ± 2.29	15.26 ± 2.03	-5.23 ± 3.06	21.49	15.64	-5.84
L2	10.34 ± 1.29	9.61 ± 1.52	-0.73 ± 1.99	10.69	9.95	-0.74

DoD, digital elevation models of difference; CI, confidence interval.

Considering the computed DoD, the adoption of the multiple error assessment method, whereby the DoD results are stripped according to specific error surfaces (Wheaton *et al*., 2010; Cucchiaro *et al*., 2018), allowed us to make a detailed volumetric estimation of erosion and deposition surfaces. In our case, threshold values describing the volumetric results underline the successful implementation of DoD related to the detected landslides.

2.5.4 Multi-temporal comparison of geomorphometric indicators

The computation of profile curvature for L1 and L2 zones is presented in Fig. 2.5, which highlights the worsening of the L1 zone due to the presence of several upwardly convex surfaces (reddish colours, Fig. 2.5C). With reference to Wilson and Gallant (2000), net erosion areas correspond to profile convexity zones, while net deposition areas correspond to profile concavity zones. Moreover, the profile curvature is parallel to the direction of the maximum slope (Krebs *et al*., 2015). In Fig. 2.5A and Fig. 2.5C, convex surfaces are identified by the positive values of the profile curvature. The comparison with the profile curvature elaborated for the same landslide area observed during the first UAV survey (*i.e*., L1-pre) (Fig. 2.5A) highlights the geomorphological changes of the L1 zone. Likewise, the activation of L2 is underlined by the presence of high values of the profile curvature close to it (Fig. 2.5D) with respect to the observations made in the same zone before its activation

(Fig. 2.5B). The computation of the profile curvature also shows negative values (blue colours) within each landslide's surface. These values indicate upwardly concave surfaces, which can potentially be deposition areas due to terrain failures and land movement into each landslide zone. Fig. 2.5 also shows the multi-temporal comparison of the roughness index calculated for L1 and L2. The roughness index calculation as the standard deviation of residual topography allowed us to calculate the surface roughness, which was not affected by the influence of slope variability along the surface. The evolution of L1 and L2 between the two UAV surveys can be recognised through the local variabilities of the elevation values (Fig. 2.5E-H). In the figure above, the higher values of the roughness index can be seen close to the top of the landslides (Fig. 2.5G and H), while the concurrent presence of high roughness values upstream and downstream the L2 zone mainly derive from the remaining noises of the residual topography computation. At the same time, lower roughness values correspond to flat areas, such as the road network or the grass surfaces close to the detected landslides.

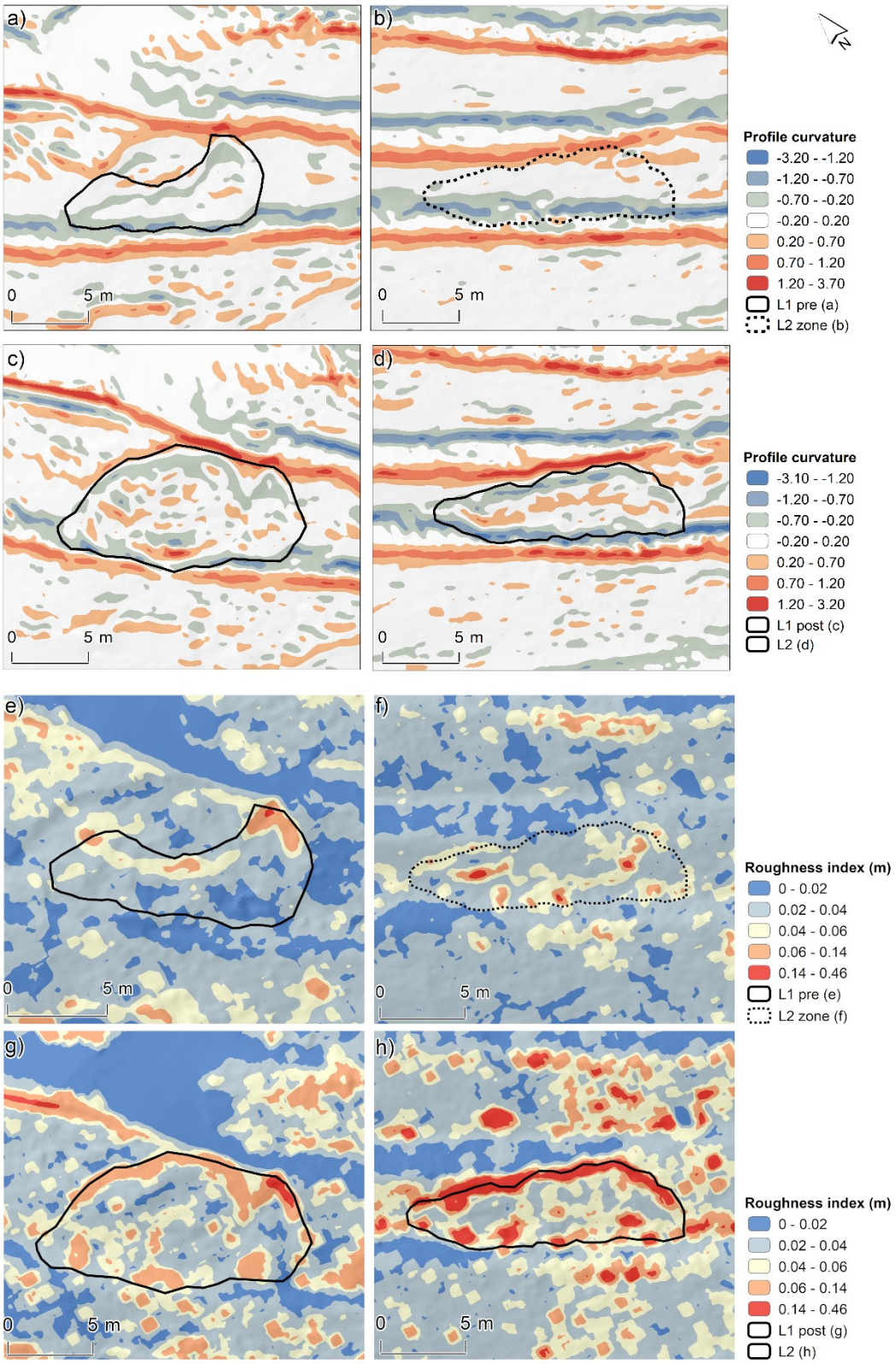

Figure 2.5. *Multi-temporal comparison of profile curvature computed for L1-pre (A) and L1-post (C) and for L2 (D). Figure 2.5B shows the profile curvature elaborated for the zone affected by L2, before its occurrence. This figure also shows the multi-temporal comparison of the roughness index performed for L1-pre (E), L1-post (G) and L2 (H). Figure 2.5F shows the roughness index elaborated for the zone affected by L2, before its occurrence.*

2.5.5 Multi-temporal feature extraction

The multi-temporal comparison of maximum curvature and feature extraction for L1 and L2 is outlined in Fig. 2.6. The evolution of L1 is shown by the elaboration of the curvature and the consequent features extraction. The comparison of the curvature maps elaborated for L1-pre and L1-post (Fig. 2.6A and B) shows an increase of the curvature values, which correspond to the convex slope breaks close to the collapsed terrain. In this regard, the feature extraction using 1.5 IQR as a threshold value successfully describes the evolution of L1 features (Figure 2.6C and D). Some noises affect the result of feature extraction, and their presence is mainly due to the choice of the *m* factor (see Equation 2.7). When this parameter increases, the feature recognition is more efficient with a concurrent reduction of hillslope noises. At the same time, however, exaggerated values of *m* can lead to the loss of information about the features being extracted (Tarolli *et al.,* 2012). Likewise, Fig. 2.6E-H shows the multi-temporal mapping of C_{max} and the feature extraction for the L2 zone before and after the landslide occurred. This figure shows an increase of the curvature values upstream the L2 site (Fig. 2.6E and F) and the presence of high C_{max} values within the L2 surface with respect to the curvature map elaborated for the same area before L2 activation. The L2-feature extraction highlights the landslide activation, underlining specific convexities that correspond to the extracted features themselves. A low presence of hillslope noises among the detected L2 surface (Fig. 2.6G and H) is evident, especially in the L2 area observed during the first UAV survey (Fig. 2.6G). The results indicate an overall consistency between the extracted and the referenced features, with a quality index equal to 0.22 for L1-pre, 0.63 for L1-post, and 0.69 for L2. Fig. 2.6 shows a multi-temporal comparison between observed and extracted features for L1 and L2. The red arrows in Fig. 2.6C, D and H, highlight the match between the detected and extracted features for both L1 and L2. At the same time, this figure also shows the presence of many detected features that were not successfully extracted by the adopted methodology. These areas of mismatch between what was on the field and what was subsequently elaborated in terms of extracted features mainly represent false positives data (*i.e.*, type I errors).

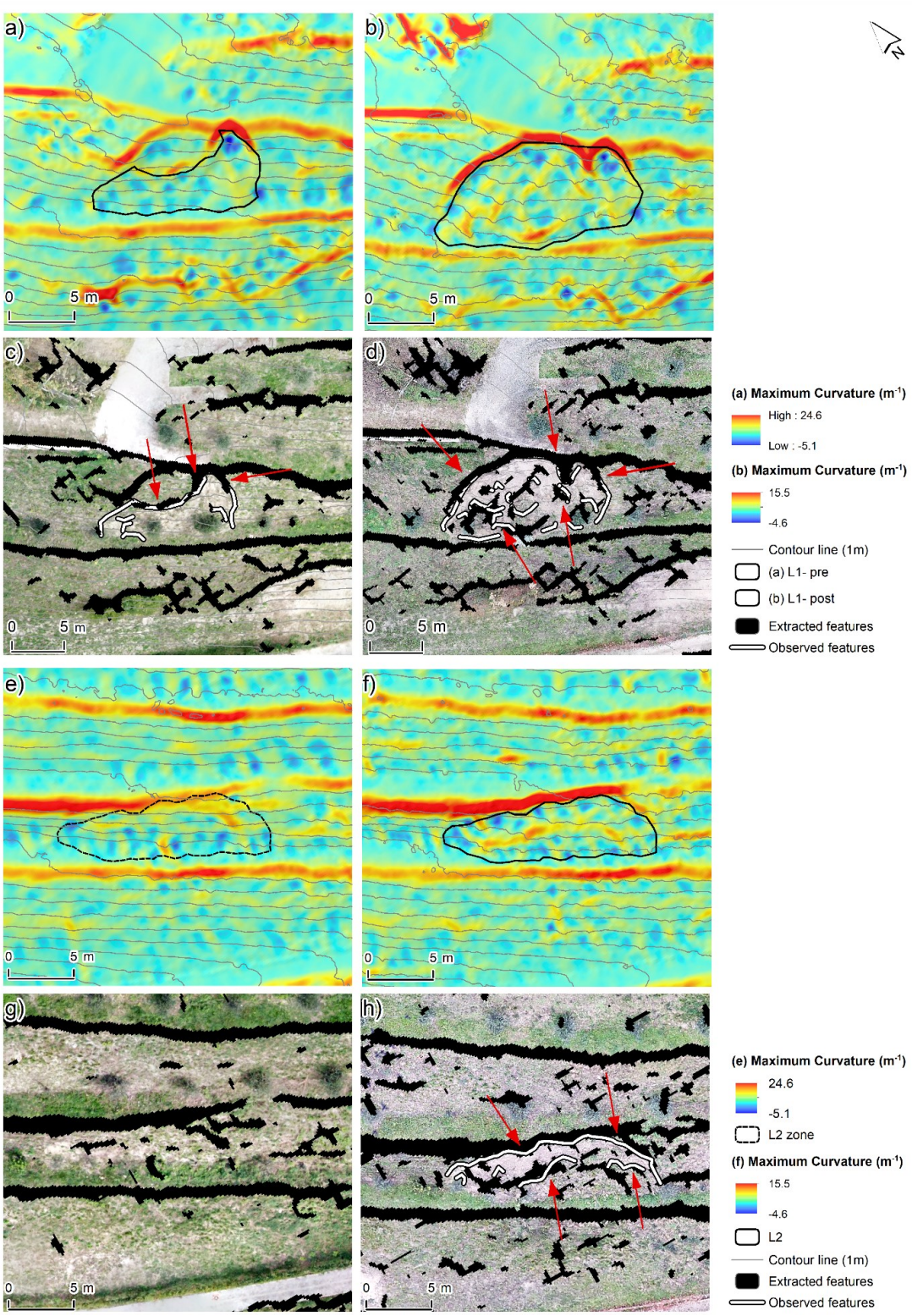

Figure 2.6. *Multi-temporal comparison of Cmax computed for L1-pre (A), L1-post (B), L2 zones before (E) and after (F) its occurrence, and multi-temporal comparison between observed and extracted features for L1-pre (C), L1-post (D), L2 zones before (G) and after (H) the failure. The red arrows indicate the position of the extracted features as observed during the field surveys.*

2.6 Discussion

This article proposes an analysis of the monitoring process of shallow landslides activated in a steep terraced agricultural system through an innovative multi-temporal comparison of geomorphometric indicators using a multitemporal survey. Our work further highlights the efficiency of 4D UAV-based SfM surveys in this kind of analysis in line with other useful UAV applications in agricultural contexts (Tucci *et al.,* 2019; Yamazaki *et al.,* 2019). The elaboration of high-resolution DEMs), allowed the computation of some key morphometric indexes to better understand the Earth surface physical process considered in our analysis. The mapping of the RPII index, for example, revealed values between 2σ and 4σ close to the road sections located above L1 and L2, showing the role played by the road network in the alteration of water flow directions, thus triggering the activation of landslides. Similar analyses were presented in Tarolli *et al.* (2013), where the RPII was applied in a mountain environment for the detection of surface water flow alteration and erosion due to mountain trails and forest roads, and in Tarolli *et al.* (2015) for the evaluation of the role of agricultural roads in the activation of soil erosion processes. The novel point of our work is the application of the RPII to multitemporal DEMs to test its predictive capability for shallow landslide phenomena. The obtained results emphasized its efficiency in identifying potentially critical interactions between the road and water directions. This information could be useful for providing effective soil and water conservation measures to mitigate the phenomena (*e.g.*, ditches). Our work also, confirmed the advantages of RPII with respect to other indexes like the index of connectivity (Cavalli *et al*., 2013) or the simple elaboration of water flow directions. While these latter are useful for detecting sediment connectivity toward specific features and the investigation of unaltered water flow dynamics, the RPII represents a rapid and efficient tool to analyse landslide triggering on terraced agricultural systems. The DoD elaboration led to a detailed volumetric estimation of erosion and deposition surface close to the collapsed hillslopes. In this connection, our research further highlights that the multiple error assessment in DoD computation can be successfully implemented in the multi-temporal investigation of landslide dynamics affecting very steep terraced agricultural systems at the hillslope scale. Comparable analyses were proposed by Wheaton *et al.* (2010), Vericat *et al.* (2017) and Cucchiaro *et al.* (2018), who investigated different environmental contexts and purposes, focusing on the possibility to adopt a spatially distributed error evaluation in the investigation of geomorphological changes affecting areas with complex topography. The innovative multi-temporal comparison of profile curvature, roughness and feature extraction proved a valuable tool to describe in-depth the evolutionary dynamics of specific landslide features, such as their crown and other detected geomorphological changes affecting the terraced agricultural area under study on a field scale over

time. The UAV-based multi-temporal analysis of shallow landslide crown evolution in a high-steep agricultural landscape is a novelty that deserves attention for planning useful mitigation strategies. Finally, the computation of the quality index was equal to 0.22 (L1-pre), 0.63 (L1-post), and 0.69 (L2), thus underlining the efficiency of features extraction and further supporting the quality of the presented outcomes and the validity of the adopted methodology. Compared to the results obtained in Tarolli *et al.* (2012), where landslide crown features were extracted in complex landscapes, the values of the quality index obtained in our work indicate better performance (L1-post and L2). Therefore, this confirms that a UAV-based multi-temporal survey, carried out with proper attention, could be an excellent tool for monitoring landslide occurrence in terraced agricultural hillslopes over time.

2.7 Conclusions

This work proposes a multi-temporal computation of geomorphometric indicators to provide a detailed analysis of the landslide dynamics affecting a very steep slope terraced agricultural system. The focus was on landslides activated by roads. We considered high-resolution digital elevation models derived from two UAV photogrammetry surveys. The 4D comparison of geomorphometric indicators revealed to be an efficient tool in the study of geomorphological changes at the field scale. The study of this topic through the proposed methodology can be a well-grounded starting point to further investigations on a larger scale. The analyses presented in this work can be seen as a useful tool for mapping landslide phenomena affecting agricultural areas, focusing on the role of road networks in their activation. This topic still needs to be deeply investigated in the literature. The geomorphic indexes tested in the work (RPII, roughness index, landform curvature) and the quantification of the soil eroded and deposited by landslides through the geomorphic change detection approach helped us to better understand (thanks to the details of the considered microtopography) the discussed phenomena in the investigated steep agricultural terraced hillslope. We believe that these findings will provide a basis for additional analysis regarding the influence of road management and design on land degradation dynamics, which are responsible for severe economic losses, geomorphological changes, and environmental alterations of agricultural systems as a whole. In this way, the proposed results and the obtained thematic maps could be useful to identify and implement sustainable actions for more efficient management of this aspect. Specific interventions on soil management, bank stabilization, and restoration could be carried out starting from the comparison of roughness, curvature, and feature extraction over time to promptly find out efficient mitigation strategies to reduce the occurrence of risk scenarios. Further investigations could be undertaken to analyse in greater depth this topic in hydrological terms, focusing on the design of alternative drainage systems along the roadway and close to the collapsed surfaces. In this connection, a more extensive scientific knowledge can be gained on the role played by roads in the alterations of superficial and sub-surface water dynamics linked with the occurrence of landslides also in agricultural systems. Moreover, identifying areas that can be potentially exposed to landslide activation represents a relevant aspect for landowners and farmers. Therefore, this has a primary relevance especially where the presence of infrastructures like roads and trails is fundamental in term of productivity and cropland management, but can also represent one of the main causes for landslides and land degradation processes.

Acknowledgements

The authors kindly thank Gabriele Bombardelli - Acetaia del Balsamico Trentino, owner of the terraced vineyard considered in the investigation of the observed land degradation processes.

2.8 References

Bajocco S., De Angelis A., Perini L., Ferrara A., Salvati L. (2012). The impact of Land Use/Land Cover Changes on land degradation dynamics: A Mediterranean case study. Environmental Management, 49, 980-9. DOI 10.1007/s00267-012-9831-8

Borga M., Tonelli F., Selleroni J. (2004). A physically based model of the effects of forest roads on slope stability. Water Resour. Res., 40. https://doi.org/10.1029/2004WR003238

Bordoni M., Vercesi A., Maerker M., Ganimede C., Reguzzi M.C., Capelli E., Wei X., Mazzoni E., Simoni S., Gagnarli E., Meisina C. (2019). Effects of vineyard soil management on the characteristics of soils and roots in the lower Oltrepo Apennines (Lombardy, Italy). Sci. Total Environ., 693, 133390. https://doi.org/10.1016/j.scitotenv.2019.07.196

Bossi G., Cavalli M., Crema S., Frigerio S., Quan Luna B., Mantovani M., Marcato G., Schenato L., Pasuto A. (2015). Multi-temporal LiDAR-DTMs as a tool for modelling a complex landslide: A case study in the Rotolon catchment (eastern Italian Alps). Nat. Hazards Earth Syst. Sci., 15, 715-722. https://doi.org/10.5194/nhess-15-715-2015

Brasington J., Langham J., Rumsby B. (2003). Methodological sensitivity of morphometric estimates of coarse fluvial sediment transport. Geomorphology, 53, 299-316. https://doi.org/10.1016/S0169-555X(02)00320-3

Cavalli M., Tarolli P. (2011). Application of LiDAR technology for rivers analysis. Ital. J. Engine. Geol. Environ., 1, 33-44. https://doi.org/10.4408/IJEGE.2011-01.S-03

Cavalli M., Trevisani S., Comiti F., Marchi L. (2013). Geomorphometric assessment of spatial sediment connectivity in small Alpine catchments. Geomorphology, 188, 31-41. https://doi.org/10.1016/j.geomorph.2012.05.007

Cucchiaro S., Cavalli M., Vericat D., Crema S., Llena M., Beinat A., Cazorzi F. (2018). Monitoring topographic changes through 4D-structure-from-motion photogrammetry: application to a debris-flow channel. Environ. Earth Sci., 77, 632. https://doi.org/10.1007/s12665-018-7817-4

Eker R., Aydin A. (2014). Assessment of forest road conditions in terms of landslide susceptibility: A case study in Yığılca Forest Directorate (Turkey). Turkish J. Agricult. Forestry, 38, 281-90. DOI: 10.3906/tar-1303-12

Evans I.S. (1979). An integrated system of terrain analysis and slope mapping. Dept. of Geography, University of Durham, England (Eds)

Heipke C., Mayer H., Wiedemann C., Jamet O. (1997). Automated reconstruction of topographic objects from aerial images using vectorized map information. Int. Archiv. Photogramm. Remote Sens., 23, 47-56.

Krebs P., Stocker M., Pezzatti G.B., Conedera A. (2015). An alternative approach to transverse and profile terrain curvature. Int. J. Geogr. Inf. Sci, 29, 643-66. DOI: 10.1080/13658816.2014.995102

Lague D., Brodu N., Leroux J. (2013). Accurate 3D comparison of complex topography with terrestrial laser scanner: application to the Rangitikei canyon (NZ). J. Photogramm. Remote Sens., 82, 10-26. https://doi.org/10.1016/j.isprsjprs.2013.04.009

Lanni C., Borga M., Rigon R., Tarolli P. (2012). Modelling shallow landslide susceptibility by means of a subsurface flow path connectivity index and estimates of soil depth spatial distribution. Hydrol. Earth Syst. Sci., 16, 3959-3971. DOI: 10.5194/hess-16-3959-2012

Persichillo M.G., Bordoni M., Cavalli M., Crema S., Meisina C., (2018). The role of human activities on sediment connectivity of shallow landslides. Catena, 160, 261-274. https://doi.org/10.1016/j.catena.2017.09.025

Remondino F., Nocerino E., Toschi I., Menna F. (2017). A critical review of automated photogrammetric processing of large datasets. Int. Archiv. Photogramm. Remote Sens. Spatial Inf. Sci., 42, 591-9. https://doi.org/10.5194/isprs-archives-XLII-2-W5-591-2017

Salvati L., Mavrakis A., Colantoni A., Mancino G., Ferrara A. (2015). Complex adaptive systems, soil degradation and land sensitivity to desertification: a multivariate assessment of Italian agro-forest landscape. Sci. Total Environ., 521, 235-45. https://doi.org/10.1016/j.scitotenv.2015.03.094

Sidle R.C., Ziegler A.D. (2012). The dilemma of mountain roads. Nature, 5, 437-8. https://doi.org/10.1038/ngeo1512

Sidle R.C., Ziegler A.D., Negishi J.N., Rahim A., Siew R., Turkelboom F. (2006). Erosion processes in steep terrain-truths, myths and uncertainties related to forest management in Southeast Asia., 224, 199-225. https://doi.org/10.1016/j.foreco.2005.12.019

Sofia G. (2020). Combining geomorphometry, feature extraction techniques and Earthsurface processes research: the way forward. Geomorphology, 355. https://doi.org/10.1016/j.geomorph.2020.107055

Tarolli P., Sofia G., Dalla Fontana G. (2012). Geomorphic features extraction from high-resolution topography: Landslide crowns and bank erosion. Nat. Hazards, 61, 65-83. https://doi.org/10.1007/s11069-010-9695-2

Tarolli P., Calligaro S., Cazorzi F., Dalla Fontana G. (2013). Recognition of surface flow processes influenced by roads and trails in mountain areas using high resolution topography. Eur. J. Remote Sens., 46, 176-97

Tarolli P., Sofia G., Calligaro S., Prosdocimi M., Preti F., Dalla Fontana G. (2015). Vineyards in terraced landscapes: new opportunities from LiDAR data. Land Degrad. Develop., 26-92- 102. https://doi.org/10.1002/ldr.2311

Tucci G., Parisi E.I., Castelli G., Errico A., Corongiu M., Sona G., Viviani E., Bresci E., Preti F. (2019). Multi-Sensor UAV Application for Thermal Analysis on a Dry-Stone Terraced Vineyard in Rural Tuscany Landscape. ISPRS Int. J. Geo-Inf., 8 (2), 87. https://doi.org/10.3390/ijgi8020087

Vericat D., Wheaton J. M., Brasington J. (2017). Revisiting the morphological approach: opportunities and challenges with repeat high-resolution topography. In: D. Tsutsumi, J.B. Laronne (Eds), Gravel-bed rivers: processes and disasters, Wiley, Oxford, 121-158. DOI: 10.1002/9781118971437.ch5

Webb N.P., Marshall N.A., Stringer L.C., Reed M.S., Chappell A., Herrick J.E. (2017). Land degradation and climate change: building climate resilience in agriculture. Front. Ecol. Environ., 15 (8),450-459. https://doi.org/10.1002/fee.1530

Wheaton J.M., Brasington J., Darby S.E., Sear D.A. (2010). Accounting for uncertainty in DEMs from repeat topographic surveys: improved sediment budgets. Earth Surf. Process Landf., 35 (2), 136-156. https://doi.org/10.1002/esp.1886

Westoby M.J., Brasington J., Glasser N.F., Hambrey M.J., Reynolds J.M. (2012). Structure-from-Motion' photogrammetry: A low-cost, effective tool for geoscience applications. Geomorphology, 179, (15), 300-14. https://doi.org/10.1016/j.geomorph.2012.08.021

Wilson J.P., Gallant J.C. (2000). Digital terrain analysis, in terrain analysis: principles and applications. John P. Wilson, John C. Gallant (Eds). ISBN: 978-0-471-32188-0

Wood J. (1996). The geomorphological characterization of digital elevation models. Ph.D. Thesis, University of Leicester, UK.

Yamazaki Y., Okazawa H., Sekiyama A., Fujikawa T. (2019). Accuracy Verification of UAV-SfM Survey of Terrace Paddy Fields in a Hilly and Mountainous Area. Int. J. Environ. Rural Develop., 10, 153-9. https://doi.org/10.32115/ijerd.10.1_153

CHAPTER 3

MULTI-TEMPORAL MODELING OF ROAD-INDUCED OVERLAND FLOW ALTERATIONS IN A TERRACED LANDSCAPE CHARACTERIZED BY SHALLOW LANDSLIDES[2]

Luca Mauri,[1] Eugenio Straffelini,[1] Paolo Tarolli[1]

[1]*Department of Land, Environment, Agriculture and Forestry, University of Padova, Legnaro, Italy*

Keywords: Terraced landscapes, Road, Landslide, Remote sensing, DEM

[2] Mauri, L., Straffelini, E., Tarolli, P. (2022). Multi-temporal modeling of road-induced overland flow alterations in a terraced landscape characterized by shallow landslides. ***International Soil and Water Conservation Research***, 10 (2): 240-253. https://doi.org/10.1016/j.iswcr.2021.07.004

3.1 Abstract

The presence of roads in high steep agricultural systems is often linked with landslides occurrence. This research aims to model multi-temporal overland flow dynamics in a shallow landslides-prone terraced landscape (northern Italy). The combined use of Remotely Piloted Aircraft Systems (RPAS) and photogrammetric techniques (e.g., Structure from Motion-SfM) allowed to elaborate multi-temporal high resolution Digital Elevation Models (DEMs). Hydrological analyses of water flow's depth alterations due to the road presence were carried out adopting the SIMulated Water Erosion model (SIMWE), focusing on different scenarios considering the presence of the road and assuming its absence through a specific DEM smoothing procedure. The possibility to perform multi-temporal hydrological simulations at a hillslope scale so as to analyse the role played by the road in overland flows alteration is still a challenge to be investigated. Results proved the role played by the road in water flows change above the two observed shallow landslides, with respective maximum water depth values equal to 0.18 m and 0.14 m. On the contrary, no-road simulations not revealed significant water flows deviations towards landslides, with water depth values around 0 m, underlining that the absence of the road would avoid relevant changes in water flow paths toward the collapsed surfaces. This work could be a solid starting point for analyse road impact on runoff dynamics and hillslopes stability also at a wider scale, as well as for planning efficient mitigation intervention so as to reduce the occurrence of similar future scenarios.

3.2 Introduction

Nowadays, one of the major issues affecting agricultural systems is represented by the occurrence of land degradation processes (Bajocco *et al*., 2012; Romm, 2011; Tarolli and Straffelini, 2020), among which landslides and soil erosion by water are the most relevant ones (Tarolli *et al*., 2021). Land degradation in agriculture is due to several factors, such as changes in land use (Fagnano *et al*., 2012), land abandonment (Lopez-Vicente *et al*., 2017; Louwagie *et al*., 2011), climate change (Webb *et al*., 2017), wildlife (Mauri *et al*., 2019) and increasing anthropogenic pressure (Sidle *et al*., 2014). In this context, the presence of rural roads and the occurrence of land degradation processes, such as shallow landslides, are strongly connected (Eker and Aydin, 2014; Mauri *et al*., 2021; Wemple *et al*., 2001). Road networks have numerous functions in agriculture, e.g., encourage efficient communications (Gollin and Rogerson, 2010), improve farmland management, and simplify farming operations (Sidle and Ziegler, 2012). On the other hand, despite their advantages, roads within a cultivated area can lead to the activation of slope failures. Several factors are involved in these processes. First, inefficient planning and design are responsible for activating landslides close to specific road sections (Marion and Leung, 2004; Salesa *et al*., 2019). Moreover, road construction induces failures on the undercut slope by altering of natural drainage systems (Sidle *et al*., 2006). Especially in steep slopes, banks stability can be seriously compromised due to the construction of a road (Sidle *et al*., 2006, 2014). The activation of landslides on steep slopes is also driven by the road-induced deviation and accumulation of the water, which successively infiltrates into soil layers above the potential slide plane (Keefer *et al*., 1987). Thus depends on several factors, e.g., pore-water pressure, drainage rate, antecedent precipitations, prior moisture content, slope materials, and road characteristics (Wieczorek, 1996; Guzzetti *et al*., 2007). Water infiltration and its subsurface accumulation increase the negative pore-water pressure (i.e., water pressure in unsaturated soil above the water table; Davison *et al*., 2000). The alteration of negative pore-water pressure is responsible for the progressive decrease of the unsaturated shear strength in the upper soil layers and consequently for landslides occurrence. In this regard, slope inclination and soil friction angle are also involved in failure dynamics. If on the one hand the reduction of stability of steep slopes is mainly driven by infiltration and consequent suction processes, on the other hand, the increase of negative pore-water pressure is mostly responsible for failures progressively affecting soft slopes (Gallage *et al*., 2021; Harp *et al*., 1990). Therefore, the drainage rate (i.e., the depth of water drained off from a specific area in a given time range) increases as the rainfall accumulates until the slope failure (Pamar, 2014). Since water and road presence have a primary role in landslides occurrence, especially in steep slopes, temporal monitoring of roads-induced water direction alterations through the application of specific

hydrological topographically-based models could help in understanding and therefore, better managing the investigated issue. Digital photogrammetry (e.g., Structure from Motion- SfM) combined with Remotely Piloted Aircraft Systems (RPAS) allows realizing rapid and efficient analysis of surface topography through high-resolution Digital Elevation Models (DEMs),) (Westoby *et al*., 2012). Therefore, the adoption of these technologies, combined with the use of hydrological models, represents an opportunity for the investigation of the relationship between road presence and landslides activation. In light of the above considerations, this research proposes a multi-temporal hydrological analysis of the road role in the alteration of water flows in a shallow landslide-prone terraced agricultural system. SIMulated Water Erosion model (SIMWE; Mitasova *et al*., 2013) was adopted for the multi-temporal investigation of road influence on overland flow dynamics using RPAS-derived high-resolution DEMs. The application of such a model in the multi-temporal investigation of the interaction between road network, water overland flows deviation, and shallow landslides activation in the high-steep terraced vineyard is, in our knowledge, novel. The proposed research fills the gap in the scientific knowledge regarding the possibility to deeply analyse the presented environmental issue through the adoption of 4D RPAS-based digital terrain modeling, focusing on the evolution of hydrological processes over time at hillslope scale, and concurrently adopting a low cost and efficient methodology.

3.3 Study area

The study area is located in the Trento province, south of the Trentino Alto Adige region, northern Italy (Fig. 3.1a). It has an overall spatial extension equal to 2.2 ha, southwest aspect and an average slope of 27.6°, with an elevation between 266 m a.s.l. at the base and 320 m a.s.l. on the top (average value equal to 287 m a.s.l.). The annual average rainfall is 1088 mm, while inter-annual rainfall standard deviation is 222 mm. The study area is characterized by terraces built on steep slopes using earth banks, with an inter-row grass cover. Within the vineyard is located a road network, made to reach the highest terraces during agricultural operations. The surface of the road is partly concrete, with some unpaved sections located around the whole vineyard. The road has a total length of about 600 m, with an average width of about 2 m, average slope equal to 15.7° (slope range between a minimum of 0.03° and a maximum of 19.2°). No drainage systems are located along the road, especially close to the landslide-prone banks, except for some paved sections located outside the rows where manholes are present. During field surveys, two shallow landslides were observed. The first RPAS survey (18 October 2019) revealed the presence of a first landslide (L1-pre) below a paved section of the road (Fig. 3.1b). The second RPAS survey (17 December 2019) highlighted an evolution of L1 (therefore called L1-post) and the activation of a second shallow landslide (L2) about 20 m away from L1 and located close to an unpaved road section placed in the terraces above (Fig. 3.1c).

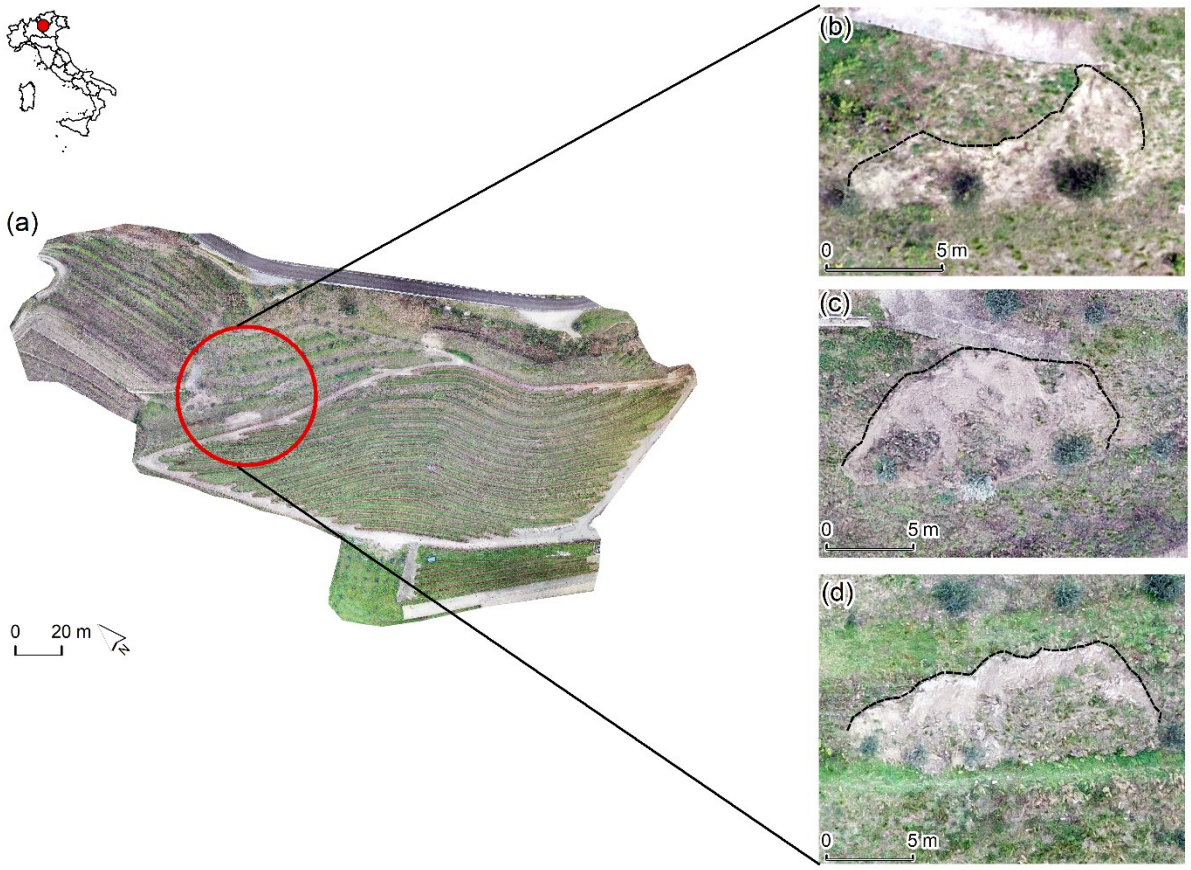

Figure 3.1. *Overview of the study area (a) and focus on the landslides L1-pre (b), L1-post (c) and L2 (d) observed during each RPAS survey. The pictures in Fig. 3.1b–d were manually taken through the RPAS surveys.*

3.4 Material and methods

3.4.1 SIMulated Water Erosion (SIMWE) model

The plot-scale Simulated Water Erosion Model (SIMWE, Mitasova *et al*., 2013) is of great utility in the investigation of water and sediment dynamics at the hillslope scale. SIMWE is a bivariate physics-based and spatially distributed model able to simulate hydrologic overland water flows and sediment transport, with the possibility to estimate soil erosion starting from a single rainfall value. It implements a path sampling method by analysing superficial water flows processes and sediment transport separately, firstly modeling the superficial hydraulic flow tie-rod map and then using the obtained output for the calculation of the sediment runoff (Cencetti *et al*., 2005; Koco, 2011). SIMWE is based on the principles describing the Water Erosion Prediction Project model (Flanagan and Nearing, 1995) and it is divided into two different components available in GRASS GIS environment, i.e., (i) r.sim.water and (ii) r.sim.sediment. Since the purpose of our work is to mainly focus on road-induced water dynamics alterations as a possible cause of landslides activation, the *r.sim.sediment* module was not considered in the analysis conducted in this work. The water module simulates overland water flows adopting a Green's function Monte Carlo path sampling method (Mitasova *et al*., 2004) whereby a system of differential equations is obtained by combining the mass conservation equation and the Manning relation (Cencetti *et al*., 2005). The continuity equation is solved assuming that water flow velocity depends on surface roughness and terrain slope and that it negligibly changes at a given location during the simulated event. Even though SIMWE does not consider antecedent moisture conditions for simulations, this model represents an optimal tool for the investigation of the issue presented in this work, starting from local rainfall peak and Manning's n inputs, to focus the analysis on road-overland flow-landslides interaction at hillslope scale among time. SIMWE requires specific inputs for its modules. As far as the *r.sim.water* module is concerned, the necessary input data are (i) DEM (m), (ii) first-order x and y derivates of the DEM (-), (iii) rainfall excess rate (mmh^{-1}), and (iv) Manning's roughness coefficient (-). Respective outputs are overland water depth (m) and water discharge ($m^3\ s^{-1}$).

3.4.2 Data acquisition and elaboration

3.4.2.1 Overview of recorded rainfall events and observed landslides

In order to carry out SIMWE simulations, the daily rainfall intensity peaks recorded by the nearest weather station in a specific time range were considered. The weather station is located in Tenno municipality (Trento province), 1 km away from the study area as the crow flies. A specific time range was set to proceed in the analysis of weather station measurements, automatically corrected and post-processed by local services. At the indications given by the landowner about the period of landslides triggering in the vineyard, the records of rainfall values from one month before the date of each computed RPAS survey were considered. The highest rainfall intensity peaks recorded by the weather station in each considered time range were equal to 33.6 mmh^{-1} (recorded on October 2, 2019) and 7.2 mmh^{-1} (recorded on November 27, 2019), referring to continuous rainfall events lasting a total of 50 min and 390 min respectively. Fig. 3.10 shows the trend of daily cumulative rainfall (mm) and daily hourly rainfall intensity peaks (mmh^{-1}) for each month. Specific codes in R environment were adopted to extract daily rainfall intensity peaks, applying accurate transformations in the analysis of the available dataset. Annual raw meteorological data were firstly divided into monthly subgroups. Then, the extraction of both daily rainfall intensity peaks (mmh^{-1}) and cumulative rainfall values ($mmday^{-1}$) was performed through consecutive *for loops* computation. Consequently, combined plots were elaborated merging the *for loops* outcomes. In this way it was possible to organize the large amount of data collected extracting the necessary information for the purposes of this work and consequently plotting them. The *data.table* R package was necessary for data sub-setting, while the *attach(mtcars)* R function allowed us to combine each plot in a single plots-matrix as reported in Fig. 3.10. During field surveys, the landslide extension and perimeter were manually measured in order to obtain a first overview of their characteristics. The width of landslides was measured with a stick meter. L1 zone observed during the first RPAS survey revealed an extension of 44 m^2, a perimeter of about 34 m and an average slope of 38°. The maximum vertical distance, between the higher point of L1 crown and the ground below, is equal to 0.85 m. The length of the paved road section located above L1 is to 11.8m, with the absence of drainage systems along it. The second RPAS survey firstly highlighted an increasing extension of L1 of more than 50 m^2 (from 44 m^2 to 98 m^2), a perimeter of about 45 m and a maximum vertical value equal to 1.20 m. Secondly, another shallow landslide was noticed (L2), covering a surface of more than 60 m^2 with a perimeter of about 40 m, a maximum vertical distance equal to 1.10 m and an average slope of 40.9°. With reference to the landslides definitions proposed by Dikau *et al*. (1996) and according to Thiery *et al*. (2017), the observed landslides can be identified as shallow translational

landslides, both considering the steep slopes of the collapsed surfaces and their overall dimensions. Moreover, landslide zones mainly involved bare soil characterized by an uneven low herbaceous cover. The maximum width between each landslides' flanks is equal to 12.8 m for L1-pre, 14.10 m for L1-post, and 16.3 m for L2, while the length of the collapsed surfaces, from each landslides' crown and the respective toe, is equal to 6.3 m for L1-pre, 6.6 m for L1-post and 4.4 m for L2 (Cruden and Varnes, 1996, p. 247).

3.4.2.2 RPAS-SfM data acquisition and processing

In light of the aims of this work, a multi-temporal RPAS survey was performed to elaborate high-resolution Digital Elevation Models (DEMs),) of the study area. The two surveys were carried out after two subsequent landslide events, using a DJI Mavic Pro® RPAS mounted with a 1/2.3″ sensor (CMOS) 12.35M effective pixels camera. Flight missions were planned using the official IOS-DJI® application. Nadir and oblique pictures were integrated to better appreciate specific features such as terraces and landslides (Rusnák *et al*., 2018). The positions of 23 GCPs and 10 CPs were measured through the Geomax Zenith40® GNSS receiver in RTK mode (EPSG 32632 coordinate system-WGS 84/UTM zone 32N). Agisoft Metashape® software was used for point clouds generation, while point clouds post-processing was performed with Cloud Compare software (http://www.cloudcompare.org). In particular, the Statistical Outlier Removal (SOR) filter, based on the Point Cloud Library (PCL) (Rusu and Cousins, 2011) was firstly used for outliers removal. Subsequently, point clouds were manually cleaned by dividing them into regular slices along the maximum slope direction, easing the removal of noises such as residual vegetation, vineyard's rows, plants and man-made features. In this regard, despite the availability of several semi-automatic algorithms for the automatic extraction of clouds-derived terrain points, manual filtering led to a more accurate cleaning procedure. Finally, point clouds co-registration was computed through the Point Pairs Picking co-registration tool in Cloud Compare. Manholes located along the paved road section around the vineyard were considered as specific stable point's pairs in both the point clouds to be aligned. DEMs elaboration was carried out adopting the Natural Neighbour Interpolation technique, which provides a value for the unknown point according to the weight assigned to each one as a function of a proportional area, basing on a subset of surrounding points. Looking at the average point distance, the two elevation models were elaborated with a resolution equal to 15 cm, in order to efficiently appreciate geomorphological features at the hillslope scale. The analysis of errors affecting point clouds and the respective DEMs highlighted the success of the measurements in terms of accuracy and precision of the results. The point clouds' accuracy and precision were estimated by selecting 1/3 of GCPs, excluding them from data georeferencing procedure and hence considering

them as check-points (CPs). Consequently, the computation of GCPs and CPs residuals was conducted (Cucchiaro *et al*., 2018). In this regard, the absolute mean and the standard deviation of CPs residuals describe the point cloud accuracy and precision respectively (Cucchiaro *et al*., 2018). The Root Mean Square Error ($RMSE_{3D}$) was computed in x, y and z directions by comparing the value of each coordinate provided by the SfM technique with the corresponding value measured by GNSS close to each GCPs and CPs. Analogously, DEM-RMSE values were obtained. Finally, the co-registration RMSE value was obtained as a result of the adopted point clouds alignment procedure. Table 3.1 reports an overview of the main parameters characterizing the RPAS-derived SfM outcomes.

Table 3.1. *Overview of main parameters describing the SfM point clouds and the obtain DEMs**),** for the first RPAS survey (18 October 2019) and the second one (17 December 2019). The table shows the point cloud accuracy (described by the absolute mean of CPs residuals), point cloud precision (described by the standard deviation of CPs residuals) for the two RPAS surveys, RMSE3D total value observed during point clouds' elaboration, respectively regarding GCPs and CPs, co-registration error and RMSE values of final DEMs.*

Point cloud	**Point cloud accuracy (m)**			**Point cloud precision (m)**			**$RMSE_{3D}$ CPs (m)**	**$RMSE_{3D}$ GCPs (m)**	**RMSE Co-reg. (m)**	**RMSE DEM (m)**
	x	**y**	**z**	**x**	**y**	**z**				
Survey 1	0.040	0.020	0.035	0.020	0.026	0.037	0.057	0.039	0.045	0.103
Survey 2	0.017	0.016	0.038	0.014	0.012	0.026	0.046	0.039		0.058

3.4.2.3 SIMWE input acquisition

Starting from each computed DEM, the flow gradient vector (given by first-order x and y partial derivates of elevation grids) was obtained through the GRASS GIS *r.slope.aspect* tool. Manning's roughness coefficients (*n*) were selected from literature (Bunya *et al*., 2010; Fernandes *et al*., 2017; Pijl *et al*., 2020). Different surface types were observed within the study area, as reported in Fig. 3.11. Specifically, vineyard (*V*), grassland (*G*), bare soil (i.e., landslides zones, *BS*), concrete road sections (*CR*) and unpaved road sections (*UR*) were noticed within the study area. Specific Manning values were adopted, setting *n* equal to 0.100 for vineyard, 0.035 for grass zones, 0.030 for bare soil, 0.012 for the concrete surface of the road and 0.035 for its unpaved sections. The rainfall excess rate was calculated by subtracting the infiltration rate (mmh^{-1}) from the fixed rainfall rate (mmh^{-1}, i.e., the rainfall intensity peaks recorded by the weather station for each month). Infiltration

rates were estimated based on the measurement of the hydraulic conductivity for each land type and resulted equal to 37.5 mmh^{-1} for vineyard, 12.7 mmh^{-1} for grassland zones and bare soil, 9.8 mmh^{-1} for unpaved road's sections and 0 mmh^{-1} for concrete road's sections. Saturated hydraulic conductivity was calculated for each surface type using a double-ring infiltrometer with a diameter equal to 80 cm, following the outcomes presented in Lai and Ren (2007) and Fatehna *et al*. (2016). Field measurements of hydraulic conductivity are in line with those reported in the respective literature (Alagna *et al*., 2018; Biddoccu *et al*., 2013; Capello *et al*., 2019; Pijl *et al*., 2020).

3.4.3 SIMWE simulations on different scenarios

Looking at the aims of the presented research, three different scenarios were considered to investigate the role played by the road network in the deviation of water flows close to the collapsed hillslopes. A multi-temporal comparison of SIMWE simulations was computed, so as to detect the evolution of water dynamics among time. DEMs), resulted from the two RPAS surveys were respectively considered (Fig. 3.2a and b). In the first scenario (henceforth called "*YesRoad-pre*") the first RPAS-derived DEM was used and water flows were simulated looking at the presence of the road, especially close to the collapsed surface detected during the survey. The second scenario (called "*YesRoad-post*") considered the second reconstructed DEM, characterized by an L1 evolution and L2 activation. The third scenario (named "*NoRoad*") was carried out simulating the absence of the road network within the study area (Fig. 3.2c). The road absence was simulated modifying each DEM through a specific smoothing approach applying the quadratic approximation introduced by Evans (1979):

$$Z = ax^2 + by^2 + cxy + dx + ey + f$$

where x, y and Z are local coordinates and parameters a to f stand for the quadratic coefficients. A moving window equal to 91 m was used in the smoothing process, so as to efficiently simulate the absence of the road network within the study area, reasonably preserving the presence of terraces (in Fig. 3.2c it is possible to note the light shadow of few terrace lines that are preserved after the smoothing procedure). Considering both DEMs resolution and road size, this revealed to be the most suitable value to properly smooth the road feature, also preventing an excessive reduction of DEMs size unavoidably deriving from the smoothing process. This smoothing approach was already satisfactorily tested in other contexts (see Tarolli *et al*., 2015).

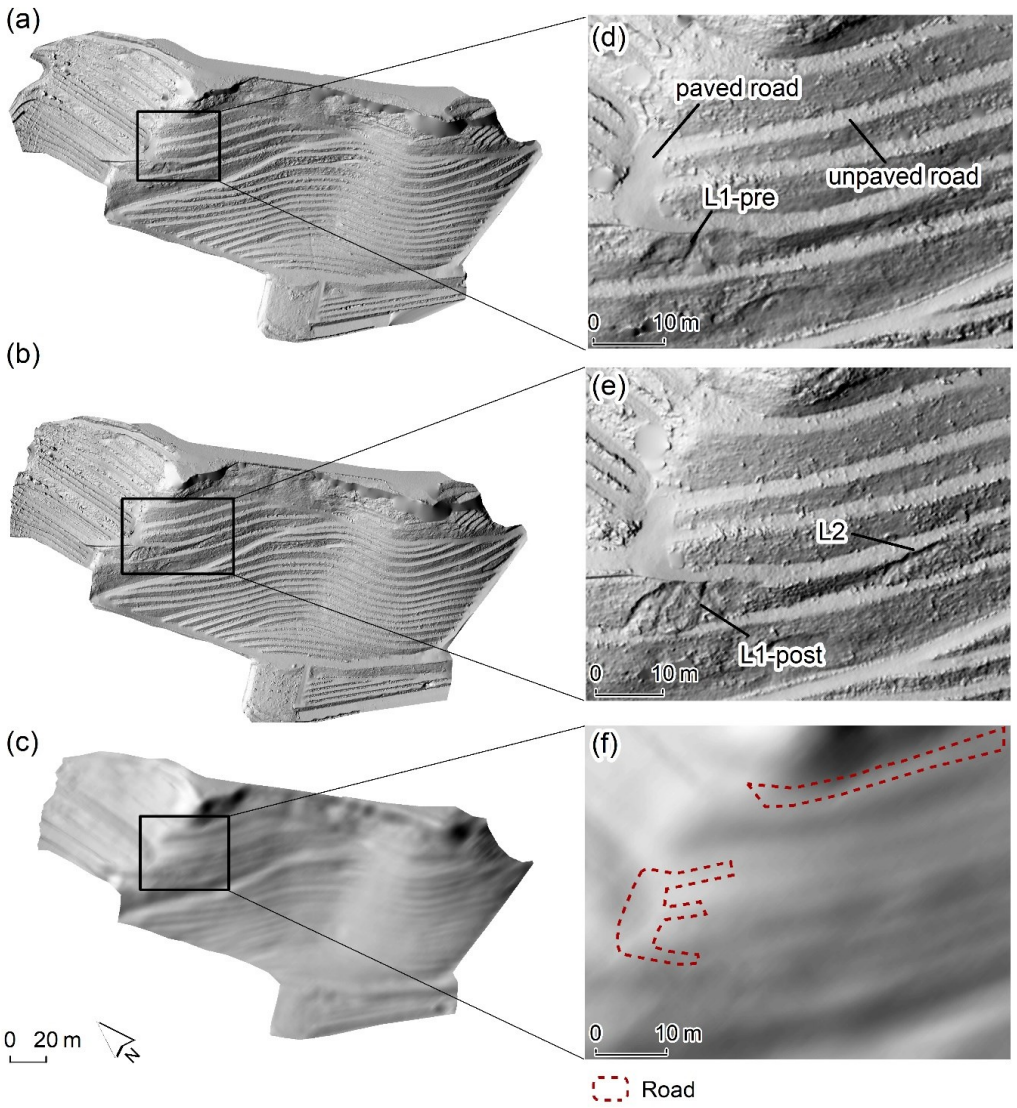

Figure 3.2. *Overview of shaded relief maps of each DEM obtained from the first RPAS survey (Fig. 3.2a), from the second one (Fig. 3.2b), and from the adopted smoothing procedure (Fig. 3.2c). The figure also shows details of each computed DEM, regarding L1-pre and the above paved road section (Fig. 3.2d), L1-post, L2 and the above unpaved road section (Fig. 3.2e) and the original location of the road in the smoothed DEM, which simulates its absence (Fig. 3.2f).*

For the *YesRoad* scenarios, the highest rainfall intensity peaks recorded by the weather station in each considered time range were firstly set in SIMWE simulations. Different tests were successively performed both decreasing and increasing rainfall intensity peaks with respect to those registered and hence modifying the excess rate respectively. Table 3.2 reports SIMWE input selected for each simulation of the *YesRoad* scenarios. The same values were used in each simulation of the *NoRoad* scenario, as reported in Table 3.3. For both the *YesRoad* and *NoRoad* scenarios, the duration of the simulations was 1 h, in agreement with the unit of measurement of the model inputs.

Table 3.2. *Overview of SIMWE input selected for each simulation of the YesRoad-pre and YesRoad-post scenarios. In particular, the table shows Manning, infiltration rate and excess rate values considered for each land type, i.e., vineyard (V), grassland (G), bare soil (i.e., landsides zones, BS), concrete road sections (CR) and unpaved road sections (UR). Simulations 1 and 3 were computed considering the highest rainfall intensity peaks recorded by the weather station in the time range referring to the first and the second RPAS survey respectively, while simulations 2, 4, 5 and 6 were computed considering hypothetical rainfall intensity peaks.*

SIMWE sim	Land type	Manning (n)	Infiltration rate (mmh^{-1})	Excess rate (mmh^{-1})
1 (7.2 mmh^{-1}) (rec)	V	0.030	37.5	0.0
	G	0.035	12.7	0.0
	BS	0.030	12.7	0.0
	CR	0.120	0.0	7.2
	UR	0.035	9.8	0.0
2 (25.0 mmh^{-1}) (sim)	V	0.030	37.5	0.0
	G	0.035	12.7	12.3
	BS	0.030	12.7	12.3
	CR	0.120	0.0	25.0
	UR	0.035	9.8	15.2
3 (33.6 mmh^{-1}) (rec)	V	0.030	37.5	0.0
	G	0.035	12.7	20.9
	BS	0.030	12.7	20.9
	CR	0.120	0.0	33.6
	UR	0.035	9.8	23.8
4 (40.0 mmh^{-1}) (sim)	V	0.030	37.5	2.5
	G	0.035	12.7	27.3
	BS	0.030	12.7	27.3
	CR	0.120	0.0	40.0
	UR	0.035	9.8	30.2
5 (60.0 mmh^{-1}) (sim)	V	0.030	37.5	22.5
	G	0.035	12.7	47.3
	BS	0.030	12.7	47.3
	CR	0.120	0.0	60.0
	UR	0.035	9.8	50.2
6 (80.0 mmh^{-1}) (sim)	V	0.030	37.5	42.5
	G	0.035	12.7	67.3
	BS	0.030	12.7	67.3
	CR	0.120	0.0	80.0
	UR	0.035	9.8	70.2

Table 3.3. *Overview of SIMWE input selected for each simulation of the NoRoad scenario. In particular, the table shows Manning, infiltration rate and excess rate values considered for each land type, i.e., vineyard (V), grassland (G) and bare soil (i.e., landsides zones, BS). SIMWE simulations were computed adopting the same rainfall intensity peak values previously set in each YesRoad scenario.*

SIMWE sim	**Land type**	**Manning (n)**	**Infiltration rate (mmh^{-1})**	**Excess rate (mmh^{-1})**
1	V	0.030	37.5	0.0
(7.2 mmh^{-1})	G	0.035	12.7	0.0
(sim)	BS	0.030	12.7	0.0
2	V	0.030	37.5	0.0
(25.0 mmh^{-1})	G	0.035	12.7	12.3
(sim)	BS	0.030	12.7	12.3
3	V	0.030	37.5	0.0
(33.6 mmh^{-1})	G	0.035	12.7	20.9
(sim)	BS	0.030	12.7	20.9
4	V	0.030	37.5	2.5
(40.0 mmh^{-1})	G	0.035	12.7	27.3
(sim)	BS	0.030	12.7	27.3
5	V	0.030	37.5	22.5
(60.0 mmh^{-1})	G	0.035	12.7	47.3
(sim)	BS	0.030	12.7	47.3
6	V	0.030	37.5	42.5
(80.0 mmh^{-1})	G	0.035	12.7	67.3
(sim)	BS	0.030	12.7	67.3

3.5 Results

3.5.1 Multi-temporal hydrological simulations

A 4D analysis of overland water flows dynamics was conducted in order to investigate the role of the road network in overland flows directions and quantify their alteration. The output of the model is expressed in terms of water depth of overland flows (m). The analysis was conducted considering the presence of the road (*YesRoad*) and then simulating its absence (*NoRoad*).

3.5.1.1 YesRoad scenarios

Fig. 3.3 shows water flows computed for L1-pre, in function of each rainfall peak set as input in SIMWE simulations. The figures highlight a significant increase in water depth, proportionally to the configured rainfall values. Water flows, coming from the upper terraces, intercept the paved road section located above the landslide zone. Surface runoff flows along the road since it falls from its wayside crossing the underlying collapsed hillslope. This is evident both in simulations computed looking at the recorded rainfall intensities (Fig. 3.3c) and in those that considered the simulated scenarios (Fig. 3.3a, b, d-f). The figure underlines the presence of water flows deviation at the paved road section (yellow arrows), where water is deviated downstream by the road, crossing L1-pre. Moreover, the highest values of water depth were noticed close to the left corner of the paved road, specifically where water deviates in the direction of the terraces located further down. As rainfall values increase, water depth reaches gradually higher values up to a maximum of over 0.13 m and 0.18 m, regarding the simulations considering recorded (Fig. 3.3c) and simulated (Fig. 3.3a, b, d-f) rainfall intensity peaks respectively. Finally, part of the incoming water is deviated by the road on the left side, along an unpaved section that partially conveys it outside the investigated landslide-prone area.

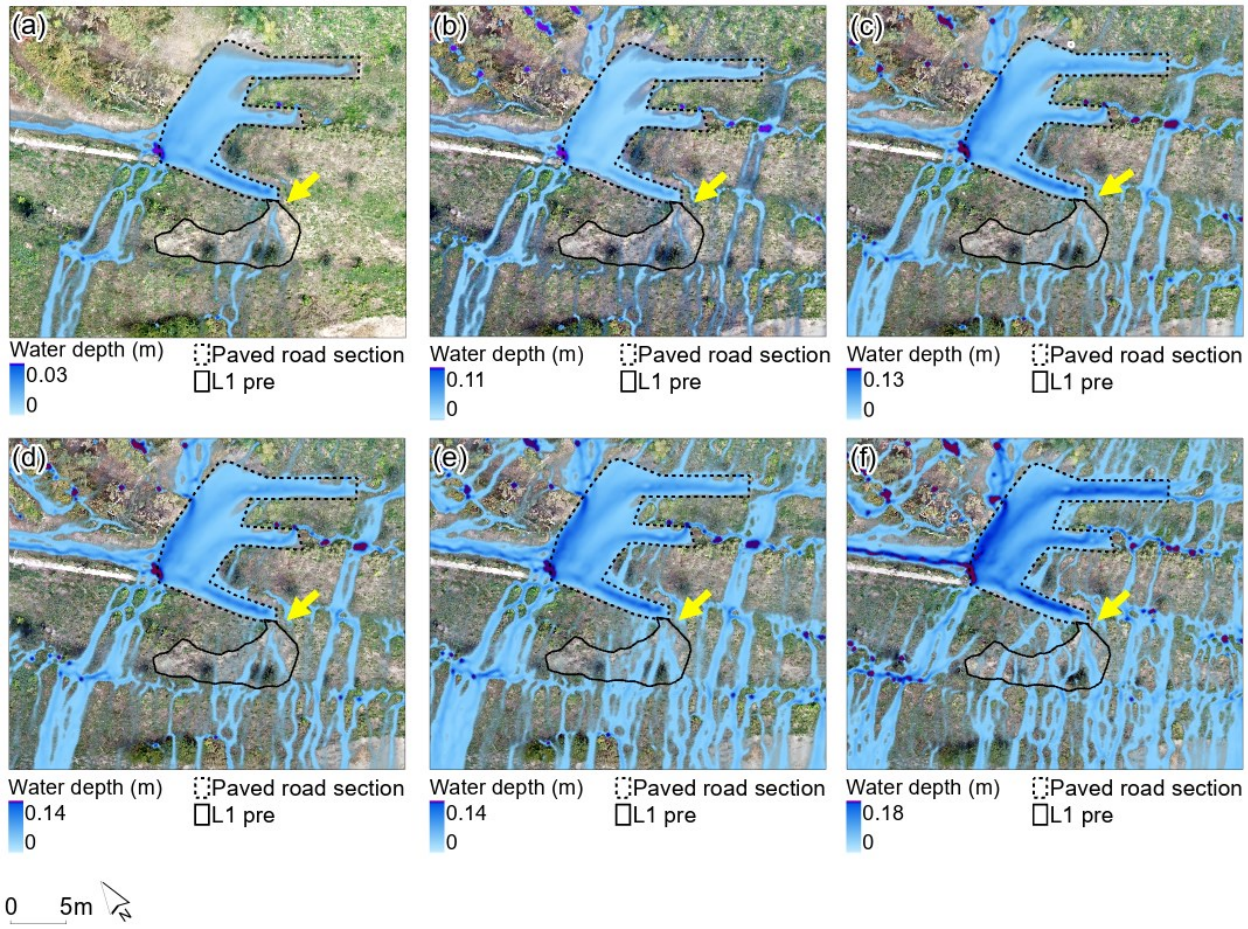

Figure 3.3. *Water depth (m) computed for SIMWE simulations regarding L1-pre (YesRoad scenario). In particular, the figure shows water depth simulation in function of rainfall intensity peaks equal to 7.2 mmh−1 (a), 25.0 mmh−1 (b), 33.6 mmh−1 (c), 40.0 mmh−1 (d), 60.0 mmh−1 (e) and 80.0 mmh−1 (f). Fig. 3.3c refers to the highest rainfall intensity peak recorded by the weather station in the considered time range, while Fig. 3.3a, b, d-f refer to the simulated rainfall intensity peaks. Yellow arrows indicate the main road-induced water flows deviations in the direction of L1-pre.*

Fig. 3.4 represents SIMWE simulations elaborated for L1-post, therefore considering the second RPAS-derived DEM, in function of progressively increasing rainfall intensity peaks values. The figure underlines the deviation of overland flows due to the presence of the paved road, which is responsible for changes in water directions and increasing water depth proportionally to the rainfall intensity peaks. L1-post is crossed by water that coming from the upper hillslopes, is then deviated by the road. The unaltered hillslope located close to L1 is likewise involved in road-altered water flows which pass through it. The highest water depth values were noticed close to the left corner of the paved road section above L1-post, with a maximum of 0.01 m and 0.12 m regarding the simulations considering recorded (Fig. 3.4a) and simulated (Fig. 3.4b–f) rainfall intensity peaks respectively.

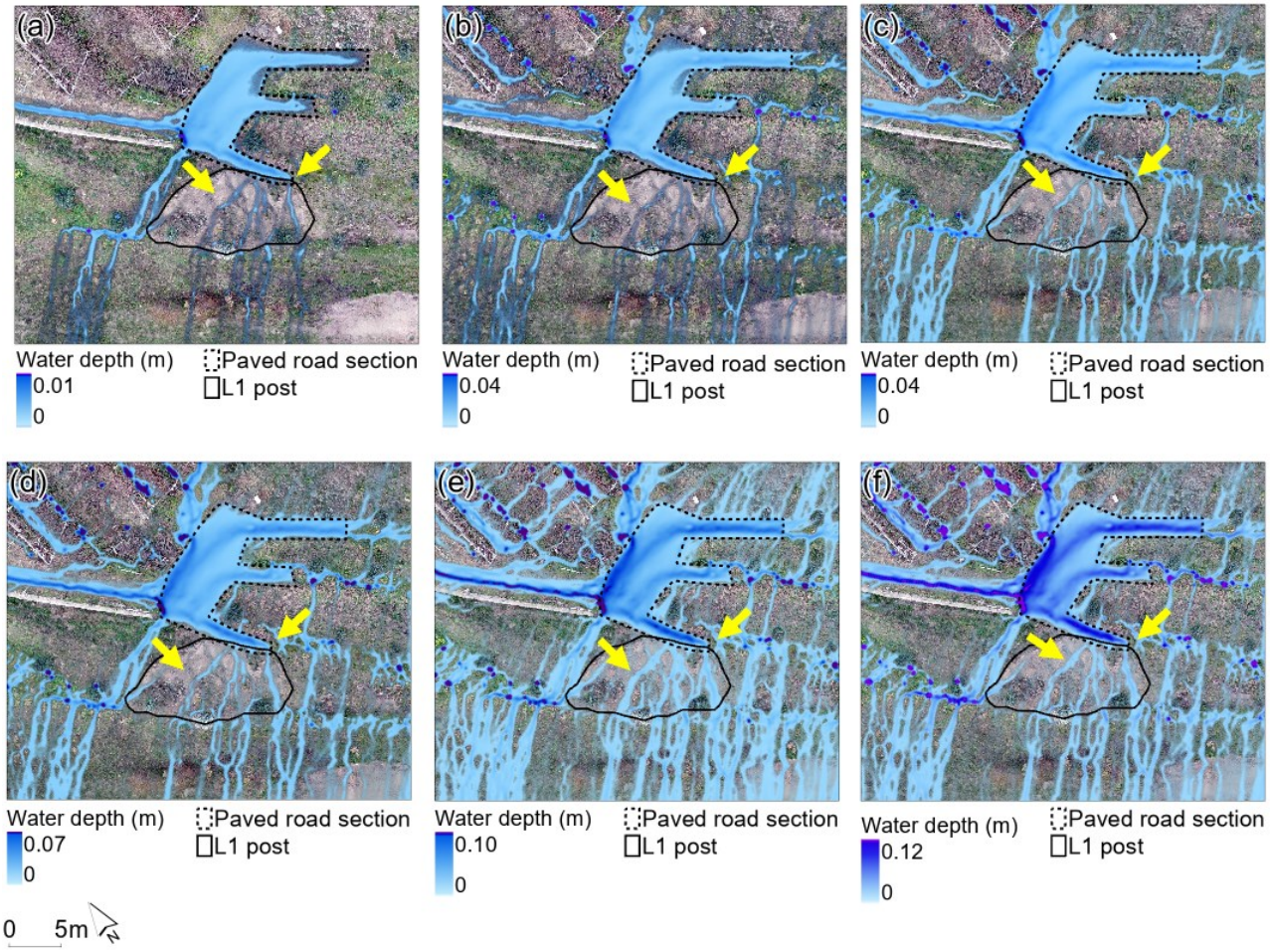

Figure 3.4. *Water depth (m) computed for SIMWE simulations regarding L1-post (YesRoad scenario). In particular, the figure shows water depth simulation in function of rainfall intensity peaks equal to 7.2 mmh−1 (a), 25.0 mmh−1 (b), 33.6 mmh−1 (c), 40.0 mmh−1 (d), 60.0 mmh−1 (e) and 80.0 mmh−1 (f). Fig. 3.4a refers to the highest rainfall intensity peak recorded by the weather station in the considered time range, while Fig. 3.4b–f refers to the simulated rainfall intensity peaks. Yellow arrows indicate main road induced water flows deviations in the direction of L1-post.*

Fig. 3.5 represents the simulation included in the *YesRoad* scenario looking to L2, observed during the second RPAS survey. Water flows deviations are more significant as the rainfall increase, with water depth values ranging from 0.01 m (Fig. 3.5a) up to a maximum of 0.14 m regarding the last simulation elaborated considering the hypothesized rainfall intensity peaks (Fig. 3.5f). Moreover, the figure shows the presence of high-water depth along the unpaved road section located above L2, proportionally to the increasing rainfall values. Yellow arrows indicate the most evident water flows that moving along the roadway deviate downstream across terraces, until intercepting the landslide zone more significantly as the rainfall intensity increases.

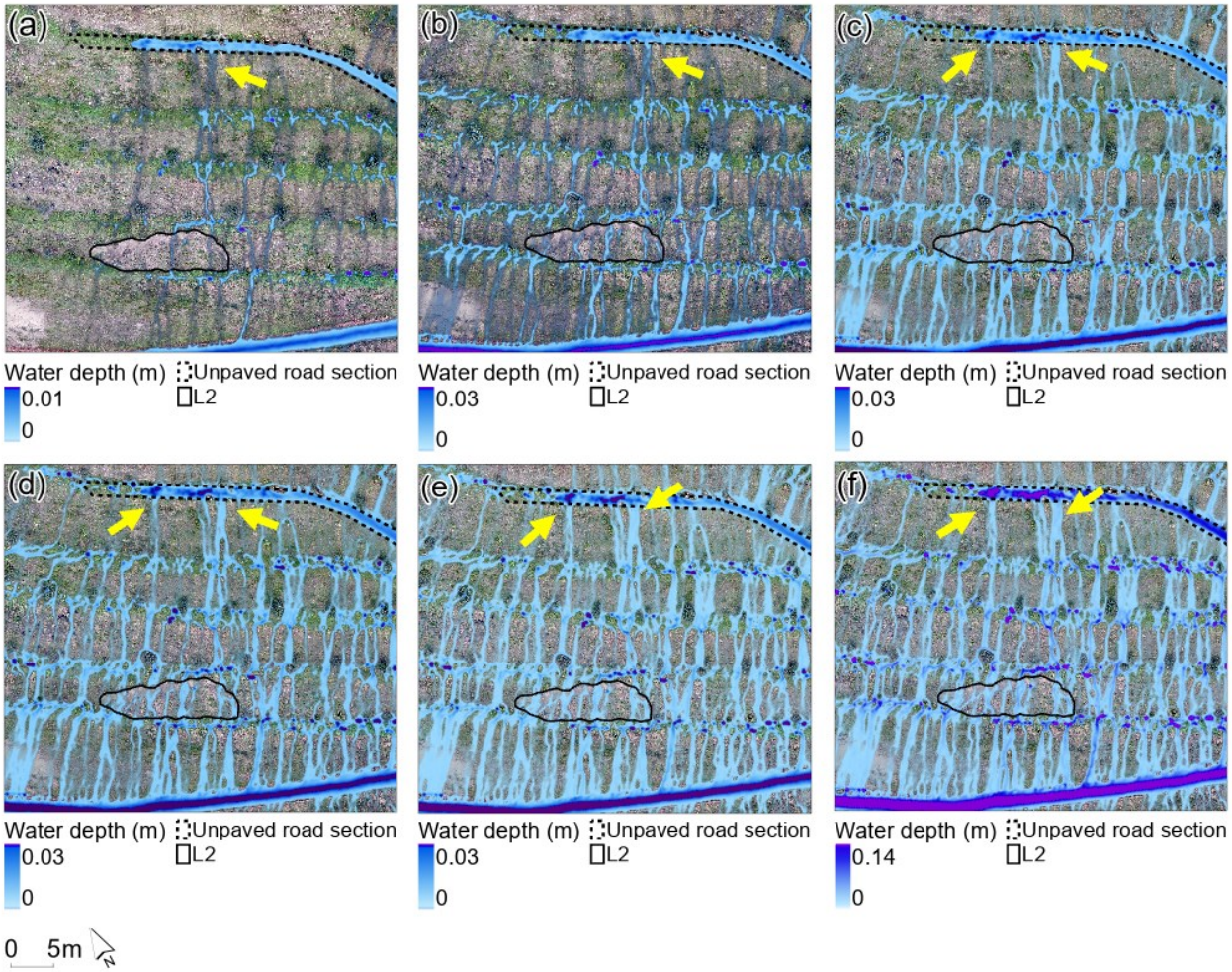

Figure 3.5. *Water depth (m) computed for SIMWE simulations regarding L2 (YesRoad scenario). In particular, the figure shows water depth simulation in function of rainfall intensity peaks equal to 7.2 mmh−1 (a), 25.0 mmh−1 (b), 33.6 mmh−1 (c), 40.0 mmh−1 (d), 60.0 mmh−1 (e) and 80.0 mmh−1 (f). Fig. 3.5a refers to the highest rainfall intensity peak recorded by the weather station in the considered time range, while Fig. 3.5b–f refers to the simulated rainfall intensity peaks. Yellow arrows indicate the most relevant water flows deviated by the unpaved road section located above L2, crossing the terraces downstream and intercepting the collapsed hillslope.*

Looking at L1, the comparison of SIMWE simulations computed for the *YesRoad-pre* and *YesRoad-post* scenarios (Fig. 3.3, Fig. 3.4) strongly proves a connection between road presence and water flows deviation towards L1 zone. Analogously, the presence of water flows diversion above L2 (Fig. 3.5) suggests as unpaved road sections can be similarly responsible for notable alterations of water overland flows.

3.5.1.2 NoRoad scenario

Fig. 3.6 reveals the absence of significant changes in water flows involving L1. Simulations identify the presence of the highest water depth values close to the left part of the paved road section located above the landslide (yellow arrows). As the rainfall increases, the water depth reaches higher values until a maximum of 0.02 m. L1 is not crossed by the water, which only drains from the left part of the road through the unaltered hillslope near the collapsed surface. Maximum water depth was noticed close to the left corner of the paved section of the road, further underlining the concentration of water toward the unaltered hillslope located near L1. Water depth increases proportionally to the rainfall value set as input in the model, without involving the landslide zone.

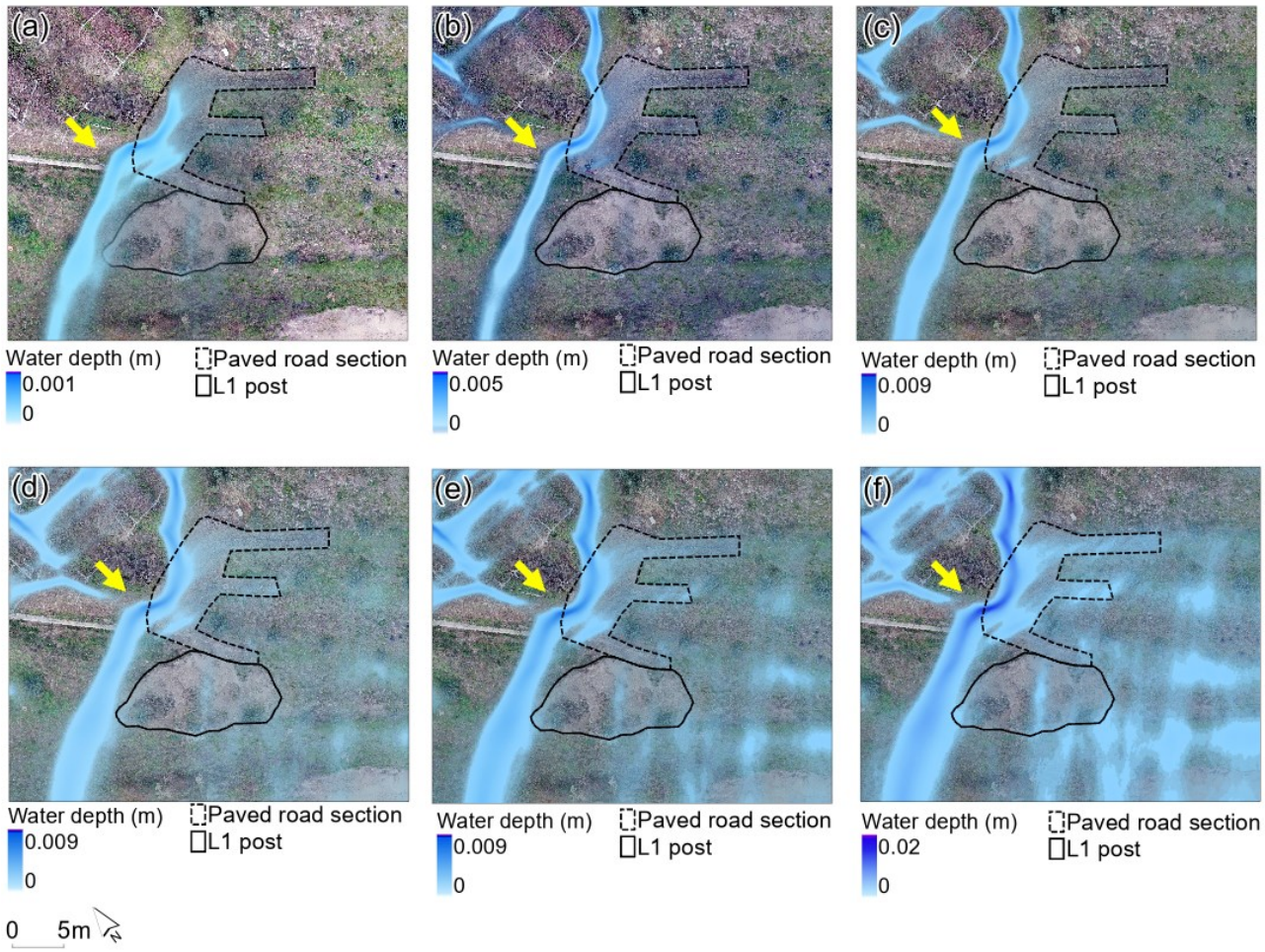

Figure 3.6. *Water depth (m) computed for SIMWE simulations regarding L1 (NoRoad scenario). In particular, the figure shows water depth simulation in function of rainfall peaks equal to 7.2 mmh−1 (a), 25.0 mmh−1 (b), 33.6 mmh−1 (c), 40.0 mmh−1 (d), 60.0 mmh−1 (e) and 80.0 mmh−1 (f). SIMWE simulations were computed adopting the same rainfall intensity peaks values previously set in the YesRoad scenarios. Yellow arrows indicate the highest water depth values involving an unaltered hillslope close to L1.*

Finally, Fig. 3.7 represents the simulations of water flows assuming the absence of the road, focusing on L2. As the rainfall increases, the landslide area reveals not to be crossed by the water, with maximum water depth values in the order of millimetres.

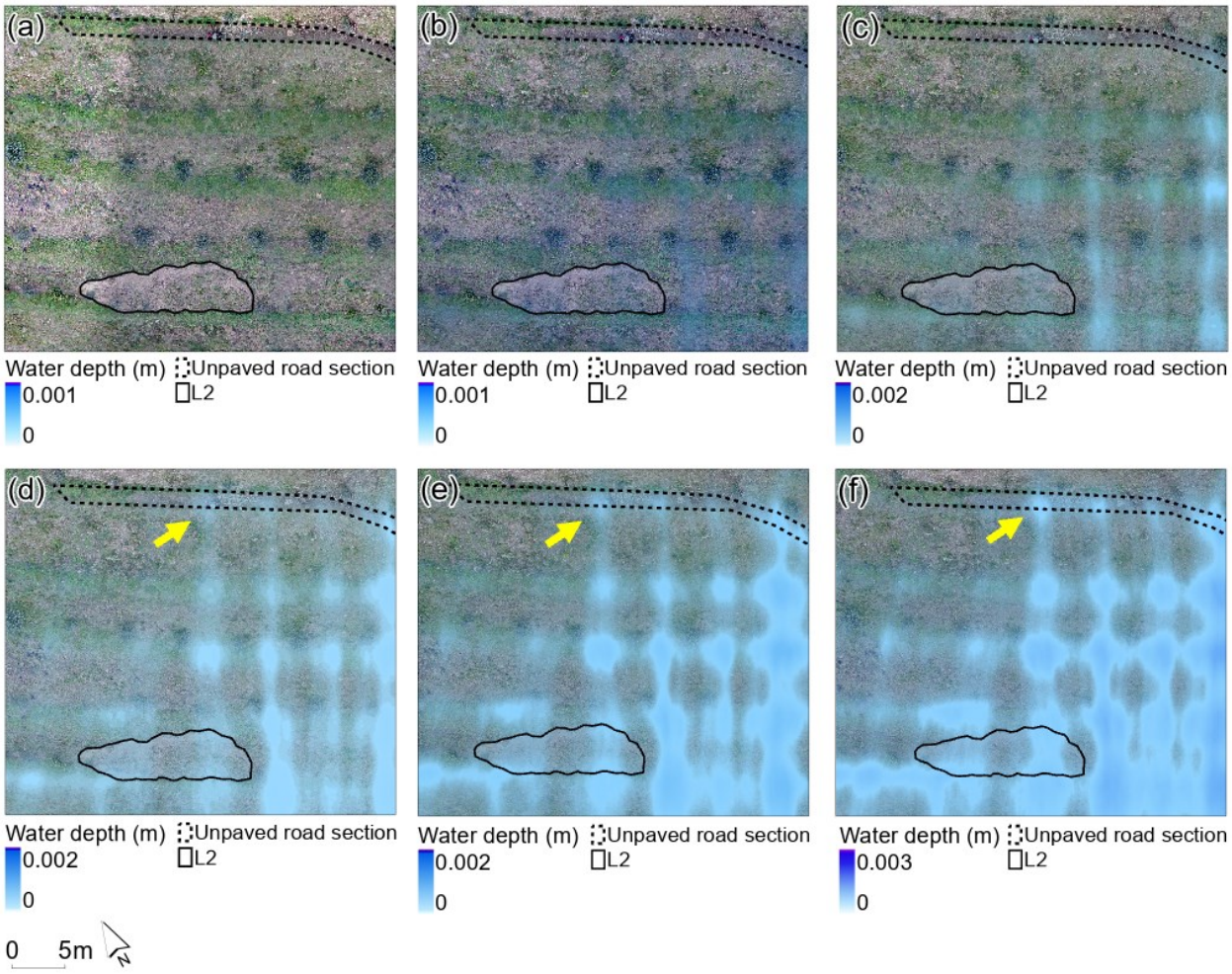

Figure 3.7. *Water depth (m) computed for SIMWE simulations regarding L2 (NoRoad scenario). In particular, the figure shows water depth simulation in function of rainfall intensity peaks equal to 7.2 mmh−1 (a), 25.0 mmh−1 (b), 33.6 mmh−1 (c), 40.0 mmh−1 (d), 60.0 mmh−1 (e) and 80.0 mmh−1 (f). SIMWE simulations were computed adopting the same rainfall intensity peaks values previously set in the YesRoad scenarios. Yellow arrows indicate the highest water depth values, regarding assumed water overland flows crossing L2.*

3.5.2 Water depth comparison and statistical validation

Looking at the purposes of this research, a quantification of water depth along the road sections was performed. In this regard, 25 control points were placed at equal distances from each other on both paved and unpaved road sections, respectively located above L1 and L2, for a total of 50 control points (Fig. 3.12). For each simulation of the three scenarios, water depth values were extracted in correspondence of each point obtaining a total of 900 water depth measures. Boxplots in Fig. 3.8 show water depth extracted from each control point placed along the paved road section above L1-pre and L1-post (Fig. 3.8a and b) and on the unpaved road section above L2 (Fig. 3.8c). Each figure compares the different values of water depth considering both *YesRoad* and *NoRoad* scenarios. Looking at the road sections above L1 and L2 (Fig. 3.8a and b and Fig. 3.8c respectively), water depth extracted from each point increases proportionally to the rainfall intensity peaks set as input in SIMWE simulations. In contrast, concerning the simulations computed assuming the absence of the road, points-derived water depth values are around 0 m for both L1 and L2, regardless of the increasing rainfall intensity peaks.

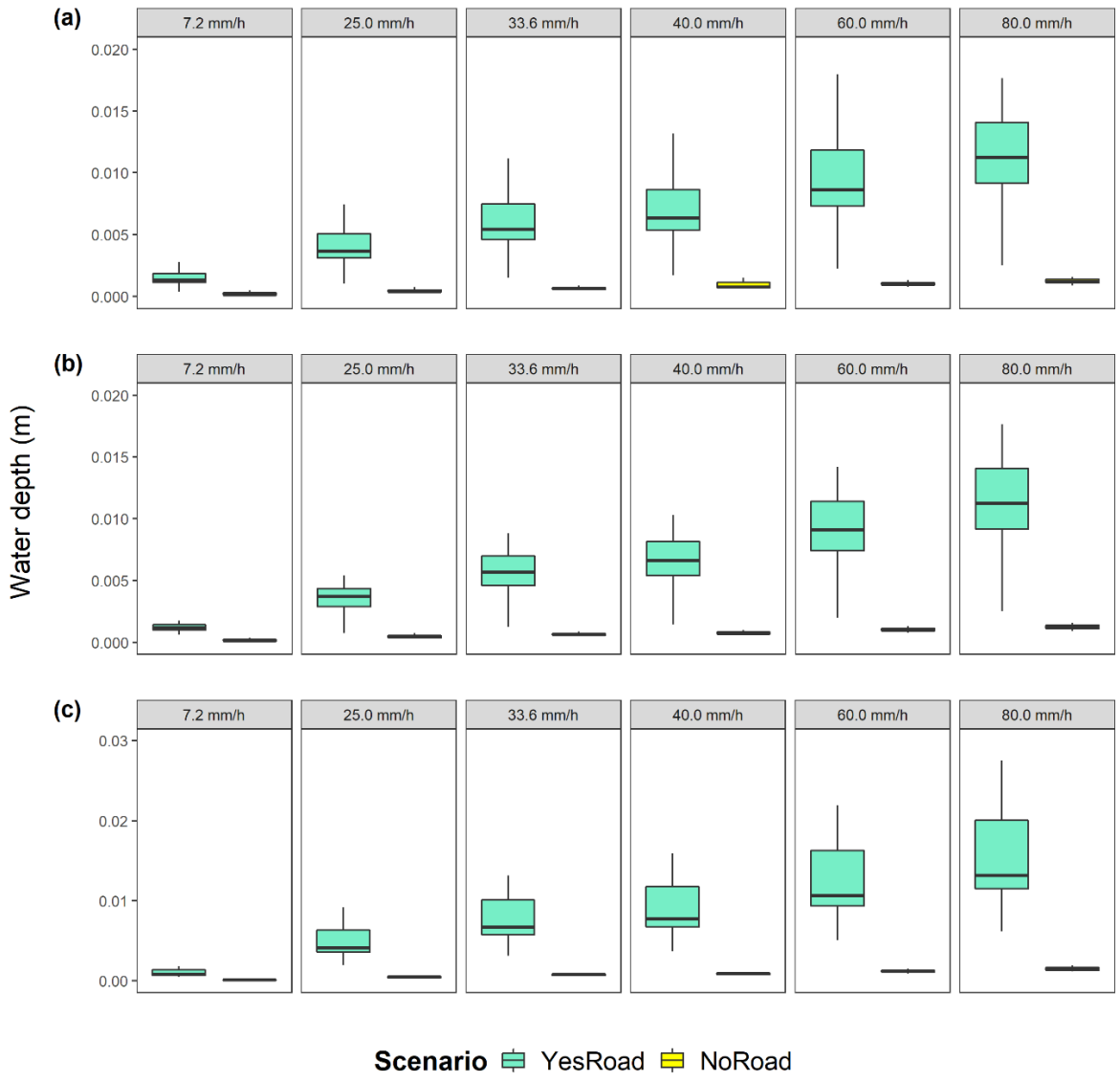

Figure 3.8. *Boxplots of water depth values extracted from each control point located along the paved and the unpaved road sections above L1-pre (a), L1-post (b) and L2 (c). The figure shows the comparison between water depth values acquired from each control point for YesRoad and NoRoad scenarios regarding each computed SIMWE simulation. Outliers have been removed to propose a clearer visualization of the graphics.*

The influence of the road network on the overland flows deviation towards the collapsed surfaces was then investigated by computing a topographic cross sections of water depth values for each landslide zones. In this regard, water depth values for *YesRoad* and *NoRoad* scenarios were extracted along a line tracked crosswise L1 and L2 respectively. Line plots in Fig. 3.9 show cross sections outcomes for each scenario. Looking at the presence and at the assumed absence of the road, the comparison of water depth cross sections extracted for L1-pre (Fig. 3.9a–b) L1-post (Fig. 3.9c–d) and L2 zone (Fig. 3.9e–f) highlights the role played by the road in water flows diversion toward the collapsed hillslopes.

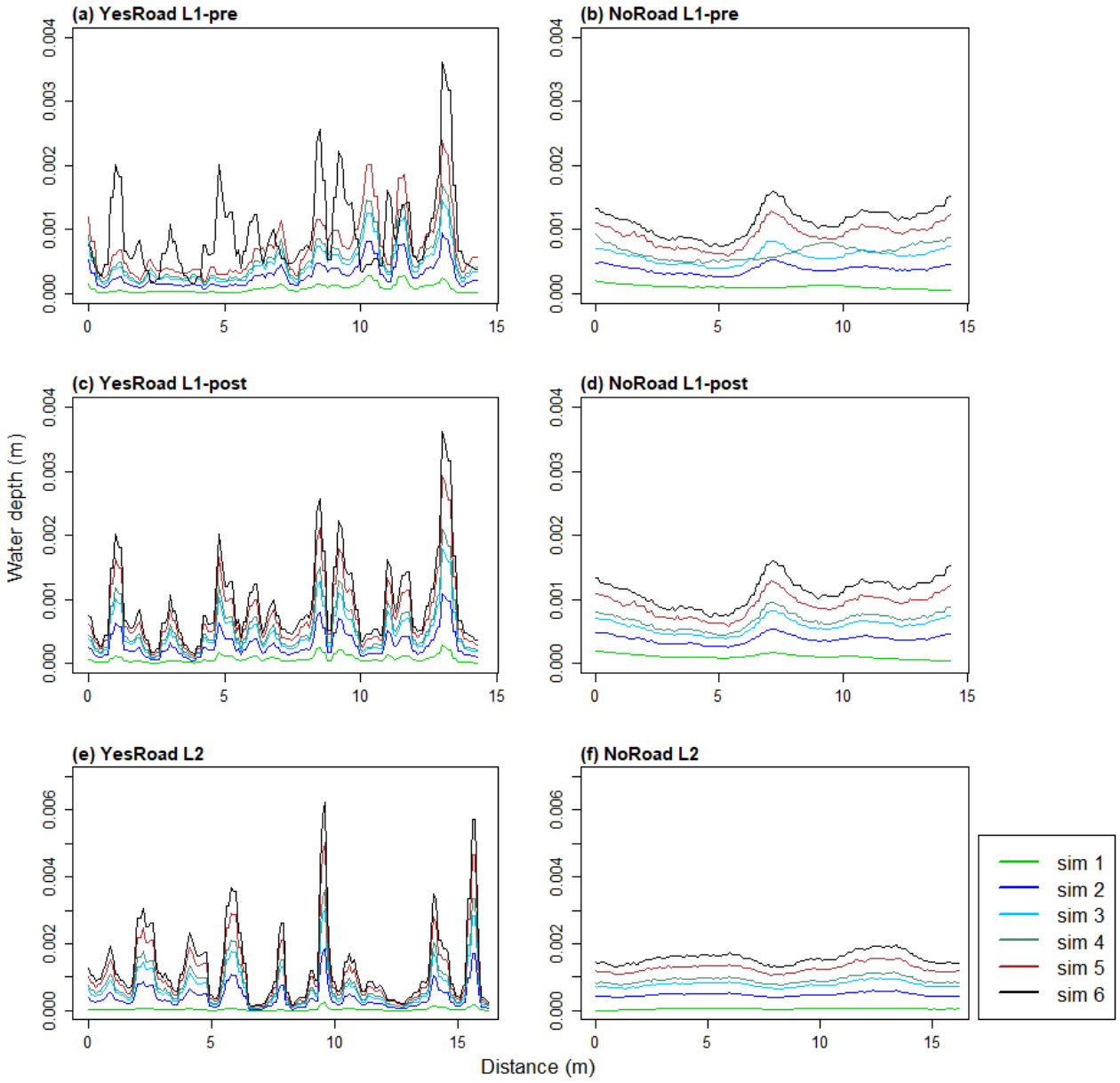

Figure 3.9. *Line plots showing water depth cross-sections computed for each simulation of the YesRoad and NoRoad scenarios. In particular, the figure shows water depth cross-sections elaborated both looking at the presence of the road and its assumed absence for L1-pre (a–b), L1-post (c–d) and L2 (e–f).*

The comparison of cross-sections computed for *YesRoad* and *NoRoad* scenarios further proves as the assumed absence of the road strongly influences the amount of water crossing the collapsed surface. Statgraphics® software and specific codes implemented in R environment were used to perform statistical analysis. Statistical hypothesis testing was carried out, through the computation of both normality test and two-sample *t*-test assuming unequal variances. Normality distribution of data was firstly checked through the application of the Shapiro-Wilk normality test. In this regard, since Shapiro-Wilk-derived p-values resulted greater than the considered significance level (alpha equal to

0.05), water depth values extracted from control points placed along the road sections above L1-pre, L1-post and L2 were found to be normally distributed. Statistical differences between the presence and the assumed absence of the road network, in terms of water accumulation along its detected sections, were investigated. Therefore, the null hypothesis (H_0) and the alternative hypothesis (H_1) were identified. H_0 assumed that the presence of the road does not affect water accumulation and deviation in the direction of the landslides-prone zones, while H_1 considered the effective role played by the road in increasing water depth along with it and therefore in the likely activation of the observed shallow landslides. Moreover, two-tail *p*-values (alpha equal to 0.05) were calculated to further support the outcomes of the statistical analysis. The following tables show the results of the computed statistical analysis regarding water depth values extracted from each control point along road sections above L1-pre (Table 3.4), L1-post (Table 3.5), and L2 (Table 3.6). Looking at the following tables, since *t*-values are greater than t-statistic, H_0 is rejected in favor of H_1 for all the scenarios. This is also confirmed by the computation of *p*-values, which are highly minor than the significance level, thus proving that the considered sample gives reasonable evidence to support the alternative hypothesis.

3.6 Discussion

This work proposes an analysis of road influence on water flows alteration in a terraced vineyard affected by shallow landslides. For this purpose, a multi-temporal hydrological analysis was computed through the adoption of a specific hydrological model in the simulation of overland flow dynamics on the landslides-prone hillslopes among time. In this perspective, our work further highlighted the efficiency of RPAS-based SfM multi-temporal surveys in the investigation of the presented issue, in line with the application of such a technology in agricultural contexts recently proposed by Tucci *et al*. (2019), Yamazaki *et al*. (2019), Meinen and Robinson (2020) and Mauri *et al*. (2021). Thanks to the adoption of this photogrammetric technique, the creation of high-resolution DEMs), allowed to perform a detailed hydrological analysis at the hillslope scale, differently from similar investigations conducted at the watershed scale (Arnone *et al*., 2011; Jebur *et al*., 2014) and on wider one (De Vita *et al*., 2013; Yang *et al*., 2019; Zhao *et al*., 2019). Several studies have been carried out about water dynamics on landslide-prone steep slopes, focusing on spatio-temporal dynamics of soil water content (Arnone *et al*., 2011), rainfall influence on landslides activation (Collins *et al*., 2004; Dai and Lee, 2001; Kefeer *et al*., 1987), changes in subsurface water and soil properties (Bogaard and Greco, 2016; Ray and Jacobs, 2007; Yang *et al*., 2019; Zhao *et al*., 2019), landslide hydrology investigation (Smith *et al*., 1995) and critical rainfall threshold evaluation (Guzzetti *et al*., 2007; Brunetti *et al*., 2010; Harmon *et al*., 2019). In this context, even though the availability of many investigations of the role played by roads and trails in land degradation phenomena like erosion processes (Elliot *et al*., 1999; MacDonald *et al*., 2001; Salesa *et al*., 2019; Yu *et al*., 2021) and landslides occurrence (Fu *et al*., 2010; Penna *et al*., 2014; Sidle and Ziegler, 2012; Tarolli *et al*., 2021), our research distinguishes from those available in the respective literature in that it proposes an innovative comparison of road-water-landslides interaction among time at centimetres scale, in function of both recorded and simulated rainfall intensity peaks. The multi-temporal comparison of SIMWE simulations for the *YesRoad* and *NoRoad* scenarios was suitable for the investigation of the role played by the road network in the alteration of superficial water flows close to the collapsed surfaces. In this regard, the assumed absence of the road and the corresponding hydrological simulations proved its active contribution in diverting overland water directions. Differently from the common applications of SIMWE (Cencetti *et al*., 2005; Fernandes *et al*., 2017; Koco, 2011; Pijl *et al*., 2020) the multi-temporality that distinguishes the adoption of the model is completely novel, as well as the investigation of superficial water dynamics looking at the assumed absence of infrastructures. In this regard, our work fills the gap in the scientific knowledge regarding the possibility to perform such a low-cost, high-resolution, multi-temporal hydrological

analysis at a hillslope scale. Looking at the examined study area, our research also suggests as the absence of drainage systems along the road sections located above the shallow landslides has a relevant influence on runoff dynamics on the roadway. Similar outcomes have been proposed by Mulder *et al*. (1994), Vlotman *et al*. (2001), Needelman *et al*. (2007), Mrvik and Bomont (2012) and Skaggs *et al*. (2012), who investigated the role played by drainage systems on efficient water management and land degradation control in agricultural environments. Furthermore, the simulation of the absence of road so as to highlight its role in the alteration of water flow directions close to the slope failure further proved the capability of the SIMWE model in the description of the interaction between road network and water runoff dynamics in hydrological terms.

3.7 Conclusions

This work proposes a multi-temporal analysis of road-induced overland flow alteration in an agricultural terraced area characterized by the activation of shallow landslides. RPAS-based SfM technique allowed to obtain high-resolution DEMs), which served as a base to perform a 4D hydrological analysis through an innovative application of the SIMWE model. Simulations under the *NoRoad* scenario were also performed, smoothing the RPAS-derived DEM and investigating water dynamics in function of the recorded and the assumed rainfall intensity peaks set as input in the model. Our work represents a solid starting point for future investigations on a wider scale. This work also underlined as the presence of rural roads within a steep slope agricultural context can be particularly critical in terms of runoff deviation towards collapsed hillslopes. In this regard, the proposed methodology can be considered as a useful tool for obtain hydrologic maps or modeling of land degradation phenomena affecting agricultural areas, in order to identify those zones that could be potentially involved in the occurrence of future land degradation processes (eg., slope failures). More investigations could be undertaken to deeply investigate the dynamics of surface water flows assuming the presence of drainage systems (e.g., ditches) along the roadway, as well as focusing on the role played by specific road characteristics in both runoff deviation and landslides activation. The multi-temporal comparison of SIMWE simulations reasonably suggests that the absence of drainage systems might represent a primary factor in the alteration of water runoff, which in turn could be involved in consequential landslides triggering. Specific interventions such as hillslopes stabilization, soil management and restoration, as well as the design of efficient drainage systems could be carried out starting from the comparison of hydrological simulations. Analogously, the proposed application of the SIMWE model could be useful in figuring out critical rainfall thresholds related to the occurrence of land degradation events such as landslides and erosion processes, focusing on detailed planning of mitigation interventions at plot scale able to reduce the occurrence of future land degradation phenomena. Finally, multi-temporal hydrological simulations could allow to conduct specific geotechnical investigation regarding shallow landslides activation and perform slope stability analysis, in order to properly prove the role played by the road network in the occurrence of these land degradation phenomena. The integration of such detailed studies would be a solid starting point for the identification of those areas that are more prone to landslide occurrence.

Acknowledgements

This research was partly founded by the University of Padova research project DOR2079232/20 “Analysis of soil erosion and surface ponding in the agricultural context”. The authors kindly thank Gabriele Bombardelli and “Acetaia del Balsamico Trentino” farm for providing the study area for the research. The authors thank the anonymous reviewers for their useful suggestions that helped us to improve our research.

3.8 Supplementary material

3.8.1 Supplementary figures

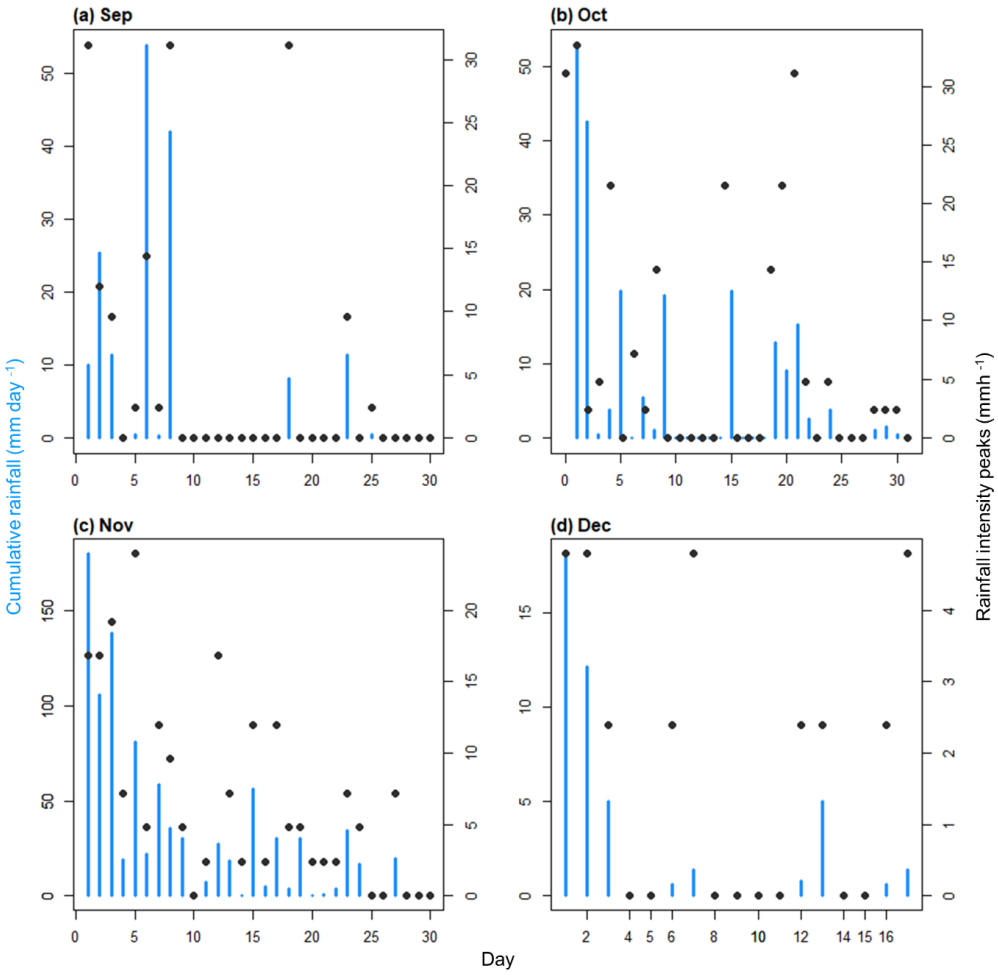

Figure 3.10. *Barplots showing the trend of daily cumulative rainfall (mm day-1) and point-plots showing the trend of daily rainfall intensity peaks (mmh-1) recorded in September 2019 (a), October 2019 (b), November 2019 (c) and December 2019 (d).*

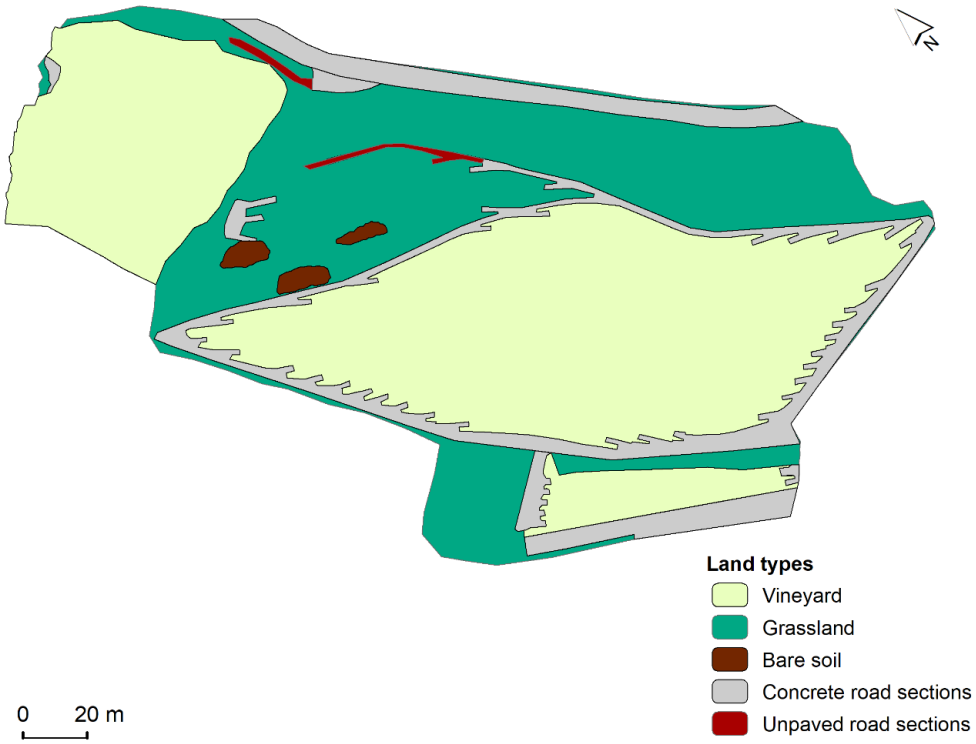

Figure 3.11. *Land types identified within the study area.*

Figure 3.12. *Overview of checkpoints location along the paved and the unpaved road section located above L1 and L2. The orthophoto was computed from the second RPAS-derived point cloud, so as to appreciate the presence of the two detected landslides within the study area.*

3.8.2 Supplementary tables

Table 3.4. *Overview of statistical parameters derived from t-test and p-value computation for water depth values extracted from control points placed along the paved road section above L1-pre*

SIMWE simulation	Scenario	Variance	p-value	t value	t statistic
SIM 1 (7.2 mmh^{-1})	YesRoad	2.68E-07	3.42E-12	11.83	2.06
	NoRoad	3.05E-06			
SIM 2 (25.0 mmh^{-1})	YesRoad	6.25E-06	2.17E-10	10.42	
	NoRoad	8.37E-06			
SIM 3 (33.6 mmh^{-1})	YesRoad	1.48E-05	9.98E-11	10.84	
	NoRoad	7.40E-05			
SIM 4 (40.0 mmh^{-1})	YesRoad	1.69E-08	1.14E-10	10.52	
	NoRoad	2.72E-08			
SIM 5 (60.0 mmh^{-1})	YesRoad	5.28E-08	5.31E-11	11.18	
	NoRoad	2.38E-07			
SIM 6 (80.0mmh^{-1})	YesRoad	1.08E-07	1.40E-06	6.36	
	NoRoad	1.66E-07			

Table 3.5. *Overview of statistical parameters derived from t-test and p-value computation for water depth values extracted from control points placed along the paved road section above L1-post*

SIMWE simulation	Scenario	Variance	p-value	t value	t statistic
SIM 1 (7.2 mmh^{-1})	YesRoad	6.14E-07	2.80E-07	6.94	2.06
	NoRoad	7.29E-09			
SIM 2 (25.0 mmh^{-1})	YesRoad	8.11E-06	3.41E-06	6.00	
	NoRoad	2.72E-08			
SIM 3 (33.6 mmh^{-1})	YesRoad	1.94E-05	2.07E-06	6.20	
	NoRoad	5.28E-08			
SIM 4 (40.0 mmh^{-1})	YesRoad	2.60E-05	1.88E-06	6.24	
	NoRoad	6.63E-08			
SIM 5 (60.0 mmh^{-1})	YesRoad	4.77E-05	1.25E-06	6.41	
	NoRoad	1.08E-07			
SIM 6 (80.0mmh^{-1})	YesRoad	7.40E-05	1.40E-06	6.36	
	NoRoad	1.66E-07			

Table 3.6. *Overview of statistical parameters derived from t-test and p-value computation for water depth values extracted from control points placed along the paved road section above L2*

SIMWE simulation	Scenario	Variance	p-value	t value	t statistic
SIM 1 (7.2 mmh^{-1})	YesRoad	5.68E-07	6.47E-07	6.69	2.06
	NoRoad	1.08E-10			
SIM 2 (25.0 mmh^{-1})	YesRoad	1.11E-05	3.42E-07	6.95	
	NoRoad	3.75E-09			
SIM 3 (33.6 mmh^{-1})	YesRoad	3.04E-05	3.45E-07	6.95	
	NoRoad	9.18E-09			
SIM 4 (40.0 mmh^{-1})	YesRoad	4.54E-05	4.40E-07	6.85	
	NoRoad	1.32E-08			
SIM 5 (60.0 mmh^{-1})	YesRoad	8.52E-05	3.97E-07	6.89	
	NoRoad	2.66E-08			
SIM 6 (80.0mmh^{-1})	YesRoad	1.37E-04	5.14E-07	6.78	
	NoRoad	4.40E-08			

3.9 References

Alagna, V., Di Prima, S., Rodrigo-Comino, J., Iovino, M., Pirastru, M., Keesstra, S. D., Novara, A., Cerdà, A. (2018). The impact of the age of vines on soil hydraulic conductivity in vineyards in eastern Spain. Water, 10 (1). https://doi.org/10.3390/w10010014

Arnone, E., Noto, L. V., Lepore, C., Bras, R. L. (2011). Physically-based and distributed approach to analyze rainfall-triggered landslides at watershed scale. Geomorphology, 133, 121-131. https://doi.org/10.1016/j.geomorph.2011.03.019

Bajocco, S., De Angelis, A., Perini, L., Ferrara, A., Salvati, L. (2012). The impact of land use/land cover changes on land degradation dynamics: a Mediterranean case study. Environmental Management, 49, 980-989. https://doi.org/10.1007/s00267-012-9831-8

Biddoccu, M., Ferraris, S., Cavallo, E., Opsi, F., Previati, M., Canone, D. (2013). Hillslope vineyard rainfall-runoff measurements in relation to soil infiltration and water content. Procedia Environmental Sciences, 19, 351-360. https://doi.org/10.1016/j.proenv.2013.06.040

Bogaard, T. A., Greco, R. (2016). Landslide hydrology: From hydrology to pore pressure. Wiley Interdisciplinary Reviews: Water, 3, 439-459. https://doi.org/10.1002/wat2.1126

Brunetti, M. T., Peruccacci, S., Rossi, M., Luciani, S., Valigi, D., Guzzetti, F. (2010). Rainfall thresholds for the possible occurrence of landslides in Italy. Nat. Hazards Earth. Syst., 10, 447-458. https://doi.org/10.5194/nhess-10-447-2010

Bunya, S., Dietrich, J. C., Westerink, J. J., Ebersole, B. A., Smith, J. M., Atkinson, J. H., Jensen, R., Resio, D. T., Luettich, R. A., Dawson, C., Cardone, V. J., Cox, A. T., Powell, M. D., Westerink, H. J., Roberts, H. J. (2010). A high-resolution coupled riverine flow, tide, wind, wind wave, and storm surge model for southern Louisiana and Mississippi. Part I: Model development and validation. Monthly Weather Review, 138, 345-377. https://doi.org/10.1175/2009MWR2906.1

Capello, G., Biddoccu, M., Ferraris, S., Cavallo, E. (2019). Effects of tractor passes on hydrological and soil erosion processes in tilled and grassed vineyards. Water, 11 (10), 2118. https://doi.org/10.3390/w11102118

Cencetti, C., De Rosa, P., Fredduzzi, A., Marchesini, I. (2005). Erosione dei suoli: Applicazioni tramite il software GRASS GIS. Giornale di Geologia Applicata, 2, 196-202. DOI: 10.1474/GGA.2005–02.0–28.0054

Collins, B. D., Znidarcic, D. (2004). Stability analyses of rainfall induced landslides. Journal of Geotechnical and Geoenvironmental Engineering, 130 (4), 362-372. https:// doi.org/10.1061/(asce)1090-0241(2004)130:4(362)

Cruden, D. M., Varnes, D. J. (1996). Landslide types and processes. Landslides: Investigation and mitigation. Transportation Research Board: Special Report - National Research Council. ISSN: 0360-859X

Dai, F. C., Lee, C. F. (2001). Frequency-volume relation and prediction of rainfall induced landslides. Engineering Geology, 59(3-4), 253-266. https://doi.org/10.1016/S0013-7952(00)00077-6

Davison, L., Springman, S., Wood, D. M. (2000). Pore water pressure. University of the West of England. https://environment.uwe.ac.uk/geocal/SoilMech/water/water.htm

De Vita, P., Napolitano, E., Godt, J. W., Baum, R. L. (2013). Deterministic estimation of hydrological thresholds for shallow landslide initiation and slope stability models: Case study from the Somma-Vesuvius area of southern Italy. Landslides, 10, 713-728. https://doi.org/10.1007/s10346-012-0348-2

Dikau, R., Brunsden, D., Shrott, L., Ibsen, M. L. (1996). In R. Dikau, D. Brunsden, L. Schrott, M. L. Ibsen (Eds.), Landslides recognition, identification, movement and causes. New York: John Wiley Sons, ISBN 978-0-471-96477-3

Eker, R., Aydin, A. (2014). Assessment of forest road conditions in terms of landslide susceptibility: A case study in yığılca forest directorate (Turkey). Turkish Journal of Agriculture and Forestry, 38 (2), 281-290. https://doi.org/10.3906/tar-1303-12

Elliot, W. J., Foltz, R. B., Luce, C. H. (1999). Modeling low-volume road erosion. Transportation Research Record, 1652 (1), 244-249. https://doi.org/10.3141/1652-64

Evans, I. S. (1979). An integrated system of terrain analysis and slope mapping. Statistical characterization of altitude matrices by computer -- report 6. University of Durham, Department of Geography (Eds).

Fagnano, M., Diodato, N., Alberico, I., Fiorentino, N. (2012). An overview of soil erosion modelling compatible with RUSLE approach. Rend. Fis. Acc. Lincei, 23, 69-80. https://doi.org/10.1007/s12210-011-0159-8

Fatehnia, M., Tawfiq, K., Ye, M. (2016). Estimation of saturated hydraulic conductivity from double-ring infiltrometer measurements. European Journal of Soil Science, 67, 135-147. DOI: 10.1111/ejss.12322

Fernandes, J., Bateira, C., Soares, L., Faria, A., Oliveira, A., Hermenegildo, C., Moura, R., Gonçalves, J. (2017). SIMWE model application on susceptibility analysis to bank gully erosion in Alto Douro Wine Region agricultural terraces. Catena, 153, 39-49. https://doi.org/10.1016/j.catena.2017.01.034

Flanagan, D. C., Nearing, M. A. (1995). Water erosion prediction Project: Hillslope profile and watershed model documentation. West Lafayette, Indiana: USDA Agricultural Research Service, National Soil Erosion Research Laboratory. NSERL Report No.10

Fu, B., Newhama, L. T. H., Ramos-Scharr_on, C. E. (2010). A review of surface erosion and sediment delivery models for unsealed roads. Environmental Modelling Software, 25 (1), 1-14. https://doi.org/10.1016/j.envsoft.2009.07.013

Gallage, C., Abeykoon, T., Uchimura, T. (2021). Instrumented model slopes to investigate the effects of slope inclination on rainfall-induced landslides. Soils and Foundations, 61 (1), 160-174. https://doi.org/10.1016/j.sandf.2020.11.006

Gollin, D., Rogerson, R. (2010). Agriculture, roads, and economic development in Uganda. National Bureau of Economic Research, 15863. https://www.nber.org/papers/w15863

Guzzetti, F., Peruccacci, S., Rossi, M., Stark, C. P. (2007). Rainfall thresholds for the initiation of landslides in central and southern Europe. Meteorology and Atmospheric Physics, 98, 239-267. https://doi.org/10.1007/s00703-007-0262-7

Harmon B.A., Mitasova, H., Petrasova, A., Vaclav, P. (2019). r.sim.terrain 1.0: a landscape evolution model with dynamic hydrology. Geoscientific Model Development, 12 (7), 2837-2854. https://doi.org/10.5194/gmd-12-2837-2019

Harp, E. L., Wells, W. G., Sarimento, J. G. (1990). Pore pressure response during failure in soils. The Geological Society of America Bulletin, 102 (4), 428-438. https://doi.org/10.1130/0016-7606(1990)102<0428:PPRDFI>2.3.CO;2

Jebur, M. N., Pradhan, B., Tehrany, M. S. (2014). Optimization of landslide conditioning factors using very high-resolution airborne laser scanning (LiDAR) data at catchment scale. Remote Sensing of Environment, 152, 150-165. https://doi.org/10.1016/j.rse.2014.05.013

Keefer, D. K., Wilson, R. C., Mark, R. K., Brabb, E. E., Brown, W. M., Ellen, S. D., Harp, E. L., Wieczorek, G. F., Alger, C. S., Zatkin, R. S. (1987). Real-time landslide warning during heavy rainfall. Science, 238, 921-925. https://doi.org/10.1126/science.238.4829.921

Koco, S. (2011). Simulation of gully erosion using the SIMWE model and GIS. Landform Analysis, 17, 81-86

Lai, J., Ren, L. (2007). Assessing the size dependency of measured hydraulic conductivity using double-ring infiltrometers and numerical simulation. Soil Science Society of America Journal, 71 (6), 1667-1675. https://doi.org/10.2136/sssaj2006.0227

Lopez-Vicente, M., Nadal-Romero, E., Cammeraat, E.L.H. (2017). Hydrological connectivity does change over 70 years of abandonment and afforestation in the Spanish pyrenees. Land Degradation Development, 28 (4), 1298-1310. https://doi.org/10.1002/ldr.2531

Louwagie, G., Gay, S. H., Sammeth, F., Ratinger, T. (2011). The potential of European Union policies to address soil degradation in agriculture. Land Degradation Development, 22 (1), 5-17. https://doi.org/10.1002/ldr.1028

McDonald, L. H., Sampson, R. W., Anderson, D. M. (2001). Runoff and road erosion at the plot and road segment scales, St John, US Virgin Islands. Earth Surface Processes and Landforms, 26 (3), 251-272. https://doi.org/10.1002/1096-9837(200103)26:3<251::AID-ESP173>3.0.CO;2-X

Marion, J. L., Leung, Y. F. (2004). Environmentally sustainable trail management. Environmental Impacts of Ecotourism. R. Buckley Eds. https://doi.org/10.1079/9780851998107.0229

Mauri, L., Sallustio, L., Tarolli, P. (2019). The geomorphologic forcing of wild boars. Earth Surface Processes and Landforms, 44 (10). https://doi.org/10.1002/esp.4623

Mauri, L., Straffelini, E., Cucchiaro, S., Tarolli, P. (2021). UAV-SfM 4D mapping of landslides activated in a steep terraced agricultural area. Journal of Agricultural Engineering, 52 (1). https://doi.org/10.4081/jae.2021.1130

Meinen, U. B., Robinson, T. D. (2020). Mapping erosion and deposition in an agricultural landscape: Optimization of UAV image acquisition schemes for SfM-MVS. Remote Sensing of Environment, 239. https://doi.org/10.1016/j.rse.2020.111666

Mitasova, H., Barton, C. M., Ullah, I., Hofierka, J., Harmon, R. S. (2013). GIS-based soil erosion modeling. Remote Sensing and GIScience in Geomorphology, 31 (3), 228-258. Elsevier Inc (Eds), ISNB: 9780080885223

Mitasova, H., Thaxton, C., Hofierka, J., McLaughlin, R., Moore, A., Mitas, L. (2004). Path sampling method for modeling overland water flow, sediment transport, and short-term terrain evolution in Open-Source GIS. Developments in Water Science, 55 (2), 1479-1490. https://doi.org/10.1016/S0167-5648(04)80159-X

Mrvìk, O., Bomont, S. (2012). Experience with treatment of road structure landslides by innovative methods of deep drainage. In Landslides, S. Mambretti (Eds). doi:10.2495/DEB100101

Mulder, G. J., Luijten, C. J. L. M., Schouten, C. P. (1994). Case study: Modelling the impact of a drainage-system along a depressed roadbed and the resulting risks to agriculture. : Proceedings of the Conference on the Future Groundwater Resources at Risk held at Helsinki, Netherlands. IAHS Publ., 222: 61-70

Needelman, B. A., Kleinman, P. J. A., Strock, J. S., Allen, A. L. (2007). Improved management of agricultural drainage ditches for water quality protection: An overview. Journal of Soil and Water Conservation, 62, 171-178. ISSN : 0022-4561

Pamar, H. V. (2014). Agricultural drainage engineering: Field and laboratory manual. Scientific Publishers (Eds)

Penna, D., Borga, M., Aronica, G. T., Brigandi, G., Tarolli, P. (2014). The influence of grid resolution on the prediction of natural and road-related shallow landslides. Hydrology and Earth System Sciences, 18 (6), 2127-2139. https://doi.org/10.5194/hess-18-2127-2014

Pijl, A., Reuter, L. E. H., Quarella, E., Vogel, T. A., Tarolli, P. (2020). GIS-based soil erosion modelling under various steep-slope vineyard practices. Catena, 193. https://doi.org/10.1016/j.catena.2020.104604

Ray, R. L., Jacobs, J. M. (2007). Relationships among remotely sensed soil moisture, precipitation and landslide events. Natural Hazards, 43, 211-222. https:// doi.org/10.1007/s11069-006-9095-9

Romm, J. (2011). Desertification: The next dust bowl. Nature, 478, 450-451. https://doi.org/10.1038/478450a

Rusnàk, M., Slàdek, J., Kidovà, A., Lehotský, M. (2018). Template for high resolution river landscape mapping using UAV technology. Measurement, 115, 139-151. https://doi.org/10.1016/j.measurement.2017.10.023

Rusu, R. B., Cousins, S. (2011). 3D is here: Point cloud library (pcl). EEE International Conference on Robotics and Automation, 1-4. DOI: 10.1109/ICRA.2011.5980567

Salesa, D., Terol, E., Cerdà, A. (2019). Soil erosion on the "*el portalet*" mountain trails in the eastern Iberian peninsula. The Science of the Total Environment, 661, 504-513. https://doi.org/10.1016/j.scitotenv.2019.01.192

Sidle, R. C., Ghestem, M., Stokes, A. (2014). Epic landslide erosion from mountain roads in Yunnan, China-challenges for sustainable development. Natural Hazards and Earth System Sciences, 14 (11), 3093-3104. https://doi.org/10.5194/ nhess-14-3093-2014

Sidle, R. C., Ziegler, A. D. (2012). The dilemma of mountain roads. Nature Publishing Group, 5 (7), 437-438. https://doi.org/10.1038/ngeo1512

Sidle, R. C., Ziegler, A. D., Negishi, J. N., Rahim, A., Siew, R., Turkelboom, F. (2006). Erosion processes in steep terrain dtruths , myths , and uncertainties related to forest management in Southeast Asia. Forest Ecology and Management, 224, 199-225. https://doi.org/10.1016/j.foreco.2005.12.019

Skaggs, R. W., Norman, R. F., Evans, R. O. (2012). Drainage water management. Journal of Soil and Water Conservation, 67, 167-172. DOI: https://doi.org/10.2489/jswc.67.6.167A

Smith, R. E., Goodrich, D. C., Quinton, J. N. (1995). Dynamic, distributed simulation of watershed erosion: The KINEROS2 and EUROSEM models. Journal of Soil and Water Conservation, 50 (5), 517-520. ISSN: 1941-3300

Tarolli, P., Pijl, A., Cucchiaro, S., Wei, W. (2021). Slope instabilities in steep cultivation systems: Process classification and opportunities from remote sensing. Land Degradation Development. https://doi.org/10.1002/ldr.3798

Tarolli, P., Sofia, G., Calligaro, S., Prosdocimi, M., Preti, F., Dalla Fontana, G. (2015). Vineyards in terraced landscapes: New opportunities from LiDAR data. Land Degradation Development, 26, 92-102. https://doi.org/10.1002/ldr.2311

Tarolli, P., Straffelini, E. (2020). Agriculture in hilly and mountainous landscapes: threats, monitoring and sustainable management. Geography and Sustainability, 1 (1), 70-76. https://doi.org/10.1016/j.geosus.2020.03.003

Thiery, Y., Vandromme, R., Maquaire, O., Bernardie, S. (2017). Landslide susceptibility assessment by EPBM (Expert Physically Based Model): strategy of calibration in complex environment. WLF4 - 4th World Landslide Forum, May 2017, Ljubljana, Slovenia. ⟨hal-01496805v1⟩

Tucci, G., Parisi, E. I., Castelli, G., Errico, A., Corongiu, M., Sona, G., Viviani, E., Bresci, E., Preti, F. (2019). Multi-sensor UAV application for thermal analysis on a dry-stone terraced vineyard in rural tuscany landscape. ISPRS Int. J. Geo-Inf, 8 (2), 87. https://doi.org/10.3390/ijgi8020087

Vlotman, W. F., Smedema, L. K., Rycroft, D. W. (2001). Modern land drainage. In Planning, design and management of agricultural drainage systems. CRC Press/ Balkema.

Webb, N. P., Marshall, N. A., Stringer, L. C., Reed, M. S., Chappell, A., Herrick, J. E. (2017). Land degradation and climate change: Building climate resilience in agriculture. Frontiers in Ecology and the Environment, 15 (8), 450-459. https:// doi.org/10.1002/fee.1530

Wemple, B. C., Swanson, F. J., Jones, A. J. (2001). Forest roads and geomorphic process interactions, Cascade Range, Oregon. Earth Surface Processes and Landforms, 26 (2), 191-204. https://doi.org/10.1002/1096-9837(200102)26:2<191::AID-ESP175>3.0.CO;2-U

Westoby, M. J., Brasington, J., Glasser, N. F., Hambrey, M. J., Reynolds, J. M. (2012). Structure-from-Motion' photogrammetry: A low-cost, effective tool for geoscience applications. Geomorphology, 179, 300-314. https://doi.org/10.1016/j.geomorph.2012.08.021

Yamazaki, Y., Okazawa, H., Sekiyama, A., Fujikawa, T. (2019). Accuracy verification of UAV-SfM survey of terrace paddy fields in a hilly and mountainous area. IJERD e International Journal of Environmental and Rural Development, 10 (1), 153-159. https://doi.org/10.32115/ijerd.10.1_153

Yang, Z., Cai, H., Shao, W., Huang, D., Uchimura, T., Lei, X., Tian, H., Qiao, J. (2019). Clarifying the hydrological mechanisms and thresholds for rainfall-induced landslide: In situ monitoring of big data to unsaturated slope stability analysis. Bulletin of Engineering Geology and the Environment, 78, 2139-2150. https://doi.org/10.1007/s10064-018-1295-5

Yu, W., Zhao, L., Fang, Q., Hou, R. (2021). Contributions of runoff from paved farm roads to soil erosion in karst uplands under simulated rainfall conditions. Catena, 196. https://doi.org/10.1016/j.catena.2020.104887

Zhao, B., Dai, Q., Han, D., Dai, H., Mao, J., Zhuo, L. (2019). Probabilistic thresholds for landslides warning by integrating soil moisture conditions with rainfall thresholds. Journal of Hydrology, 574, 276-287. https://doi.org/10.1016/j.jhydrol.2019.04.062

CHAPTER 4

EVALUATING THE INTERACTION BETWEEN SNOWMELT RUNOFF AND ROAD IN THE OCCURRENCE OF HILLSLOPE INSTABILITIES AFFECTING A LANDSLIDE-PRONE MOUNTAIN BASIN: A MULTI-MODELING APPROACH[3]

Luca Mauri,[1] Sara Cucchiaro[1,2], Stefano Grigolato[1], Giancarlo Dalla Fontana[1], Paolo Tarolli[1]

[1]*Department of Land, Environment, Agriculture and Forestry, University of Padova, Legnaro, Italy*
[2]*Department of Agricultural, Food, Environmental and Animal Sciences, University of Udine, Udine, Italy*

Keywords: Snowmelt, Road network, Steep terrain, Landslide, GIS, Modeling

[3] Mauri, L., Cucchiaro, S., Grigolato, S., Dalla Fontana, G., Tarolli, P. (2022). Evaluating the interaction between snowmelt runoff and road in the occurrence of hillslope instabilities affecting a landslide-prone mountain basin: A multi-modeling approach. ***Journal of Hydrology***, 612 (B) https://doi.org/10.1016/j.jhydrol.2022.128200

4.1 Abstract

The presence of roads in steep slope mountain areas is often linked with the occurrence of landslides and erosive dynamics. The use of Airborne Laser Scanning (ALS)-derived high-resolution topographic data increased the possibilities to better represent landscapes and related physical processes at the watershed scale. Additionally, the adoption of topographically-based hydrological models allows to simulating water overland flows and investigate the occurrence of specific degradative phenomena. Snowpack melting plays a primary role in altering superficial water dynamics in mountain landscapes, but accurate investigation of the interaction between snowmelt runoff and human infrastructures (such as roads and trails) in the occurrence of hillslope failures is still obscure. This research aims to assess the relationship between snowmelt runoff, road presence and terrain instabilities affecting a landslide-prone steep slope mountain meadow (northern Italy). An innovative multi-modeling approach was proposed to detect the alteration of snowmelt overflows due to the presence of the road and its relation with the activation of a shallow landslide. The road role in altering snowmelt runoff was investigated both considering its presence and assuming its absence. Different hydrological and slope stability models were interactively considered, starting from pre-event ALS-derived DEM to compute predictive basin-scale simulations. Results attested the key role played by the road in altering snowmelt runoff pathways, as well as their combined contribution to the foreseen activation of the observed shallow landslide. Starting from on-field observations conducted after the landslide triggering, the accuracy of instabilities predictions was finally tested through the statistical computation of the *Area Under* the *Receiver Operating Characteristic curve (AUC-ROC)* and the *Cohen's kappa*-index (*k*), respectively resulted around 0.9 and 0.6. This work could be a useful tool for planning mitigation interventions able to reduce the occurrence of similar risk scenarios, also providing suggestions for developing and promoting efficient sustainable actions for mountain landscapes.

4.2 Introduction

Water runoff and road networks can jointly activate land degradation processes on steep slopes mountain regions (Sidle *et al*., 2014; Tarolli *et al*., 2020). The impact of roads in mountain ecosystems is worldwide recognized (Wemple and Jones, 2003, Daigle, 2010, Soulis *et al*., 2014, Wang *et al*., 2021). First, road presence is responsible for the alteration of hydro-geomorphological processes (Luce, 2002, Dutton *et al*., 2005, Bernardi De León, 2009, Penna *et al*., 2011), potentially leading to soil degradation (Conant *et al*., 2001, Gao *et al*., 2001, Mauri *et al*., 2021, Mauri *et al*., 2022). Both terrain cohesion and strength can seriously decrease because of hillside cutting, slopes' toe removal and filling operations characterizing road construction (Sidle *et al*., 2014; Achour *et al*., 2017, Zhao *et al*., 2019). Roadcut embankments, fill slopes and ditch relief also can activate water runoff and consequential terrain instabilities (Arnáez *et al*., 2007, Jordan, 2008, Xu *et al*., 2009). In addition, the presence of road is responsible for altering water dynamics and flows pathways that are intercepted by road's surface and cut slopes (Montgomery, 1994, Wemple *et al*., 2001, Borga *et al*., 2004, Penna *et al*., 2014, Zhao *et al*., 2019). Finally, both the absence and the inefficient location of drainage systems can critically re-route runoff patterns (Buchanan *et al*., 2013, Tarolli *et al*., 2013, Salesa *et al*., 2019). In this regard, the relation between negative pore-water pressure and soil shear strength primarily regulates the occurrence of landslides and erosive dynamics due to road-diverted water flows (Davison *et al*., 2000, Bogaard and Greco, 2016). The vertical translocation of water across soil strata induces an increase in upslope pore-water pressure of the unsaturated layers (Hinds *et al*., 2021). Such a loss of negative pore-water pressure results in the reduction of both matric suctions and shear strength of soil, which encourages soil weakening until the slope failure (Brand *et al*., 1984, Brubaker *et al*., 1996, Gasmo *et al*., 2000, Collins and Znidarcic, 2004, Gallage *et al*., 2021). Snowmelt processes can similarly participate in terrain failures affecting mountain landscapes (Kawagoe *et al*., 2009, Ashland, 2009, Arghiuş *et al*., 2011, Trandafir *et al*., 2015, Krøgli *et al*., 2018, Miao *et al*., 2019, Al-Umar *et al*., 2020, Hinds *et al*., 2021). Snow accumulations are important sources of water and several factors take part in snow melting, such as (i) spatial variability of snow cover, (ii) elevation ranges inside the basin, (iii) aspect, (iv) slope, (v) vegetation coverage, (vi) wind, (vii) precipitation and (viii) diurnal temperature variation (Ferguson, 1999, Pistocchi, 2016). In addition, water movements through the snowpack influences snowmelt dynamics, according to the internal structure of the snow, its conditions and the availability of water at the surface (Obled and Harder, 1978, Mullem *et al*., 2004). Therefore, the interaction between snowmelt runoff (henceforth called *Sr*) and road presence can be critically responsible for slope instabilities. In the last decades, the need to increase the understanding of complex hydrological and geomorphological phenomena

translated into the development of specific coding and models. Therefore, hydro-geomorphological models become a powerful instrument for analyse landscapes evolution, improve water management and prevent the occurrence of land degradation processes over time (Van der Meij *et al*., 2018, Guo *et al*., 2020, Onate-Valdivieso and Bosque, 2010, Jonas and Hobbs, 2021). Similarly, *Airborne Laser Scanning* (ALS) using the *Light Detection and Ranging* (LiDAR) technology increased our possibilities to obtain spatial environmental point cloud data at basin scale. Similarly, LiDAR-ALS permitted to perform geomorphological and hydrological analysis starting from high-resolution *Digital Elevation Models* (DEMs),) reconstruction. Also, such a technology encouraged the rapid and feasible acquisition of multi-temporal big-data worldwide (Jaboyedoff *et al*., 2012, Cucchiaro *et al*., 2020), useful for detecting land degradative dynamics affecting the earth surface. Considering the above considerations, a predictive analysis of the contribution of snowmelt runoff in the occurrence of hillslope instabilities in mountain basins is actually lacking in the scientific literature. Even more so, the role played by roads in landslides activation due to snowmelt runoff deviation is still obscure. This research aims therefore to investigate the interaction between snowmelt runoff, road presence and hillslope instabilities affecting a landslides-prone, steep slope mountain meadow (northern Italy). In this regard, an innovative multi-modeling approach is proposed. Looking at the aims of this research, pre-event 1 m resolution ALS-derived DEM was used for computing the proposed predictive analysis. Daily snowmelt and rainfall runoff values were firstly simulated by the *Snowmelt Runoff Model* (SRM; Martinec, 1975, Martinec *et al*., 2008), that overcoming the traditional degree-day approach provides a more precise, physically-based simulations of snowmelt processes at watershed scale. *Road Erosion Steady-State* model (RESS; Dietrich *et al*., 1992, Montgomery and Dietrich, 1994, Borga *et al*., 2005) was consequently implemented, looking at its capability to provide spatial mapping of the minimum rainfall intensity able to potentially compromise hillslope stability and the consequent distribution of instability susceptibility areas within the basin. Finally, the *SIMulated Water Erosion* model (SIMWE- Mitasova *et al*., 2013) was applied to detect spatial directions of snowmelt overflow looking at the specific land cover and hydraulic properties. Therefore SRM, RESS and SIMWE models were jointly applied. Model outcomes were finally validated by specific statistical analysis. The proposed research fills the gap in the scientific knowledge regarding the possibility to predict the occurrence of terrain instabilities due to road-deviated snowmelt runoff at the watershed scale through an innovative low-cost, model-based methodological workflow.

4.3 Study area

The study area is a high steep slope mountain grassland located close to the mountain Pordoi pass, in Trentino Alto Adige region, northern Italy (Fig. 4.1). The considered watershed has an overall extension of 1.22 km^2, an average slope equal to 26.9° (between a minimum of 0.02° and a maximum of 88.4°) and an average elevation equal to 2350 m a.s.l. (ranging from a minimum of 2010 m a.s.l and a maximum of 2924 m a.s.l.). The basin is characterized by the presence of rocky areas at the top, while the remaining part is entirely covered by low grass, so it can be with confidence defined as a mountain grassland system. A paved road network is located inside the study area, crossing the slope in the lower part. The road has a total length of about 900 m and an average slope equal to 5.0°. Concrete manholes are located between the roadway and the upper slope, at the bottom of the bank, with a square section of sides ranging from 0.8 m and 1.4 m. A local weather station, located 800 m away from the watershed as the crow flies was used for meteorological data acquisition. During field surveys conducted in 2020, a shallow landslide was observed. Its activation involved a structural failure of a road's section that overturned on the bank below. Several erosion zones were also detected on the upper zones of the entire grassland, further revealing its susceptibility to the occurrence of land degradation phenomena. Such a watershed (henceforth called "*RESS watershed*") was used in soil stability simulations. Differently, a sub-basin (called "*SRM watershed*") was considered for snowmelt computation, setting its outlet at the observed landslide's triggering area (i.e., at the point of the road failure, further upstream to the landslide area below). The daily snowmelt rate was therefore obtained at the latter. SRM watershed covers an area of 0.08 km^2, with an average elevation value equal to 2302 m a.s.l (ranging from a minimum of 2210 m a.s.l, i.e., the outlet location, and a maximum of 2366 m a.s.l) and an average slope equal to 21.8° (between a minimum of 0.01° and a maximum of 88.0°). SRM watershed is almost entirely covered by low herbaceous grass, except for a small rocky part further upstream.

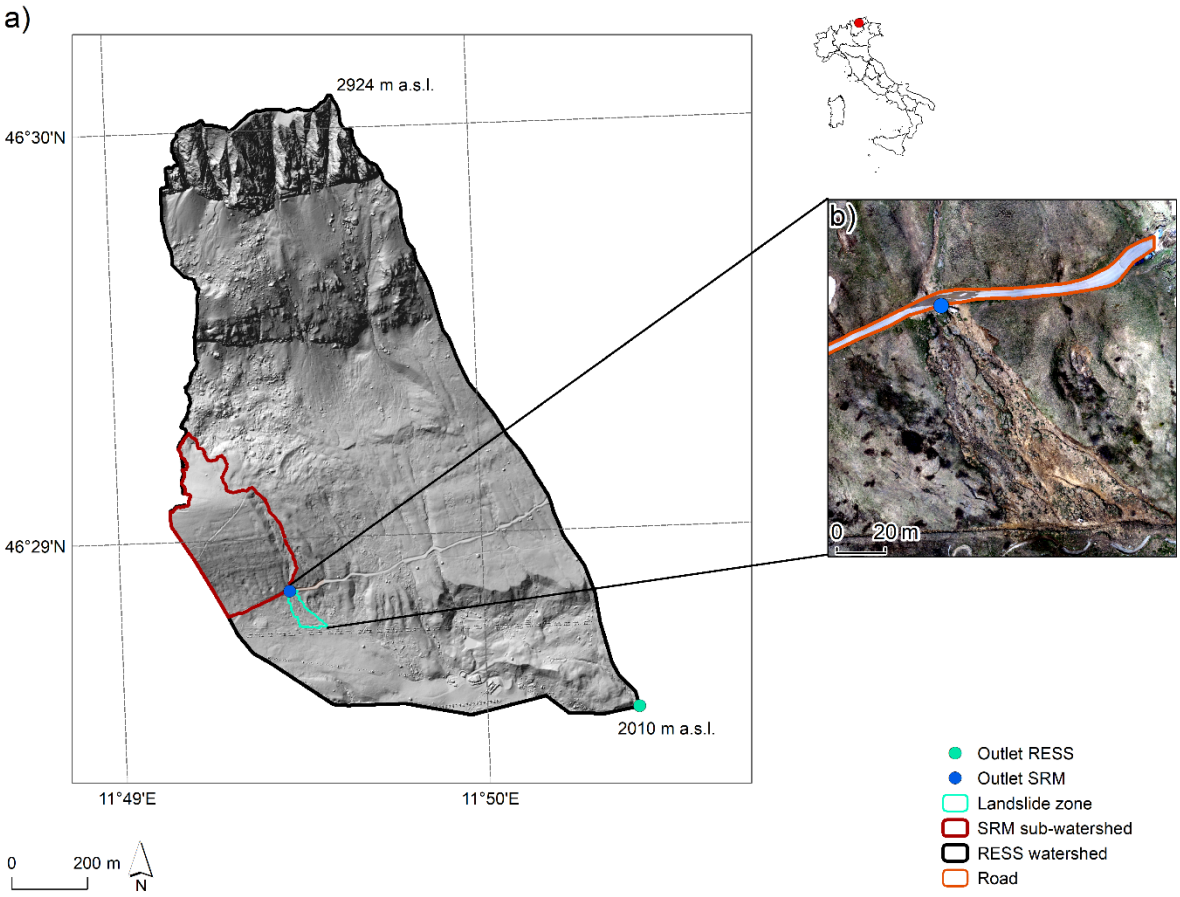

Figure 4.1. *ALS-derived shaded relief of the study area (a) and focus on the detected shallow landslide (b). The figure shows the watershed considered for soil stability analysis performed through the Road Erosion Steady-State (RESS) model (black area) and the sub-watershed considered for snowmelt simulations elaborated with the Snowmelt Runoff Model (SRM, red area). The figure also underlines the location of the respective outlets, as well as the road (orange polygon) and the observed shallow landslide (cyan polygon). Fig. 1b was obtained from high-resolution Uncrewed Aerial Vehicle (UAV)-derived aerial orthomosaic acquired during the post-event (2020) field survey. (For interpretation of the references to colour in this figure legend, the reader is referred to the web version of this article.)*

Field surveys conducted in 2020 after the landslide activation, specifically during the snowmelt period, also highlighted the relevance of the interaction between snowmelt runoff and road surface. In this regard, on-field observations revealed the presence of constant snowmelt runoff coming from the residual melting snowpack, flowing downstream along the grassy hillslope and hence intercepting the paved road (Fig. 4.2a-d). Snowmelt overflows consequently turn out to fall from the roadway to the collapsed hillslope below (Fig. 4.2e, f).

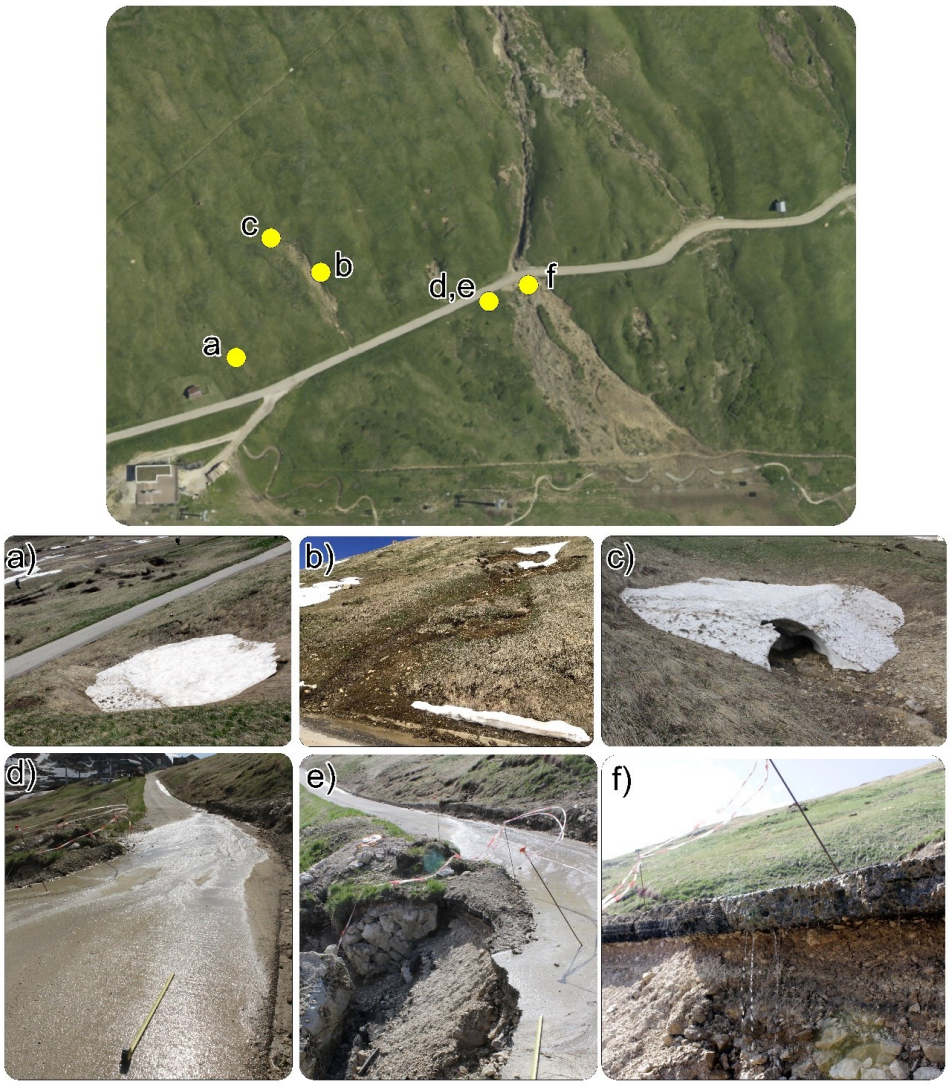

Figure 4.2. *Snowmelt runoff dynamics observed during field surveys conducted in 2020 (post-event conditions). The figure shows snowmelt runoff coming from the melting snow accumulations located on the grassy hillslope above the road (a-c), snowmelt overland flows along the roadway (d, e) and therefore snowmelt runoff falling toward the area involved in the observed shallow landslide (f).*

4.4 Material and methods

4.4.1 Data acquisition and elaboration

A flowchart illustrating the ALS-derived DEM generation, the interactive application of SRM, RESS and SIMWE models and the computed statistical analysis is reported in Fig. 4.3A thorough theoretical overview of each model is presented in the provided supplementary documentation. Table 4.8 summarizes the computed model simulations, while a summary of symbols and abbreviations is available in Table 4.9.

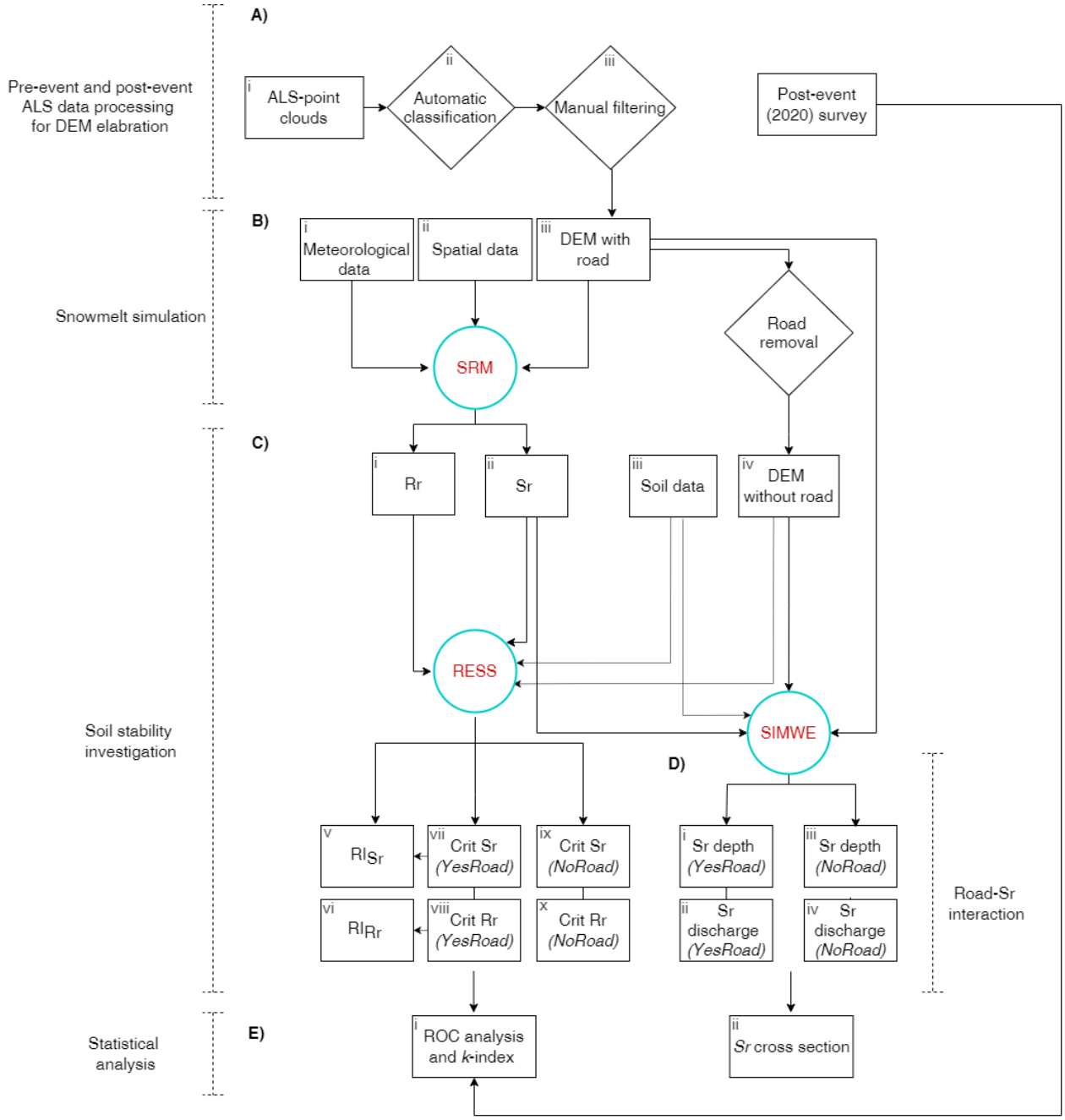

Figure 4.3. *Research flowchart showing the ALS data post-processing (A), the interactive application of Snowmelt Runoff Model - SRM (B), Road Erosion Steady-State - RESS model (C) and SIMulated Water Erosion model - SIMWE (D), and the final statistical analysis (E). Respective model inputs and outputs are represented in rectangular boxes, while models are shown in cyan circles. The rhomboidal box represents data post-processing procedures used for DEM creation and road removal operations. (For interpretation of the references to colour in this figure legend, the reader is referred to the web version of this article.)*

4.4.1.1 Overview of the observed landslide

During field surveys, the features of the observed landslide were manually measured by a surveyor tape to obtain an overview of its characteristics. In addition, an Uncrewed Aerial Vehicle (UAV)-based field-scale survey was conducted in 2020 in order to appreciate local geomorphological characteristics of the landslide surface. The extension of the landslide zone is about 4155 m^2, with a perimeter of 368 m and an average slope equal to 20.6°. Accordingly to the definitions proposed by Dikau *et al*., 1996, Sidle and Bogaard, 2016 and Thiery *et al*., 2017, the observed landslide can be identified as a shallow translational landslide, looking at both the steepness of the failure surface and its dimensions. Looking at Fig. 4b, the main scarp height ($\overline{AB}$) is equal to 1.29 m; the length of the road section over the landslide ($\overline{CD}$) is 33.5 m; the maximum width between landslide's flanks ($\overline{EF}$) is equal to 53.5 m; the length of the landslide zone, from its crown to the respective toe ($\overline{GH}$), is 123 m (Cruden and Varnes, 1996). The surface involved in the landslide activation was mainly covered by a low irregular herbaceous cover, with the compresence of small rocks of a few centimeters in the upper part of the basin.

Figure 4.4. *Details of landslide's features manually measured during the post-event field survey conducted in 2020. The 3D mesh was obtained through the UAV-derived point cloud data elaboration.*

4.4.1.2 ALS-derived DEM elaboration

ALS surveys conducted in 2018 allowed to elaborating pre-event DEM at the catchment scale. Table 4.1 specifies the characteristics of ALS flights. Original raw ASL data (Fig. 4.3Ai) were firstly filtered into ground (soil) and overground (vegetation and infrastructures) points (Fig. 4.3Aii) by applying specific classification tools and algorithms using the R studio *lidR* package (Roussel *et al*., 2020). Then, to perform an accurate removal of potential residuals coming from errors affecting the automatic classification procedure, the classified point cloud was manually filtered (Fig. 4.3Aiii) through specific tools of the Cloud Compare software (https://www.danielgm.net/). In particular, the point cloud was divided into slices of equal dimensions, to efficiently remove the remaining small overground noises. The DEM resolution of 1 m was hence obtained from the processed point cloud through the *grid_terrain* R studio package and the respective application of the classification-based *knnidw* algorithm for spatial data interpolation (Roussel *et al*., 2020).

Table 4.1. *Overview of ALS surveys parameters and characteristics*

ALS-survey parameters	**Information / Value**
Period of the survey	April-December 2018
Survey conditions	Snow-free conditions, minimal leaves presence
LiDAR system	Optech ALTM Gemini
Number of flights	46
Average flight altitude (a.g.l.)	850 m
Flying speed	75 knots
Scan angle	32°
Laser frequency	100 kHz
Average point density	5 pt/m^2

4.4.1.3 Snowmelt runoff model (SRM)

Table 4.2 shows input variables of SRM, whose description is detailed presented in the supplementary documentation. SRM model is divided into meteorological (Fig. 4.3Bi) and spatial data (Fig. 4.3Bii). Pre-event DEM was considered for daily snowmelt rate estimation for the 2018 snowmelt season (Fig. 4.3Biii). Following the suggestions provided by Martinec *et al*. (2008), the basin considered for snowmelt estimation was not divided into elevation zones, given the fact that the elevation range between the outlet and the highest point of the watershed resulted lower than 500 m, indicated by model's developers as the threshold for basin subdivision. Therefore, the calculation of the hypsometric curve was not required. Moreover, since the basin was not divided into zones, no altitude adjustment in the function of zonal hypsometric mean elevation values was necessary (Martinec *et al*., 2008).

Table 4.2. *Overview of Snowmelt Runoff Model (SRM) inputs*

Input	**Unit of measurement**
Temperature (T)	°C
Precipitation (P)	mm/h
Snow Covered Area (SCA)	%
Temperature Lapse Rate (γ)	$°C \cdot m^{-1}$
Critical Temperature (T_{CRIT})	°C
Degree-day factor (An)	$cm \cdot °C^{-1} d^{-1}$
Rainfall Contributing Area (RCA)	(-)
Recession coefficient (k)	(-)
Runoff coefficient snow (Cs)	(-)
Runoff coefficient rain (Cr)	(-)
Time lag (L)	(h)

The daily maximum temperature (T_{MAX}), minimum temperature (T_{MIN}) and precipitation (P) values recorded by the weather station were considered for 2018. Snow cover was estimated starting from satellites observations and the daily percentage of the Snow-Covered Area (SCA) concerning the total extension of the basin was hence obtained. In particular, SCA was mapped from Landsat 8 (L8) data

by applying the *Normalized Index of Differences in Snow cover* (NDSI; Kour and Patel, 2013, Kurakina *et al*., 2020) for the considered year. NDSI was hence calculated by Equation (4.1):

$$NDSI = \frac{Green - SWIR}{Green + SWIR} \tag{4.1}$$

where *Green* stands for the L8-band 3 and *SWIR* stands for the L8 short-wave infrared band 6. A threshold value of NDSI > 0.4 was used to automatically map the snow presence inside the basin (Dietz *et al*., 2012, Donmez *et al*., 2021). Daily snow cover was extrapolated from the acquired Landsat 8 satellite data by using the interpolation method expressed by Equation (4.2) (Kour and Patel, 2013):

$$S_n = S_1 + \frac{S_2 - S_1}{t_2 - t_1} \cdot (t_m - t_1) \tag{4.2}$$

where S_n is the snow cover on nth day, S_1 is the snow cover derived from the first image, S_2 is snow cover derived from the second image, t_n is the number of nth days, t_1 is the Julian date of the first image and t_2 is the Julian date of the second image. Temperature lapse rate (γ) was obtained by looking at the availability of weather stations at different altitudes (i.e. Pordoi weather station, located at 2154 m a.s.l. and 0.57 km far away from the watershed, and Arabba station, placed at 1642 m a.s.l and 5 km far away from the study area). The temperature lapse rate was therefore calculated by dividing the difference between daily average temperatures measured at each weather station with their altitude range (Martinec *et al*., 2008). Following the suggestions provided by model developers, the critical temperature (T_{CRIT}) was set equal to 3 °C from May to Jun, 0.75 °C in July and 0 °C from August to March (Martinec *et al*., 2008). These values resulted to be specifically suitable for mountain basins, as also reported by uncertainty detection of SRM input proposed by Xiang *et al*. (2009). The degree-day factor (An) was obtained from the empirical relation expressed by Equation (4.3) (Matinec, 1960):

$$An = 1.1 \cdot \frac{\rho_S}{\rho_w} \tag{4.3}$$

where ρ_s is the density of the snow and ρ_w is the density of the water. In particular, ρ_s was determined following Equation (4.4) (Pistocchi, 2016):

$$\rho_S = 0.2 + 0.001 \cdot DOY \tag{4.4}$$

where DOY represents the day number from the beginning of the snow season. Looking at the collected snowfall data and at the suggestions provided by model designers, the Rainfall Contributing Area (RCA) was set equal to 1 from April to October and equal to 0 from November to March

(Martinec *et al*., 2008). The recession coefficient (k) is expressed by Equation (4.5):

$$k_{n+1} = \frac{Q_{n+1}}{Q_n} = x \cdot Q_n^{-y} \tag{4.5}$$

where Q_n and Q_{n+1} are daily measured discharge values, x and y are parameters determined through linear regression analysis starting from measured discharge values. Since the absence of available historical discharge data at the basin's outlet, x and y coefficients were set equal to 0.85 and 0.086 respectively, therefore following the indications provided by Martinec *et al*. (2008). In agreement with the input setting proposed by similar applications of the model (Tahir *et al*., 2011, Panday *et al*., 2014), the runoff coefficient for snow (C_s) was set equal to 0.2 from Jun to August and equal to 0.15 from September to May, while the runoff coefficient for rain (C_r) was 0.15 from July and August and equal to 0.10 from September to June. The time lag (L) was set equal to 1 h. Since the absence of historical snowmelt hydrographs for the *SRM-watershed*, the L parameter was set looking at its size and accordingly with model application in similar basins, in agreement with the suggestions provided by Martinec *et al*. (2008).

4.4.1.4 Road Erosion Steady-State model (RESS)

Table 4.3 reports the inputs obtained for RESS simulations. We refer the reader's attention to the supplementary documentation for details regarding the model.

Table 4.3. *Overview of Road Erosion Steady-State (RESS) inputs necessary for soil stability investigations.*

Input	Value	Unit of measurement
DEM without road	/	(-)
Road points	/	(-)
Drainage systems location	/	(-)
Soil depth (z)	0.5	m
Internal friction angle (ϕ)	35.0	Decimal degrees
Soil density (ρ_s)	1800	$kg \cdot m^{-3}$
Soil transmissivity (Tr)	$0.3 \cdot 10^{-3}$	$m^2 \cdot s^{-1}$
Soil cohesion (Coh_s)	0.1	$kg \cdot m^{-1} \cdot s^{-2}$
Root cohesion (Coh_r)	0.0	$kg \cdot m^{-1} \cdot s^{-2}$
Vegetation surcharge (W)	0.0	$kg \cdot m^{-1} \cdot s^{-2}$
Road width	4.0	m
Relative road cut depth (r_{rc})	0.5	(-)
Max rainfall runoff (Rr_{max})	62.8 (May 2018)	$mm \cdot h^{-1}$
Max snowmelt runoff (Sr_{max})	11.3 (May 2018)	$mm \cdot h^{-1}$
Rainfall intensity increment step	1.0	$mm \cdot h^{-1}$
Water density (ρ_w)	1000	$kg \cdot m^{-3}$
Flow direction algorithm	D-inf	(-)

The model needs DEM without the presence of the road (Fig. 4.3Civ). Since the available ALS-derived pre-event elevation model was acquired after the road construction, a novel smoothing procedure was developed to remove it. Therefore, a scenario with the presence of the road (*YesRoad* scenario) and a second one with its simulated absence (*NoRoad* scenario) were respectively considered for RESS simulations. DEM was firstly clipped on the RESS-watershed boundaries and the road was masked creating a vector polygon following its edges. Successively, Euclidean buffers were created outside the top and the bottom side of the road polygon. Point features were therefore located at a fixed distance of 10 m along with them, through the *Generate Points Along Lines* ArcGIS tool and elevation values from the DEM were then extracted for each point. The "Topo to Raster"

interpolation was applied for the buffer zones through the *Topo to Raster* ArcGIS tool and then clipped on the original road mask previously designed. In this way, the interpolated surface was merged on the original elevation model through the ArcGIS *Mosaic to New raster* tool, setting the elevation values of the interpolated-road mask as output cell values of the overlapping areas. This specific interpolation method was adopted aiming to create a modified but hydrologically correct DEM (Esri, 2021), simulating the absence of the road and avoiding evident alteration of grassy zones included in the process. A comparison between DEMs), with and without the road is presented in Fig. 4.11.

Every drainage system needed to be provided with x and y coordinates, as well as with a value (*p*) ranging from 0 to 100 %, representing the portion of water flows diverted by it and routed out of the road. Looking at the location and the types of drainage systems along the road, a constant value of 60 % was set as *p*. This value turned out to be the more suitable given the water deviation induced by drainage systems toward the hillslope under the road. Road width was measured equal to 4 m and the relative road cut depth, describing the potential interception of each road cell at the foot of the upstream slope, was set equal to the default value of 0.5 m. According to on-field measurements previously conducted in the same area (Borga *et al*., 2002b, Borga *et al*., 2005, Tarolli *et al*., 2008, Tarolli *et al*., 2011), geotechnical parameters were set looking at the respective average values detected across the catchment. Therefore, soil depth () was set equal to 0.5 m, the internal friction angle (ϕ) to 35°, the saturated soil density (ρ_s) to 1800 kgm^{-3}, soil transmissivity (Tr) to $0.3 \cdot 10^{-3}$ m^2s^{-1} and soil cohesion (Coh_s) to 0.1 $kg \cdot m^{-1}s^{-2}$ Additionally, water density (ρ_w) was 1000 kgm^{-3}, while root cohesion (Coh_r) and vegetation surcharge (W) were set equal to 0, because of the mere presence of low herbaceous cover among the watershed (Kokutse *et al*., 2016; Fig. 4.3Ciii). Sr and Rr peaks obtained with SRM for the 2018 melting period were set as input in the RESS model (Fig. 4.3Ci, ii), with a corresponding increment step equal to the default value of 1 mmh^{-1}. In this regard, the use of single *Sr* and *Rr* peaks calculated at the outlet of the *SRM-watershed* for the spatially predictive detection of slope instabilities relies on the assumption that is possible to create large-scale, predictive mapping of terrain failures starting from snowmelt values obtained at a specific point of interest placed inside the basin. Finally, the D-infinite flow direction algorithm (Tarboton, 1997) was selected to let the model route subsurface multipath flows.

4.4.1.5 Simulated water Erosion (SIMWE)

The use of pre-event DEM for SIMWE application allowed the predictive analysis of the dynamics of road-diverted *Sr* overflows toward the below hillslope. In particular, *Sr* discharge and flow depth intercepting the landslide area were estimated for both the *YesRoad* and the *NoRoad* scenarios (Fig. 4.3D). SIMWE inputs are summarized in Table 4.4, while accurate model description is presented in the supplementary documentation. Maximum *Sr* obtained for the 2018 melt season was considered as input for SIMWE modeling (Fig. 4.3Cii). As similarly highlighted in the previous section, such a set of a single SRM-derived *Sr* peak value for the spatial modeling of road-diverted *Sr* dynamics at basin scale assumes the possibility to innovatively apply such a model by overtaking the use of spatially distributed water input as commonly propose in the available literature (see section 4.6.1).

Table 4.4. *Overview of SIMulated Water Erosion (SIMWE) inputs. G stands for grassland, Rd stands for road and Rk stands for rocky areas located on the top of the watershed.*

Input	Value	Unit of measurement
Max snowmelt runoff (Sr_{max})	11.3 (May 2018)	mmh^{-1}
Saturated soil conductibility (k)	10^{-3} (G) 0.0 (Rd, Rk)	ms^{-1}
Excess rate (May 2018)	0.0 (G) 11.3 (Rd, Rk)	mmh^{-1}
Manning (n)	0.045 (G) 0.016 (Rd) 0.099 (Rk)	(-)

Moreover, the excess rate was calculated by subtracting the infiltration rate (mmh^{-1}) from the snowmelt intensity peaks (mmh^{-1}). Infiltration rates were set in function of the measurements of the hydraulic conductivity for each land type, in line with previously conducted field measurements (Tarolli *et al*., 2011, Borga *et al*., 2002b). Looking at tabular values for specific soil categories (Bunya *et al*., 2010, Hofierka *et al*., 2018, Pijl *et al*., 2020), Manning's *n* values were set equal to 0.045 for grassland, 0.016 for the paved road and 0.099 for rocky areas located at the top of the watershed (Fig. 4.3Ciii).

4.4.2 Statistical validation of instability susceptibility mapping

RESS-derived instability susceptibility maps were validated through the *Receiver Operating Characteristic* (ROC) analysis (Fig. 4.3Ei). The magnitude of the agreement between predicted and observed instabilities was hence calculated by the Cohen's kappa-index (Fig. 4.3Eii; Lee *et al*., 2007, Pourghasemi *et al*., 2012, Vakhshoori and Zare, 2018). Such statistical analysis was performed focusing on the grassy hillslope located downstream of the road, aiming to support our outcomes regarding its interaction with *Sr* dynamics in terms of landslide occurrence. The predictive capabilities of RESS model to foresee the activation of terrain failures were validated by looking at the key participation of the road in altering *Sr* and *Rr* overflow paths, thus potentially encouraging the occurrence of hydro-erosive phenomena. The null hypothesis was defined, in this case corresponding to the condition that the slope is not involved in soil instabilities. It is therefore necessary to define whether it was correctly discarded in favor of the alternative one (i.e. the presence of instabilities within the hillslope). Detected instabilities and stable zones were mapped and rasterized starting from UAV-derived 1 cm orthomosaic and post-event field observations. Two classes (i.e. stable and unstable) were selected defining a classification threshold, applied by distinguishing stable and unstable zones as similarly done in Borga *et al*. (2005). Each raster cell of observations and modeled predictions were therefore assigned to one of the two selected classes. Classes overlay defined four types of pixels, i.e. (i) true positives (*TP*) where observed unstable zones are predicted as unstable, (ii) true negatives (*TN*) where observed stable cells are predicted as stable, (iii) false positives (*FP*) where observed stable cells are predicted as unstable and (iv) false negatives (*FN*) where observed unstable cells are predicted as stable (Palacio Cordoba *et al*., 2020, Vakhshoori and Zare, 2018). *True Positive Rate* (TPR) and *False Positive Rates* (FPR) were calculated following Equation (4.6), (4.7):

$$TPR = \frac{TP}{TP+FN} \tag{4.6}$$

$$FPR = \frac{FP}{TN+FP} \tag{4.7}$$

The values of the *Area Under the ROC Curve* (AUC) finally express the model's ability to correctly classify those zones more or less susceptible to the occurrence of instabilities. ArcGIS-based *Spatial Data Modeller* (*ArcSDM*) geoprocessing tool was used for ROC analysis and AUC calculation. AUC values range between 0 (failed prediction) and 1 (perfect prediction) (Fawcett, 2006).

The predictive reliability of RESS model was also tested by mapping the terrain instabilities observed

downstream of the road on the RESS-derived map of critical *Sr* and *Rr*, and therefore by comparing the proportion of the respective catchment area placed in each critical *Sr* and Rr interval to the corresponding fraction of the detected unstable zones. The assessment of RESS results translates in a larger divergence between observed degraded surfaces and the respective regions of the catchment corresponding to low values of critical *Sr* and Rr (Borga *et al*., 2002a, Borga *et al*., 2002b, Borga *et al*., 2005). Plausible inaccuracies arising from the post-event identification of degraded regions were considered in this statistical procedure by associating the observed unstable zones to the low critical *Sr* values computed in a 3x3 grid-cell moving window (Borga *et al*., 2002a, Borga *et al*., 2002b). This specifically allowed to consider the eventual detection of terrain instabilities occurred on zones defined by the model as relatively stable, but initiated by the failure of a nearby grid characterized by low critical *Sr* values (Borga *et al*., 2005).

Cohen's *kappa-index* (Cohen, 1960) was calculated by Equation (4.8) (Guzzetti *et al*., 2006):

$$k = \frac{P_C - P_E}{1 - P_C} \tag{4.8}$$

where P_C stands for the proportion of cells correctly classified as unstable or stable and P_E stands for the proportion of cells for which the agreement between observations and predictions is expected by chance. In particular, P_C and P_E are expressed by the following Equation (4.9), (4.10) respectively:

$$P_C = \frac{TP + TN}{N} \tag{4.9}$$

$$P_E = \frac{(TP + FN) \cdot (TP + FP) + (FP + TN) \cdot (FN + TN)}{N^2} \tag{4.10}$$

where N is the total number of pixels in the investigated zone. Cohen's k ranges between a minimum of −1 (total disagreement between observed and predicted instabilities) and a maximum of +1 (perfect agreement between observed and predicted instabilities) (Guzzetti *et al*., 2006).

4.5 Results

4.5.1 Snowmelt runoff computation

Simulations revealed that the melt period in 2018 was limited to May (Fig. 4.5c). Daily snowmelt values (mm/h) resulted between a minimum of 1.09 mm/h and a maximum of 11.36 mm/h (Fig. 4.5b) and rain contributing to runoff (*Rr*) resulted between a minimum of 2.08 mm/h and a maximum of 62.8 mm/h (Fig. 4.5c). In this regard, the extraction of *Sr* and *Rr* peaks for the application of RESS and SIMWE models was computed looking at those periods for 2018.

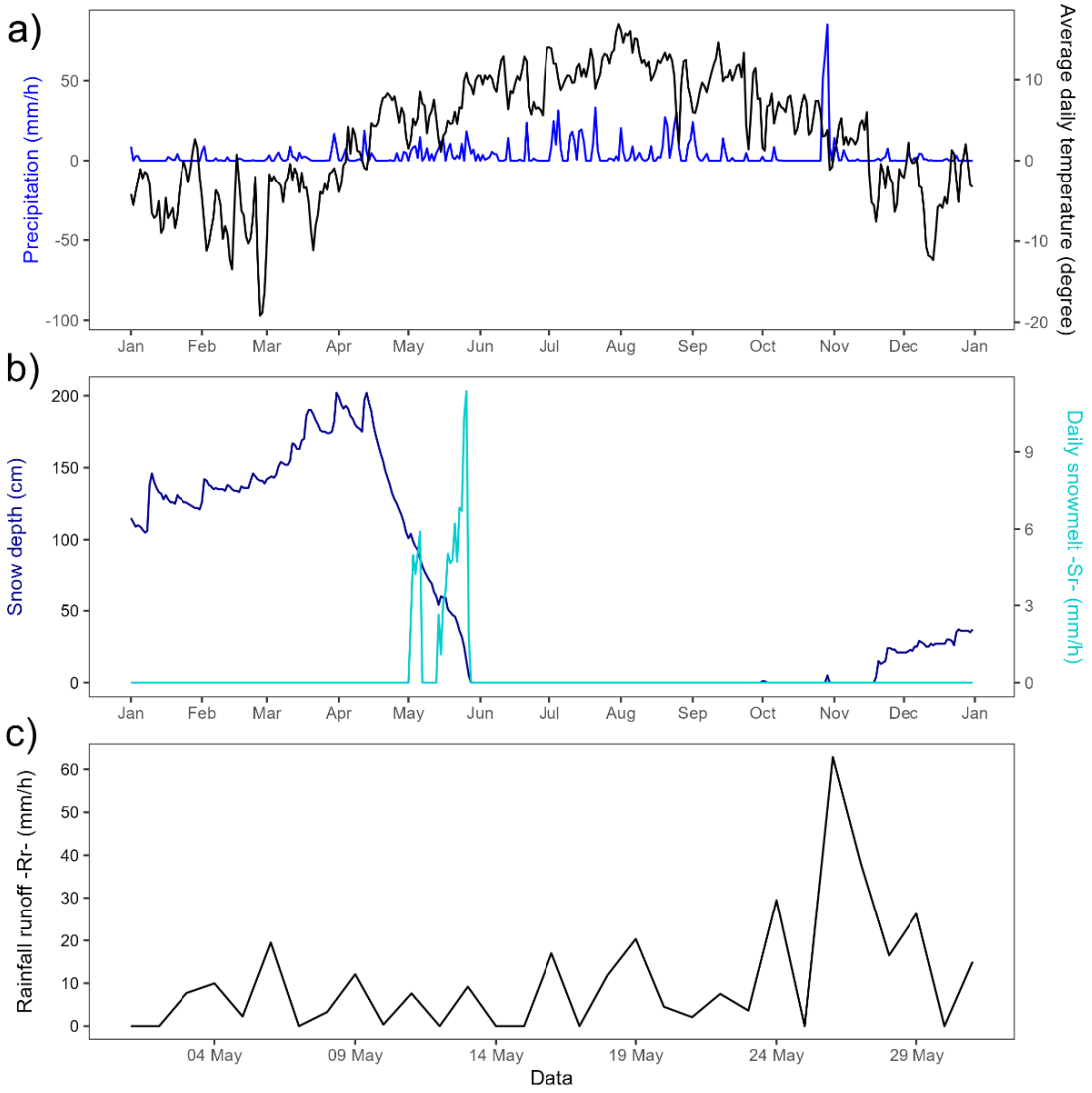

Figure 4.5. *Overview of precipitation and average temperatures recorded by the Pordoi weather station during 2018 (a). The figure also shows the trend of both snow depth and Snowmelt Runoff Model (SRM)-derived daily snowmelt runoff values (Sr) for the 2018 melting season (b), as well as the rain contributing to runoff (Rr) during it (c).*

4.5.2 Slope stability analysis

Fig. 4.6 and Fig. 4.7 represent the comparison of critical *Sr* and *Rr* for the *YesRoad* and *NoRoad* scenarios (Fig. 4.3Cvii-x) starting from pre-event SRM outcomes. The calculation of critical *Sr* showed an increase in its values inside the landslide area for the *NoRoad* scenario (Fig. 4.6b) compared with the *YesRoad* one (Fig. 4.6a). Moreover, road contribution in critical *Sr* deviation toward the landslide surface is expressed by the calculation of the difference between *NoRoad* and *YesRoad*-critical Sr (Fig. 4.6c). The presence of reddish pixels within the landslide surface represents those zones where this difference is greater. This suggests that road presence induces an increase of the minimum *Sr* able to potentially compromise the stability of the hillslope below. Similar results are appreciable by comparing the spatial variability of critical *Rr* computed for the two scenarios (Fig. 4.7a,b respectively). The difference between *NoRoad* and *YesRoad*-critical *Rr* (Fig. 4.7c) supports such statements. In this connection, RESS results for the *YesRoad* condition highlight the distribution of lower critical *Rr* values inside the landslide-prone surface, compared to the *YesRoad* situation. Therefore, the involvement of *Sr* overflows in landslide activation results to be comparable with terrain instabilities encouraged by *Rr*. This further underlines the active contribution of snowmelt in landslide occurrence, also suggesting the key role of the road in its critical deviation toward the unstable hillslope below.

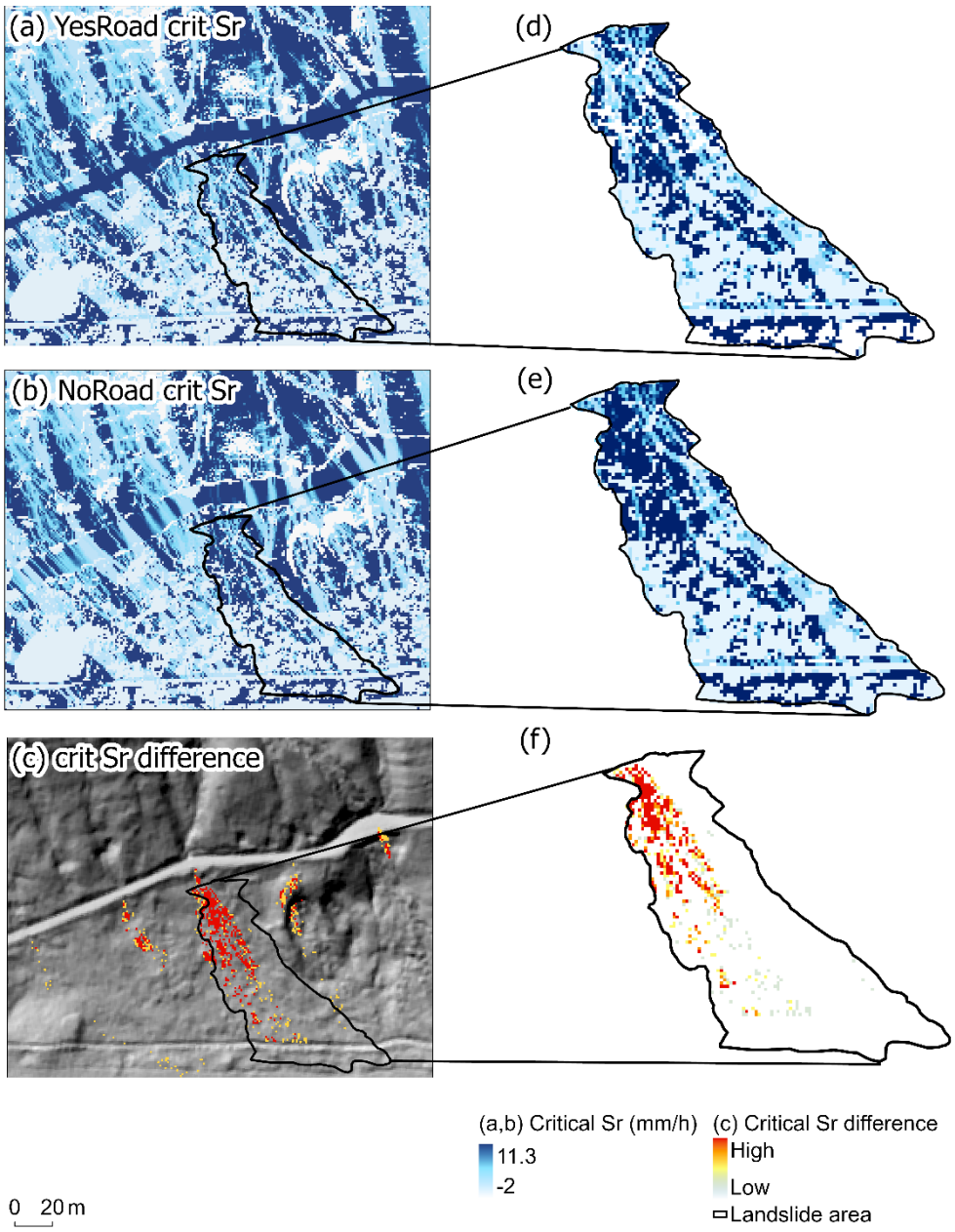

Figure 4.6. *Comparison of critical snowmelt runoff (Sr) calculated for the YesRoad (a) and NoRoad (b) scenarios. The figure also shows the calculated difference between NoRoad and YesRoad critical Sr (c). Fig. 4.6d-f represents a focus of critical Sr computed for the two scenarios and of critical Sr difference inside the landslide zone (black polygon). Reddish pixels stand for higher differences between NoRoad and YesRoad critical Sr, while bluish pixels stand for lower differences. No difference zones are represented in transparent coloring. In critical Sr computation, unconditionally unstable cells have values equal to −2. DEM-derived shaded relief is represented in the background.*

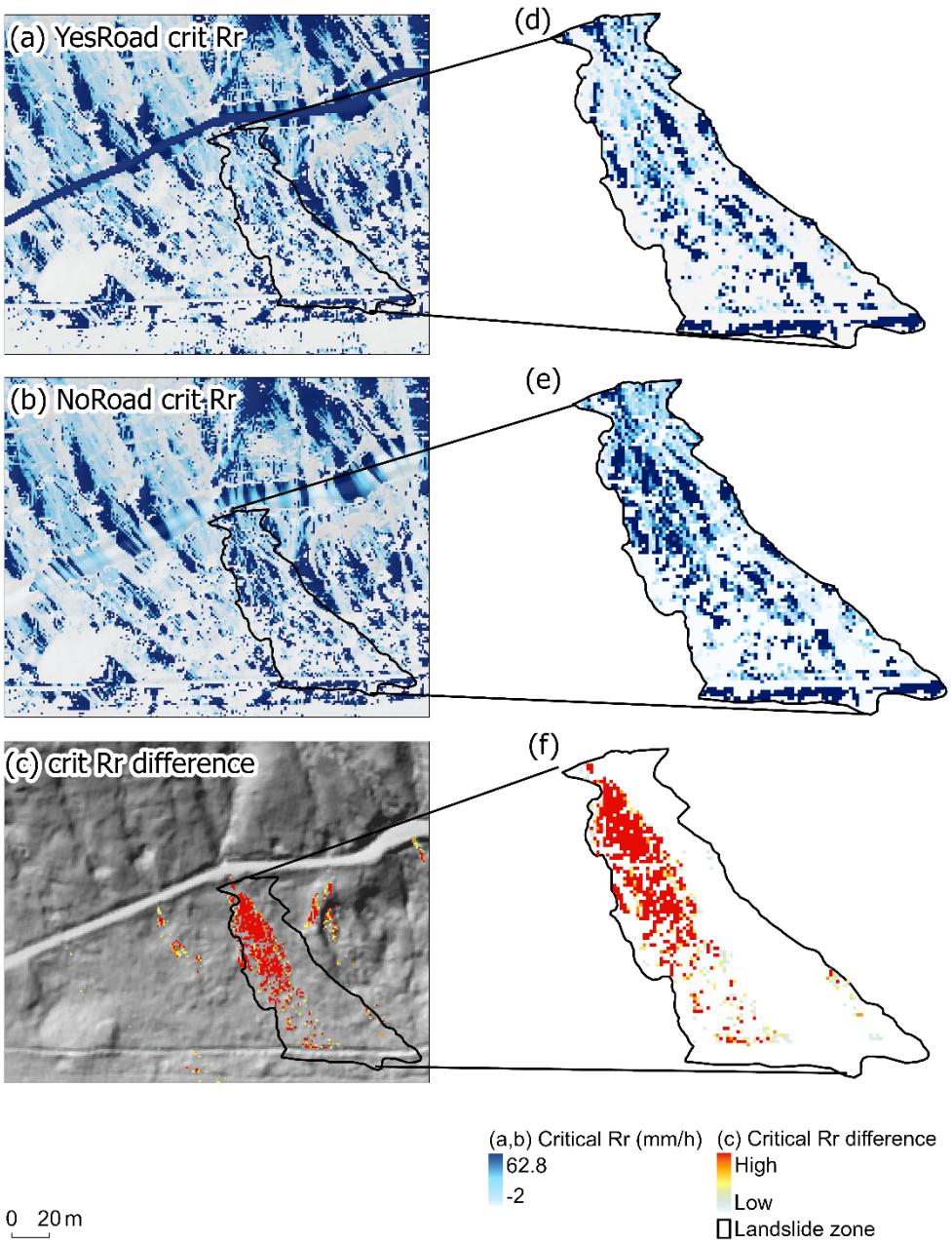

Figure 4.7. *Comparison of critical rainfall runoff (Rr) calculated for the YesRoad (a) and NoRoad (b) scenarios. The figure also shows the calculated difference between NoRoad and YesRoad critical Rr (c). Fig. 4.7d-f represents a focus of critical Rr computed for the two scenarios and of critical Rr difference inside the landslide zone (black polygon). Reddish pixels stand for higher differences between NoRoad and YesRoad critical Rr, while bluish pixels stand for lower differences. No difference zones are represented in transparent coloring. In critical Rr computation, unconditionally unstable cells have values equal to −2. DEM-derived shaded relief is represented in the background.*

Fig. 4.8 shows the comparison of the RI index (Fig. 4.3Cv, vi) calculated from the pre-event critical *Sr* (Fig. 4.8a) and critical *Rr* (Fig. 4.8b). Reddish colors of RI indicate unstable areas, while blue colors represent stable ones. Besides the identification of local unconditionally unstable regions within the hillslope above the road, the RESS model particularly revealed the potential activation of land degradation dynamics in correspondence with the observed shallow landslide surface starting from pre-event snowmelt computation (Fig. 4.8a). Similarly, the calculation of RI starting from critical *Rr* mapping predicted the occurrence of terrain instabilities inside the landslide area (Fig. 4.8b). This firstly reveals as snowmelt overflows can actively contribute to triggering local land degradation processes and terrain instabilities.

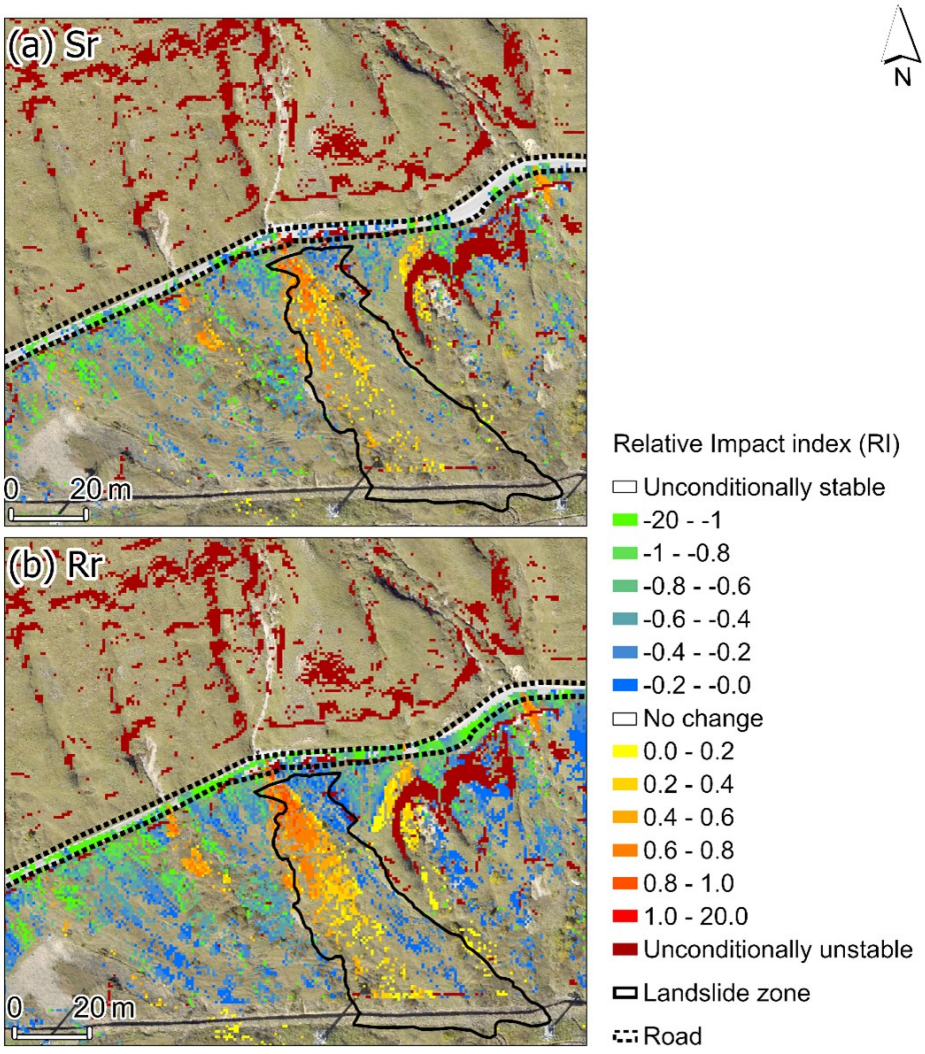

Figure 4.8. *Pre-event RI index calculated from Snowmelt Runoff Model-derived critical snowmelt runoff (Sr) (a) and critical rainfall runoff (Rr) (b) for 2018. No change and unconditionally stable areas (i.e., grassland and road network) are represented with a transparent coloring to better appreciate the location of instabilities regions inside the landslide area. ALS-derived aerial orthophoto is reported in the background.*

4.5.3 SIMWE simulations

Fig. 4.9 shows the comparison between *Sr* dynamics at the landslide zone for the *YesRoad* and *NoRoad* scenarios in terms of water discharge and flow depth (Fig. 4.3Di-iv), starting from pre-event DEM. SIMWE mapping of snowmelt directions revealed as *Sr* flows downstream along the grassy bank in the direction of the road. Then, water coming from the melting snowpack intercepts the roadway and moves along with it. Such road-diverted snowmelt water successively falls to the unstable slope below crossing the surface involved in landslide activation (Fig. 4.9a, c; Fig. 2d-f). The drainage systems located along the roadway seem to inefficiently catch *Sr*, which is diverted in such a way as to contribute to slope destabilization. Results also illustrate that a fraction of *Sr*, coming from the grassy hillslope upstream of the landslide, converges in the direction of the manhole located at its trigger point (yellow point in Fig. 4.9). In particular, its water-regulating capacity was revealed to be critically stressed by *Sr* coming from the upper part of the basin. This encourages its progressive overload, which translates into *Sr* deviation across the road and toward the landslide surface. In this connection, the maximum *Sr* discharge and water depth at this specific point resulted equal to 1.06 m^3s^{-1} and 0.33 m respectively.

Sr flow directions elaborated for the *NoRoad* scenario in terms of water discharge and flow depth are shown in Fig. 4.9b, d. These simulations highlighted that in the supposed absence of the road, *Sr* coming from the upstream zones of the watershed would flow along the slope without evident deviations unlike what is observed in the *YesRoad* one. On the contrary, the *NoRoad* scenario highlighted the critical deviation of *Sr* outflows due to the ineffective water management of the manhole, similarly to what was observed in the *YesRoad* simulations.

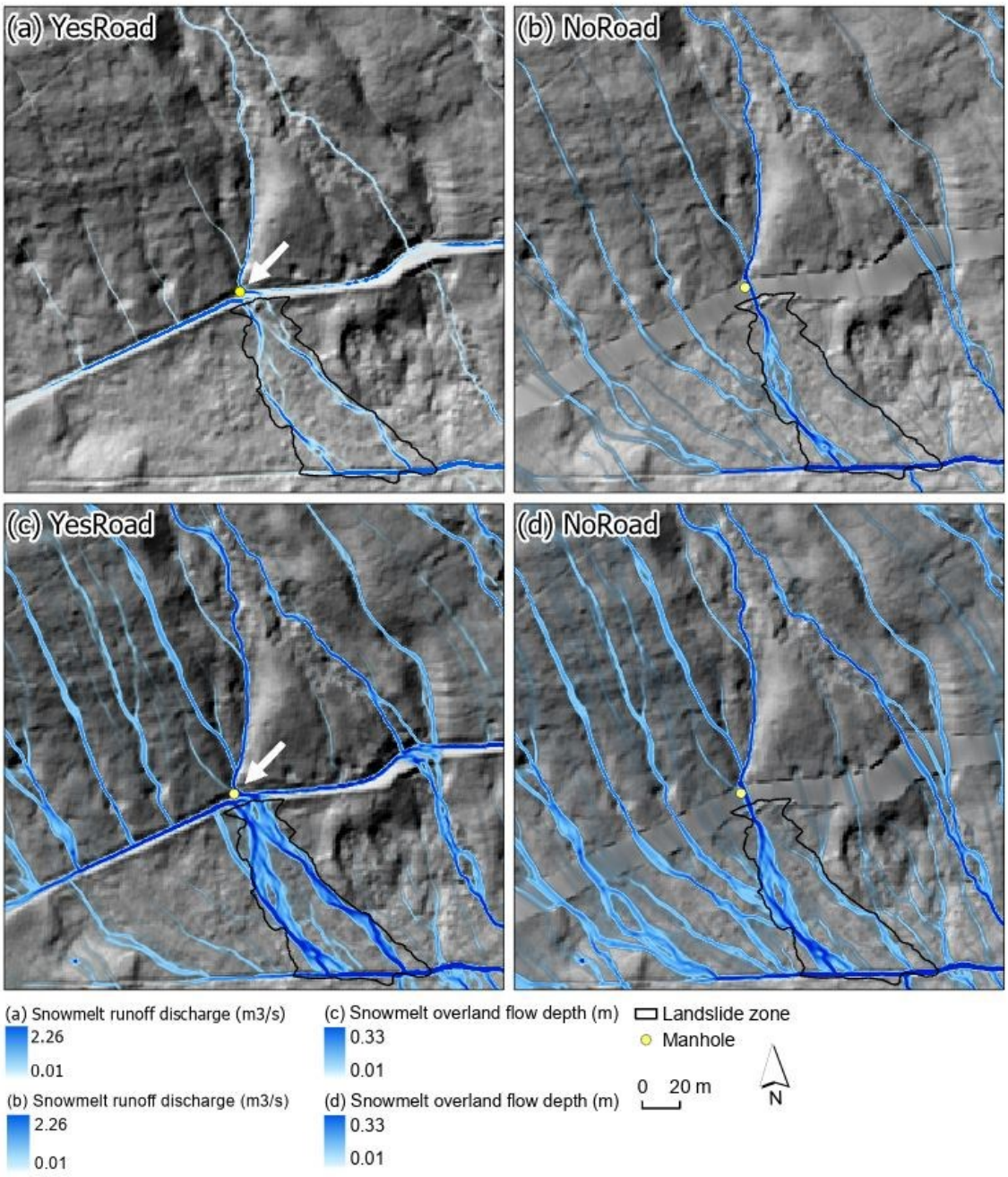

Figure 4.9. *SIMWE outcomes. The figure shows snowmelt runoff (Sr) discharge computed for the YesRoad (a) and NoRoad (b) scenarios, and Sr flow depth for the YesRoad (c) and NoRoad (d) scenarios obtained using the pre-event DEM. For the YesRoad scenario, the white arrow indicates the point of critical convergence of Sr coming respectively from the road and the upper hillslope, in the direction of the manhole (yellow point) located on the top of the landslide's triggering area. (For interpretation of the references to colour in this figure legend, the reader is referred to the web version of this article.)*

4.5.4 Statistical analysis

4.5.4.1 Snowmelt discharge and flow depth cross-section

The influence of road network on runoff overflows deviation was further investigated through the computation of a topographic cross-section of snowmelt runoff discharge and flow depth values for the landslide area. A transect line was therefore designed crosswise the landslide surface. Control Points (CPs) were placed along with it at an equal distance of 10 cm, for a total of 30 CPs (Fig. 4.12). For each CP, SIMWE-derived discharge and depth values of *Sr* were respectively extracted. Fig. 4.10 shows cross-sections results regarding *Sr* discharge (Fig. 4.10a) and water depth (Fig. 4.10b) for the *YesRoad* and *NoRoad* scenarios. Looking at the presence of the road, *Sr* discharge and depth along the transect resulted higher than those extracted simulating its absence. *Sr* discharge and flow depth peaks of the *NoRoad* cross-sections shown in Fig. 4.10 represent the fraction of snowmelt runoff coming from the upper hillslope and critically converging at the landslide aside from road presence.

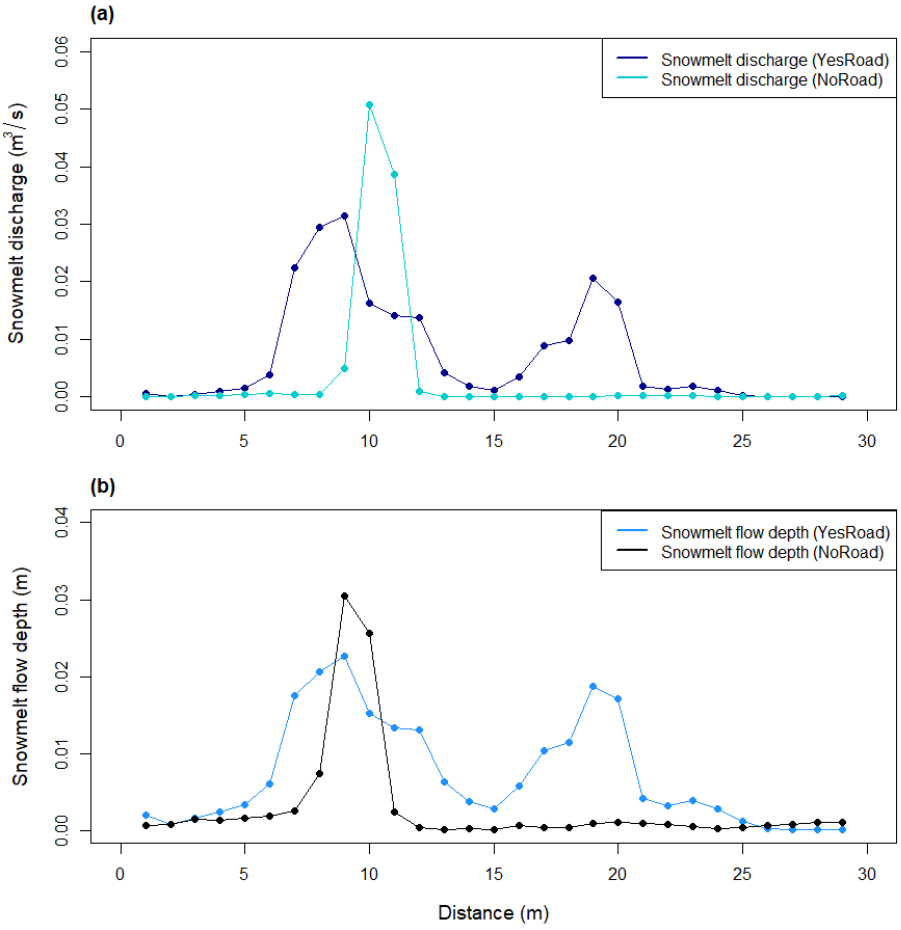

Figure 4.10. *Cross-section line plots of snowmelt runoff (Sr) discharge and Sr flow depth extracted at each Control Point for the YesRoad and NoRoad scenarios.*

4.5.4.2 Statistical validation of predicted instabilities

Post-event field inspections allowed for detecting and localizing the failures that occurred in the study area, in order to check the accuracy of predictive soil stability simulations by comparing such observations with model outcomes. Looking at the aims of the presented research, post-event field surveys were focused on both the shallow landslide and local instabilities triggered on the hillslope located downstream of the road. Therefore, the validation of the RESS-derived prediction of soil instabilities was firstly computed by the calculation of the *Area Under the ROC Curve* (AUC) for the section of the *RESS-watershed* under the roadway. AUC was calculated starting from the creation of the confusion matrix reported in Table 4.5. In this regard, the low percentage of FN and FP pixels highlighted the good potentiality of the RESS model in predicting soil instabilities, in particular due to *Sr* overflows. AUC values resulted equal to 0.94 and 0.92, respectively for the forecast of *Sr* and *Rr*-induced soil instabilities. Finally, RESS performance in the prediction of soil failures was expressed by the Cohen's *k*-index, resulting equal to 0.58 and 0.55 respectively referring to *Sr* and *Rr*-derived RESS simulations.

Table 4.5. *Confusion matrix for ROC analysis computation. The table shows the number of pixels for true positives (TP), true negatives (TN), false positives (FP) and false negatives (FN), and the respective percentage compared with the total number of pixels defining the section of the watershed below the road, considered for investigating predictive RESS performance. Stable and NoChange zones cover the remaining 64.08% and 77.07% of the considered RESS-watershed's section under the road, looking at RESS-derived Rr and Sr simulations respectively.*

RESS sim	**TP**		**TN**		**FP**		**FN**	
	Pixe	**Percentag**	**Pixe**	**Percentag**	**Pixe**	**Percentag**	**Pixe**	**Percentag**
Rr	975	17.38%	9167	12.14%	845	1.12%	296	5.28%
Sr	634	11.30%	5596	7.41%	559	0.74%	195	3.48%

The comparison of the observed unstable zones placed downstream of the road to the fraction of the respective catchment area for each critical pre-event *Sr* and *Rr* interval is reported in the following Table 4.6 and Table 4.7. The assessment of RESS model reliability was hence reflected by a larger difference between the proportion of instabilities that occurred within the lower critical *Sr* and *Rr* ranges (critical $Sr < 5$ mm/h, critical $Rr < 15$ mm/h) or in those zones considered as unconditionally unstable, and the percentage of the corresponding catchment area. The proportion of instabilities that occurred within the lowest critical *Sr* and *Rr* ranges resulted respectively around 53 % (Table 4.6) and 45 % (Table 4.7), while the percentage of the corresponding catchment area

respectively decreased to around 20 % (Table 4.6) and 25 % (Table 4.7). This suggests as the occurrence of instabilities mostly recurs in the sections of the watershed characterized by low-critical *Sr* values, therefore predicted to be unstable.

Table 4.6. *Percentage of observed instabilities area and respective catchment area for each range of critical snowmelt runoff (Sr).*

Crit S*r* (mm/h)	**Instabilities area (%)**	**Total crit Sr < 5 mm/h (%)**	**Catchment area (%)**	**Total crit Rr < 5 mm/h (%)**
Unconditionally unstable	29.8%	53.1%	8.9%	20.5%
0-2	15.9%		7.3%	
2-5	7.4%		4.3%	
5-10	6.5%		5.0%	
> 10	19.7%		26.3%	
Unconditionally stable	20.8%		48.1%	

Table 4.7. *Percentage of observed instabilities area and respective catchment area for each range of critical rainfall runoff (Rr).*

Crit *Rr* (mm/h)	**Instabilities area (%)**	**Total crit Rr < 15 mm/h (%)**	**Catchment area (%)**	**Total crit Rr < 15 mm/h (%)**
Unconditionally unstable	29.7%	45.4%	8.9%	24.7%
0-5	19.2%		9.0%	
5-15	9.4%		6.8%	
15-45	9.1%		11.3%	
> 45	11.7%		15.9%	
Unconditionally stable	20.9%		48.2%	

4.6 Discussion

This work investigates the interaction between road and snowmelt runoff in the activation of hillslope instabilities. For this purpose, a challenging predictive, multi-modeling approach was implemented through the adoption of three different models. This allowed to quantify snowmelt-runoff at the watershed scale and obtain a mapping of local terrain instabilities related to road-induced surface water deviation. Several studies have been carried out regarding the single application of SRM, RESS and SIMWE, respectively focusing on snowmelt calculation (Ferguson, 1999, Eigdir, 2003, Tahir *et al*., 2011, Butt and Bilal, 2011, Devi, 2017, Siemens *et al*., 2021), landslide susceptibility mapping (Borga *et al*., 2005, Tarolli *et al*., 2011, Cordoba *et al*., 2020, Al-Umar *et al*., 2020) and water overland flows (Arnone *et al*., 2011, Bogaard and Greco, 2016, Zhao *et al*., 2019, Yang *et al*., 2019, Mauri *et al*., 2022). However, in this context, the proposed multi-modeling approach is novel. This research additionally supports SRM testing for small mountain watersheds, in line with the analysis provided by Rango and Martinec, 1979, Brubaker *et al*., 1996, DeBeer and Pomeroy, 2010, and Gomez-Landesa and Rango (2002). Despite the availability of many researches about the role of roads and trails in the occurrence of land degradation dynamics such as landslides (Fu *et al*., 2010, Sidle and Ziegler, 2012, Penna *et al*., 2014) and erosion processes (Elliot *et al*., 1999, Salesa *et al*., 2019, Yu *et al*., 2021), our work stands out from the scientific literature in that it proposes an innovative methodology able to forecast the activation of local instabilities at meters detail by analyzing the interaction between road, snowmelt runoff and shallow landslides at the watershed scale. Differently from the accessible scientific investigations about soil stability (Dietrich *et al*., 1992, Montgomery and Dietrich, 1994, Borga *et al*., 2002a, Borga *et al*., 2005) and water runoff dynamics in mountain environments (Cencetti *et al*., 2005, Fernandes *et al*., 2017, Koco, 2011, Pijl *et al*., 2020, Mauri *et al*., 2022), the use of such models considering the simulated absence of infrastructures in a DEM is in line with the innovative outcomes provided by Mauri *et al*. (2022). In this regard, our results attest the validity of such a methodology not only for degraded agricultural areas but also for mountain ones. In addition, models application looking at post-event conditions for the detection of evolutive dynamics affecting the degraded hillslope is a further ground-breaking aspect of our research. As similarly highlighted by Tague and Band, 2001, Royer, 2006, Buchanan *et al*., 2013, our research further suggests that the inefficient location of drainage systems along the road has a key influence on critical snowmelt runoff alterations. Specific interventions aimed at correctly positioning drainage systems (e.g. cross ditches, gutters, manholes, pipes and culverts) could be undertaken starting from our work. This is in line with the outcomes recently provided by Hearn and Shakya, 2017, Reed and Kite, 2020, Guo *et al*., 2020, Tshering *et al*., 2020, Raga *et al*., 2020, who

highlighted the key relevance of drainage systems location and maintenance for efficiently routing water runoff along the roadway and toward the above hillslopes. Looking at the notable effects of climate change in increasing both snowmelt intensity and snowfall amounts in mountain regions (Rasmussen *et al*., 2011, Wi *et al*., 2012, Marshall *et al*., 2020, Ikeda *et al*., 2021), our research further stresses the importance of considering superficial snowmelt dynamics in road planning and construction, aiming to avoid the future occurrence of erosion and landslides events. Finally, such a predictive, spatially-distributed analysis of land degradation dynamics affecting mountain hillslopes could be also considered for planning effective slope stability interventions.

4.6.1 Limitations

Some limitations have emerged during the simulations workflow. First, the selection of models inputs particularly affects the respective outcomes (as for any physical models), which makes this an issue aspect to be considered. Furthermore, the detection of snow-covered areas starting from satellites observations requires the exclusion of low-quality images and those characterized by an excessive cloud cover. This led to the availability of fewer valid input data for SRM simulations. Moreover, since the only availability of Landsat 8 products for the considered year, 30 m resolution images were used for snow coverage detection inside the basin. In fact, specific factors such as residual cloudiness, inefficient covered area and error in images acquisition by satellites can jointly affect the quality of acquired data for input preparation. This could potentially translate into bias and distortions in the resulting data interpolation, specifically in analyzing snow presence close to terrain depressions and local surface alterations, which certainly requires higher satellite resolution. Despite the possibility to run the SRM model for ungauged basins (Martinec and Rango, 1986), the lack of historical snowmelt discharge measurement at the basin outlet prevents the validation of SRM outcomes and therefore the detection of SRM accuracy was not feasible. Additionally, notwithstanding the evidences provided by models results and their respective statistical analysis, a last potential limit could translate in having assumed the possibility to predict the spatial distribution of slope instabilities and detect the role of the road in diverting *Sr* overflows starting from the computation of single *Sr* and *Rr* peaks at the basin outlet. Finally, site-specific geotechnical models could offer a more complete view of the mechanisms of the landslide that occurred downslope the roads, a point that will be explored soon by the authors.

4.7 Conclusions

This work proposes a multi-modeling analysis of the interaction between snowmelt runoff and road presence in the activation of hillslope instabilities in a mountain watershed. ALS-derived DEMs), served as the basis for computing predictive and post-event basin-scale soil stability simulations. The role of snowmelt runoff in affecting surface destabilizations was highlighted by comparing models outcomes starting from the calculation of snowmelt runoff, rainfall-runoff and their joint contribution to water overflow dynamics. The role of road network in altering surface snowmelt runoff was investigated both considering its presence and assuming its absence by a novel DEM post-processing procedure. Despite the highlighted limitations of the proposed innovative multi-modeling approach, results attested the key role played by the road in altering snowmelt runoff directions, as well as its contribution in the foreseen likely activation of a shallow landslide. Statistical analysis validated the accuracy of instabilities predictions. In this connection, despite the unfeasible possibility to validate SRM outcomes, the computed statistics evinces the reliability of *Sr* and *Rr* simulation. Given the importance of model validations, considering the objectives of our work it represents an interesting element to evaluate in applying the multi-modelling methodology proposed in our research. Finally, the relevance of inefficient water management by road drainage systems in potentially encouraging the occurrence of instabilities phenomena was also verified. More investigations could be undertaken aiming to find out the optimal location of ditches and culverts able to efficiently intercept and collect water runoff. Analogously, the proposed interactive application of SRM, RESS and SIMWE models could be suitable for likewise investigating the interaction between snowmelt runoff and roads presence in larger mountain basins. Similar analysis could be therefore performed, aiming to map terrain instabilities at both hillslope and watershed scale over time, as well as in investigating such issue focusing on the presence of infrastructures at different altitude levels regionwide. This work can be considered a useful tool for planning mitigation interventions able to reduce the occurrence of similar risk scenarios, also looking at the effects of climate changes in this regard. Therefore, valuable suggestions for developing and promoting efficient sustainable actions for mountain landscapes could be applied.

CRediT authorship contribution statement

Luca Mauri: Conceptualization, Methodology, Data curation, Writing - original draft. Sara Cucchiaro: Writing - review & editing. Stefano Grigolato: Writing - review & editing, Co-supervision. Giancarlo Dalla Fontana: Methodology. Paolo Tarolli: Conceptualization, Supervision, Project administration.

4.8 Supplementary material

4.8.1 Supplementary figures

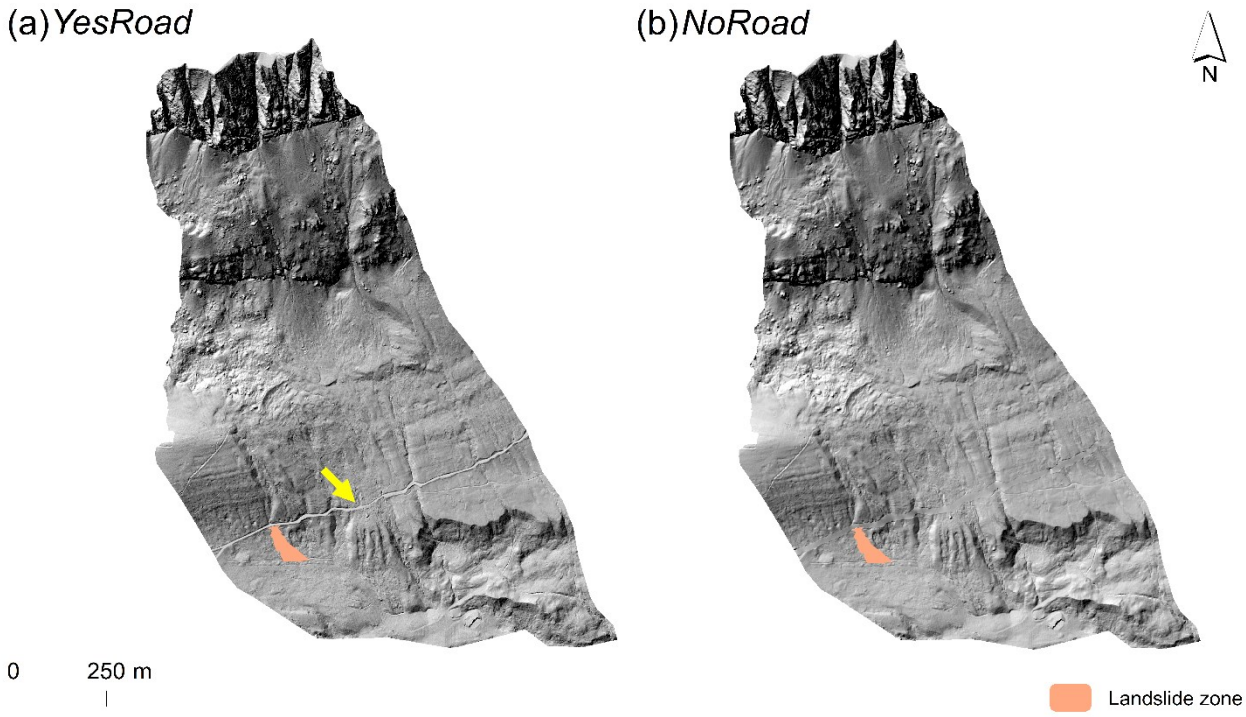

Figure 4.11. *Comparison of the shaded relief computed from the original (a) and the modified (b) pre-event ALS-derived DEM. The figure also shows the location of the observed shallow landslide (orange polygon) under the roadway (yellow arrow).*

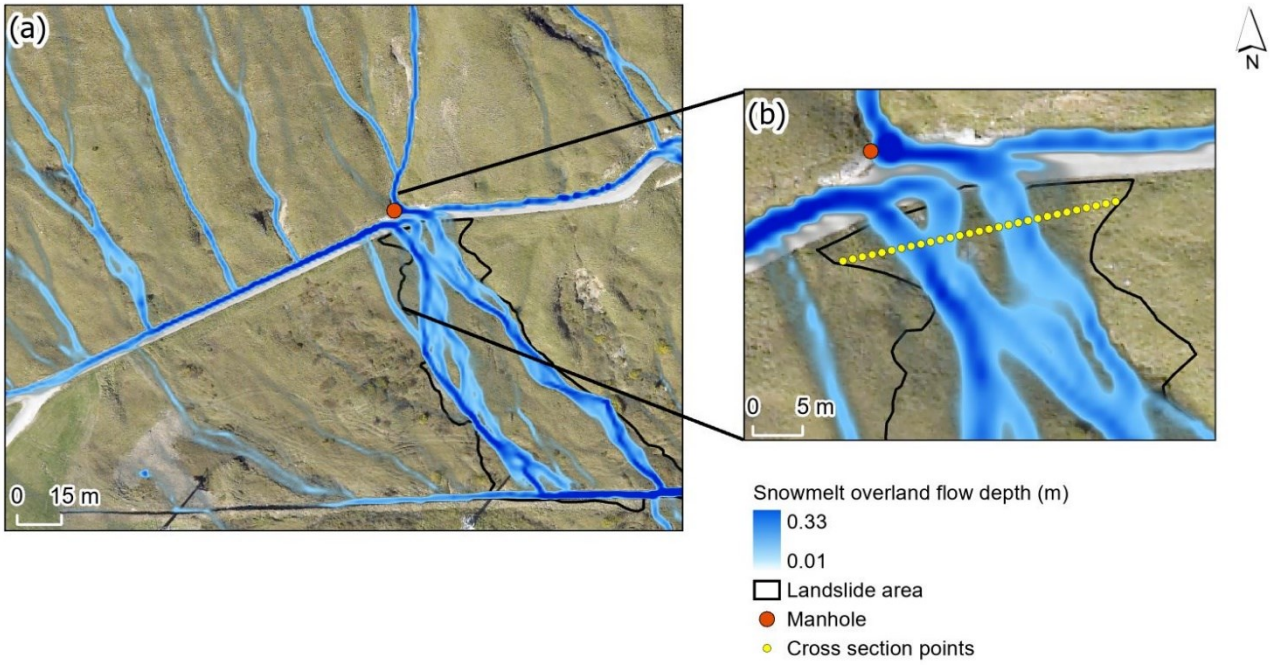

Figure 4.12. *Detail of the location of cross section points inside the landslide zone. In particular, a focus on snowmelt overflows intercepting the manhole located above the unstable surface is appreciable in the figure b. Cross section points were placed at an equal distance of 10 cm along a line traced inside the landslide surface under the road. SIMWE-derived Sr overland flows are represented in the background.*

4.8.2 Supplementary tables

Table 4.8. *Overview of the computed SRM, RESS and SIMWE predictive simulations, looking at both YesRoad and NoRoad scenarios.*

Model	**Output**	**Scenario**
SRM	Snowmelt rate (mm/h)	*YesRoad*, pre-event (2018)
	Rainfall runoff contribution (mm/h)	
RESS	Critical snowmelt (mm/h)	*YesRoad*, pre-event (2018) *NoRoad*, pre-event (2018)
	Critical rainfall (mm/h)	
	RI index (-)	*YesRoad*, pre-event (2018)
SIMWE	Snowmelt discharge (m^3/s) Snowmelt flow depth (m)	*YesRoad*, pre-event (2018) *NoRoad*, pre-event (2018)

Table 4.9. *Overview of symbols and abbreviations used in models application*

Model	Symbol / Abbreviation	Description
Snowmelt Runoff Model (SRM)	Sr	Snowmelt runoff
	Rr	Rainfall runoff
	SRr	Combined Sr and Rr
	T	Temperature
	P	Precipitation
	SCA	Snow Covered Area
	γ	Temperature Lapse Rate
	Tcrit	Critical temperature
	An	Degree-day factor
	RCA	Rainfall Contributing Area
	K	Recession coefficient
	Cs	Runoff coefficient snow
	Cr	Runoff coefficient rain
	L	Time lag
Road Erosion Steady-State model (RESS)	z	Soil depth
	ϕ	Internal friction angle
	ρ_s	Soil density
	ρ_w	Water density
	Tr	Soil transmissivity
	Coh_s	Soil cohesion
	Coh_r	Root cohesion
	W	Vegetation surcharge
	r_{rc}	Relative road cut depth
	$Crit_{Sr}$	Critical Sr
	$Crit_{Rr}$	Critical Rr
	$Crit_{SRr}$	Critical SRr
	RI_{Sr}	Relative Impact index from Sr
	RI_{Rr}	Relative Impact index from Rr
	RI_{SRr}	Relative Impact index from SRr
SIMulated Water Erosion model (SIMWE)	k	Saturated soil conductibility
	n	Manning's n

4.8.3 Supplementary documentation

4.8.3.1 Models overview

Snowmelt models are generally divided into two categories, i.e., energy balance and degree day models. While the former aim to quantify snowmelt as residual in the heat balance equation, the latter assumes an empirical linear relation between air temperatures and melt rates (Mullem *et al*., 2004; Karimi *et al*., 2016) applying a coefficient of proportionality called the degree-day factor. Therefore, degree-day models refer to the conceptual temperature index approach, i.e., the degree-day method. This physically-based approach only needs for air temperature and precipitation values as meteorological input data and it is based on the following Equation (4.11):

$$M = An \cdot Td \tag{4.11}$$

where M is the snowmelt (cm), An is the degree-day factor ($cm \cdot day^{-1} °C^{-1}$) and Td stands for the degree-days ($°C \cdot day$), i.e., the daily mean temperature or the average value between its maximum and minimum. Many hydrological models simulating snowmelt runoff are based on the degree-day method and revealed to be efficiently applicable notwithstanding their limited input data requirements (Rango and Martinec, 1995; Siemens *et al*., 2021). Slope stability investigation and modeling of shallow landslide spatial susceptibility are principally based on deterministic, physically-based models (van Westen *et al*., 2006). This modeling approach mainly depends on the combination between infinite slope stability and hydrological infiltration models. Especially for soil mantle with a thickness noticeably smaller than the slope length and where the failure plane is approximately parallel to the slope surface, planar infinite-slope models have been largely adopted in slope stability analysis (Borga *et al*., 1998). Therefore, the prediction of terrain failures at both hillslope and watershed scale reveals to be efficiently achievable through these models coupling (Montgomery and Dietrich, 1994; Wilkinson *et al*., 2002; Xie *et al*., 2004; Godt *et al*., 2008; Mergili *et al*., 2014). Infinite-slope stability models refer to the general assumption that the slope is planar and of infinite length, and the failure plane is parallel to the topographic surface. Such an initial postulation significantly simplifies these models also easing their application in Geographic Information Systems (*GIS*) environment (Burton and Bathurst, 1998; Baum *et al*., 2002; Mergili *et al*., 2014). In infinite-slope stability models, the relation between the shear strength of the materials resisting along the slip surface and the shear stress acting on it is particularly important and is expressed by the Factor of Safety (FS; Hammond *et al*., 1992; Carson and Kirkby, 1972; Borga *et al*., 2005; Crozier, 2010). Starting from the above considerations, the concept of critical rainfall proposed by Montgomery and Dietrich (1994) needs to be taken into account for slope stability modeling. Critical rainfall stands for

the minimum steady-state rainfall forecast to promote slope instabilities (Borga *et al*., 2005). In this regard, zones with lower critical rainfall values are expected to be more susceptible to shallow landsliding, while those with higher critical rainfall values are predicted to be more stable (Borga *et al*, 1998). Based on the concept of critical rainfall, soil stability can be grouped into four classes i.e. (i) unconditionally unstable, (ii) unstable, (iii) stable and (iv) unconditionally stable (Montgomery and Dietrich, 1994). As mathematically analyzed by Borga *et al*. (2005), the terrain is unconditionally unstable if it is unstable even when dry and unconditionally stable if its elements are forecast to be stable even when saturated; unstable zones are those predicted to fail and stable ones are those predicted to not fail. Accordingly, the impact of road-induced water flows alterations can be investigated by comparing the critical rainfall before and after the drainage alterations due to the road presence (R_{pre} and R_{post} respectively) through the Relative Impact (RI) index Equation (4.12).

$$RI = \frac{R_{pre} - R_{post}}{R_{pre}} \tag{4.12}$$

RI ranges between 0 and 1. RI=0 when water runoff propagation is not influenced by the road network; RI > 0 if road's drainage systems concentrate and encourage water flows hence decreasing the critical rainfall, while RI < 0 if road drainage systems lead to the reduction of saturated water flows increasing critical rainfall values (Borga *et al*., 2005).

4.8.3.2 Snowmelt Runoff Model (SRM)

The Snowmelt Runoff Model-SRM (Martinec, 1975; Martinec and Rango, 1986; Martinec and Rango, 2008) is a conceptual, deterministic, degree-day hydrological model able to simulate daily snowmelt and rainfall runoff in mountain basins, starting from hydrological and meteorological data (Panday *et al*., 2014). SRM goes beyond the traditional degree-day approach by requiring remotely sensed observations of the snow-covered area, hence providing a more physically-based application at the watershed scale (Kustas *et al*., 1994). The yearly monitoring of snowy areas from satellites observations and the extrapolation of meteorological data from nearby stations allow the model to evaluate daily runoff also in ungauged basins (Martinec *et al*., 2008). Accordingly to Equation (4.13), SRM computes the daily streamflow derived from snowmelt and rainfall, overlaying it on the calculated recession flows and then converting it into daily discharge from the basin at its outlet location.

$$Q_{n+1} = [c_{sn} * A_n(T_n + \Delta T_n)S_n + c_{Rn}P_n]\frac{A*1000}{86400}(1 - k_{n+1}) + Q_n k_{n+1} \tag{4.13}$$

where Q is average daily discharge (m^3s^{-1}), c is the runoff coefficient (-) with c_S referring to snowmelt

and c_R to rain, *An* is the degree-day factor ($cm°C^{-1}d^{-1}$), *T* is the number of degree-days (°C·d), *ΔT* is the adjustment by temperature lapse rate (°C·d), *S* is the ratio of the snow-covered area to the total extension of the basin (-), *P* is the precipitation contributing to runoff (cm), *A* is the area of the watershed (km^2), *k* is the recession coefficient representing the decline of discharge in a snowmelt or rainfall period (-), *n* is the sequence of days during the discharge computation period and the fraction *1000/86400* inserted as a multiplication factor of the *A* coefficient stands for the conversion from $cm·km^2d^{-1}$ to m^3s^{-1}. Starting from the satellite-derived snowpack distribution, as the snowpack depletes, the degree-day method is applied only to those areas of the basin characterized by snow presence during the simulation period. The acquisition of the model's inputs represents a key aspect to performing accurate snowmelt simulations. In this regard, SRM needs for the definition of the elevation range between the outlet and the upper part of the basin, divided into intervals of about 500 m. Therefore, the area-elevation curve can be defined to apply each model variable to each zone to calculate snowmelt runoff. SRM accepts either the daily mean temperature or the respective minimum and maximum values. For the latter, the average temperature is computed. SRM also accepts temperature and precipitation data derived from a single station or several ones. In the first case, temperature data are extrapolated to the hypsometric mean elevations for each zone through the lapse rate variable. In the second one, a synthetic station must be defined by the user (Richard and Gratton, 2001; Martinec *et al*., 2008) therefore applying the single basin option. Snow cover seasonally variates during the melt period. Starting from satellite-derived snow cover mapping, depletion curves of the snow coverage can be interpolated in order to compute the daily extent of snow-covered surfaces inside the basin. In addition, critical temperature (T_{CRIT}) specifies whether the measured precipitation is rain or snow. In this regard, such a variable is relevant for establishing if rainfall immediately contributes to runoff as rain ($T > T_{CRIT}$) or snow ($T < T_{CRIT}$; Martinec *et al*., 2008). The degree-day factor (*An*) converts the number of degree-days (°C·day) into the daily snowmelt depth (cm) and variates according to the alteration of snow properties during the snowmelt season. To account for rain-on-snow events, the Rainfall Contributing Area (*RCA*) allows determining whether rain that falls on the snowpack is retained by it or added to the snowmelt runoff. In this regard, *RCA* is generally set to 0 in those months in which is assumed that rain falling on the snowy areas, at the beginning of the melt season, is retained by the dry snow. In this case, the model adds *Rr* to *Sr* only for the snow-free zones. Successively, as the end of the melt season approaches, the snow becomes ripe and it is assumed that if rain falls on snow cover, the same amount of water is released from the snowpack, until its complete dissolution. Therefore, rain is entirely added to snowmelt and *RCA* is set to 1. The recession coefficient (*k*) represents the decline of discharge in a period without snowmelt or rainfall, while its inverse factor *1-k* indicates the meltwater proportion which immediately appears

in runoff. SRM accepts separate runoff coefficients for snow (*Cs*) and rain (*Cr*). The runoff coefficient represents the difference between the available water volume from both snowmelt and rainfall and the outflow from the watershed. If at the beginning of the melting period losses are generally limited to evaporation processes from the snow surfaces, during the snowmelt season they are expected to increase. Differently, flow channels from the remaining snow-covered areas tend to prevail towards the end of the snowmelt season with decreasing losses and increasing runoff coefficient. Finally, the time lag (*L*) represents the total time required for the water to reach the outlet of the basin (Martinec *et al*., 2008). SRM returns several outputs, i.e. (i) contributing rainfall-runoff (*Rr*), (ii) total potential zonal snowmelt depth (*SumAT*), (iii) contribution made to runoff of stored snow (*NewMelt*), (iv) melt of snow that temporally covers a free-snow area ($M_{1\text{-}S}$), (v) daily potential snowmelt depth (*aT*), (vi) daily melt from the existing snowpack (*Zonal Melt*) and (vii) water watershed-scale discharge produced from both snowmelt and rainfall (*Total Melt*).

4.8.3.3 Road Erosion Steady-State model (RESS) model

The Road Erosion Steady-State model (RESS) is a steady-state model that couples a shallow saturated subsurface model with an infinite-slope Coulomb stability model of a cohesionless soil of constant slope and thickness (Montgomery and Dietrich, 1994). RESS evaluates soil saturation deficit for each cell based on the upslope contributing area, soil transmissivity and local slope. In particular, a road interception algorithm is implemented to describe the amount of subsurface flow intercepted by the road cut, therefore turned into overland flow and redirected along the roadway and its drainage systems. In particular, RESS calculates the minimum rainfall intensity able to destabilize each cell of the basin, looking at both the presence and the assumed absence of the road (Dietrich *et al*., 1992; Montgomery and Dietrich, 1994; Borga *et al*., 2005). RESS calculates drainage systems starting from user-defined coordinates of specific points falling on their location along the road. The closest road-axis cell to each point is identified, assuming each drainage system passing through that cell in a perpendicular direction respect to the road. Specific algorithms are implemented in the model in this regard, as well as for road creation (Dietrich *et al*., 1992; Montgomery and Dietrich, 1994; Borga *et al*., 2005). RESS outcomes are represented by several outputs, i.e. (i) road cells representing road elevation, (ii) on-road flow direction, (iii) drainage systems position along the roadway, (iv) critical rainfall without the road ($mm \cdot h^{-1}$), (v) critical rainfall with the road ($mm \cdot h^{-1}$) and (vi) Relative Impact statistics (*RI*).

4.8.3.4 SIMulated Water Erosion (SIMWE) model

The SIMulated Water Erosion model is a landscape scale, bivariate, physics-based and spatially distributed model that simulates hydrological overland water flows and sediment dynamics. It implements a path sampling method by distinctly analyzing superficial water flows processes and sediment transport, by modeling superficial hydraulic flow tie-road map and consecutively using the obtained output for the estimation of sediment runoff (Cencetti *et al*., 2005). SIMWE is built on the principles that define the Water Erosion Prediction Project model (Flanagan and Nearing, 1995) and is divided into two modules available in the GRASS GIS environment, i.e. *r.sim.water* and *r.sim.sediment*. In particular, in the *r.sim.water* module a bidimensional shallow water flow is described by the bivariate form of the Saint Venant equations (Saint-Venant, 1871), which are specifically solved by the stochastic Monte Carlo method. In this regard, the model assumes that overland water flows are close to the kinematic wave approximation, including a diffusion term that improves the kinematic solution by overcoming small shallow DEM's pits (Mitasova *et al*., 2003) and smoothing out the flow over slope discontinuities or unexpected changes in Manning's coefficient. The *r.sim.water* outputs are (i) overland water depth (m) and (ii) overland water discharge (m^3s^{-1}).

4.8.3.5 References of supplementary documentation

Baum, R., Savage, W., Godt, J., 2002. TRIGRS-A fortran program for transient rainfall infiltration and grid-based regional slope-stability analysis, Open file report 02-424, p.25

Borga, M., Dalla Fontana, G., Da Ros, D., Marchi, L., 1998. Shallow landslide hazard assessment using a physically based model and digital elevation data. Environmental Geology, 35 (2–3), 81–88. https://doi.org/10.1007/s002540050295

Borga, M., Tonelli, F., Dalla Fontana, G., Cazorzi, F., 2005. Evaluating the influence of forest roads on shallow landsliding. Ecological Modelling, 187(1 SPEC. ISS.), 85–98. https://doi.org/10.1016/j.ecolmodel.2005.01.055

Burton, A., Bathurst, J. C., 1998. Physically based modelling of shallow landslide sediment yield at a catchment scale. Environmental Geology, 35(2–3), 89–99. https://doi.org/10.1007/s002540050296

Carson, M.A., Kirkby, M. J., 1972. Hillslope Form and Process. Cambridge University Press, London. ISBN: 9780521109116

Cencetti, C., Rosa, P. De, Fredduzzi, A., Marchesini, I., 2005. Erosione dei suoli: applicazioni tramite il software GRASS GIS. G. di Geol. Appl. 2, 196–202. DOI: 10.1474/GGA.2005–02.0–28.0054

Crozier, M. J., 2010. Deciphering the effect of climate change on landslide activity: A review. Geomorphology, 124(3–4), 260–267. https://doi.org/10.1016/j.geomorph.2010.04.009

Dietrich, W.E., Wilson, C.J., Montgomery, D.R., McKean, J., Bauer, R., 1992. Erosion thresholds and land surface morphology. Geology 20, 675–679. https://doi.org/10.1130/0091-7613(1992)020<0675:ETALSM>2.3.CO;2

Flanagan, D., Nearing, M., 1995. USDA-Water Erosion Prediction Project (WEPP), Hillslope Profile and Watershed Model Documentation. USDA. ARS National Soil Erosion Research Laboratory, NSERL Report No. 10

Godt, J., Baum, R., Savage, W., Salciarini, D., Schulz, W., Harp, E., 2008. Transient deterministic shallow landslide modeling: Requirements for susceptibility and hazard assessments in a GIS framework. Engineering Geology 102 (3-4), 214-226. DOI: 10.1016/j.enggeo.2008.03.019

Hammond, C., Hall, D., Miller, S., Swetik, P., 1992. Level I Stability Analysis (LISA). Documentation for Version 2.0 General Technical Report, INT-285

Karimi, H., Zeinivand, H., Tahmasebipour, N., Haghizadeh, A., Miryaghoubzadeh, M., 2016. Comparison of SRM and WetSpa models efficiency for snowmelt runoff simulation. Environmental Earth Sciences, 75(8), 1–16. https://doi.org/10.1007/s12665-016-5490-z

Kustas, W. P., Rango, A., Uijlenhoet, R., 1994. A simple energy budg*et al*gorithm for the snowmelt runoff model. Water Resources Research, 30(5), 1515–1527. https://doi.org/10.1029/94WR00152

Martinec, J., 1975. Snowmelt - runoff model for stream flow forecasts. Nordic Hydrology, 6 (3), 145–154. https://doi.org/10.2166/nh.1975.0010

Martinec, J., Rango, A., 1986. Parameter values for snowmelt runoff modelling. J. Hydrol. 84, (3-4), 197–219. https://doi.org/10.1016/0022-1694(86)90123-X

Martinec J., Rango A., Roberts R., 2008. Snowmelt Runoff Model (SRM) User's Manual. Agricultural Experiment Station, Special Report 100

Mergili, M., Marchesini, I., Rossi, M., Guzzetti, F., Fellin, W., 2014. Spatially distributed three-dimensional slope stability modelling in a raster GIS. Geomorphology, 206, 178–195. https://doi.org/10.1016/j.geomorph.2013.10.008

Mitasova, H., Mitas, L., Hofierka, J., Thaxton, C., 2003. r.sim.water - Overland flow hydrologic simulation using path sampling method (SIMWE). GRASS GIS 7.9.Dev Reference Manual

Montgomery D.R., Dietrich W. E., 1994. A physically based model for the topographic control on shallow landsliding. Water Resources Research, 30 (4), 1153–1171. https://doi.org/10.1029/93WR02979

Mullem, A., Garen, D., Woodward, D., 2004. Snowmelt, in: Part 630 Hydrology National Engineering Handbook, United States Department of Agriculture (eds), USA, pp. 1-21

Panday, P. K., Williams, C. A., Frey, K. E., & Brown, M. E., 2014. Application and evaluation of a snowmelt runoff model in the Tamor River basin, Eastern Himalaya using a Markov Chain Monte Carlo (MCMC) data assimilation approach. Hydrological Processes, 28(21), 5337–5353. https://doi.org/10.1002/hyp.10005

Pierre Y. Julien, Bahram Saghafian, Ogden F. L., 1995. Raster-based hydrologic modeling of spatially-varied surface runoff. Journal of the American Water Resources Association, 31(3), 523–536. https://doi.org/10.1111/j.1752-1688.1995.tb04039.x

Rango, A., Martinec, J., 1995. Revisiting the degree-day method for snowmelt computations. Journal of the American Water Resources Association, 31 (4), 657–669. https://doi.org/10.1111/j.1752-1688.1995.tb03392.x

Richard C., Gratton D. J., 2001. The importance of the air temperature variable for thesnowmelt runoff modelling using the SRM. Hydrological Processes 15 (18), 3357-3370. https://doi.org/10.1002/hyp.1031

Saint-Venant, de A.J.C. Barrè, 1871. Théorie du mouvement non-permanent des eaux, avec application aux crues des rivières et a l'introduction de marées dans leurs lits. Comptes Rendus de l'Académie des Sciences 73, 147-154

Siemens, K., Dibike, Y., Shrestha, R. R., Prowse, T., 2021. Runoff projection from an alpine watershed in western canada: Application of a snowmelt runoff model. Water (Switzerland), 13(9), 1–19. https://doi.org/10.3390/w13091199

Van Westen C. J., Van Asch, T. W. J., Soeters, R., 2006. Landslide hazard and risk zonation - Why is it still so difficult? Bulletin of Engineering Geology and the Environment, 65(2), 167–184. https://doi.org/10.1007/s10064-005-0023-0

Wilkinson, P. L., Anderson, M. G., Lloyd, D. M., 2002. An integrated hydrological model for rain-induced landslide prediction. Earth Surface Processes and Landforms, 27(12), 1285–1297. https://doi.org/10.1002/esp.409

Xie, M., Esaki, T., & Cai, M., 2004. A time-space based approach for mapping rainfall-induced shallow landslide hazard. Environmental Geology, 46(6–7), 840–850. https://doi.org/10.1007/s00254-004-1069-1

4.9 References of Chapter 4

Achour, Y., Boumezbeur, A., Hadji, R., Chouabbi, A., Cavaleiro, V., Bendaoud, E.A., 2017. Landslide susceptibility mapping using analytic hierarchy process and information value methods along a highway road section in Constantine, Algeria. Arab. J. Geosci. 10, 1–16. https://doi.org/10.1007/s12517-017-2980-6

Al-Umar, M., Fall, M., Daneshfar, B., 2020. GIS-based modeling of snowmelt-induced landslide susceptibility of sensitive marine clays. Geoenviron. Disasters 7. https:// doi.org/10.1186/s40677-020-0142-8

Arghius¸, V., Arghius¸, C., Ozunu, A., Nour, E., Ros¸ian, G., Muntean, L.O., 2011. The relation between the landslide activity and irregular rainfall and snowmelt in the codrului hills, romania. Environ. Eng. Manage. J. 10 (1), 3–6

Arn´aez, J., Lasanta, T., Ruiz-Flaño, P., Ortigosa, L., 2007. Factors affecting runoff and erosion under simulated rainfall in Mediterranean vineyards. Soil Tillage Res. 93, 324–334. https://doi.org/10.1016/j.still.2006.05.013

Arnone, E., Noto, L.V., Lepore, C., Bras, R.L., 2011. Physically-based and distributed approach to analyze rainfall-triggered landslides at watershed scale. Geomorphology 133, 121–131. https://doi.org/10.1016/j.geomorph.2011.03.019

Ashland, F.X., 2009. Snowmelt-induced ground-water fluctuations in selected northern Utah landslides-preliminary results from the 2007–08 landslide water year. Utah Dep. Nat. Resour. Utah Geol. Surv. Open-File Rep. 550, 1–19

Bernardi De Leòn, R., 2009. Road development in Podocarpus National Park: an assessment of threats and opportunities. J. Sustain. For. 28, 735–754. https://doi. org/10.1080/10549810902936607

Bogaard, T.A., Greco, R., 2016. Landslide hydrology: from hydrology to pore pressure. Wiley Interdiscip. Rev. Water 3 (3), 439–459. https://doi.org/10.1002/wat2.1126

Borga, M., Dalla Fontana, G., Gregoretti, C., Marchi, L., 2002a. Assessment of shallow landsliding by using a physically based model of hillslope stability. Hydrol. Process. 16 (14), 2833–2851

Borga, M., Dalla Fontana, G., Cazorzi, F., 2002b. Analysis of topographic and climatic control on rainfall-triggered shallow landsliding using a quasi-dynamic wetness index. J. Hydrol. 268 (1–4), 56–71. https://doi.org/10.1002/hyp.1074

Borga, M., Tonelli, F., Selleroni, J., 2004. A physically based model of the effects of forest roads on slope stability. Water Resour. Res. 40 (12) https://doi.org/10.1029/2004WR003238

Borga, M., Tonelli, F., Dalla Fontana, G., Cazorzi, F., 2005. Evaluating the influence of forest roads on shallow landsliding. Ecol. Modell. 187, 85–98. https://doi.org/10.1016/j.ecolmodel.2005.01.055

Brand, E.W., Premchitt, J., Philippson, H.B., 1984. Relationship between rainfall and landslides in Hong Kong. Proceedings of the 4th International Symposium on Landslides in Toronto, Canada 1, 377–384

Brubaker, K., Rango, A., Kustas, W., 1996. Incorporating radiation inputs into the snowmelt runoff model. Hydrol. Process. 10 (10), 1329–1343. https://doi.org/10.1002/(SICI)1099-1085(199610)10:10<1329::AID-HYP464>3.0.CO;2-W

Buchanan, B., Easton, Z.M., Schneider, R.L., Walter, M.T., 2013. Modeling the hydrologic effects of roadside ditch networks on receiving waters. J. Hydrol. 486, 293–305. https://doi.org/10.1016/j.jhydrol.2013.01.040

Bunya, S., Dietrich, J., Westerink, J., Ebersole, B., Smith, J., Atkinson, J., Jensen, R., Resio, D., Luettich, R., Dawson, C., Cardone, V., Cox, A., Powell, M., Westerink, H., Roberts, H. A high-resolution coupled riverine flow, tide, wind, wind wave, and storm surge model for southern Louisiana and Mississippi. Part I: Model development and validation. Monthly Weather Review 138 (2), 345–377. doi:10.1175/2009MWR2906.1

Butt, M., Bilal, M., 2011. Application of snowmelt runoff model for water resource management. Hydrol. Process. 25 (24), 3735–3747. https://doi.org/10.1002/hyp.8099

Cencetti, C., Rosa, P.D., Fredduzzi, A., Marchesini, I., 2005. Erosione dei suoli: applicazioni tramite il software GRASS GIS. G. di Geol. Appl. 2, 196–202. DOI: 10.1474/GGA.2005–02.0–28.0054

Cohen, J., 1960. A coefficient of agreement for nominal scales. A coefficient of agreement for nominal scales. Educ. Psychol. Measur. 20 (1), 37–46. https://doi.org/10.1177/001316446002000104

Collins, B.D., Znidarcic, D., 2004. Stability analyses of rainfall induced landslides. J. Geotech. Geoenvironmental Eng. 130, 362–372. https://doi.org/10.1061/(ASCE)1090-0241(2004)130:4(362)

Conant, R.T., Paustian, K., Elliott, E.T., 2001. Grassland management and conversion into grassland: effects on soil carbon. Ecol. Appl. 11, 343–355. https://doi.org/10.1890/1051-0761(2001)011[0343:GMACIG]2.0.CO;2

Cordoba, P.J., Mergili, M., Aristizàbal, E., 2020. Probabilistic landslide susceptibility analysis in tropical mountainous terrain using the physically based r.slope.stability model. Nat. Hazards Earth Syst. Sci. 20 (3), 815–829. https://doi.org/10.5194/nhess-20-815-2020

Cruden, D.M., Varnes, D.J., 1996. Landslide Types and Processes, Special Report, Transportation Research Board , National Academy of Sciences, 247, 36–75. Cucchiaro, S., Maset, E., Cavalli, M., Crema, S., Marchi, L., Beinat, A., Cazorzi, F., 2020. How does co-registration affect geomorphic change estimates in multi-temporal surveys? GIScience Remote Sens. 57 (5), 611–632. https://doi.org/10.1080/15481603.2020.1763048

Davison, L., Springman, S., Wood, D.M., 2000. Pore water pressure Univ. West Engl. URL http://environment.uwe.ac.uk/geocal/SoilMech/water/water.htm

Daigle, P., 2010. A summary of the environmental impacts of roads, management responses, and research gaps: A literature review. BC Journal of Ecosystems and Management 10 (3), 65–89. https://doi.org/10.22230/jem.2010v10n3a38

DeBeer, C.M., Pomeroy, J.W., 2010. Simulation of the snowmelt runoff contributing area in a small alpine basin. Hydrol. Earth Syst. Sci. 14, 1205–1219. https://doi.org/10.5194/hess-14-1205-2010

Devi, G., 2017. Snowmelt runoff estimation of Jhelum Basin with SRM model. Int. J. Eng. Res. Technol. 6 (4), 42–48. https://doi.org/10.17577/ijertv6is040040

Dietrich, W.E., Wilson, C.J., Montgomery, D.R., McKean, J., Bauer, R., 1992. Erosion thresholds and land surface morphology. Geology 20, 675–679. https://doi.org/10.1130/0091-7613(1992)020<0675:ETALSM>2.3.CO;2

Dietz, A.J., Kuenzer, C., Gessner, U., Dech, S., 2012. Remote sensing of snow - a review of available methods. Int. J. Remote Sens. 33, 4094–4134. https://doi.org/10.1080/01431161.2011.640964

Dikau, R., Brunsden, D., Shrott, L., & Ibsen, M.L., 1996. Landslides Recognition, Identification, Movement and Causes, Dikau R, B. ed. ISBN: 978-0-471-96477-3.

Donmez, C., Berberoglu, S., Cicekli, S.Y., Cilek, A., Arslan, A.N., 2021. Mapping snow cover using landsat data: toward a fine-resolution water-resistant snow index. Meteorol. Atmos. Phys. 133 (2), 281–294

Dutton, A.L., Loague, K., Wemple, B.C., 2005. Simulated effect of a forest road on near surface hydrologic response and slope stability. Earth Surf. Process. Landf. 30, 325–338. https://doi.org/10.1002/esp.1144

Eigdir, A.N., 2003. Investigation of the snowmelt runoff in the Orumiyeh region , using modelling , GIS and RS techniques. International Institute for Geo-Information Science and Earth Observation (ITC)

Elliot, W.J., Foltz, R.B., Luce, C.H., 1999. Modeling low-volume road erosion. J. Transp. Res. Board 1652 (1), 244–249. https://doi.org/10.3141/1652-64

Esri, 2021. Mosaic To New Raster (Data Management). Esri tool Ref. tools. https://pro.arcgis.com/en/pro-app/latest/tool-reference/data-management/mosaic-to-newraster.htm

Fawcett, T., 2006. An introduction to ROC analysis. Pattern Recognit. Lett. 27 (8), 861–874. https://doi.org/10.1016/j.patrec.2005.10.010

Ferguson, R.I., 1999. Snowmelt runoff models. Prog. Phys. Geogr. 23, 205–227. https://doi.org/10.1191/030913399672720559

Fernandes, J., Bateira, C., Soares, L., Faria, A., Oliveira, A., Hermenegildo, C., Moura, R., Goncalves, J., 2017. SIMWE model application on susceptibility analysis to bank gully erosion in Alto Douro Wine Region agricultural terraces. Catena 153, 39–49. https://doi.org/10.1016/j.catena.2017.01.034

Fu, B., Newhama, L.T.H., Ramos-Scharron, 2010. A review of surface erosion and sediment delivery models for unsealed roads. Environ. Model. Softw. 25, 1–14

Gallage, C., Abeykoon, T., Uchimura, T., 2021. Instrumented model slopes to investigate the effects of slope inclination on rainfall-induced landslides. Soils Found. 61 (1), 160–174

Gao, Q., Wan, Y., Li, Y., Sheng, W., Jiangcun, W., Wang, B., Li, W., 2001. Trends of grassland NPP and its response to human activity in Northern Tibet. Acta Ecol. Sin. 27, 4612–4619

Gasmo, J.M., Rahardjo, H., Leong, E.C., 2000. Infiltration effects on stability of a residual soil slope. Comput. Geotech. 26, 145–165. https://doi.org/10.1016/S0266-352X(99)00035-X

Gomez-Landesa, E., Rango, A., 2002. Operational snowmelt runoff forecasting in the Spanish Pyrenees using the snowmelt runoff model. Hydrol. Process. 16 (8), 1583–1591. https://doi.org/10.1002/hyp.1022

Guo, Y., Zhang, Y., Zhang, L., Wang, Z., 2020. Regionalization of hydrological modeling for predicting streamflow in ungauged catchments: a comprehensive review. WIRES 8 (1). https://doi.org/10.1002/wat2.1487

Guzzetti, F., Reichenbach, P., Ardizzone, F., Cardinali, M., Galli, M., 2006. Estimating the quality of landslide susceptibility models. Geomorphology 81, 166–184. https://doi. org/10.1016/j.geomorph.2006.04.007

Hearn, G.J., Shakya, N.M., 2017. Engineering challenges for sustainable road access in the Himalayas. Q. J. Eng. Geol. Hydrogeol. 50, 69–80. https://doi.org/10.1144/qjegh2016-109

Hinds, E.S., Lu, N., Mirus, B.B., Godt, J.W., Wayllace, A., 2021. Evaluation of techniques for mitigating snowmelt infiltration-induced landsliding in a highway embankment. Eng. Geol. 291, 106240 https://doi.org/10.1016/j.enggeo.2021.106240

Hofierka, J., Gallay, M., Bandura, P., Šašak, J., 2018. Identification of karst sinkholes in a forested karst landscape using airborne laser scanning data and water flow analysis. Geomorphology 308, 265–277. https://doi.org/10.1016/j.geomorph.2018.02.004

Ikeda, K., Roy, R., Changhai, L., Andrew, N., Fei, C., Mike, B., Ethan, G., Jimy, D., Aiguo, D., Charles, L., Keith, M., 2021. Snowfall and snowpack in the Western U.S. as captured by convection permitting climate simulations: current climate and pseudo global warming future climate. Clim. Dyn. 57, 2191–2215. https://doi.org/10.1007/s00382-021-05805-w

Jaboyedoff, M., Oppikofer, T., Abellàn, A., Derron, M.-H., Loye, A., Metzger, R., Pedrazzini, A., 2012. Use of LiDAR in landslide investigations: a review. Nat. Hazards 61, 5–28. https://doi.org/10.1007/s11069-010-9634-2

Jonas, L., Hobbs, P., 2021. The Application of Terrestrial LiDAR for Geohazard Mapping, Monitoring and Modelling in the British Geological Survey. Remote Sensing 13 (3), 395. https://doi.org/10.3390/rs13030395

Jordan, A., 2008. Soil loss and runoff rates on unpaved forest roads in southern Spain after simulated rainfall. For. Ecol. Manage. 255, 913–919. https://doi.org/10.1016/j.foreco.2007.10.002

Kawagoe, S., Kazama, S., Sarukkalige, P.R., 2009. Assessment of snowmelt triggered landslide hazard and risk in Japan. Cold Reg. Sci. Technol. 58 (3), 120–129. https://doi.org/10.1016/j.coldregions.2009.05.004

Koco, S., 2011. Simulation of gully erosion using the SIMWE model and GIS. Landf. Anal. 17, 81–86

Kokutse, N.K., Temgoua, A.G.T., Kavazovìc, Z., 2016. Slope stability and vegetation: Conceptual and numerical investigation of mechanical effects. Ecol. Eng. 86, 146–153. https://doi.org/10.1016/j.ecoleng.2015.11.005

Kour, R., Patel, N. A. K., 2013. Estimation of snowmelt runoff in Chenab basin, western Himalayas. Climate change & Himalayan ecosystem-indicator, bio & water resource

Krøgli, K.I., Devoli, G., Colleuille, H., Boje, S., Sund, M., Engen, I.K., 2018. The Norwegian forecasting and warning service for rainfall- and snowmelt-induced landslides. Nat. Hazards Earth Syst. Sci. 18, 1427–1450. https://doi.org/10.5194/nhess-18-1427-2018

Kurakina, N. I., Mikhailova, A. A., Kuzmina, A. D., 2020. Satellite Monitoring of Snow Cover Based on GIS. IEEE Conference of Russian Young Researchers in Electrical and Electronic Engineering (EI. Con. Rus.). DOI: 10.1109/EIConRus49466.2020.9039485

Lee, S., Ryu, J.H., Kim, I.S., 2007. Landslide susceptibility analysis and its verification using likelihood ratio, logistic regression, and artificial neural network models: Case study of Youngin, Korea. Landslides 4, 327–338. https://doi.org/10.1007/s10346-007-0088-x

Luce, C.H., 2002. Hydrological processes and pathways affected by forest roads: what do we still need to learn? Hydrol. Process. 16. (1), 2901–2904. https://doi.org/10.1002/hyp.5061

Marshall, A.M., Timothy, E.L., Andrew, P.R., John, T.A., 2020. Higher snowfall intensity is associated with reduced impacts of warming upon winter snow ablation. Geophys. Res. Lett. 47 (4) https://doi.org/10.1029/2019GL086409

Martinec, J., 1975. Snowmelt - runoff model for stream flow forecasts. Nord. Hydrol. 6 (3), 145–154. https://doi.org/10.2166/nh.1975.0010

Martinec, J., Rango, A., 1986. Parameter values for snowmelt runoff modelling. J. Hydrol. 84 (3–4), 197–219. https://doi.org/10.1016/0022-1694(86)90123-X

Martinec, J., Rango, A., Roberts, R., 2008. Snowmelt-Runoff Model (Srm) User'S Manual. E. Gomez-Landesa & M. P. Bleiweiss (eds), New Mexico State University, Las Cruces, New Mexico, USA

Matinec, J., 1960. The degree-day factor for snowmelt runoff forecasting. IUGG Gen Assem Helsinki IAHS Comm Surf Waters 51, 468–477

Mauri, L., Straffelini, E., Tarolli, P., 2022. Multi-temporal modeling of road-induced overland flow alterations in a terraced landscape characterized by shallow landslides. Int. Soil Water Conserv. Res. 10 (2), 240–253. https://doi.org/10.1016/j.iswcr.2021.07.004

Mauri, L., Straffelini, E., Cucchiaro, S., Tarolli, P., 2021. UAV-SfM 4D mapping of landslides activated in a steep terraced agricultural area. J. Agric. Eng. Res. 52 (1) https://doi.org/10.4081/jae.2021.1130

Miao, F., Wu, Y., Li, L., Liao, K., Zhang, L., 2019. Risk assessment of snowmelt-induced landslides based on GIS and an effective snowmelt model. Nat. Hazards 97, 1151–1173. https://doi.org/10.1007/s11069-019-03693-2

Mitasova, H., Barton, C.M., Ullah, I., Hofierka, J., Harmon, R.S., 2013. GIS-Based Soil Erosion Modeling. Treatise Geomorphol. Elsevier Inc. 3, 228–258. doi:10.1016/ B978-0-12-374739-6.00052-X

Montgomery, D.R., 1994. Road surface drainage, channel initiation, and slope instability. Water Resour. Res. 30 (6), 1925–1932. https://doi.org/10.1029/94WR00538

Montgomery, D.R., Dietrich, W.E., 1994. A physically based model for the topographic control on shallow landsliding. Water Resour. Res. 30 (4), 1153–1171. https://doi.org/10.1029/93WR02979

Mullem, A., Van, Garen, D., Woodward, D.E., 2004. Snowmelt, in: National Engineering Handbook, Part 630

Obled, C., Harder, H., 1978. A review of snowmelt in the mountain environment, in: Modeling of Snow Cover Runoff, Colbeck S.C., Ra, M. (eds), Proc. Meeting, Hanover, New Hampshire, Sept. 1978: US Army Cold Regions Research and Engineering Laboratory, pp. 179-204

Onate-Valdivieso, F., Bosque Senda, J., 2010. Application of GIS and remote sensing techniques in generation of land use scenarios for hydrological modeling. J. Hydrol. 395 (3–4), 256–263. https://doi.org/10.1016/j.jhydrol.2010.10.033

Palacio Cordoba, J., Mergili, M., Aristizàbal, E., 2020. Probabilistic landslide susceptibility analysis in tropical mountainous terrain using the physically based r.slope.stability model. Nat. Hazards Earth Syst. Sci. 20, 815–829. https://doi.org/10.5194/nhess-20-815-2020

Panday, P.K., Williams, C.A., Frey, K.E., Brown, M.E., 2014. Application and evaluation of a snowmelt runoff model in the Tamor River basin, Eastern Himalaya using a Markov Chain Monte Carlo (MCMC) data assimilation approach. Hydrol. Process. 28, 5337–5353. https://doi.org/10.1002/hyp.10005

Penna, D., Borga, M., Aronica, G.T., Brigandì, G., Tarolli, P., 2014. The influence of grid resolution on the prediction of natural and road-related shallow landslides 2127–2139. doi:10.5194/hess-18-2127-2014

Penna, D., Meerveld, H.J.T., Gobbi, A., Borga, M., Fontana, G.D., 2011. The influence of soil moisture on threshold runoff generation processes in an alpine headwater catchment 689–702. doi:10.5194/hess-15-689-2011

Pijl, A., Reuter, L.E.H., Quarella, E., Vogel, T.A., Tarolli, P., 2020. GIS-based soil erosion modelling under various steep-slope vineyard practices. Catena 193, 104604. https://doi.org/10.1016/j.catena.2020.104604

Pistocchi, A., 2016. Simple estimation of snow density in an Alpine region. J. Hydrol. Reg. Stud. 6, 82–89. https://doi.org/10.1016/j.ejrh.2016.03.004

Pourghasemi, H.R., Pradhan, B., Gokceoglu, C., 2012. Application of fuzzy logic and analytical hierarchy process (AHP) to landslide susceptibility mapping at Haraz watershed. Iran. Nat. Hazards 63, 965–996. https://doi.org/10.1007/s11069-012-0217-2

Raga, M.F., Garcìa-Dìez, I., Campo, J., Viejo, J., Palencia, C., 2020. Effectiveness of a new drainage system for decreasing erosion in road hillslopes. Air, Soil and Water Research 14, 1–12. https://doi.org/10.1177/1178622120988722

Rango, A., Martinec, J., 1979. Application of a Snowmelt-Runoff Model Using Landsat Data. Nord. Hydrol. 10, 225–238

Rasmussen, R., Changhai, L., Kyoko, I., David, G., David, Y., Fei, C., Mukul, T., Michael, B., Jimy, D., Wei, Y., Kathleen, M., Kristi, A., Vanda, G., Greg, T., Ethan, G., 2011. High-resolution coupled climate runoff simulations of seasonal snowfall over Colorado: a process study of current and warmer climate. J. Clim. 24 (2), 3015–3048. https://doi.org/10.1175/2010JCLI3985.1

Reed, M., Kite, S., 2020. Peripheral gully and landslide erosion on an extreme anthropogenic landscape produced by mountaintop removal coal mining. Earth Surf. Proc. Land. 45 (9), 2078–2090. https://doi.org/10.1002/esp.4867

Roussel, J.-R., Auty, D., Coops, N.C., Tompalski, P., Goodbody, T.R.H., Meador, A.S., Bourdon, J.-F., de Boissieu, F., Achim, A., 2020. lidR: An R package for analysis of Airborne Laser Scanning (ALS) data. Remote Sens. Environ. 251, 112061

Royer, T., 2006. Scaling hydrologic impacts from road segments to a small watershed. MSc Thesis in Forest Engineering, Oregon State University

Salesa, D., Terol, E., Cerdà, A., 2019. Soil erosion on the " El Portalet " mountain trails in the Eastern Iberian Peninsula. Sci. Total Environ. 661, 504–513. https://doi.org/10.1016/j.scitotenv.2019.01.192

Sidle, R.C., Bogaard, T.A., 2016. Dynamic earth system and ecological controls of rainfall-initiated landslides. Earth Sci. Rev. 159, 275–291. https://doi.org/10.1016/j.earscirev.2016.05.013.

Sidle, R.C., Ziegler, A.D., 2012. The dilemma of mountain roads. Nat. Geosci. 5, 437–438. https://doi.org/10.1038/ngeo1512

Sidle, R.C., Ghestem, M., Stokes, A., 2014. Epic landslide erosion from mountain roads in Yunnan, China-challenges for sustainable development. Nat. Hazards Earth Syst. Sci. 14, 3093–3104. https://doi.org/10.5194/nhess-14-3093-2014

Siemens, K., Dibike, Y., Shrestha, R. R., Prowse, T., 2021. Runoff projection from an alpine watershed in western canada: Application of a snowmelt runoff model. Water 13, 1199. https://doi.org/10.3390/w13091199

Soulis, K.X., Dercas, N., Papadaki, C., 2014. Effects of forest roads on the hydrological response of a small-scale mountain watershed in Greece. Hydrol. Process. 29 (7), 1772–1782. https://doi.org/10.1002/hyp.10301

Tague, C., Band, L., 2001. Simulating the impact of road construction and forest harvesting on hydrologic response. Earth Surf. Proc. Land. 26 (2), 135–151. https://doi.org/10.1002/1096-9837(200102)26:2<135::AID-ESP167>3.0.CO;2-J

Tahir, A.A., Chevallier, P., Arnaud, Y., Neppel, L., Ahmad, B., 2011. Modeling snowmelt runoff under climate scenarios in the Hunza River basin, Karakoram Range, Northern Pakistan. J. Hydrol. 409, 104–117. https://doi.org/10.1016/j.jhydrol.2011.08.035

Tarboton, D.G., 1997. new method for the determination of flow directions and upslope areas in grid digital elevation models. Water Resour. Res. 33 (2), 309–319. https://doi.org/10.1029/96WR03137

Tarolli, P., Borga, M., Dalla Fontana, G., 2008. Analysing the influence of upslope bedrock outcrops on shallow landsliding. Geomorphology 93 (3–4), 186–200. https://doi.org/10.1016/j.geomorph.2007.02.017

Tarolli, P., Borga, M., Chang, K.-T., Chiang, S.-H., 2011. Modeling shallow landsliding susceptibility by incorporating heavy rainfall statistical properties. Geomorphology 133 (3–4), 199–211. https://doi.org/10.1016/j.geomorph.2011.02.033

Tarolli, P., Calligaro, S., Cazorzi, F., Dalla Fontana, G., 2013. Recognition of surface flow processes influenced by roads and trails in mountain areas using high-resolution topography. Eur. J. Remote Sens. 46, 176–197. https://doi.org/10.5721/EuJRS20134610

Tarolli, P., Pijl, A., Cucchiaro, S., Wei, W., 2020. Slope instabilities in steep cultivation systems: process classification and opportunities from remote sensing. Land Degrad. Dev. 32 (3), 1368–1388. https://doi.org/10.1002/ldr.3798

Thiery, Y., Vandromme, R., Maquaire, O., Bernardie, S., 2017. Advancing Culture of Living with Landslides. Springer Cham (Eds). doi:10.1007/978-3-319-53498-5

Trandafir, A., Ertugrul, O., Giraud, R., McDonald, G., 2015. Geomechanics of a snowmelt-induced slope failure in glacial till. Environ. Earth Sci. 73 (7), 3709–3716. https://doi.org/10.1007/s12665-014-3658-y

Tshering, D., Dorji, L., Shukla, S.K., 2020. A study on subsurface drainage of mountain roads in Bhutan. Lecture Notes in Civil Engineering 72, 185–196. https://doi.org/10.1007/978-981-15-3677-9_18

Vakhshoori, V., Zare, M., 2018. Is the ROC curve a reliable tool to compare the validity of landslide susceptibility maps? Geomatics. Nat. Hazards Risk 9, 249–266. https://doi.org/10.1080/19475705.2018.1424043

Van der Meij, W.M., Temme, A.J.A.M., Lin, H.S., Gerke, H.H., Sommer, M., 2018. On the role of hydrologic processes in soil and landscape evolution modeling: concepts, complications and partial solutions. Earth Sci. Rev. 185, 1088–1106. https://doi.org/10.1016/j.earscirev.2018.09.001

Wemple, B.C., Swanson, F.J., J.J., 2001. Forest roads and geomorphic process interactions, Cascade Range, Oregon. Earth Surf Process Landf, 26 (2),191–204. doi:10.1002/1096-9837(200102)26:2<191::AID-ESP175>3.0.CO;2-U

Wang, C., Liu, B., Yang, Q., Pang, G., Long, Y., Wang, L., Cruse, R.M., Dang, W., Liu, X., Wang, E., 2021. Unpaved road erosion after heavy storms in mountain areas of northern China. Int. Soil Water Conserv. Res. 10, 29–37. https://doi.org/10.1016/j.iswcr.2021.04.012

Wemple, B.C., Jones, J.A., 2003. Runoff production on forest roads in a steep, mountain catchment. Water Resour. Res. 39 (8) https://doi.org/10.1029/2002WR001744

Wi, S., Francina, D., Matej, D., Juan, V., Henry, F.D., Christopher, L.C., 2012. Climate change projection of snowfall in the Colorado River Basin using dynamical downscaling. Water Resour. Res. 48 (5) https://doi.org/10.1029/2011WR010674

Xiang, Y., Lu, L., Jie, C., Chong-Yu, X., Jun, X., Hua, C., Jie, L., 2009. Parameter Uncertainty of a Snowmelt Runoff Model and Its Impact on Future Projections of Snowmelt Runoff in a Data-Scarce Deglaciating River Basin. Water, Advances in Hydrologic Forecasts and Water Resources Management 11 (11), 2417. https://doi.org/10.3390/w11112417

Xu, L., Liu, W., Kong, Y., Zhang, K., Yu, B., 2009. Runoff and water erosion on road side slopes: Effects of rainfall characteristics and slope length. Transp. Res. 14 (7), 497–501. https://doi.org/10.1016/j.trd.2009.05.006

Yang, Z., Cai, H., Shao, W., Huang, D., Uchimura, T., Lei, X., Tian, H., Qiao, J., 2019. Clarifying the hydrological mechanisms and thresholds for rainfall-induced landslide: in situ monitoring of big data to unsaturated slope stability analysis. Bull. Eng. Geol. Environ. 78, 2139–2150. doi:10.1007/s10064-018-1295-5

Yu, W., Zhao, L., Fang, Q., Hou, R., 2021. Contributions of runoff from paved farm roads to soil erosion in karst uplands under simulated rainfall conditions. Catena 196, 104887. https://doi.org/10.1016/j.catena.2020.104887

Zhao, B., Dai, Q., Han, D., Dai, H., Mao, J., Zhuo, L., 2019. Probabilistic thresholds for landslides warning by integrating soil moisture conditions with rainfall thresholds. J. Hydrol. 574, 276–287. https://doi.org/10.1016/j.jhydrol.2019.04.062

CHAPTER 5

MODELLING WINDTHROW EFFECTS ON WATER RUNOFF AND HILLSLOPE STABILITY IN A MOUNTAIN CATCHMENT AFFECTED BY THE VAIA STORM[4]

Luca Mauri,[1] Paolo Tarolli[1]

[1]*Department of Land, Environment, Agriculture and Forestry, University of Padova, Legnaro, Italy*

Keywords: Windthrows, Landslide, Runoff, GIS, HEC-HMS, Modeling

[4] Mauri, L., Tarolli, P. (2022-23). Modelling windthrow effects on water runoff and hillslope stability in a mountain catchment affected by the VAIA storm. ***Paper under review***.

5.1 Abstract

Windthrows represent one of the most relevant natural disturbances affecting forest landscapes. Airborne Laser Scanning (ALS) topographic data increased the opportunity to investigate in details physical processes at the catchment scale. Moreover, the use of topographically-based hydrological and geomorphological models led to quantify runoff alteration due to windthrows-driven land use changes and detect the occurrence of land degradative processes at sub-basin scale. Despite the renowned effects of blowdowns in affecting environmental properties of forest areas, accurate investigations about their role in varying local runoff regime over time is still obscure. The possibility to foresee the activation of terrain instabilities due to windstorm occurrence is likewise unclear. This research aims to investigate the interaction between windthrows, runoff alterations and hillslope failures affecting a landslide-prone, wind-damaged mountain catchment (northern Italy). Hydrological HEC-HMS and geomorphological RESS models were applied in this regard. The role of windthrows in altering runoff regimes and hillslope stability was investigated starting from the elaboration of ALS-derived points clouds acquired before (pre-event scenario) and after (post-event scenario) the occurrence of the Vaia storm. Digital Terrain Models (DTMs) were therefore elaborated for the two scenarios, to compare daily runoff variations and predict the activation of terrain instabilities looking land use changes driven by the blowdown event at sub-basin detail. Results attested the key role of windstorm in altering local runoff values and encouraging the activation of the observed shallow landslide. The correlation between windthrows occurrence and runoff alterations was statistically validated by performing regression analysis, while the accuracy of instabilities predictions was tested through the Distance to Perfect Classification (D2PC) index and True Skill Statistic (TSS) score. This research could be a valid tool for investigate similar issues at wider scale, also providing suggestions for improving and promoting efficient interventions in wind-disturbed forest areas.

5.2 Introduction

Among the several natural disturbances affecting forested landscapes such as fires, landslides and biotic hazards (Edburg *et al*., 2012; Seidl and Rammer, 2017), windstorms represent the most relevant one (Laurin *et al*., 2021). Despite such events have a key role in term of forest ecology and natural dynamics (Ulanova, 2000; Turner, 2010; Seidl and Rammer, 2017), more than half of primary damages distressing forest ecosystems are due to wind (Schelhaas, 2008; Dalponte *et al*., 2020). The past decades were characterized by an increasing occurrence of severe windstorms (Usbeck *et al*., 2010; Laurin *et al*., 2020), with an estimated yearly average volume of European forest lost due to wind of around 40 million of cubic meters (Motta *et al*., 2018; Gennari *et al*., 2021; Laurin *et al*., 2021). In this regard, the recent decrease of anthropogenic pressure on forests further encouraged their susceptibility to similar natural disturbances (Bottero *et al*., 2013). Windthrow dynamics are driven by several factors, such as (i) topography, (ii) soil properties, (iii) stand conditions, (iv) previous disturbances, (v) trees species, (vi) climate and (vii) forest management practices (Everham and Brokaw, 1996; Albrecht *et al*., 2012; Mitchell, 2013; Seidl *et al*., 2014). At the same time, windthrows involve several issues like (i) canopy destruction, (ii) soil degradation, (iii) reduction of slope stability, (iv) alteration of hydrological properties of the forests, (v) changes of landscape patterns and (vi) limitation of ecosystem services (Lingua and Marangon, 2022; Ulanova, 2000). At watershed scale, water runoff regimes and water balance are generally influenced by several factors, such as (i) land conversion, (ii) clear cut, (iii) deforestation, (iv) alteration of canopy structure due to natural disturbances (e.g., wildfires and windstorms) and (v) climate variability, as well as subsurface water flows processes, directly regulating the connectivity of saturated areas at the soil-bedrock interface (Uhlenbrook, 2006; Li *et al*., 2018; Holko *et al*., 2012; Lanni *et al.,* 2013). In this regard, canopy cover removal due to natural disturbances commonly led to several issues, specifically in hydrological terms such as (i) increasing infiltration of water within the soil layers and soil water storage, (ii) more relevant snowpack accumulation during the winter season, (iii) increasing hydrologic yields and peak flows over time (Du et al., 2016). In concert with the above issue, sediment yield and widespread translocation of soil particles notable increase after windthrows of forest stands (Constantine *et al*., 2012), thus encouraging soil destabilization especially on steep slopes areas (Gerber *et al*., 2002). Specifically, landslides activation and windstorms are strictly connected, mainly due to the jointly interaction among several issues associated to windthrows, such as (i) loss of root reinforcement and strength, (ii) increasing exposure of soil, (iii) dislodgment of rocks, (iv) weakening of root system and (v) deviation of water overland flows across the hillslope (Iverson, 2000; Keim

and Skaugset, 2003; Mcdonald, 2007; Wohlgemuth *et al*., 2017; Bebi *et al*., 2019). Recently, the development of Geographic Informatic Systems (GIS), softwares and codes notably increased our possibility to investigate complex hydrological and geomorphological dynamics at watershed and hillslope scale. In this regard, hydro-geomorphological models allowed scientists to perform detailed analysis of landscape changes, improving water management and preventing the occurrence of natural hazards over time. Similarly, Airborne Laser Scanner (ALS) using the Light Detection and Ranging (LiDAR) technology led to the acquisition of spatial environmental point cloud data at basin detail. In particular, the adoption of LiDAR-ALS let researchers to elaborate multi-temporal Digital Terrain Models (DTMs) at centimeter scale, in order to perform geomorphological and hydrological analysis on degraded areas (Cucchiaro *et al*., 2020; Guo *et al*., 2020; Jones and Hobbs, 2021). Looking at the above considerations, an analysis of the hydrologic response of not harvested windthrown forest in terms of runoff alterations at the sub-basin scale is actually lacking in the scientific literature. In addition, the possibility to predict the activation of hillslope instabilities due to land use changes driven by the blowdown event is still unclear. This research aims therefore to analyse the role of windthrows in altering water runoff regimes and hence encouraging the activation of slope instabilities affecting a landslide-prone mountain basin (northern Italy). Accordingly, a novel modeling procedure is proposed. LiDAR-derived point clouds were processed and elaborated to obtain 1m DTMs for both the stand-forest condition (i.e., pre-event scenario) and windthrown forest condition (i.e., post-event scenario). DTMs were therefore used to perform the proposed modeling analysis. Daily runoff values were firstly quantified at sub-basin scale by using the Hydrologic Engineering Center-Hydrologic Modelling System model (HEC-HMS; US Army Corps of Engineers, 2000). HEC-HMS is a semi-distributed, event-scale model that simulates rainfall-runoff processes at sub-basin detail focusing on land use distribution within the watershed. Then, the Road Erosion Steady-State model (RESS; Borga *et al*., 2005; Dietrich *et al*., 1992; Montgomery and Dietrich, 1994) was implemented looking at its capabilities to provide predictive mapping of instability susceptibility areas considering land use changes affecting the study site. Models' outcomes were finally statistically validated. The proposed research fills the gap in the scientific knowledge regarding the possibility to quantify the effects of a windstorm on local runoff regimes over time, as well as foresee the occurrence of hillslope instabilities due to land use changes driven by the windstorm, through a novel low-cost modeling approach.

5.3 Study area

The study area is a mountain watershed located close to the Livinallongo del Col di Lana municipality, in the Veneto region, northern Italy (Fig 5.1a). It is mainly composed by Norway spruce (*Picea abies* (L.) H. Karst.) and secondary by European larch (*Larix decidua* Mill.). The study area has a predominantly cold alpine climate, with a temperature ranging from a maximal mean annual of 10 °C and a minimal mean annual of -0.5 °C, and a mean annual temperature equal to 3.9 °C. The annual average rainfall is equal to 1031 mm (data recorded by the Falzarego weather station in 2019, 4 km away as the crow flies from the study area). The basin has an overall extension of 1.393 km^2 (equal to 139.3 ha), an average slope equal to 36.6° (between a minimum of 0.03° and a maximum of 85.6°) and an average elevation equal to 2004 m a.s.l. (ranging from a minimum of 1517 m a.s.l. and a maximum of 2512 m a.s.l.). Snow cover generally persists from late October to May. The basin is mainly covered by forest (deciduous forest up to an altitude of about 2100 m a.s.l), with an increasing presence of grassland and rocky areas in the upper part (higher altitudes). An unpaved road crosses the study area at the bottom, with a total length of about 1.5 km and an average slope equal to 16.7°. The road is characterized with wooded cross ditches along it.

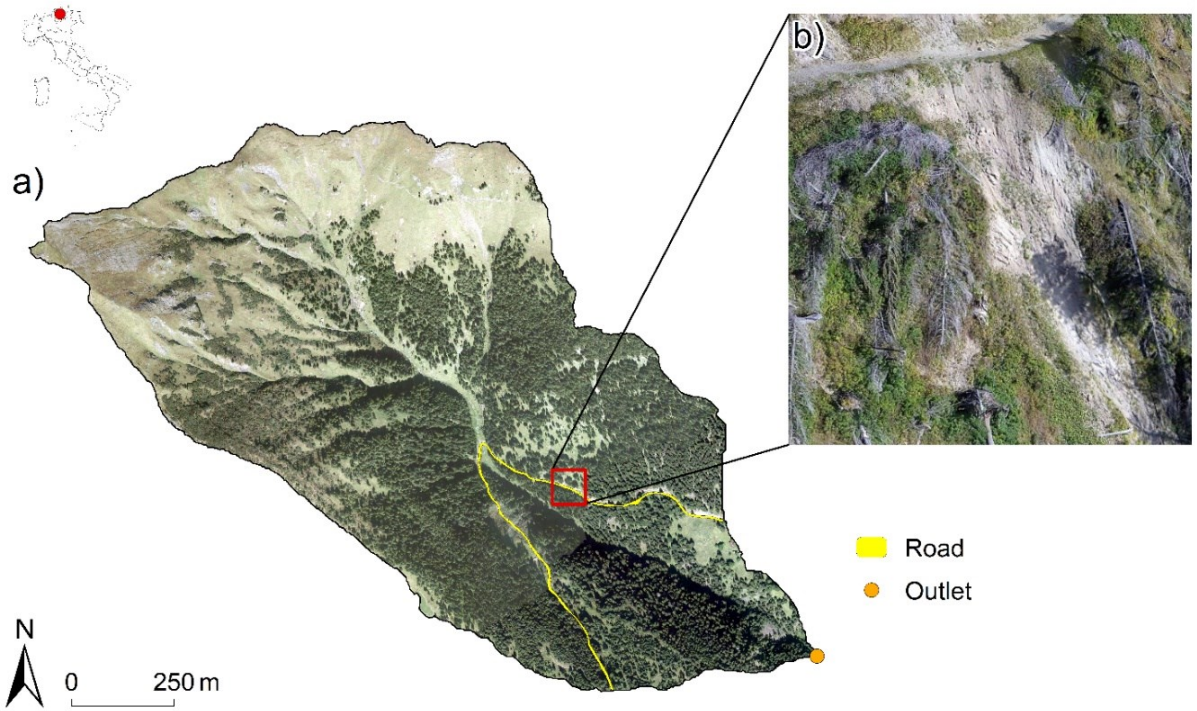

Figure 5.1 *Overview of the study area (a) and focus on the shallow landslide observed during filed surveys conducted in 2019 (b).*

Field surveys were conducted in October 2019, about a year after the occurrence of the renamed "Vaia" storm, a strong depression originated between the Balearic Islands and Sardinia that affected the eastern Alps from the 27th until the 30th of October 2018, causing extreme winds and heavy rains. During the windstorm, precipitation peaks ranging from 30 to 50 mm/h, cumulated rainfall of more than 700 mm and wind's speed of around 200 km/h were recorded (Pellegrini *et al*., 2021). The Vaia storm triggered widespread windthrows in the north-east Alps of Italy, with an estimated extension of affected forests of more than 50,000 ha and windthrown woods of around 9 million m^3 (Chirici *et al*., 2019; Giannetti *et al*., 2021). In addition, field surveys carried out in October 2019 revealed the activation of a landslide (Fig. 5.1b), that involved the slope below the unpaved road. Moreover, several failures were noticed on the disturbed-hillslope above the landslide area. Widespread windthrows were also detected around the failure zones.

5.4 Material and methods

5.4.1 Input acquisition and data elaboration

5.4.1.1 Overview of the observed landslide

Field inspections conducted in 2019 in the windthrown area revealed the activation of a landslide in the lower part of the catchment. Landslide's features were manually measured using a surveyor tape in order to obtain a fist overview of the failure area. Accordingly with the definitions proposed by Dikau *et al*. (1996), Sidle and Bogaard (2016) and Thiery *et al*. (2017), the landslide occurred in the study area is identifiable as a shallow translational landslide, both considering its steepness and dimensions. The extension of the landslide is about 505 m^2, with a perimeter equal to 133 m and an average slope equal to 44.2°. The main scarp height is equal to 1.75 m; the maximum width between landslide's flanks is equal to 18.2 m; the length of the landslide zone, from its crown to the respective toe is equal to 53.5 m (Cruden and Varnes, 1996). The surface affected by the shallow landslide is characterized by the widespread location of low herbaceous cover and the presence of numerous windthrown trees. The landslide occurred below a section of the unpaved road crossing the wind disturbed hillslope.

5.4.1.2 ALS-point clouds processing

ALS-surveys conducted in 2015 and 2019 led to elaborate pre-event and post-event DTMs and *Canopy Height Models* (CHMs) at the catchment scale. Supplementary Table 5.5 summarizes all the parameters of ALS-flights. In this regard, original raw ALS data were firstly classified into ground (soil) and overground (vegetation and infrastructures) points by applying specific classification algorithms of the Terrasolid software combined with the R-studio *lidR* package (Roussel *et al*., 2020). The classified point clouds were finally filtered in Cloud Compare in order to remove further noises due to errors affecting the classification process. In particular, the Statistical Outlier Removal (SOR) filter, based on the Point Cloud Library (PCL) was applied. Point clouds co-registration was hence computed through the Point Pairs Picking co-registration tool available in the Cloud Compare software (https://www.danielgm.net/). In this regard, cross ditches located along the road network and rocky areas were upstream of the watershed were used as stable points for point clouds processing. Regarding the pre-event scenario, the *grid_terrain* R-studio package and the classification-based *Cloth Simulation Filter (csf)* algorithm for spatial data elaboration (Zhang *et al*., 2016) were used for DTM computation. Looking at both point cloud density and average point

density, pre-event DTM was elaborated from *ground* points with a resolution equal to 1m, that efficiently allowed to appreciate local geomorphological features within the catchment. The classification-based *knnidw* algorithm for spatial data interpolation (Roussel *et al*., 2020) was used in this regard. Crowns of standing trees and their respective location were extracted and rasterized through the *silva2016 Individual Tree Segmentation* algorithm (Silva *et al*., 2016). Pre-event 1m CHM was then created by applying the *grid_canopy* function of *lidR* package and normalized on the obtained DTM through the *normalized_height* tool. Differently, post-event DTM was processed after detecting the location of standing trees in the watershed and extracting the windthrown areas from the respective ALS point cloud. Specific *lidR* functions were used and several tests were conducted to derive optimal lower and upper height thresholds for both standing trees detection in windthrown conditions and DTM creation. In this connection, the *find_trees* tool was used for individual tree-tops identification by applying the *lmf* algorithm (Popescu and Wynne, 2004). The location of standing trees and their crowns were extracted as computed for the pre-event scenario. Post-event 1m CHM was elaborated and masked looking at tree-tops detection and crowns delineation through the *clean_raster* tool available in the *LiDARtRee* R-studio package (Monnet, 2019). Residual errors deriving from such an automatic extraction were solved by manually filtering false standing trees were uprooted plants overlapped each other and removing low biomass on the ground such as stumps, dead branches and roots plates. Manual filtering tools available in Cloud Compare were used in this regard. Finally, 1m post-event DTM was created using the *grid_terrain* tool and Spatial Interpolation *tin* algorithms implemented in R environment. Looking at windthrown extractions and referring to the spatial distribution of standing trees in pre-event conditions, the percentage of blowdown areas was estimated for each sub-basin.

5.4.1.3 Hydrologic Modelling System (HEC-HMS)

The application of HEC-HMS required as a first step the adoption of the GIS-based pre-processor tool HEC-GeoHMS (Fleming and Doan, 2003), needed to disaggregate the watershed into several interconnected sub-basins looking at the delineation of the drainage network. ALS-derived DTMs were used in this regard, also deriving the topographic attributes of each sub-basin. Project file resulted from HEC-GeoHMS elaborations was therefore set as basic input for HEC-HMS simulations. Considering the objectives of this research, simulations period was set ranging from April to October, therefore focusing on snow-free conditions. Supplementary Table 5.6 summarizes input variables for each component constituting the HEC-HMS model. Terrain processing was firstly implemented starting from ALS-derived DTM by defining stream network, junctions and reaches for each sub-basin composing the watershed. In particular, several processing step such as (i) fill sinks,

(ii) elaboration of flow direction and accumulation, (iii) stream definition, (iv) drainage line processing and (v) outlet definition were iteratively computed by using the GIS-based Arc-Hydro and HEC-GeoHMS tools. Discretization method defined how sub-basins discretization is implemented in HEC-HMS. Looking at suggestions provided by model's developers (US Army Corps of Engineers, 2000) the *Structured Discretization* method was set for model simulations, in order to create a Cartesian grid within the boundary of each sub-basin. The selected discretization method was implemented to efficiently visualize spatial discrete elements within the watershed, as well as to sample values from geospatial data if needed (US Army Corps of Engineers, 2000). A grid cell size equal to 50 m (default minimum) was set (EPSG 32632 coordinate system-WGS 84 / UTM zone 32N). The presence of forest within the watershed was considered by setting the parameters of the Canopy method required by HEC-HMS. Basing on the available literature and looking at trees' species and physiology, the canopy water storage capacity was therefore estimated (i.e., the amount of precipitation reaching the ground surface net of canopy interception and evapotranspiration). The *Gridded Simple Canopy* method was implemented in order to consider canopy water storage variability due to the spatial distribution of standing trees and windthrown ones within the catchment. Maximum canopy storage capacity (S^c_{max}) was calculated considering its relationship with the *Leaf Area Index* (LAI) parameter, as suggested by the Equation 5.1 (Sibanda *et al*., 2019):

$$S^c_{max} = 0.935 + 0.498 \cdot LAI - 0.00575 \cdot (LAI)^2 \quad (5.1)$$

Assuming an increasing trees defoliation one year after the windthrown occurrence (Li *et al*., 2019) and considering further parameters such as trees ages, species and LAI, the maximum canopy water storage was assumed equal to 3.5 mm for stand forest, 1.5 mm for blowdown forest and 0.7 mm for grassland, in line with outcomes provided by Llorens and Gallart (2000), Taylor and MacLean (2007), Thimonier *et al*. (2010); Pokorný and Stojnič (2012) and Li *et al*. (2019). In addition, crop coefficient was set around 0.7 (Corbari *et al*., 2017; Kuriata-Potasznik and Szymczyk, 2016; Sridhar, 2017), while initial water storage was set equal to 0.0 (default value assuming no percentage of canopy storage full of water at the beginning of the simulations; US Army Corps of Engineers, 2000). The Soil Conservation Service Curve Number (SCS-CN) method was selected to estimate precipitation excess and water losses at sub-basin scale depending on land use and soil types. In particular, the *Gridded SCS-CN Loss* method was used in model simulations, applying different CN values on a grid cell basis. CN grid was hence elaborated looking at the suggestion provided by model's developers (US Army Corps of Engineers, 2000), combining soil type and land cover data. Soil types were therefore reclassified into four hydrological soil groups with increasing potential for generating runoff

(i.e., HSHs groups A, B, C and D; USDA-SCS, 1972) and specific values for different land cover information were assigned referring to the tables reported in the Technical Release 55 (TR-55; US Army Corps of Engineers, 2000). Following the suggestions provided by model developers, the *CN Lookup Table* was finally elaborated relating land use and hydrological groups to the respective gridded CN values at sub-basin scale (Faouzi *et al*., 2022). Water accumulation in depression storages of the terrain is considered by HEC-HMS model by setting the parameters of the Surface method, in order to properly simulate water accumulation and infiltration of water. In this regard, the *Gridded Simple Surface* method was implemented, in order to rasterize initial and maximum water storage depending on soil type and land cover conditions at sub-basin detail. In particular, initial water storage stands for the percentage of the water stored by the soil at the beginning of the simulation, while maximum water storage represents the maximum amount of water that can be hold on the soil surface before runoff begins (US Army Corps of Engineers, 2000). Initial storage was set to 0%, while maximum storage was set around 3.5 mm for lawn areas, 1.3 mm for impervious surface (including rocky areas and the unpaved road), 7.5 mm for standing forest and 4.8 mm for windthrown areas (Xiao and McPherson, 2016; Qiao *et al*., 2017; American Society of Civil Engineers, 2018). HEC-HMS model also needs to specify the Transform method, to efficiently calculate surface runoff within each sub-basin. Water runoff calculation was therefore achieved by adopting the *ModClark* algorithm, a modified version of the Clark unit hydrograph conceptual transformation method (Clark, 1945) able to overcame the time-area curve implementation by computing the travel time index for each cell of the sub-basin. Time of concentration (i.e., the maximum travel time of water) was estimated for each cell of sub-basins in line with the Natural Resources Conservation Service (NRCS) *TR-55* methodology, by applying the Equation 5.2:

$$T_{cell} = T_c \cdot \left(\frac{d_{cell}}{d_{max}}\right) \tag{5.2}$$

where T_c is the time of concentration for each sub-basin which depends on basin length and slope (Knebl *et al*. (2005), d_{cell} is the travel distance from each cell to the sub-basin outlet, d_{max} is the travel distance from the furthest cell to the sub-basin outlet. Storage coefficient (R) needs also to be calculated, representing the temporary precipitation excess stored in the sub-basin as it drains to the respective outlet (Clark, 1945). The relationship between R and T_c is expressed by the Equation 5.3 and led the computation of the storage coefficient required by the selected Transform method (Fleming and Doan, 2003) :

$$\frac{R}{T_c+R} = 0.65 \tag{5.3}$$

Since HEC-HMS model was applied for simulating long term hydrologic response of the catchment at sub-basin level, an evapotranspiration method was markedly required (US Army Corps of Engineers, 2000). In this regard, the *Hamon* evapotranspiration method was applied (Hamon, 1963) suitable for the estimation of potential evapotranspiration in data-limited situations. The Hamon coefficient was hence set equal to the default value of 0.16 $mm \cdot g^{-1}m^{-3}$. In line with the aims of this research, daily average precipitation and temperature data recorded by the weather station in 2015 were used as input for HEC-HMS pre-event and post-event simulations.

5.4.1.4 Road Erosion Steady-State model (RESS)

RESS model evaluates possible unstable zones affected by road-related drainage modifications, by mapping the critical rainfall before and after drainage modifications due to road network (R_{pre} and R_{post} respectively; Borga *et al*., 2005; Mauri *et al*., 2022). Therefore, the *Relative Impact* (RI) index is computed by the Equation 5.4:

$$RI = \frac{R_{pre} - R_{post}}{R_{pre}} \quad (5.4)$$

RI ranges between 0 and 1. In particular, RI is equal to 0 when runoff dynamics are not influenced by the road; RI is major than 0 if road's drainage systems concentrate and encourage water flows hence decreasing the critical rainfall; RI is minor than 0 if drainage systems cause the reduction of saturated water flows therefore increasing critical rainfall values (Borga *et al*., 2005). Supplementary Table 5.7 reports inputs required for RESS simulations. The model firstly needs for DTM without the presence of the road (Borga *et al*., 2005). Pre-event DTM (standing forest, no-landslide conditions) was therefore used for both pre-event and post-event RESS simulations, to analyse the influence of blowdown-induced land use changes in the potential activation of hillslope instabilities in predictive terms. In this regard, since the road was already present during the conducted ALS-surveys, the methodology proposed in Mauri *et al*. (2022) was applied in DTMs editing procedure assuming the absence of the road. *Extract by Mask*, *Buffer*, *Generate Points Along Lines*, *Extract Multi Values to Points* and *Topo to Raster* ArcGIS tools were respectively used to mask the road area, extrapolate elevation quotes along the hillslope upstream and downstream the road and create an interpolated surface at the road boundaries. The absence of the road was therefore simulated by merging such an interpolated surface to the original DTM, in order to create a modified and hydrologically accurate terrain model for both the scenarios (Esri, 2021). The location of the road was specified by setting x and y coordinates of a series of points placed along it, extracted through the *Add X and Y coordinates* ArcGIS tool. Similarly, the location of drainage systems was set by defining their X and Y coordinates

and setting a value (p) ranging from 0 to 100%. The p value represents the percentage of water effectively deviated by each cross ditches placed along the road (Borga *et al*., 2005). Since on field observations made in 2019 revealed the almost total occlusion and deterioration of wooden cross ditches, a constant value of 20% was set as p for each of them. Road width was measured equal to 5 m and the relative road cut depth (i.e., value describing the potential interception of each road cell at the foot of the upstream slope) was set equal to the default value of 0.5 m. Geotechnical parameters were assumed in line with values recorded in similar conditions and with the suggestions provided by model developers (Borga *et al*., 2002, 2005; Bischetti *et al*., 2009; Tarolli *et al*., 2011; Penna *et al*., 2014; Vergani *et al*., 2016; Maedeh *et al*., 2018). Looking at pre-event scenario, saturated soil density (ρ_s) was set equal to 1800 kgm^{-3}, soil depth (z) to 1 m, internal friction angle (ϕ) to 35 degrees, soil transmissivity (Tr) to 30 m^2s^{-1} and soil cohesion (Coh_s) to 1000 $kg \cdot m^{-1}s^{-2}$. The presence of standing trees was considered by setting specific values for root cohesion (Coh_r) and vegetation surcharge (W) parameters, respectively equal to 3000 $kg \cdot m^{-1}s^{-2}$ and 2000 $kg \cdot m^{-1}s^{-2}$ (Schmidt *et al*., 2001; Dhakal and Sidle, 2003; Sakals and Sidle, 2004; Bischetti *et al*., 2009; Masi *et al*., 2021). Considering the aims of the presented research, the maximum rainfall peak recorded by the Falzarego weather station in 2019 (equal to 72.2 $mm \cdot h^{-1}$) was set as rainfall input for predictive soil instability RESS simulations. The corresponding intensity increment step was set equal to the default value of 0 $mm \cdot h^{-1}$. Finally, water density was set equal to 1000 $kg \cdot m^{-3}$ and the *D-infinite* flow direction algorithm was adopted (Tarboron, 1997). Moreover, post-event RESS simulations were implemented by changing specific vegetation and soil parameters. In line with outcomes provided by previous researches focused on wind-disturbed forested catchments, Coh_s was et equal to 1000 $kg \cdot m^{-1}s^{-2}$, Coh_r equal to 1500 $kg \cdot m^{-1}s^{-2}$ and W equal to 500 $kg \cdot m^{-1}s^{-2}$ (Sidle, 1991; Gray, 2009; Dhakal and Sidle, 2003; Sakals and Sidle, 2004; Buma and Johnson, 2015; Vergani *et al*., 2016).

5.4.2 Statistical analysis

5.4.2.1 HEC-HMS runoff quantification

Statistical analysis of HEC-HMS results was performed by using specific codes implemented in R environment. In this regard, statistical hypothesis testing was carried out through the computation of normality test and two-sample *Student t-test* assuming unequal variances. Normal distribution of daily runoff values for both the pre-event and post-event scenarios was firstly checked applying the Kolmogorov-Smirnov test (Smirnov, 1939), given the large data samples derived from model

simulations (Nguyen, 2018). Statistical differences between the two scenarios were investigated, in terms of quantitative runoff alteration at each sub-basin's outlet. Therefore, student t-test was computed by identifying the null hypothesis (H_0) and the alternative one (H_1). H_0 assumed that windthrow-driven land use changes affecting the study area did not influence runoff dynamics in the disturbed catchment, while H_1 considered the effective role of Vaia storm in runoff alterations at sub-basin scale. Finally, a regression analysis was carried out to further investigate the relationship between land use changes affecting each sub-basin and runoff alterations modeled in HEC-HMS. The R-studio *lm* function was used to fit the regression model and export statistical outcomes.

5.4.2.2 RESS instability maps

In line with the aims of this research, statistical validation of RESS outcomes was computed looking at the wind-disturbed, landslide-prone hillslope close to the unpaved road located in the watershed. Post-event survey performed in 2019 led to delineate and rasterize terrain instabilities detected at the degraded hillslope upstream and downstream the road. Following the methodology proposed by Borga *et al*. (2005) and successively applied in Mauri *et al*. (2022), stable and unstable areas were classified as two different classes, given a threshold identified by the model as a linear relationship between soil wetness index and ground slope (Montgomery and Dietrich, 1994; Borga *et al*., 2002b). Observations and model prediction were hence assigned to one of the two classes previously defined. *True Positive Rate* (TPR) and *False Positive Rate* (FPR) were calculated through the following Equations 5.5 and 5.6:

$$TPR = \frac{TP}{TP+FN} \tag{5.5}$$

$$FPR = \frac{FP}{TN+FP} \tag{5.6}$$

where *TP* stands for true positives (where observed unstable zones are predicted as unstable), *FN* stands for false negatives (where observed unstable cells are predicted as stable), *FP* stands for false positives (where observed stable cells are predicted as unstable) and *TN* stands for true negatives (where observed stable cells are predicted as stable). The performance of RESS model to predict the potential activation of terrain failures depending on windthrows-driven land use changes was therefore investigated by computing the *Distance to Perfect Classification* index (D2PC) and *True Skill Statistic* score (TSS); (Formetta *et al*., 2016). The former estimates the distance between a supposed perfect point having coordinates (0,1) and the point expressed by coordinates (FPR, TPR) calculated from model outcomes. D2PC ranges between 0 (best value) to 1 (worst value). The latter measures the capability of the model to efficiently discriminate unstable areas from non-unstable

zones inside the study area. TSS ranges from -1 (worst value) and 1 (best value). D2PC index was calculated by applying the Equation 5.7, while TSS score was computed through the Equation 5.8:

$$D2PC = \sqrt{(1 - TPR)^2 + FPR^2} \tag{5.7}$$

$$TSS = \frac{(TP*TN)-(FP*FN)}{(TP+FN)\cdot(FP+TN)} = TPR - FPR \tag{5.8}$$

5.5 Results

5.5.1 ALS-point clouds elaboration

The processing procedure of ALS point clouds allowed to elaborate pre-event and post-event 1m DTMs. In this regard, the co-registration of classified point clouds was computed with a RMSE co-registration error equal to 0.055 m. CHMs elaborated through the post-processing procedure of point clouds are shown in the Supplementary Figure 5.10. Land use changes caused by the Vaia storm were further investigated by extracting the spatial distribution of standing and windthrown areas at the catchment scale. Such an automatic procedure led therefore to the spatialization of key parameters required for runoff computation such as CN, windthrows distribution, canopy and surface water storage at the sub-basin detail. The elaboration of standing trees extraction is reported in the Figure 5.2. In particular, Fig. 5.2a shows the spatial distribution of standing trees within the entire watershed. A focus on the hillslope involved in the landslide occurrence (black box in Fig. 5.2a) is reported in the Fig. 5.2b-c, the former showing the ALS-derived orthophoto, the latter highlighting the spatial distribution of standing trees. Residual errors in stand forest spatialization and mapping mainly derived from inaccuracies of thresholds and parameters setting during the extraction procedure.

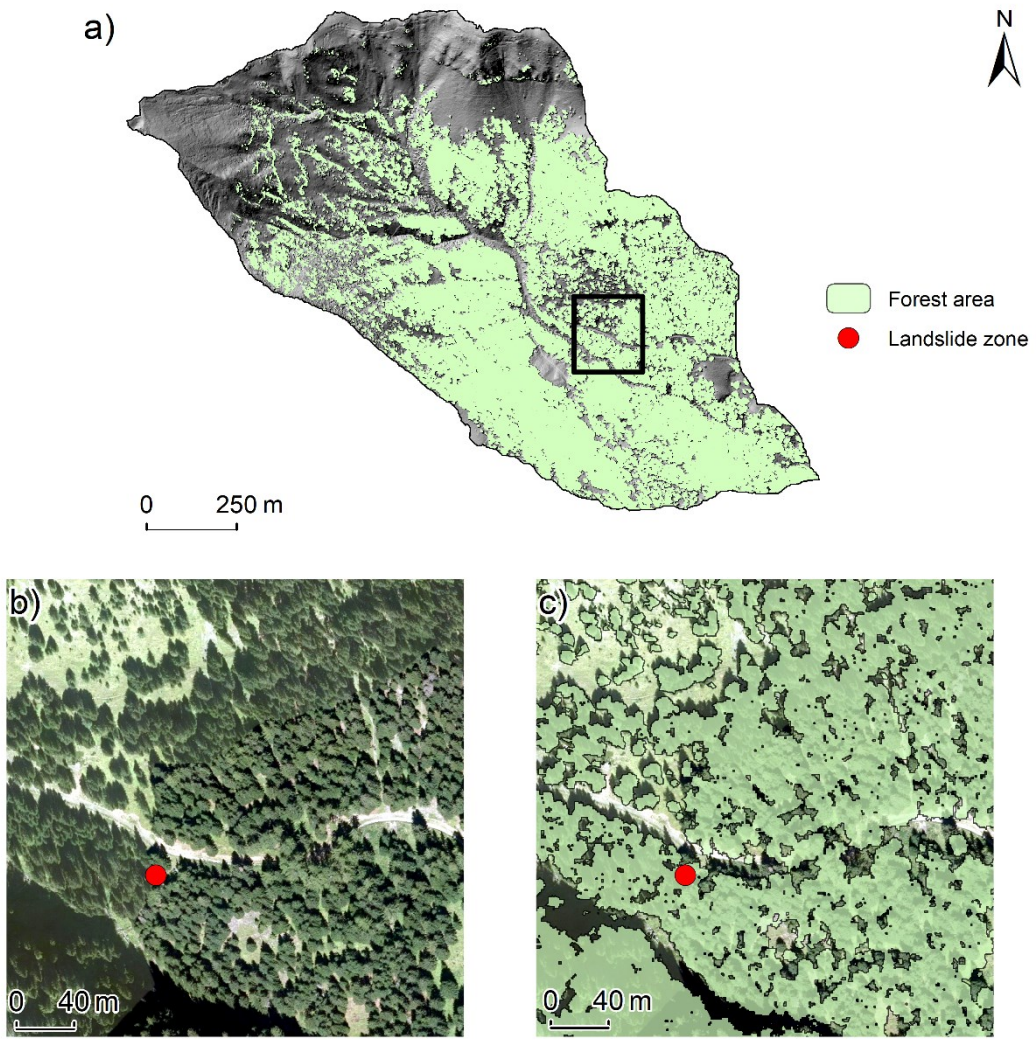

Figure 5.2 *Overview of stand forest within the watershed (Fig. 5.2a) and focus on the distribution of standing trees at the hillslope (black box) involved in the occurrence of the shallow landslide (red dot; Fig. 5.2c). Fig. 5.2b shows the aerial orthophoto acquired during ALS-surveys in 2015, before the occurrence of the Vaia storm (pre-event scenario).*

The extraction of the distribution of blowdown trees is presented in the Figure 5.3. In particular, Fig. 5.3a shows the distribution of windthrows within the watershed, while in Fig. 5.3c is reported a focus of windthrown trees close to the hillslope involved in the activation of the shallow landslide. Small inaccuracies in the spatial mapping of windthrown trees unavoidably resulted from parameters setting in the remote extraction procedure.

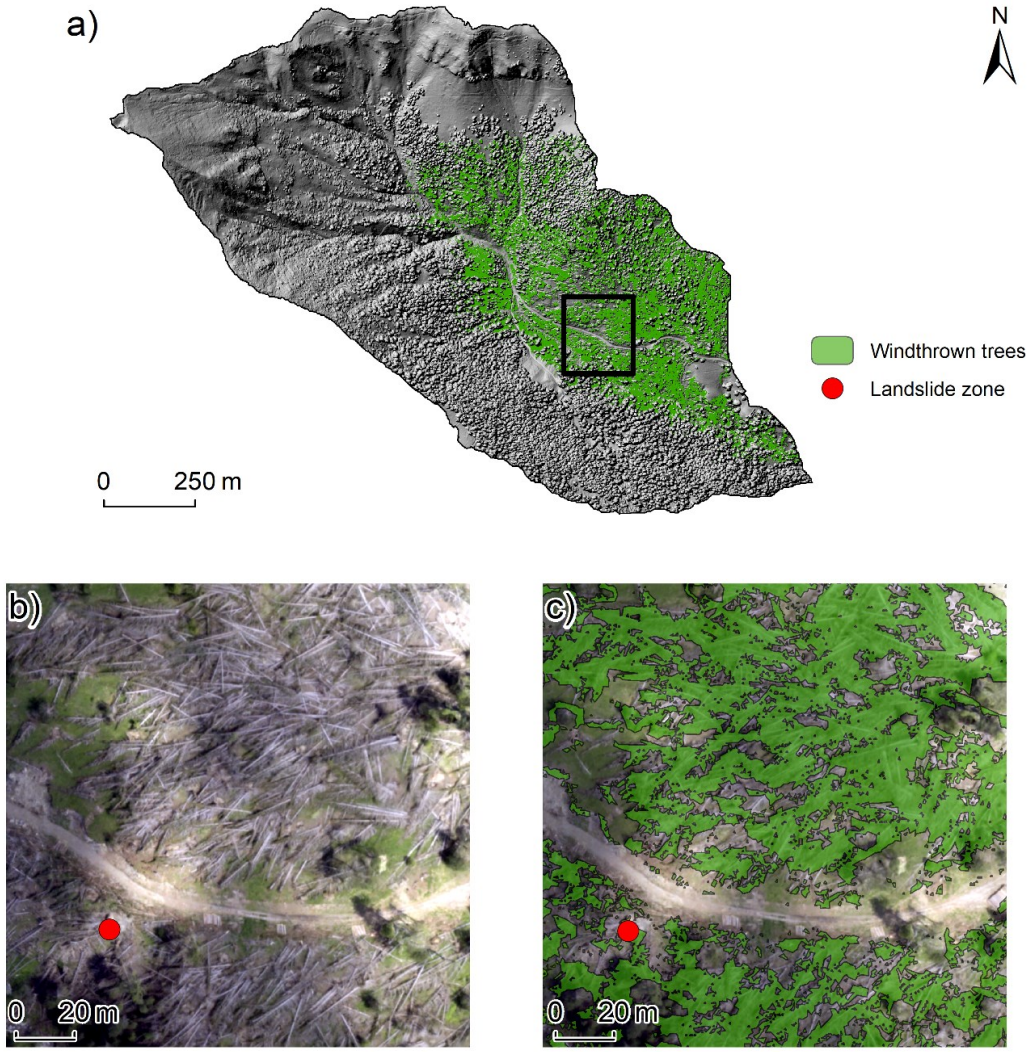

Figure 5.3 *Overview of windthrows within the watershed (Fig. 5.3a) and focus on the windthrown trees located at the hillslope (black box) involved in the occurrence of the shallow landslide (red dot; Fig. 5.3c). Fig. 5.3b shows the aerial orthophoto acquired during ALS-surveys in 2019, after the occurrence of the Vaia storm (post-event scenario).*

Land use changes affecting the study area translated into a variability of CN values, accordingly with the spatial mapping of standing trees and windthrown ones. In this regard, the combination and classification of land types and soil cover led to the discretization of CN values respectively for pre-event and post-event scenarios. Spatial mapping of CN values computed on a grid cell basis for both pre-event and post-event scenarios is reported in the Supplementary Figure 5.11. Looking at the available literature, CN values equal to 62.5 and 82.5 were set respectively for standing and windthrown forest (Yeo *et al*., 2004; US Army Corps of Engineers, 2020; Faouzi *et al*., 2022). Analogously, pre-event and post-event spatial gridded mapping of canopy and surface water storage capacity are respectively reported in the supplementary Figure 5.12 and 5.13.

5.5.2 HEC-HMS model

Starting from DTMs computed for pre-event and post-event scenarios, the watershed was divided into 24 sub-basins (Figure 5.4), in order to estimate daily runoff values at the respective outlet looking at land use changes induced by windthrows.

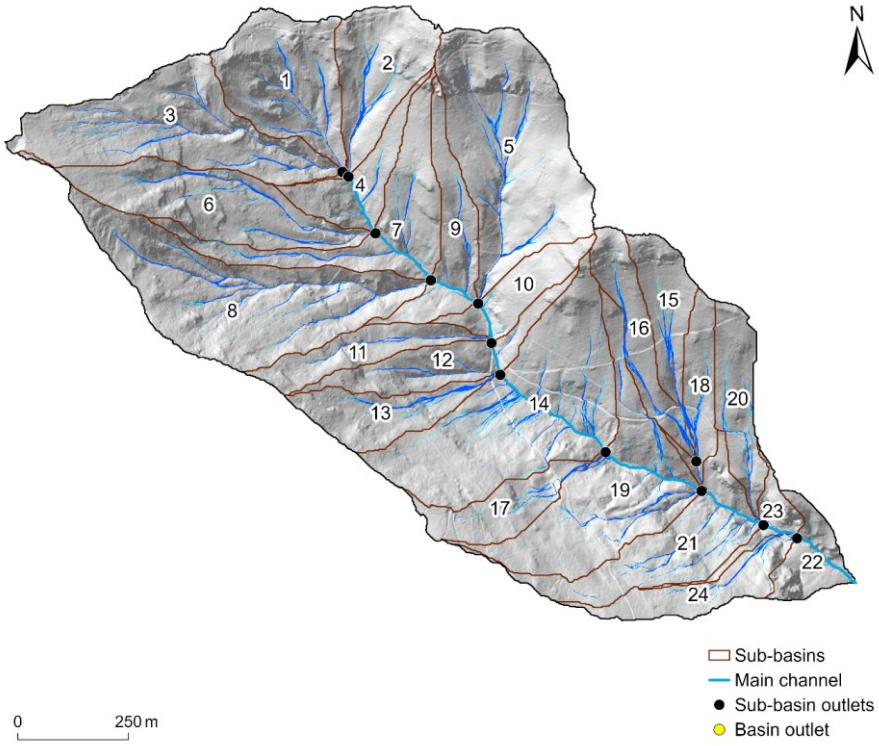

Figure 5.4 *Sub-basins (brown polygons) delineated through the HEC-GeoHMS tool. The figure shows sub-basins outlets (black circles), watershed outlet (yellow circle), the main channel (cyan line) and D-inf water flow directions within the watershed (blue paths). Since the small extension and the closeness of sub-basins, their respective outlets partially overlap in the figure. ALS-derived DTM is reported in background for enhance the visualization of the map.*

The delineation of each sub-basin was obtained considering several elements, such as stream networks, junctions and sub-basins outlets, as well as sub-basin centroids and longest flow paths elaborated with the HEC-GeoHMS tool of ArcGIS. Details of geomorphological parameters of each sub-basins considered for model simulations are summarized in the Table 5.1.

Table 5.1 *Geomorphological parameters of sub-basins computed for HEC-HMS simulations*

Sub-basin (S)	Surface (ha)	Perimeter (m)	Average slope (degrees)	Longest flow path (m)
1	7.15	1480.00	37.00	518.19
2	5.44	1328.00	35.88	451.83
3	10.59	2266.00	36.97	1469.64
4	3.13	1526.00	36.65	60.88
5	13.52	2086.00	33.85	470.20
6	7.61	2150.00	38.48	1027.96
7	6.54	2562.00	37.67	1053.71
8	13.42	2566.00	38.99	582.98
9	4.07	1780.00	36.01	1608.24
10	2.86	1272.00	38.27	413.56
11	3.26	1492.00	37.42	275.96
12	4.13	1984.00	39.77	175.99
13	3.72	1404.00	39.08	252.43
14	14.21	2442.00	37.96	326.15
15	3.33	1450.00	36.63	788.78
16	3.50	1570.00	35.83	483.40
17	3.24	1548.00	31.04	195.02
18	2.56	1444.00	37.80	154.40
19	9.99	2678.00	35.31	236.92
20	3.56	1340.00	35.05	697.21
21	6.50	2436.00	33.28	342.21
22	2.41	1052.00	40.99	593.25
23	1.31	1568.00	39.94	447.47
24	3.29	1642.00	28.95	307.88

An overview of summary statistics of pre-event and post-event HEC-HMS results is reported in the Table 5.2.

Table 5.2 *Summary statistics of HEC-HMS derived runoff values estimated for each sub-basin looking at pre-event and post-event scenarios*

	Pre-event		**Post-event**	
Sub-basin (S)	**Average runoff (mmh^{-1})**	**Max runoff (mmh^{-1})**	**Average runoff (mmh^{-1})**	**Max runoff (mmh^{-1})**
1	0.1353	4.232	0.1351	4.232
2	0.1335	4.260	0.1353	4.260
3	0.1349	4.094	0.1255	4.094
4	0.1288	4.185	0.1270	4.185
5	0.1354	4.176	0.1593	5.936
6	0.1349	4.237	0.1344	4.237
7	0.1352	4.317	0.1580	7.277
8	0.1348	4.055	0.1253	4.085
9	0.1316	4.210	0.1622	7.290
10	0.1313	4.228	0.1602	7.178
11	0.1288	4.021	0.1229	7.111
12	0.1316	4.144	0.1570	7.174
13	0.1299	4.063	0.1180	7.103
14	0.1347	4.184	0.1632	7.174
15	0.1301	4.235	0.1558	7.135
16	0.1271	4.034	0.1587	7.084
17	0.1270	3.501	0.1228	3.501
18	0.1296	4.337	0.1588	7.397
19	0.1321	4.136	0.1631	7.176
20	0.1302	4.242	0.1271	7.132
21	0.1335	4.189	0.1479	7.069
22	0.1296	4.186	0.1548	7.176
23	0.1219	3.836	0.1660	6.956
24	0.1292	4.286	0.1216	4.286
Catchment Outlet	0.1351	4.188	0.1446	4.232

Bar plots of daily runoff values computed for the pre-event scenario at each sub-basin's outlet are reported in the Figure 5.5, while the distribution of daily runoff values for the post-event scenario is shown in the Figure 5.6. Considering the presence of snow cover during the first and last months of the year and in line with the simulation period set for model elaborations, daily runoff values accordingly range between April to October. Looking at the hyetograph in the Supplementary figure 5.14, runoff peaks resulted from model simulations correspond to rainfall peaks recorded by the weather station in the simulation period.

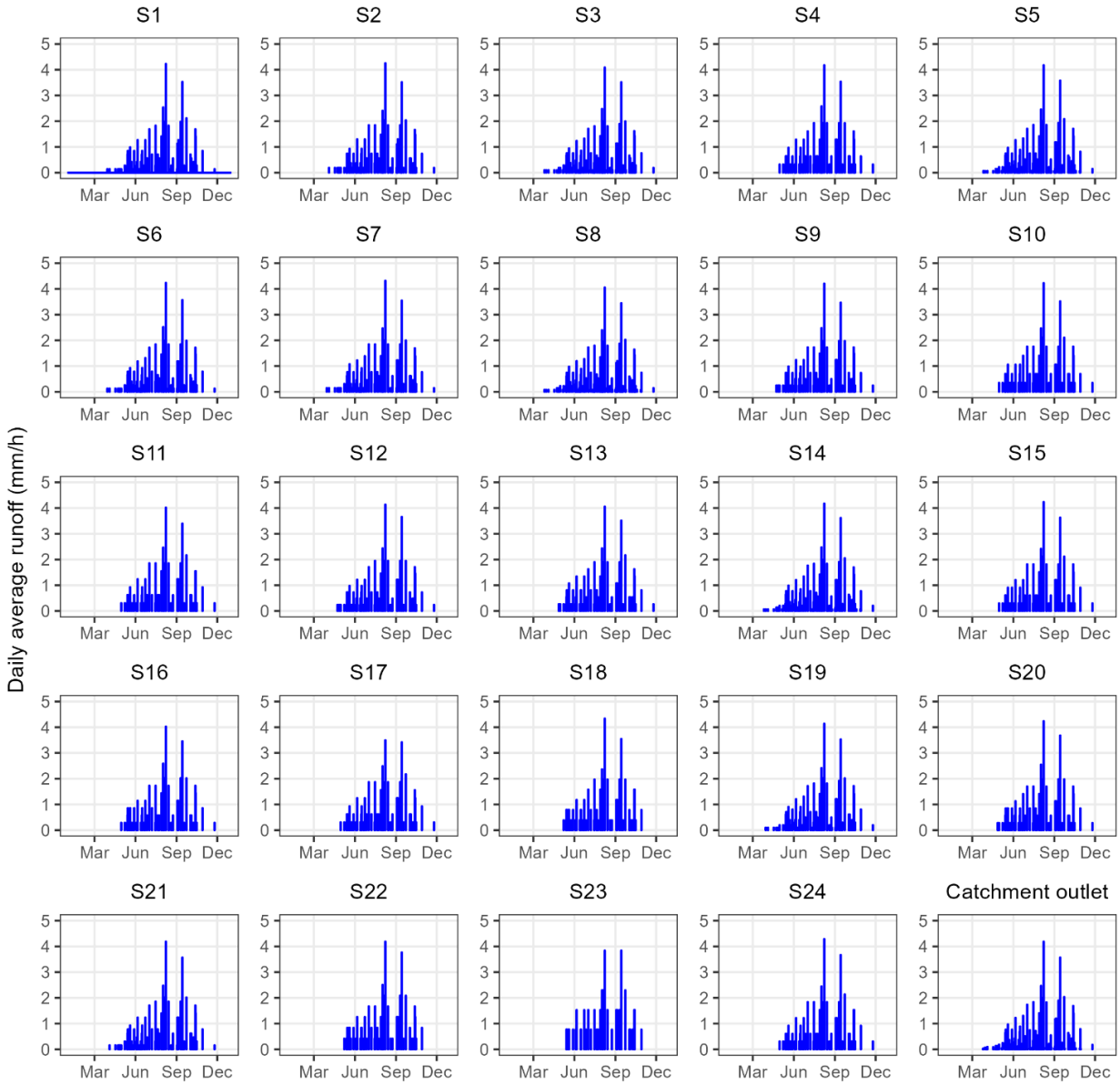

Figure 5.5 *Bar plots showing daily average runoff values resulted by HEC-HMS simulations for the pre-event scenario. The figure shows daily runoff values for each sub-basin considered, as well as daily runoff values at the outlet of the catchment.*

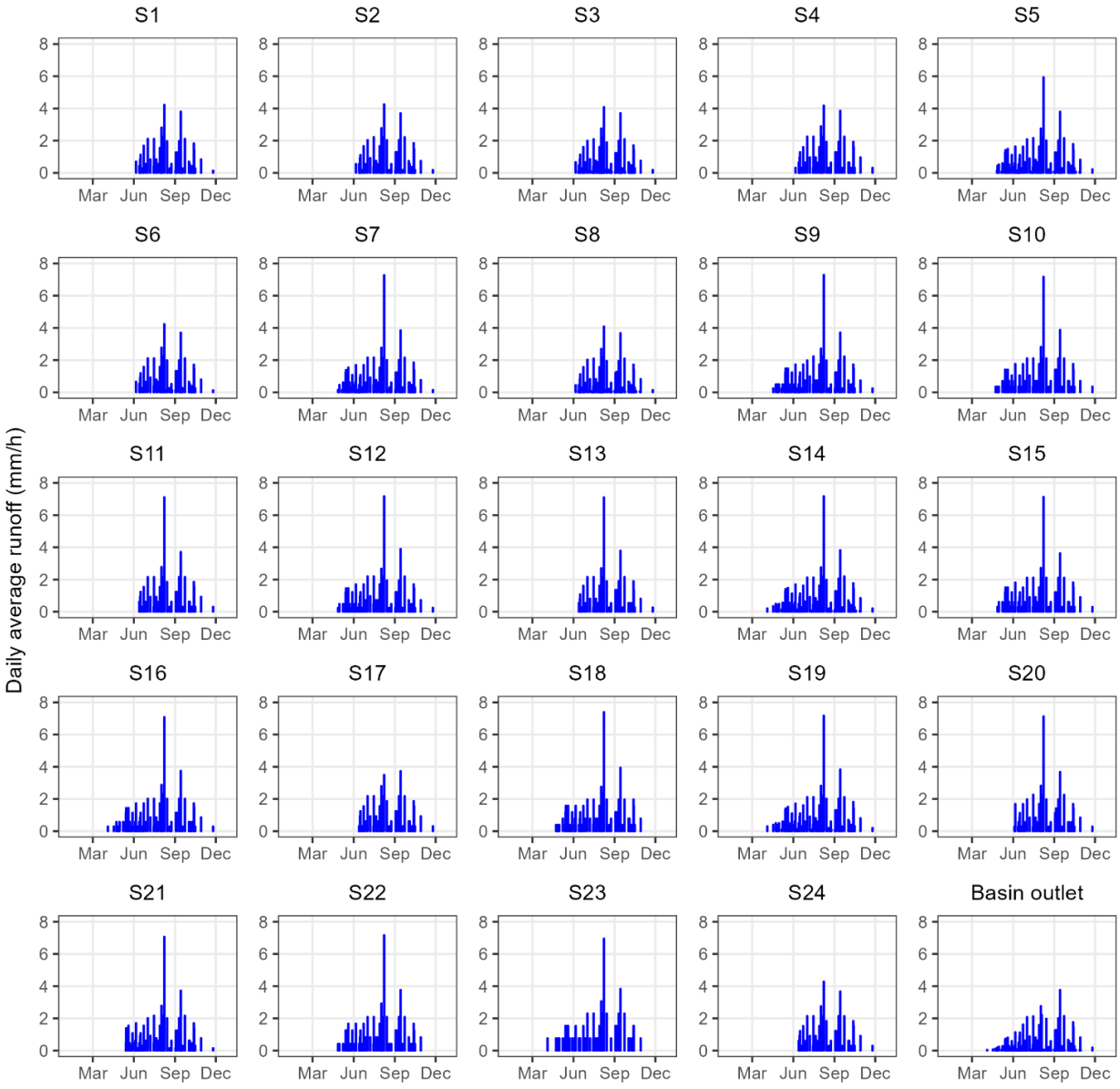

Figure 5.6 *Bar plots showing daily average runoff values resulted by HEC-HMS simulations for the post-event scenario. The figure shows daily runoff values for each sub-basin considered, as well as daily runoff values at the outlet of the catchment*

The effects of windthrow-driven land use changes in terms of runoff alteration at sub-basin detail were analyzed by computing the difference between daily runoff values calculated for the pre-event and post-event scenarios. In this regard, Table 5.3 shows the percentage of windthrown forest for each sub-basin and the respective relative increment of modeled runoff. The percentage of areas affected by blowdown ranges from a minimum of 0.0% to a maximum of 42.5%, while the runoff increment ranges between a minimum of 0.0% and a maximum of 2.56%. Maximum runoff difference between pre-event and post-event HEC-HMS quantification ranges between a minimum of 0.0 mmh^{-1} and a maximum of 3.12 mmh^{-1}. Model results firstly underline as the occurrence of the blowdown

event affected local runoff regimes at sub-basin scale. In line with results proposed by recent researches under similar conditions (Knebl *et al*., 2005; Koneti *et al*., 2018; Yuan *et al*., 2019) modeled runoff variations are on the order of a few mm per hour, mainly due to the small size of the considered sub-basins.

Table 5.3 *Overview of percentage of windthrown trees and relative percent runoff increment for each sub-basin*

Sub-basin	**Windthrown forest (%)**	**Relative runoff increment (-)**	**Max runoff difference (mmh^{-1})**
1	0.00%	0.00	0.00
2	0.00%	0.00	0.00
3	0.00%	0.00	0.00
4	1.40%	0.24	0.00
5	9.30%	0.62	1.76
6	0.00%	0.00	0.00
7	12.0%	1.77	2.96
8	0.20%	0.02	0.03
9	23.30%	2.29	3.08
10	29.70%	2.41	2.95
11	7.30%	1.99	3.09
12	21.80%	2.49	3.03
13	2.00%	1.93	3.04
14	21.70%	2.45	2.99
15	42.50%	2.37	2.90
16	42.40%	2.56	3.05
17	1.10%	0.20	0.00
18	41.00%	2.43	3.06
19	20.90%	1.90	3.04
20	40.90%	2.36	2.89
21	8.90%	1.78	2.88
22	11.20%	1.84	2.99
23	16.00%	2.11	3.12
24	1.70%	0.18	0.12

Boxplots in Figure 5.7 show the variation of runoff values due to land use changes affecting the wind-disturbed catchment at sub-basin detail. The figure particularly highlights the lack of evident runoff variations characterizing those sub-basins that substantially were not affected by windthrows. Looking at boxplots above and in line with data reported in the Table 3, small variances of runoff values between the pre-event and post-event scenario translated, for a few sub-basins, in the forced possibility to only appreciate outliers inside the plot area.

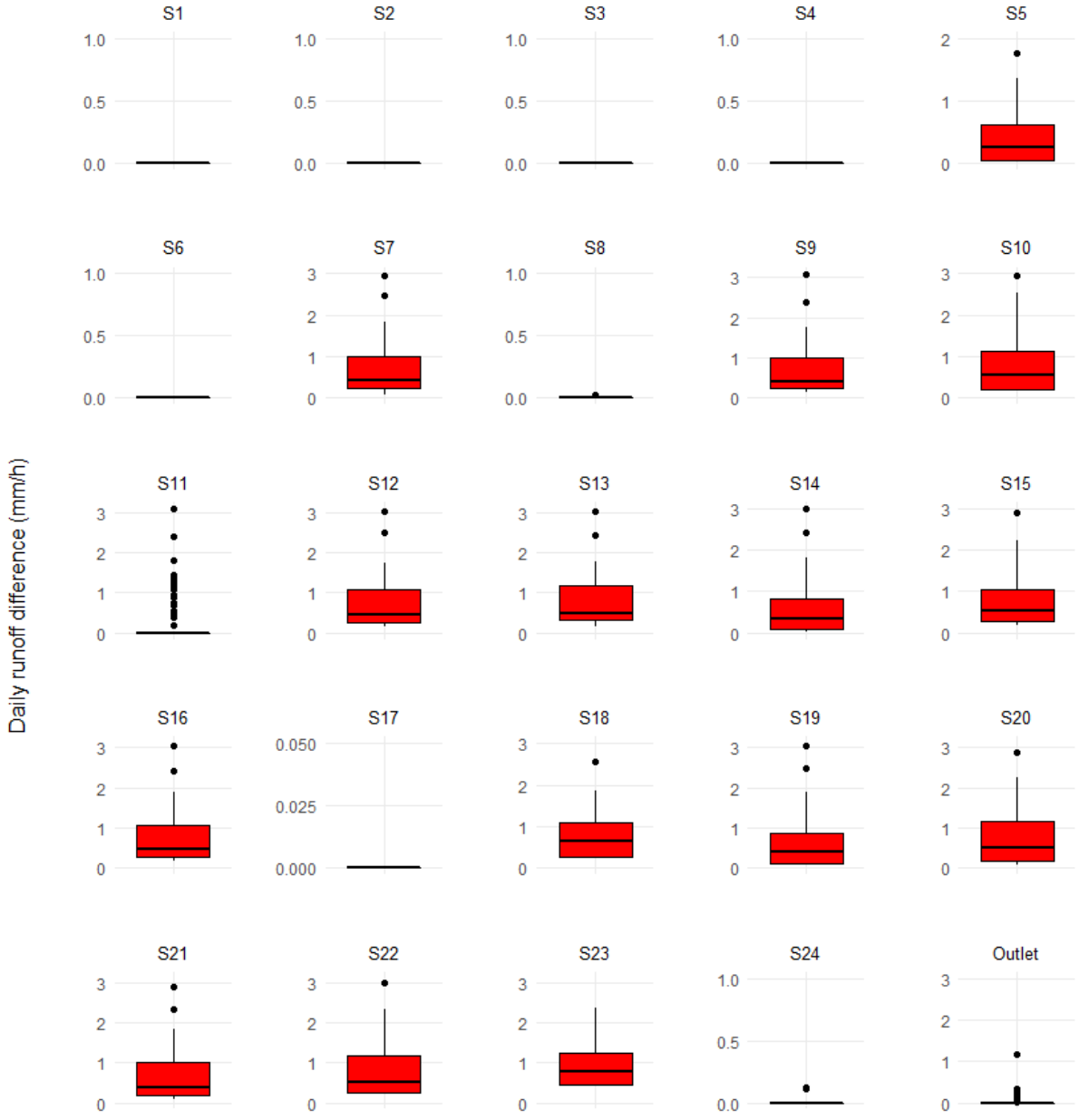

Figure 5.7 *Boxplots showing the difference of daily average runoff values estimated by HEC-HMS model for the pre-event and post-event scenarios, for each sub-basin and looking at the outlet of the entire watershed.*

5.5.3 RESS model

Figure 5.8 shows the comparison of RI index calculated for the pre-event (Fig. 5.8a) and post-event (Fig. 5.8c) scenarios, specifically looking at the disturbed hillslope close to the road. In addition, a focus on the foreseen soil instabilities at the landslide area for standing and wind-disturbed forest conditions is respectively represented in the Figure 5.8b-c. Reddish colors of RI index refer to unstable zones, while blue colors indicate stable ones. RESS elaborations particularly revealed the potential activation of land degradation dynamics at the observed shallow landslide surface in windthrown conditions, respect to the predictive detection of soil instabilities susceptibility areas computed for the pre-event scenario. Moreover, the potential role of windthrows in the occurrence of soil instabilities was suggested by the presence of unstable areas within the hillslope located above the road network, as well as across the upstream blowdown forested surface (Fig. 5.8c).

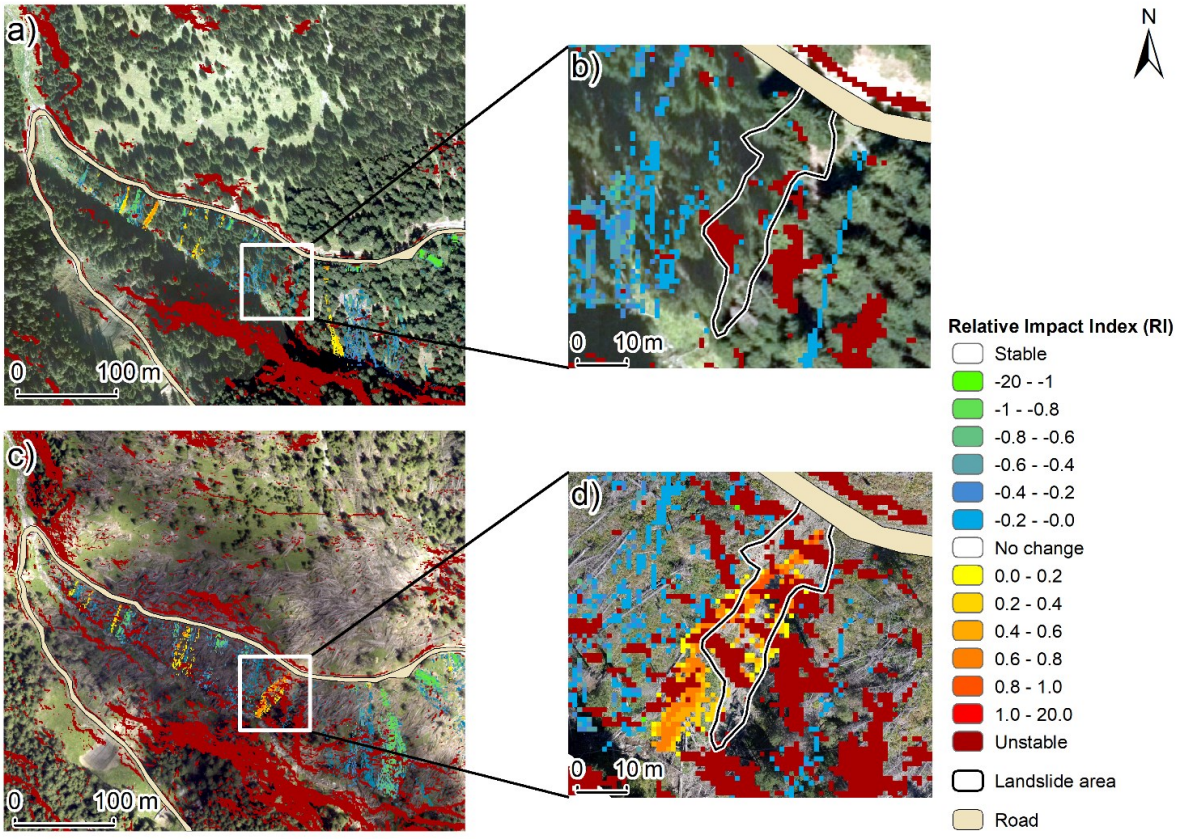

Figure 5.8 *Pre-event RI index computed for the pre-event scenario (standing forest; Fig. 5.8a) and post-event scenario (windthrown forest; Fig. 5.8c). Fig. 5.8b, d show a focus of the predictive instability susceptibility mapping at the landslide area respectively for the pre-event and post-event scenarios. No changes and unconditionally stable area are represented with a transparent coloring in order to better appreciate model outcomes. ALS-derived pre-event and post-event orthophoto are reported in the background*

5.5.4 Statistical analysis

5.5.4.1 HEC-HMS runoff variation due to land use changes

Specific codes implemented in R environment were used to perform statistical analysis of HEC-HMS results. In particular, runoff alteration due to windthrown-driven land use changes were statistically investigated by firstly check normality distribution of model results. In this regard, since Kolmogorov-Smirnov p-value resulted greater than the considered significance level (alpha equal to 0.05), average daily runoff values at each sub-basin outlet were found to be normally distributed for both the pre-event and post-event scenarios. Therefore, statistically differences between runoff computed in standing forest and windthrown forest conditions were investigated. Student t-test assuming unequal variances was computed (Table 5.4). In this regard, since p-value resulted highly minor than the significance level, statistical analysis led to reject H_0 (i.e., no influence of windthrows on runoff) in favor of H_1 (i.e., established influence of windthrown-induced land use changes on runoff production at sub-basin detail). As reported in Supplementary Table 4, the variance of daily runoff values calculated for those basins not or narrowly affected by windthrows was found to be the same for both the scenarios. Consequently, missing p-values at these sub-basins resulted from R-codes implementation. Statistical outcomes resulted by the computation of regression analysis are reported in the Supplementary Table 5.5 and Figure 5.8. Since residual median results around 0, the regression model reveals to evenly predict data correlation at both low and high ends of the dataset. Therefore, regression analysis further validates the correlation between land use changes due to windstorm occurrence and runoff alterations within the watershed. Also, F-stat and the respective p-value confirmed the rejection of H_0 in favor of H_1. The scatterplot in Figure 5.9 and the respective regression line suggests as the increasing runoff at sub-basin outlets is mostly related with a corresponding high percentage of blowdown forest (represented with the greens palette). Moreover, regression analysis highlights notable changes in runoff values for sub-basins moderately involved in windthrows (specifically affecting from 5% to 15% of standing forest). A less significant effect of windthrows on runoff variation is beyond noticeable from the regression result, specifically looking at windthrown percentage greater than 20%. In this regard, the interaction between several factors (e.g., slope exposure, stems defect, trees ages, topography and soil characteristics) could potentially induce such a trend of data distribution resulted by model implementation (Krejci *et al*., 2018; Čuchta, 2020; Ruel, 2000). R squared calculated in the regression analysis resulted equal to 0.76, highlighting such an investigated correlation.

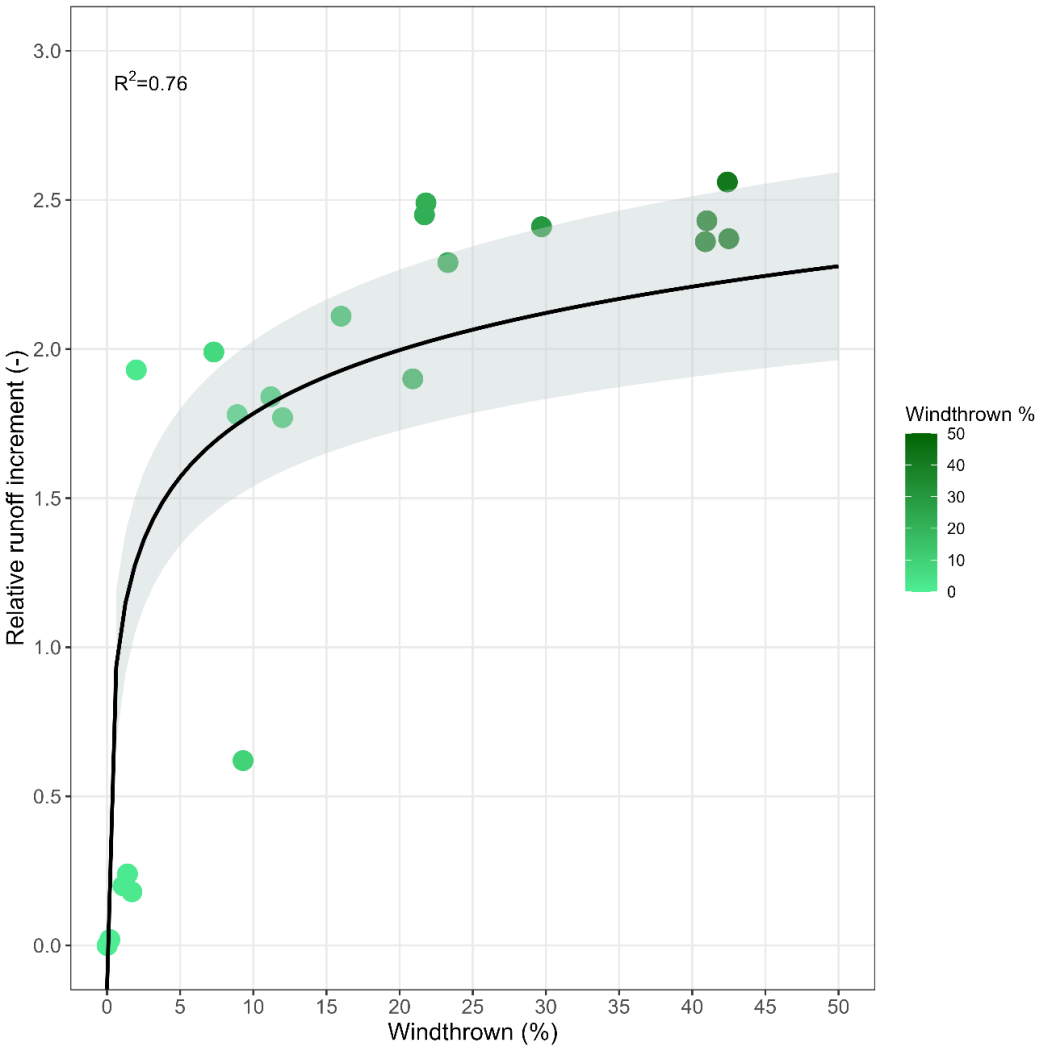

Figure 5.9 *Scatter plot showing the correlation between relative runoff increment and percentage of windthrown trees resulted from HEC-HMS simulations and ALS-derived point cloud elaboration. The color palette represents lower (light green) to higher (dark green) percentage of fallen trees. Regression line is in black color, confidence interval (alpha equal to 0.05) is shown in light grey.*

5.5.4.2 RESS soil instability susceptibility mapping

In line with the purpose of this research, *Distance to Perfect Classification* (D2PC) index and *True Skill Statistic* (TSS) score were calculated considering the disturbed-hillslope located upstream and downstream the unpaved road. RESS capability to efficiently predict the occurrence of hillslope instabilities looking at land use changes driven by the Vaia storm was therefore investigated. In this regard, *D2PC* index resulted equal to 0.076, while *TSS* score resulted equal to 0.898. Further details about statistics computed for D2PC and TSS elaborations are reported in the Table 5.4.

Table 5.4 *Results of D2PC and TSS calculation. The table shows the number of pixels for true positives (TP), true negatives (TN), false positives (FP) and false negatives (FN), and the respective percentage compared to the total number of pixels for the section of the watershed considered in investigating predictive RESS performance. Table and NoChange areas cover the remaining 45.67% of the considered watershed section.*

	TP	**TN**	**FP**	**FN**	**TPR**	**FPR**	**D2PC**	**TSS**
Pixel	5932	1519	51	441	0.931	0.032	0.076	0.898
Percentage	38.03%	9.74%	0.68%	5.88%				

5.6 Discussion

This research investigates the role of land use changes due to windthrows in the alteration of runoff regimes and in the consequent activation of hillslope failures. The combination of two different models allowed to detect the interaction between blowdown event, runoff variation and terrain instabilities looking at standing forest and wind-damaged forest conditions. This led to quantify rainfall runoff at sub-basin scale for both the scenarios and mapping terrain instabilities related with observed land use alterations. Several studies proposed the application of HEC-HMS and RESS model, respectively aiming to quantify rainfall runoff at sub-basin scale (Ali *et al*., 2011; Abushandi and Merkel, 2013; Halwatura and Najim, 2013; Shukur, 2017; Zema *et al*., 2017; Koneti *et al*., 2018; Sarminingsih *et al*., 2019; Hamdan *et al*., 2021; Guduru *et al*., 2022) and elaborate landslide susceptibility mapping (Borga *et al*., 1998; Borga *et al*., 2005; Tarolli *et al*., 2011; Cordoba *et al*., 2020; Mauri *et al*., 2022). In this context, the proposed application of these model focusing on the role played by windthrows in altering soil cover conditions is new. The implemented post-processing procedures of ALS point clouds further highlights the usefulness of remote sensing data in computing hydrological and geomorphological analysis for small catchments. This is in line with outcomes provided by Tseng *et al*. (2013), Jebur *et al*. (2014), Bossi *et al*. (2015), Cucchiaro *et al*. (2020), Steffen *et al*. (2021). Despite the availability of several recent researches about blowdowns effects on geomorphological and hydrological dynamics of forested catchments (Camarero *et al*., 2021; Costa *et al*., 2021; Rainato *et al*., 2021; Strzyżowski *et al*., 2021), our work differs from the scientific literature in that it explores the role of windthrows in altering runoff regimes at sub-basin detail through a model-based quantification of runoff changes over time. In this regard, a comparison of daily runoff quantified before and after windstorm occurrence in small sub-basins represents an innovative aspect characterizing the proposed analysis. Although runoff differences resulted from model simulations are on the order of a few millimetres per hour, our results suggest that the application of HEC-HMS for larger wind-disturbed catchments may returns more remarkable increases in runoff values over time. This is in line with outcomes provided by Brown *et al*. (2005), Wei and Zhang (2010), Li *et al*. (2017) and Li *et al*. (2018), concerning the impact of windstorms in surface hydrological variations. Starting from numerous studies concerning the preventive detection of terrain instabilities due to land use changes and roads presence (Borga *et al*., 1998; Tarolli *et al*., 2011; Penna *et al*., 2014; Huang and Zhao, 2018; Sun *et al*., 2020; Wang *et al*., 2020) our research fills the gap in the scientific knowledge regarding the possibility to foresee the occurrence of shallow landslides and terrain instabilities in relation with the occurrence of windstorm affecting a forested landscape characterized by the presence of road networks. The validity of such a methodology for

mountain areas was hence evidenced. Looking at the increasing frequency of natural disturbances affecting forests (Bebi *et al*., 2017), our research further stresses the importance of consider their role in altering water runoff dynamics over time, in order to promote adequate silvicultural interventions of wind damaged forests, regulate superficial water dynamics and prevent the occurrence of resultant land degradation processes. In line with outcomes provided by Borga *et al*. (2005), Fu *et al*. (2010), Tarolli *et al*. (2011), Sidle and Ziegler (2012), Sidle *et al*., (2014), Penna *et al*. (2014) and Mauri *et al*. (2022), this work could be considered a starting point for further investigations concerning the role of roads in altering runoff overflows, specifically after extended land use changes due to windstorm or severe meteorological events. Detailed evaluations about water management along the road network could be therefore undertaken starting from the outcomes proposed in our research. Finally, such a predictive, spatially-distributed analysis of land degradation dynamics affecting forest hillslopes could be also considered for planning efficient and sustainable slope stability interventions at both watershed and plot scale.

5.6.1 Limits

Some limitations emerged during the proposed analysis. First, the processing procedure of ALS-derived point clouds was unavoidably affected by small inaccuracies, mainly derived by parameters settings and algorithm selections. In particular, such limits translated into residual errors in the automatic extraction of both standing trees and windthrows spatial distribution within the catchment. Moreover, specific characteristics of the acquired raw ALS-data (e.g., average point density and average point spacing) allowed the elaboration of DEMs), and CHMs with a spatial resolution of no less than 1m. Despite the possibility to run HEC-HMS model for ungauged basis (Gunter, 2006; Wale *et al*., 2009; Nazirah *et al*., 2021), the lack of historical runoff measurements at the watershed outlet forbade the validation of model outcomes. For this reason, model simulations were performed without specifying the baseflow method, elaborating outflows only including direct runoff from the adopted transform method (US Army Corps of Engineers, 2000). In addition, intrinsic limits of HEC-HMS need to be considered, specifically regarding constant parameters that the model unavoidably assumes as stationary also for long period simulations. Regarding the application of RESS model, the preventive detection of instability susceptibility areas within the catchment though the Relative Impact (RI) index approach led to describe terrain failures only at their initial stage. In this regard, multi-temporal surveys at landslide-scale could overcome such a model limitation in order to detect the evolution of landslides and unstable areas. The need to set numerous inputs to run HEC-HMS and RESS simulations represents a further limitation in models application at the study scale, specifically

in relation with difficulties came upon in collecting robust field measurements over time. Finally, site-specific geotechnical models could permit more complete investigations of landslides mechanisms and interactions with roads over time.

5.7 Conclusion

This work proposes a modeling analysis of windthrows role in altering runoff regimes at sub-basin scale and in encouraging the occurrence of hillslope instabilities affecting a wind-disturbed forested watershed. The elaboration of ALS point clouds led to obtain pre-event and post-event CHMs and DTMs, aiming to extract windthrown areas and therefore quantify pre-event and post-event water runoff at sub-basin scale. Moreover, the role of blowdowns in encouraging terrain instabilities was investigated by comparing predictive soil instability susceptibility maps for both the scenarios, specifically focusing on land use changes characterizing the study area. Our analysis attested the key role played by windthrows in altering local runoff regime over time, as well as in potentially encouraging the foreseen activation of shallow landslide and terrain instabilities. Statistical analysis validated the accuracy of instabilities prediction, specifically regarding wind-damaged forest areas within the catchment. The reliability of RESS instabilities susceptibility maps was therefore evinced by the computation of statistical indexes. In this regard, notwithstanding the unfeasible possibility to validate HEC-HMS results, statistics revealed the reliability of the correlation between windthrows occurrence and runoff alterations. Considering the relevance of model validations and looking at the purposes of our research, this represents a primary aspect to consider in implementing the proposed methodology. More investigations could be also undertaken to detect the role played by the road in altering runoff directions, looking at both standing forest and wind-disturbed forest conditions. Given the availability of multi-temporal ALS-surveys, this work could be the starting point for investigate evolutionary dynamics affecting the landslide surface through specific geomorphological analysis. In this connection, ALS-data could be integrated with local-scale photogrammetric inspections using Unmanned Aerial Vehicles (UAV). The presented research lays the groundwork for computing analogous analysis at wider scale and can be considered a valid reference for planning specific interventions, in order to prevent the occurrence of similar issues encouraged by the occurrence of analogous natural disturbances.

5.8 References

Abushandi, E., Merkel, B., 2013. Modelling Rainfall Runoff Relations Using HEC-HMS and IHACRES for a Single Rain Event in an Arid Region of Jordan 2391–2409. https://doi.org/10.1007/s11269-013-0293-4

Albrecht, A., Hanewinkel, M., Kohnle, U., 2012. How does silviculture affect storm damage in forests of south-western Germany ? Results from empirical modeling based on long-term observations 229–247. https://doi.org/10.1007/s10342-010-0432-x

Ali, M., Khan, S.J., Aslam, I., Khan, Z., 2011. Landscape and Urban Planning Simulation of the impacts of land-use change on surface runoff of Lai Nullah Basin in Islamabad, Pakistan 102, 271–279. https://doi.org/10.1016/j.landurbplan.2011.05.006

American Society of Civil Engineers (ASCE), 2018. Design and Construction of Urban Stormwater Management Systems. DOI: 10.1061/9780872628557

Bebi, P., Seidl, R., Motta, R., Fuhr, M., Firm, D., Krumm, F., Conedera, M., Ginzler, C., Wohlgemuth, T., Kulakowski, D., 2017. Forest Ecology and Management Changes of forest cover and disturbance regimes in the mountain forests of the Alps q. Forest Ecology and Management 388, 43–56. https://doi.org/10.1016/j.foreco.2016.10.028

Bischetti, G.B., Chiaradia, E.A., Epis, T., Morlotti, E., 2009. Root cohesion of forest species in the Italian Alps. Plant and Soil 324, 71–89. https://doi.org/10.1007/s11104-009-9941-0

Borga, M., Dalla Fontana, G., Da Ros, D., Marchi, L., 1998. Shallow landslide hazard assessment using a physically based model and digital elevation data. Environmental Geology 35, 81–88. https://doi.org/10.1007/s002540050295

Borga, M., Dalla Fontana, G., Gregoretti, C., Marchi, L., 2002a. Assessment of shallow landsliding by using a physically based model of hillslope stability. Hydrological Processes 16, 2833–2851. https://doi.org/10.1002/hyp.1074

Borga, M., Dalla, G., Cazorzi, F., 2002b. Analysis of topographic and climatic control on rainfall-triggered shallow landsliding using a quasi-dynamic wetness index. Journal of Hydrology, 268 (1-4), 56–71. https://doi.org/10.1016/S0022-1694(02)00118-X

Borga, M., Tonelli, F., Dalla Fontana, G., Cazorzi, F., 2005. Evaluating the influence of forest roads on shallow landsliding. Ecological Modelling 187, 85–98. https://doi.org/10.1016/j.ecolmodel.2005.01.055

Bossi, G., Cavalli, M., Crema, S., Frigerio, S., Quan Luna, B., Mantovani, M., Marcato, G., Schenato, L., Pasuto, A., 2015. Multi-temporal LiDAR-DTMs as a tool for modelling a complex landslide: A case study in the Rotolon catchment (eastern Italian Alps). Natural Hazards and Earth System Sciences 15, 715–722. https://doi.org/10.5194/nhess-15-715-2015

Bottero, A., Garbarino, M., Long, J.N., Motta, R., 2013. Forest Ecology and Management The interacting ecological effects of large-scale disturbances and salvage logging on montane spruce forest regeneration in the western European Alps. Forest Ecology and Management 292, 19–28. https://doi.org/10.1016/j.foreco.2012.12.021

Camarero, J.J., Colangelo, M., Gazol, A., Pizarro, M., Valeriano, C., Igual, J.M., 2021. Effects of Windthrows on Forest Cover , Tree Growth and Soil Characteristics in Drought-Prone Pine Plantations.

Chirici, G., Giannetti, F., Travaglini, D., Nocentini, S., Francini, S., D'Amico, G., Calvo, E., Fasolini, D., Broll, M., Maistrelli, F., Tonner, J., Pietrogiovanna, M., Oberlechner, K., Andriolo, A., Comino, R., Faidiga, A., Pasutto, I., Carraro, G., Zen, S., Contarin, F., Alfonsi, L., Wolynski, A., Zanin, M., Gagliano, C., Tonolli, S., Zoanetti, R., Tonetti, R., Cavalli, R., Lingua, E., Pirotti, F., Grigolato, S., Bellingeri, D., Zini, E., Gianelle, D., Dalponte, M., Pompei, E., Stefani, A., Motta, R., Morresi, D., Garbarino, M., Alberti, G., Valdevit, F., Tomelleri, E., Torresani, M., Tonon, G., Marchi, M., Corona, P., Marchetti, M., 2019. Forest damage inventory after the "Vaia" storm in Italy. Forest@-Rivista di Selvicoltura ed Ecologia Forestale 16, 3–9. https://doi.org/10.3832/efor3070-016

Clark, C.O., 1945. Storage and the unit hydrograph. Transactions of the American Society of Civil Engineers 110 (1), 1419–1488. https://doi.org/10.1061/TACEAT.0005800

Constantine, J.A., Schelhaas, M.J., Gabet, E., Mudd, S.M., 2012. Limits of windthrow-driven hillslope sediment flux due to varying storm frequency and intensity. Geomorphology 175–176, 66–73. https://doi.org/10.1016/j.geomorph.2012.06.022

Corbari, C., Ravazzani, G., Galvagno, M., Cremonese, E., Mancini, M., 2017. Assessing crop coefficients for natural vegetated areas using satellite data and eddy covariance stations. Sensors 17. https://doi.org/10.3390/s17112664

Cordoba, J.P., Mergili, M., Aristizábal, E., 2020. Probabilistic landslide susceptibility analysis in tropical mountainous terrain using the physically based r . slope . stability model. Nat. Hazards Earth Syst. Sci., 20 815–829. https://doi.org/10.5194/nhess-20-815-2020

Costa, M., Marchi, N., Bettella, F., Bolzon, P., Lingua, E., 2021. Biological Legacies and Rockfall : The Protective Effect of a Windthrown Forest. Forests 12 (9), 1–17. https://doi.org/10.3390/f12091141

Cruden, D.M., Varnes, D.J., 1996. Landslide Types and Processes, Special Report. Transportation Research Board , National Academy of Sciences 247, 36–75.

Cucchiaro, S., Maset, E., Cavalli, M., Crema, S., Marchi, L., Beinat, A., Cazorzi, F., 2020. How does co-registration affect geomorphic change estimates in multi-temporal surveys? GIScience and Remote Sensing 57, 611–632. https://doi.org/10.1080/15481603.2020.1763048

Čuchta, P., 2020. Natural disturbances (with a special reference to windthrow): A literature review In: Daniels J.A. (ed.): Advances in Environmental Research 72, 153-172. Nova Science Publishers

Dalponte, M., Marzini, S., Solano-correa, Y.T., Tonon, G., Vescovo, L., Gianelle, D., 2020. Int J Appl Earth Obs Geoinformation Mapping forest windthrows using high spatial resolution multispectral satellite images. Int. J. Appl. Earth Obs. Geoinformation 93, 102206. https://doi.org/10.1016/j.jag.2020.102206

Dhakal, A.S., Sidle, R.C., 2003. Long-term modelling of landslides for different forest management practices. Earth Surface Processes and Landforms 28, 853–868. https://doi.org/10.1002/esp.499

Dietrich, W.E., Wilson, C.J., Montgomery, D.R., McKean, J., Bauer, R., 1992. Erosion thresholds and land surface morphology. Geology 20 (8), 675–679. DOI: 10.1130/0091-7613(1992)020<0675:ETALSM>2.3.CO;2

Dikau, R., Brunsden, D., Shrott, L., & Ibsen, M.L., 1996. Landslides Recognition, Identification, Movement and Causes, Dikau R, B. ed., Wiley. ISBN: 978-0-471-96477-3

Edburg, S.L., Hicke, J.A., Brooks, P.D., Pendall, E.G., Ewers, B.E., Norton, U., Gochis, D., Gutmann, E.D., Meddens, A.J.H., 2012. Cascading impacts of bark beetle-caused tree mortality on coupled biogeophysical and biogeochemical processes. Frontiers in Ecology and the Environment 10 (8). https://doi.org/10.1890/110173

Esri, 2021. Mosaic To New Raster (Data Management). Esri tool Ref. tools.

Everham, E.M., Brokaw, N.V.L., 1996. Forest Damage and Recovery from Catastrophic Wind. Botanical Review 62, 113–185. https://doi.org/10.1007/BF02857920

Faouzi, E., Arioua, A., Hssaisoune, M., Boudhar, A., Elaloui, A., Karaoui, I., 2022. Sensitivity analysis of CN using SCS-CN approach, rain gauges and TRMM satellite data assessment into HEC-HMS hydrological model in the upper basin of Oum Er Rbia, Morocco. Modeling Earth Systems and Environment. https://doi.org/10.1007/s40808-022-01404-8

Fleming, M.J., Doan, J.H., 2003. Geospatial hydrologic modeling extension, HEC-GeoHMS, User's Manual. US Army Corps of Engineers, Institute for Water Resources Hydrologic Engineering Center (HEC), Davis (CA).

Fu, B., Newham, L.T.H., Ramos-Scharrón, C.E., 2010. A review of surface erosion and sediment delivery models for unsealed roads. Environmental Modelling and Software 25, 1–14. https://doi.org/10.1016/j.envsoft.2009.07.013

Gennari, E., Latterini, F., Venanzi, R., Picchio, R., 2021. Single Tree Stability Assessment in Beech High Forest and Factors that Could Induce Windbreak. Environ. Sci. Proc. 3 (1). https://doi.org/10.3390/IECF2020-07953

Gerber, W., Rickli, C., Graf, F., 2002. Surface erosion in cleared and uncleared mountain windthrow sites. Forest Snow and Landscape Research 77 (1-2), 109–116. https://www.dora.lib4ri.ch/wsl/islandora/object/wsl:15324

Giannetti, F., Pecchi, M., Travaglini, D., Francini, S., Amico, G.D., Vangi, E., Cocozza, C., Chirici, G., 2021. Estimating VAIA Windstorm Damaged Forest Area in Italy Using Time Series Sentinel-2 Imagery and Continuous Change Detection Algorithms. Forests 12 (6), 1–16. https://doi.org/10.3390/f12060680

Guduru, J.U., Jilo, N.B., Rabba, Z.A., Namara, W.G., 2022. Rainfall-runoff modeling using HEC-HMS model for Meki River watershed, rift valley basin, Ethiopia. Journal of African Earth Sciences 197. https://doi.org/10.1016/j.jafrearsci.2022.104743

Gunter, B., 2006. Rainfall-Runoff Modeling of Ungauged Catchments. Encyclopedia of Hydrological Sciences. https://doi.org/10.1002/0470848944.hsa140

Guo, Y., Zhang, Y., Zhang, L., Wang, Z., 2021. Regionalization of hydrological modeling for predicting streamflow in ungauged catchments: A comprehensive review. Wiley Interdisciplinary Reviews: Water 8, 1–32. https://doi.org/10.1002/wat2.1487

Halwatura, D., Najim, M.M.M., 2013. Environmental Modelling & Software Application of the HEC-HMS model for runoff simulation in a tropical catchment. Environmental Modelling and Software 46, 155–162. https://doi.org/10.1016/j.envsoft.2013.03.006

Hamdan, A.N.A.., Almuktar, S.., Scholz, M., 2021. Rainfall-Runoff Modeling Using the HEC-HMS Model for the Al-Adhaim River Catchment, Northern Iraq . Hydrology 8 (2). https://doi.org/10.3390/hydrology8020058

Holko, L., Fleischer, P., Novák, V., Kostka, Z., Bi Č Árová, S., Novák, J., 2012. Hydrological Effects of a Large Scale Windfall Degradation in the High Tatra Mountains, Slovakia. In: Krecek, J., Haigh, M.J., Hofer, T., Kubin, E. (eds). Management of Mountain Watersheds. Springer. https://doi.org/10.1007/978-94-007-2476-1_13

Huang, Y., Zhao, L., 2018. Review on landslide susceptibility mapping using support vector machines. Catena 165, 520–529. https://doi.org/10.1016/j.catena.2018.03.003

Iverson, R.M., 2000. Landslide triggering by rain infiltration. Water Resources Research 36 (7), 1897–1910. https://doi.org/10.1029/2000WR900090

Jean-Matthieu, M., 2019. LiDARtRee: Forest Analysis with Airborne Laser Scanning (LiDAR) Data. Available at: https://gitlab.irstea.fr/jean-matthieu.monnet/lidaRtRee

Jebur, M.N., Pradhan, B., Tehrany, M.S., 2014. Optimization of landslide conditioning factors using very high-resolution airborne laser scanning (LiDAR) data at catchment scale. Remote Sensing of Environment 152, 150–165. https://doi.org/10.1016/j.rse.2014.05.013

Jones, L., Hobbs, P., 2021. The Application of Terrestrial LiDAR for Geohazard Mapping , Monitoring and Modelling in the British Geological Survey. Remote Sensing 13 (3). https://doi.org/10.3390/rs13030395

Keim, R.F., Skaugset, A.E., 2003. Modelling effects of forest canopies on slope stability. Hydrological Processes. Special Issue: Hydrological and Geochemical Processes in Large-Scale River Basins 17 (7), 1457–1467. https://doi.org/10.1002/hyp.5121

Knebl, M.R., Yang, Z., Hutchison, K., Maidment, D.R., 2005. Regional scale flood modeling using NEXRAD rainfall , GIS , and HEC-HMS / RAS : a case study for the San Antonio River Basin Summer 2002 storm event 75, 325–336. Journal of Environmental Management 75 (4) https://doi.org/10.1016/j.jenvman.2004.11.024

Koneti, S., Sunkara, S.L., Roy, P.S., 2018. Hydrological Modeling with Respect to Impact of Land-Use and Land-Cover Change on the Runoff Dynamics in Godavari River Basin Using the HEC-HMS Model. ISPRS Int. J. Geo-Inf. 7 (6). https://doi.org/10.3390/ijgi7060206

Krejci, L., Kolejka, J., Vozenilek, V., Machar, I., 2018. Application of GIS to Empirical Windthrow Risk Model in Mountain Forested Landscapes. Forests 9 (2), 1–18. https://doi.org/10.3390/f9020096

Kuriata-Potasznik, A.B., Szymczyk, S., 2016. Variability of the water availability in a river lake system - A case study of lake symsar. Journal of Water and Land Development 31, 87–96. https://doi.org/10.1515/jwld-2016-0039

Lanni, C., McDonnell, J., Hopp, L., Rigon, R., 2013. Simulated effect of soil depth and bedrock topography on near-surface hydrologic response and slope stability. Earth Surface Processes and Landforms 38, 146-159. DOI: 10.1002/esp.3267

Laurin, V., Puletti, G., Tattoni, G., Ferrara, C., Pirotti, F., 2021. Estimated biomass caused by the Vaia windthrow in northern Italy: Evaluation of active and passive remote sensing options. Remote Sensing 13. https://doi.org/10.3390/rs13234924

Li, M., Maclean, D.A., Hennigar, C.R., Ogilvie, J., 2019. Spatial-Temporal Patterns of Spruce Budworm Defoliation within Plots in Québec. Forests 10 (3), 1–21. https://doi.org/10.3390/f10030232

Li, Q., Wei, X., Zhang, M., Liu, W., Giles-Hansen, K., Wang, Y., 2018. The cumulative effects of forest disturbance and climate variability on streamflow components in a large forest-dominated watershed. Journal of Hydrology 557, 448–459. https://doi.org/10.1016/j.jhydrol.2017.12.056

Lingua, E., Marangon, D., 2022. Forest Ecology and Management Windthrown elements : a key point improving microsite amelioration and browsing protection to transplanted seedlings. Forest Ecology and Management 508. https://doi.org/10.1016/j.foreco.2022.120050

Llorens, P., Gallart, F., 2000. A simplified method for forest water storage capacity measurement. Journal of Hydrology 240, 131–144. https://doi.org/10.1016/S0022-1694(00)00339-5

Maedeh, P.A., Wu, W., Irdmoosa, K.G., Acharya, M.S., 2018. A new approach to estimate the factor of safety for rooted slopes with an emphasis on the soil property, geometry and vegetated coverage. Advances in Computational Design 3, 269–288. https://doi.org/10.12989/acd.2018.3.3.269

Mauri, L., Cucchiaro, S., Grigolato, S., Dalla Fontana, G., Tarolli, P., 2022. Evaluating the interaction between snowmelt runoff and road in the occurrence of hillslope instabilities affecting a landslide-prone mountain basin: A multi-modeling approach. Journal of Hydrology 612, 128200. https://doi.org/10.1016/j.jhydrol.2022.128200

Mauri, L., Eugenio, S., Tarolli, P., 2022. Multi-temporal modeling of road-induced overland flow alterations in a terraced landscape characterized by shallow landslides. International Soil and Water Conservation Research 10 (2), 240-253. https://doi.org/10.1016/j.iswcr.2021.07.004

Mcdonald, J.I., 2011. The Effects of Timber Harvesting and Windthrow on Landslide Initiation, Southwestern Vancouver Island. MSc in the Department of Earth Sciences Faculty of Science, Simon Fraser University

Mitchell, S.J., 2013. Wind as a natural disturbance agent in forests: A synthesis. Forestry 86, 147–157. https://doi.org/10.1093/forestry/cps058

Montgomery D.R., Dietrich W.E., 1994. A physically based model for the topographic control on shallow landsliding. Water Resources Research 30 (4), 1153–1171. https://doi.org/10.1029/93WR02979

Motta, R., Ascoli, D., Corona, P., Marchetti, M., Vacchiano, G., 2018. Silviculture and wind damages. The storm "Vaia." Forest@-Rivista di Selvicoltura ed Ecologia Forestale 15, 94–98. https://doi.org/10.3832/efor2990-015

Nazirah, A., Sabki, W.O.W.M., Zulkarnian, H., Afizah, A., 2021. Simulation of runoff using HEC-HMS for ungauged catchment. AIP Conference Proceedings 2347. https://doi.org/https://doi.org/10.1063/5.0051957

Nguyen, H.., 2018. A Two-Sample Kolmogorov-Smirnov-Like Test for Big Data. In: Boo, Y., Stirling, D., Chi, L., Liu, L., Ong, KL., Williams, G. (eds) Data Mining. AusDM 2017. Communications in Computer and Information Science, Springer 845. https://doi.org/10.1007/978-981-13-0292-3_6

Pellegrini, G., Martini, L., Cavalli, M., Rainato, R., Cazorzi, A., Picco, L., 2021. The morphological response of the Tegnas alpine catchment (Northeast Italy) to a Large Infrequent Disturbance. Science of the Total Environment 770, 145209. https://doi.org/10.1016/j.scitotenv.2021.145209

Penna, D., Borga, M., Aronica, G.T., Brigandì, G., Tarolli, P., 2014. The influence of grid resolution on the prediction of natural and road-related shallow landslides. Hydrol. Earth Syst. Sci., 18, 2127–2139. https://doi.org/10.5194/hess-18-2127-2014

Pokorný, R., Stojnič, S., 2012. Leaf area index of Norway spruce stands in relation to age and defoliation. Beskydy 5, 173–180. https://doi.org/10.11118/beskyd201205020173

Ponce V.M, 1994. Engineering Hydrology, Principles and Practices. Available at: http://ponce.sdsu.edu/enghydro/

Popescu, S., Wynne, R., 2004. Seeing the Trees in the Forest: Using LiDAR and Multispectral Data Fusion with Local Filtering and Variable Window Size for Estimating Tree Height. Photogrammetric Engineering and Remote Sensing 70, 589–604. DOI: 10.14358/PERS.70.5.589

Qiao, K., Zhu, W., Hu, D., Hao, M., Chen, S., Cao, S., 2017. Examining the distribution and dynamics of impervious surface in different functional zones of Beijing. J. Geogr. Sci. 28, 669–684. https://doi.org/10.1007/s11442-018-1498-5

Rainato, R., Martini, L., Pellegrini, G., Picco, L., 2021. Catena Hydrological , geomorphic and sedimentological responses of an alpine basin to a severe weather event (Vaia storm). Catena 207, 105600. https://doi.org/10.1016/j.catena.2021.105600

Roussel, J.R., Auty, D., Coops, N.C., Tompalski, P., Goodbody, T.R.H., Meador, A.S., Bourdon, J.F., de Boissieu, F., Achim, A., 2020. lidR: An R package for analysis of Airborne Laser Scanning (ALS) data. Remote Sensing of Environment 251, 112061. https://doi.org/10.1016/j.rse.2020.112061

Ruel, J., 2000. Factors influencing windthrow in balsam fir forests: from landscape studies to individual tree studies. Forest Ecology and Management 135 (1-3), 169–178. https://doi.org/10.1016/S0378-1127(00)00308-X

Russel, H.W., 1963. Computation of direct runoff amounts from storm rainfall. Available at: https://iahs.info/uploads/dms/063006.pdf

Sakals, M.E., Sidle, R.C., 2004. A spatial and temporal model of root cohesion in forest soils. Canadian Journal of Forest Research 34, 950–958. https://doi.org/10.1139/x03-268

Sarminingsih, A., Rezagama, A., Ridwan, 2019. Simulation of rainfall-runoff process using HEC-HMS model for Garang Watershed, Semarang, Indonesia. Journal of Physics: Conference Series 1217. https://doi.org/10.1088/1742-6596/1217/1/012134

Seidl, R., Rammer, W., 2017. Climate change amplifies the interactions between wind and bark beetle disturbances in forest landscapes. Landscape Ecology 32, 1485–1498. https://doi.org/10.1007/s10980-016-0396-4

Seidl, R., Schelhaas, M.-J., Rammer, W., Verkerk, P.J., 2014. Increasing forest disturbances in Europe and their impact on carbon storage. Nature Climate Change 4, 806–810. https://doi.org/10.1038/nclimate2318

Shukur, H.K., 2017. Estimation Curve Numbers using GIS and Hec-GeoHMS Model. Journal of Engineering 23 (5), 1–11. https://joe.uobaghdad.edu.iq/index.php/main/article/view/37

Sibanda, M., Mutanga, O., Dube, T., Vundla, T.S., 2019. Estimating LAI and mapping canopy storage capacity for hydrological applications in wattle infested ecosystems using Sentinel-2 MSI derived red edge bands. GIScience & Remote Sensing 56, 68–86. https://doi.org/10.1080/15481603.2018.1492213

Sidle, R.C., Bogaard, T.A., 2016. Earth-Science Reviews Dynamic earth system and ecological controls of rainfall-initiated landslides. Earth Science Reviews 159, 275–291. https://doi.org/10.1016/j.earscirev.2016.05.013

Sidle, R.C., Ghestem, M., Stokes, A., 2014. Epic landslide erosion from mountain roads in Yunnan, China-challenges for sustainable development. Natural Hazards and Earth System Sciences 14, 3093–3104. https://doi.org/10.5194/nhess-14-3093-2014

Sidle, R.C., Ziegler, A.D., 2012. The dilemma of mountain roads. Nature Publishing Group 5, 437–438. https://doi.org/10.1038/ngeo1512

Silva, C.A., Hudak, A.T., Vierling, L.A., Loudermilk, E.L., O'Brien, J.J., Hiers, J.K., Khosravipour, A., 2016. Imputation of Individual Longleaf Pine (Pinus palustris Mill.) Tree Attributes from Field and LiDAR Data. Canadian Journal of Remote Sensing 42, 554–573.

Smirnov, N.., 1939. Estimating the deviation between the empirical distribution functions of two independent samples. Bulletin de l'Universite de Moscou 2, 3–16.

Sridhar, V., 2017. DigitalCommons @ University of Nebraska - Lincoln Evapotranspiration Estimation and Scaling Effects Over The Nebraska Sandhills.

Steffen, M., Schipek, M., Anne-Farina Lohrengel Lennart Meine, 2021. Identification of windthrow-endangered infrastructure combining LiDAR-based tree extraction methods using GIS. Journal of Applied Remote Sensing 15. https://doi.org/https://doi.org/10.1117/1.JRS.15.014522

Strzyżowski, D., Gorczyca, E., Krzemień, K., Żelazny, M., 2021. The intensity of slope and fluvial processes after a catastrophic windthrow event in small catchments in the Tatra Mountains. Journal of Mountain Science. https://doi.org/10.1007/s11629-021-6726-2

Sun, D., Wen, H., Wang, D., Xu, J., 2020. Geomorphology A random forest model of landslide susceptibility mapping based on hyperparameter optimization using Bayes algorithm. Geomorphology 362, 107201. https://doi.org/10.1016/j.geomorph.2020.107201

Tarboron, D.G., 1997. A new method for the determination of flow directions and upslope areas in grid digital elevation models. Water Resources Research 33 (2), 309–319. ttps://doi.org/10.1029/96WR03137

Tarolli, P., Borga, M., Chang, K.T., Chiang, S.H., 2011. Modeling shallow landsliding susceptibility by incorporating heavy rainfall statistical properties. Geomorphology 133, 199–211. https://doi.org/10.1016/j.geomorph.2011.02.033

Tarolli, P., Borga, M., Fontana, G.D., 2008. Analysing the influence of upslope bedrock outcrops on shallow landsliding. Geomorphology 93, 186–200. https://doi.org/10.1016/j.geomorph.2007.02.017

Taylor, S.L., Maclean, D.A., 2007. Spatiotemporal patterns of mortality in declining balsam fir and spruce stands 253, 188–201. Forest Ecology and Management 253 (1-3). https://doi.org/10.1016/j.foreco.2007.07.016

Thiery, Y., Vandromme, R., Maquaire, O., Bernardie, S., 2017. Advancing Culture of Living with Landslides. Advances in Landslide Science 2. Mikos, Tiwari, Yin, Kyoji and Sassa (Eds). https://doi.org/10.1007/978-3-319-53498-5

Thimonier, A., Sedivy, I., Schleppi, P., 2010. Estimating leaf area index in different types of mature forest stands in Switzerland : a comparison of methods 543–562. European Journal of Forest Research 129, 543-562. https://doi.org/10.1007/s10342-009-0353-8

Tseng, C.M., Lin, C.W., Stark, C.P., Liu, J.K., Fei, L.Y., Hsieh, Y.C., 2013. Application of a multi-temporal, LiDAR-derived, digital terrain model in a landslide-volume estimation. Earth Surface Processes and Landforms 38, 1587–1601. https://doi.org/10.1002/esp.3454

Turner, M.G., 2010. Disturbance and landscape dynamics in a changing world. Ecology 91 (10), 2833–284. https://doi.org/10.1890/10-0097.1

Ulanova, N.G., 2000. The effects of windthrow on forests at different spatial scales : a review. Forest Ecology and Management 135 (1-3), 155–167. https://doi.org/10.1016/S0378-1127(00)00307-8

US Army Corps of Engineers (USACE), 2000. Hydrologic Modeling System (HEC-HMS) Technical Reference Manual.

Usbeck, T., Wohlgemuth, T., Dobbertin, M., Pfister, C., Bürgi, A., Rebetez, M., 2010. Increasing storm damage to forests in Switzerland from 1858 to 2007. Agric. For. Meteorol 150, 47–55. https://doi.org/10.1016/j.agrformet.2009.08.010

USDA-SCS, 1972. Soil Conservation Service, National engineering handbook, USDA. Washington DC (Eds)

Vergani, C., Schwarz, M., Soldati, M., Corda, A., Giadrossich, F., Chiaradia, E.A., Morando, P., Bassanelli, C., 2016. Root reinforcement dynamics in subalpine spruce forests following timber harvest: A case study in Canton Schwyz, Switzerland. Catena 143, 275–288. https://doi.org/10.1016/j.catena.2016.03.038

Wale, A., Rientjes, T.H.M., Gieske, A.S.M., Getachew, H.A., 2009. Ungauged catchment contributions to Lake Tana's water balance. Hydrol. Process 23, 3682–3693. https://doi.org/10.1002/hyp.7284

Wang, Y., Fang, Z., Wang, M., Peng, L., Hong, H., 2020. Computers and Geosciences Comparative study of landslide susceptibility mapping with different recurrent neural networks. Computers and Geosciences 138, 104445. https://doi.org/10.1016/j.cageo.2020.104445

Wei, X., Zhang, M., 2010. Quantifying streamflow change caused by forest disturbance at a large spatial scale : A single watershed study. Water Resources Research 46 (12), 1–15. https://doi.org/10.1029/2010WR009250

Xiao, Q., McPherson, E.G., 2016. Surface Water Storage Capacity of Twenty Tree Species in Davis, California. Journal of Environmental Quality 45, 188–198. https://doi.org/10.2134/jeq2015.02.0092

Yeo, I.-Y., Gordon, S.I., Guldmann, J.-M. Optimizing Patterns of Land Use to Reduce Peak Runoff Flow and Nonpoint Source Pollution with an Integrated Hydrological and Land- Use Model. Earth Interactions 8 (6). https://doi.org/10.1175/1087-3562(2004)008<0001:OPOLUT>2.0.CO;2

Yuan, W., Liu, M., Wan, F., 2019. Calculation of Critical Rainfall for Small-Watershed Flash Floods Based on the HEC-HMS Hydrological Model. Water Resources Management 33, 2555–2575. https://doi.org/10.1007/s11269-019-02257-0

Zhang, W., Qi, J., Wan, P., Wang, H., Xie, D., Wang, X., Yan, G., 2016. An Easy-to-Use Airborne LiDAR Data Filtering Method Based on Cloth Simulation. Remote Sensing 8 (6). https://doi.org/10.3390/rs8060501

5.9 Supplementary material

5.9.1 Graphical abstract

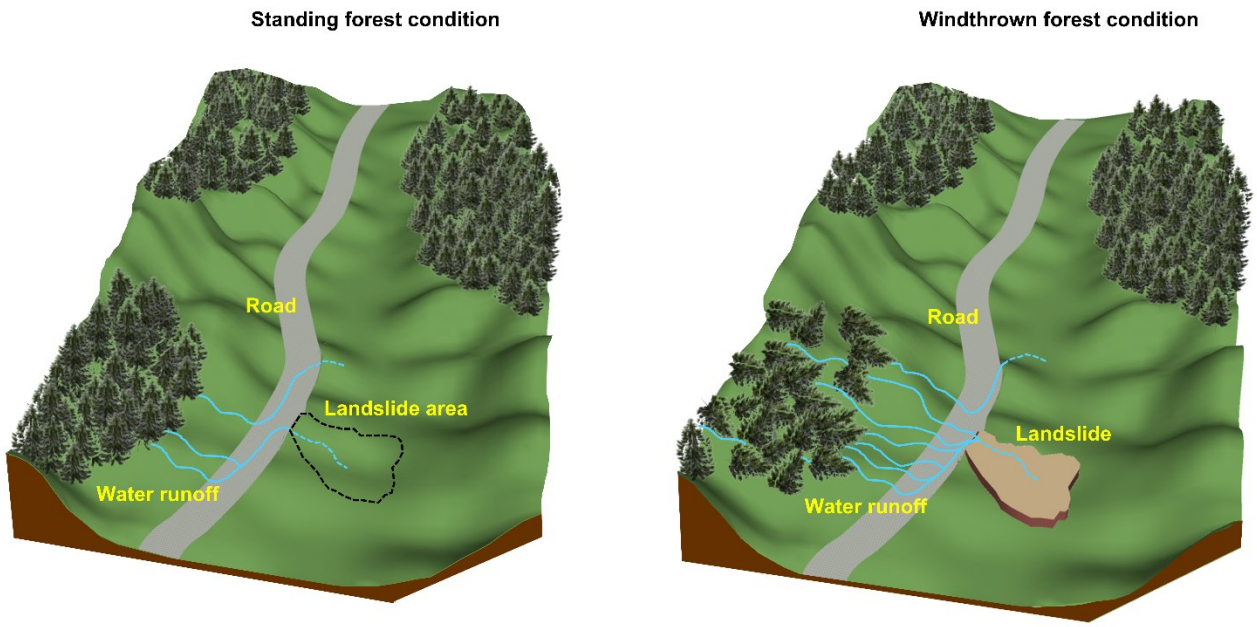

5.9.2 Supplementary figures

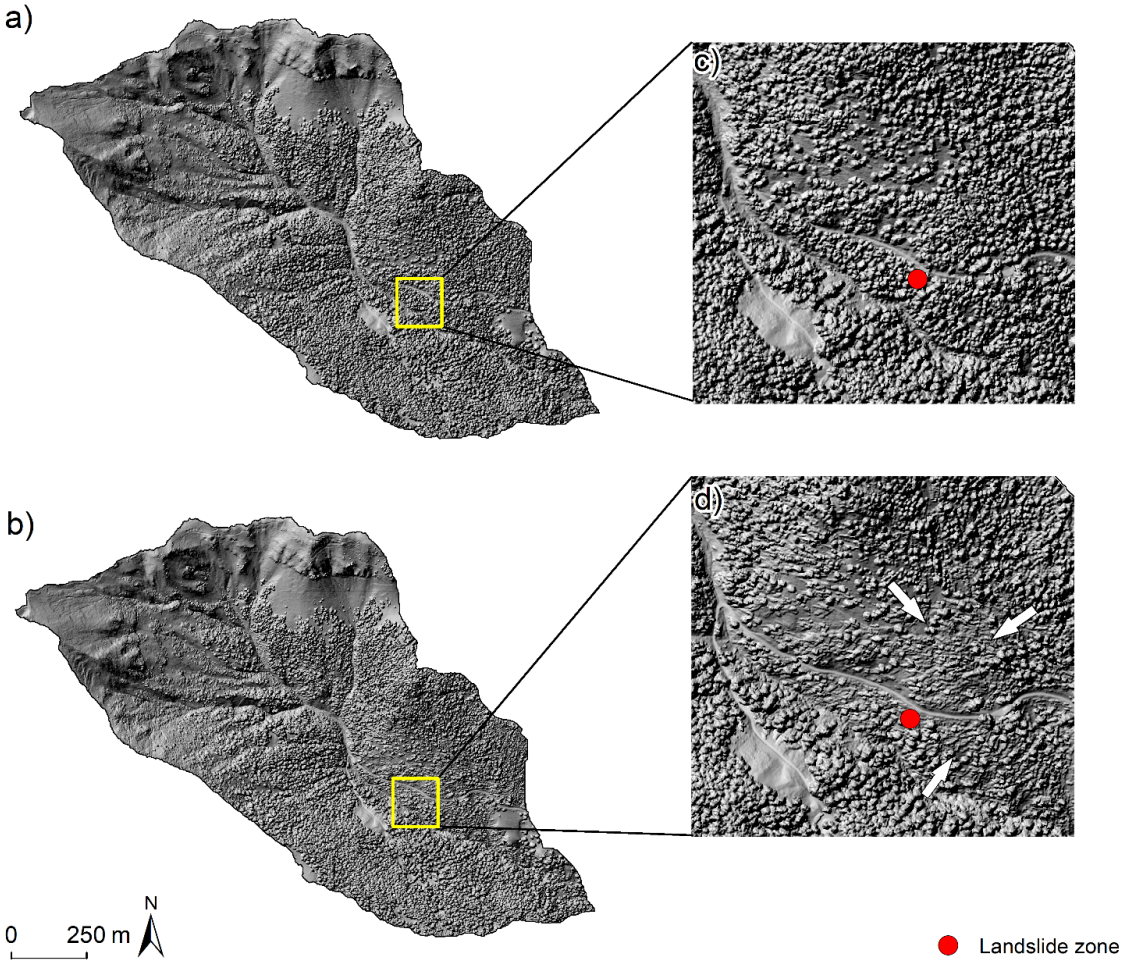

Figure 5.10 *Shaded relief of the forested catchment computed starting from pre-event (a) and post-event (b) ALS-data acquisition and elaboration. The figure also shows a detail of the pre-event (c) and post-event (d) shaded relief at the hillslope affected by the shallow landslide activated under the unpaved road section.*

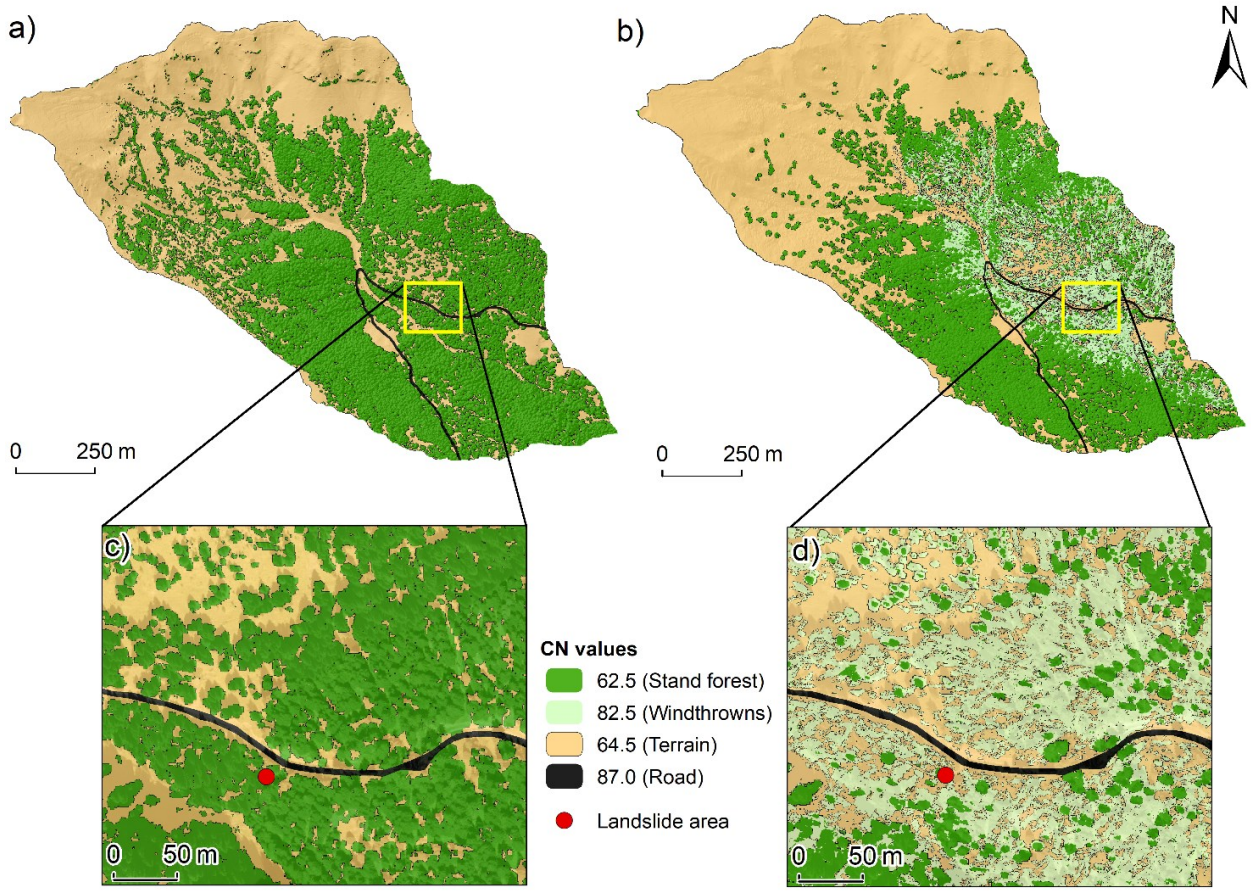

Figure 5.11 *Spatial discretization of CN values set for different land cover (i.e., stand forest, windthrows, terrain and road). The figure also shows a detail of CN values spatial distribution at the hillslope involved in the activation of the shallow landslide, occurred downstream a section of the unpaved road located in the catchment, looking at pre-event (c) and post-event (d) conditions.*

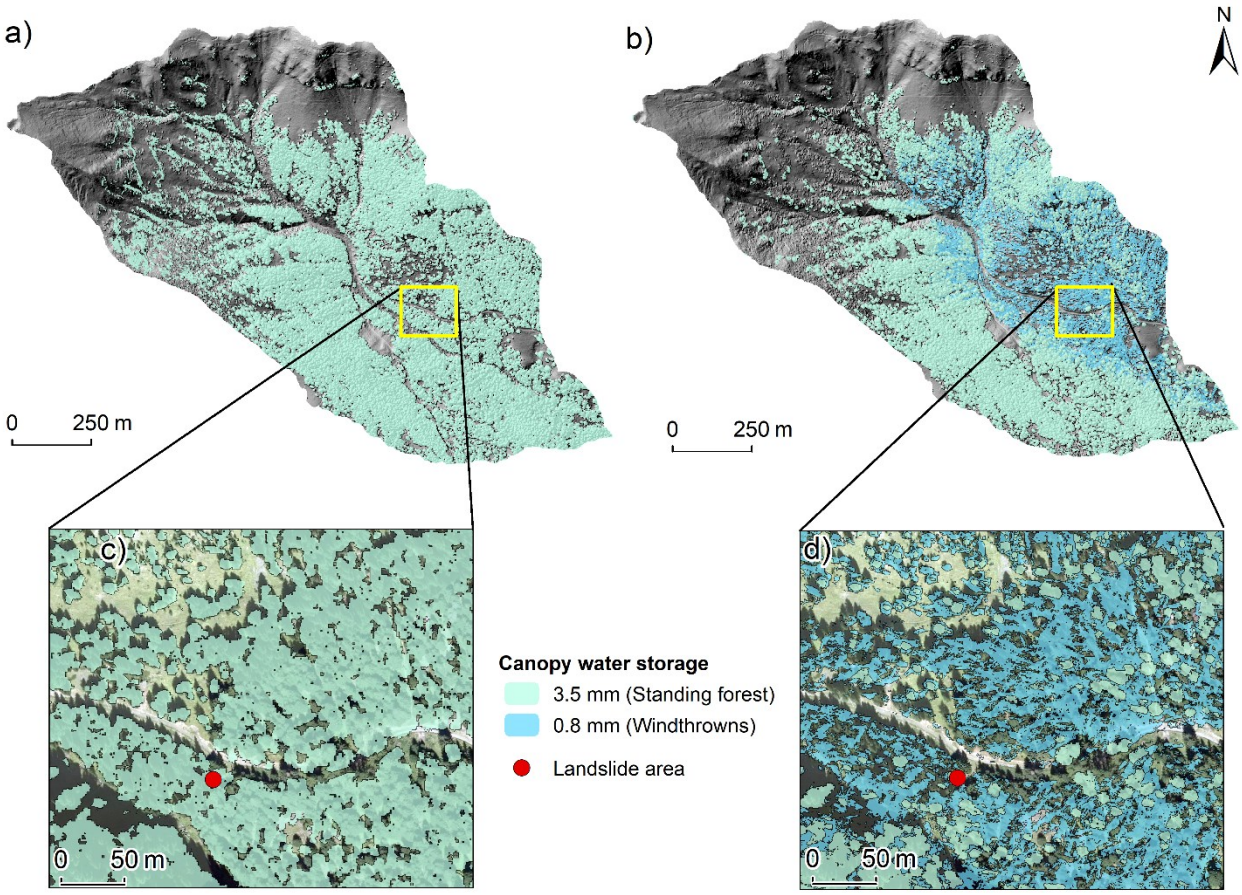

Figure 5.12 *Spatial discretization of canopy water storage set for different land cover (i.e., stand forest and windthrows). The figure also shows a detail of canopy water storage spatial distribution at the hillslope involved in the activation of the shallow landslide, occurred downstream a section of the unpaved road located in the catchment, looking at pre-event (c) and post-event (d) conditions.*

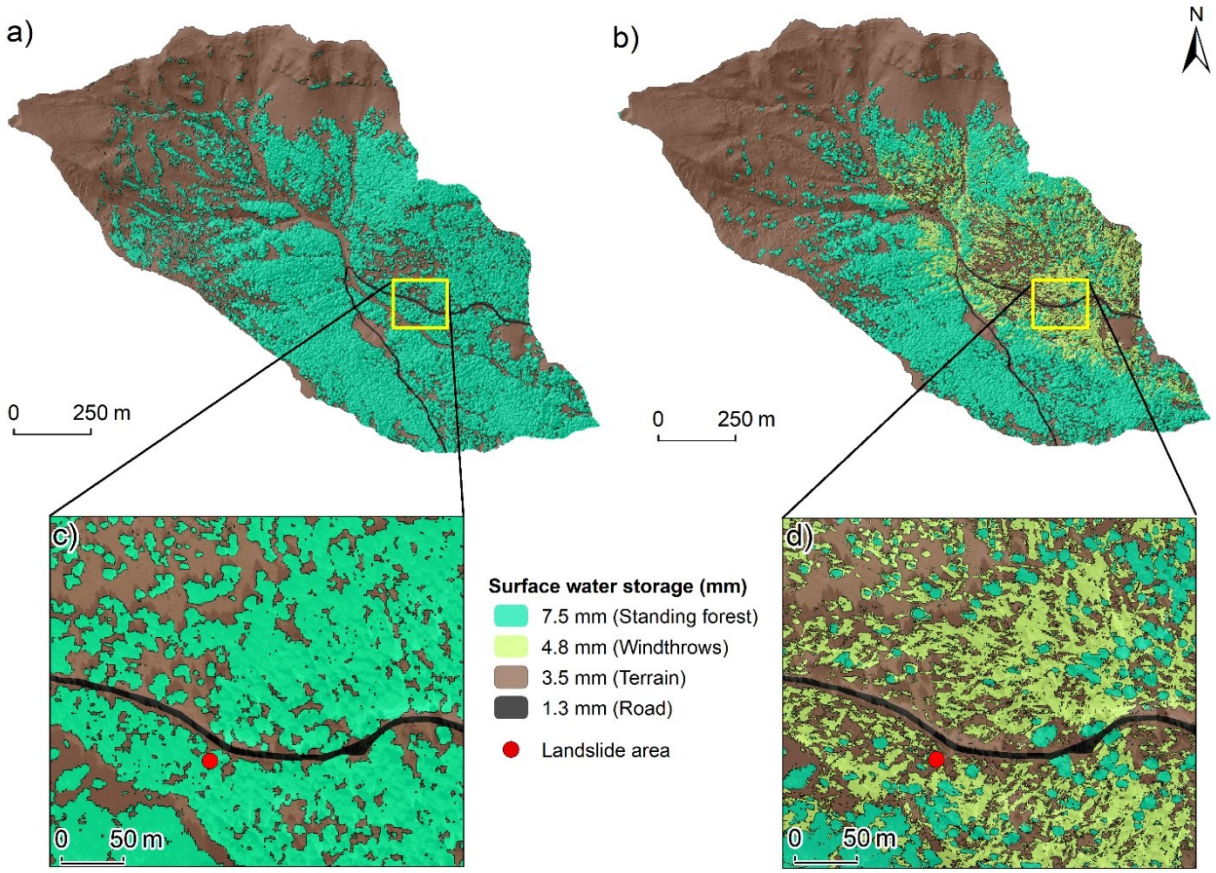

Figure 5.13 *Spatial discretization of surface water storage set for different land cover (i.e., standing forest, windthrows, terrain and road). The figure also shows a detail of surface water storage spatial distribution at the hillslope involved in the activation of the shallow landslide, occurred downstream a section of the unpaved road located in the catchment, looking at pre-event (c) and post-event (d) conditions.*

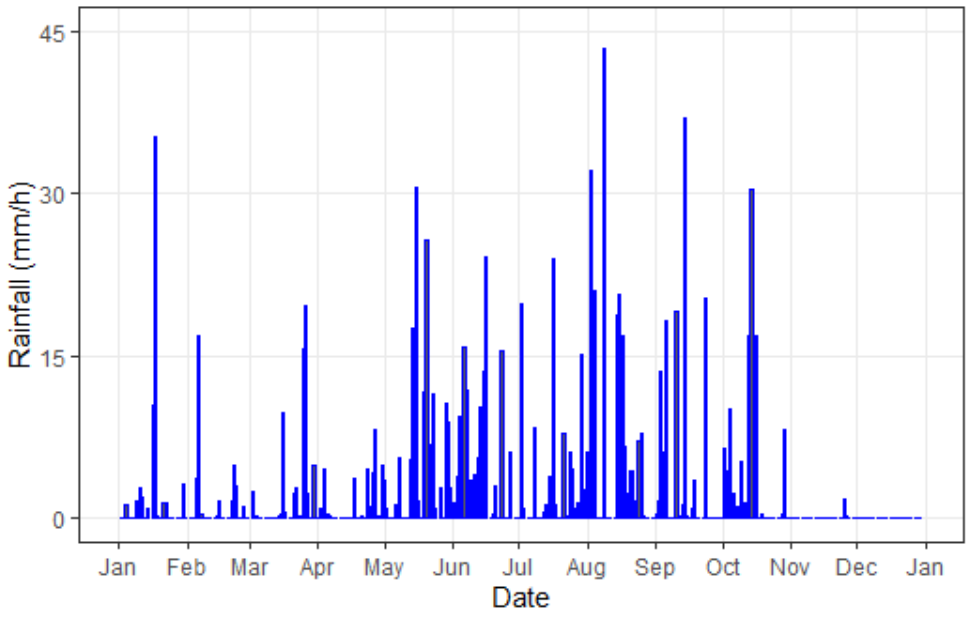

Figure 5.14 *Hydrograph computed starting from rainfall data collected by the Falzarego weather station in 2019*

5.9.3 Supplementary tables

Table 5.5 *Overview of ALS surveys parameters and main characteristics*

ALS-surveys parameters	**Description / Value**
Period of the survey	June/July 2015-2019
Survey general conditions	Snow-free conditions, standing forest (2015), windthrown forest (2019)
LiDAR system	Riegl LiDAR VQ780i
Average flight altitude (a.g.l.)	1400 m
Flying speed	132 knots
Scan angle	32°
Laser frequency	100kHz
Average point density	40pt/m^2

Table 5.6 *Overview of HEC-HMS components and respective inputs necessary for model simulations*

HEC-HMS component	Parameter	Method	Input	Unit
Basin component	Basin discretization	Structured Discretization	DEM	m
	Canopy	Gridded Simple Canopy	Initial water storage	%
			Max water storage	mm
			Crop coefficient	(-)
	Loss	Gridded SCS-CN	CN grid	(-)
	Surface	Gridded Simple Surface	Initial water storage	%
			Max water storage	mm
	Transform	ModClark	Time of concentration	hours
			Storage coefficient	hours
Meteorological component	Precipitation Temperature	/	Average daily precipitation	mm/h
			Average daily temperature	°C
	Evapotranspiration	Hamon	Average daily temperature	°C
			Hamon coefficient	(-)

Table 5.7 *Overview of RESS inputs necessary for computing soil stability simulations. Pre and post terms stand for pre-event scenario (standing forest conditions) and post-event scenario (windthrows conditions)*

Input	Value	Unit of measurement
DEM without road	1.0	m
Road location	/	(-)
Drainage systems location	/	(-)
Soil depth (z)	1.0	m
Internal friction angle (ϕ)	35.0	Decimal degrees
Soil density (ρ_s)	1800	$kg \cdot m^{-3}$
Soil transmissivity (Tr)	30.0	$m^2 \cdot s^{-1}$
Soil cohesion (Coh_s)	1000	$kg \cdot m^{-1} \cdot s^{-2}$
Root cohesion (Coh_r)	3000 (pre-event) 1500 (post-event)	$kg \cdot m^{-1} \cdot s^{-2}$
Vegetation surcharge (W)	2000 (pre-event) 500 (post-event)	$kg \cdot m^{-1} \cdot s^{-2}$
Road width	5.0	m
Relative road cut depth (r_{rc})	0.5	m
Max rainfall ($Rain_{max}$)	43.4 (2015)	$mm \cdot h^{-1}$
Rainfall intensity increment step	0.0	$mm \cdot h^{-1}$
Water density (ρ_w)	1000	$kg \cdot m^{-3}$
Flow direction algorithm	D-inf	(-)

Table 5.8 *Statistical results of the Student t-test computed looking at daily average runoff values calculated by HEC-HMS model in function of windthrown-induced land use changes at sub-basin detail*

Sub-basin		**Scenario**		
		Standing forest (pre-event)	Windthrown forest (post-event)	
	Windthrown trees (%)	**Variance**		**p-value**
1	0.0%	0.0306	0.0306	-
2	0.0%	0.0304	0.0304	-
3	0.0%	0.0294	0.0294	-
4	1.4%	0.0302	0.0302	-
5	9.3%	0.0962	0.2750	1.57E-04
6	0.0%	0.0097	0.0097	-
7	12.0%	0.0310	0.0867	1.71E-03
8	0.2%	0.0287	0.0289	-
9	23.3%	0.0303	0.0890	1.51E-03
10	29.7%	0.0305	0.0897	2.10E-03
11	7.3%	0.0296	0.0298	2.20E-16
12	21.8%	0.0306	0.0879	1.53E-03
13	2.0%	0.0298	0.0746	3.49E-02
14	21.7%	0.0306	0.0893	1.94E-06
15	42.5%	0.0310	0.0861	2.50E-03
16	42.4%	0.0296	0.0893	1.06E-03
17	1.1%	0.0295	0.0295	-
18	41.0%	0.0308	0.0898	6.49E-03
19	20.9%	0.0297	0.0892	1.72E-05
20	40.9%	0.0307	0.0762	2.19E-02
21	8.9%	0.0304	0.0834	2.36E-03
22	11.2%	0.0311	0.0904	1.87E-03
23	16.0%	0.0312	0.0885	3.06E-03
24	1.7%	0.0309	0.0312	-

Table 5.9 *Outcomes of R-based linear regression analysis computed looking at HEC-HMS outcomes in function of windthrown-induced land use changes*

Residuals Median	t stat	p-value	F stat	Residual std error	Multiple R-squared
0.184	8.444	2.38E-08	71.30	0.514	0.76

CHAPTER 6

6.1 Final remarks

The thesis project was structured into four research studies that jointly improved the scientific knowledge regarding the dilemma of land degradation processes induced by the presence of road networks. Looking at the main research objective mentioned above, specific research purposes were defined as detailed in the respective introductive section. Specific objectives were therefore achieved through the development of four different studies, successively finalized in four respective research articles proposed to the scientific community during the doctoral period.

In line with the above, the role of rural roads in altering geomorphological and hydrological properties of a steep-slope agricultural system was initially investigated in the first two scientific articles (chapters 2 and 3), while roads contribution in the occurrence of terrain instabilities affecting a steep-slope mountain grassland was explored in the following chapter 4. Finally, in chapter 5 the effects on land use changes driven by windthrows in the alteration of hydrological regimes and terrain stability of a forested catchment characterized by the presence of a rural road was analyzed. In this connection, it is needful to point out as the first two studies relied on the multi-temporal acquisition and elaboration of UAV-based terrain reconstruction at the hillslope scale, while the third and fourth were achieved through ALS-derived data analysis and processing at the watershed detail. Just as importantly, physical models implementation and geographic data analysis commonly distinguished the proposed researches.

Along the first study (chapter 2), geomorphological alterations affecting a steep-slope terraced vineyard (Trentino Alto-Adige region, northern Italy) involved in the occurrence of shallow landslides were investigated starting from multi-temporal UAV surveys. The contribution of the rural road located within the study area in altering water overland flows was detected through the morphological RPII index (Tarolli *et al.*, 2013), while UAV-derived high-resolution terrain reconstructions led to quantify morphological changes affecting the landslide-prone area by Digital elevation models of Difference (DoD) computation. Multi-temporal comparison of profile curvature, roughness and features extraction led to described geomorphological dynamics involving the instable hillslope and observe changes in specific landslides features over time. Results attested the usefulness of high-resolution and multi-temporal UAV-based photogrammetric surveys to investigate landslides

occurrence potentially related with the presence of rural road within a steep-slope terraced system. Moreover, the proposed multi-temporal comparison of geomorphometric indicators and landslides' features turned out to be particularly useful to detect geomorphological changes occurring at the field scale over time. Research findings lays the groundwork for future challenges concerning the influence of road management and design on the occurrence of similar land degradation phenomena. Moreover, further investigations could be conducted to detect the presented issue in hydrologic terms, therefore focusing on effective planning of drainage systems along the roadway in order to prevent future occurrence of such dynamics.

The same study area was successively considered for more in-depth analysis relating the role played by the rural road in altering water runoff directions and amount, to further detect its contribution in the observed land degradative processes (chapter 3). Hydrological analyses of water flow's depth alterations due to the presence of the road were carried out by applying the SIMulated Water Erosion model (SIMWE; Mitasova *et al*., 2013). Model simulations focused on different scenarios looking at the presence of the road and assuming its absence through specific DEM smoothing procedure. Local quantification of water runoff deviated by the road toward the shallow landslides was as well performed in function of increasing rainfall peaks set as input for model simulations. The critical interaction between road and water runoff affecting the terraced vineyard was hence evinced. Results attested as the presence of rural roads within a steep slope agricultural area can be particularly troublesome in terms of runoff deviation on the way to the collapsed hillslopes. In addition, research outcomes proved the usefulness of multi-temporal hydrological modeling in the detection of road-water-landslides interaction at the centimetres scale, starting from high-resolution UAV-based terrain reconstructions. A new methodology to compute hydrologic maps and modeling is therefore proposed, aiming to identify specific zones potentially involved in the occurrence of similar issues in the future. The presented comparison of hydrological simulations could allow the fulfillment of valid solutions for hillslopes management and stabilization, as well as for the design of cost-effective drainage systems along the road. Critical rainfall thresholds related with the occurrence of shallow landslides and erosion processes could be hence identified starting from the proposed application of SIMWE model, in order to plan aimed at mitigation interventions. In this regard, more in-depth investigation of model's parameters setting could be conducted looking at uncertainties related with their choice, for example considering the proven relationship between antecedent previous rainfall events, soil moisture and Manning's *n*. Finally, detailed geotechnical investigations (e.g., predictive slope stability analysis) could be undertaken starting from research results, to thoroughly attest the effective role of rural roads in landslides triggering and hillslopes destabilization in different

scenarios.

Advanced study concerning the contribution of roads in the occurrence of land degradation processes was furthermore achieved in the third research (chapter 4). Researches moved therefore from the hillslope-scale of the first two studies to the catchment level. Specifically, the interaction between snowmelt runoff and road presence in the occurrence of terrain instabilities affecting a landslide-prone mountain grassland (Trentino Alto-Adige region, northern Italy) was examined. ALS-derived data were processed to obtain high-resolution DEM of the mountain basin. Groundbreaking multi-modeling approach was hence set out. The hydrological Snowmelt Runoff Model (SRM; Martinec *et al*., 2008) was firstly implemented, to quantify water runoff resulting from the melting snowpack within the grassland area. Starting from SRM outcomes, a predictive mapping of terrain instabilities resulting from the deviation of snowmelt runoff along both the hillslope and the roadway was elaborated through the geomorphological Road Erosion Steady-State model (RESS; Dietrich *et al*., 1992, Montgomery and Dietrich, 1994, Borga *et al*., 2005). Finally, the hydrological SIMulated Water Erosion model (SIMWE) was jointly applied to detect the interaction between road and snowmelt overflows. Specifically, the role of the road in altering superficial snowmelt pathways was proved by comparing model outcomes looking at its presence and supposing its absence by an improved application of the smoothing procedure proposed in chapter 3 for DEMs. Results proved the key contribution played by the road in altering snowmelt runoff directions, as well as its influence in the foreseen activation of terrain instabilities at the observed landslide area. Starting from research outcomes, future challenges could involve the identification of the optimal location of drainage system along the roadway, to efficiently intercept water runoff resulting from rainfall and snowmelt process. Moreover, similar analysis could be conducted looking at larger basins, also focusing on the impact of the wide variability of model parameters on simulation results. Finally, the proposed multi-models application could be applied to mapping terrain instabilities affecting similar catchments at different altitudes levels.

The last study is presented in the chapter 5. In light of the previous researches, with the latter special attention was paid to analyze the contribution of windthrown-driven land use changes in the alteration of hydrological regimes and terrain stability of a wind-disturbed forested catchment, characterized by the presence of a rural road and affected by the nearby activation of a shallow landslide. The study considered a forested basin located in Veneto region (northern Italy), impacted by widespread windthrows occurred during the Vaia storm of late October 2018. ALS-data were combined with the application of the Hydrologic Engineering Center-Hydrologic Modelling System model (HEC-HMS; US Army Corps of Engineers, 2000) and the geomorphological RESS model. The effects of the

blowdown event in term of rainfall runoff alteration and hillslope destabilization was therefore quantified through an integrated multi-temporal GIS-based approach. Starting from high-resolution DTMs and CHMs reconstruction, ALS-data and models simulations were processed considering pre-event and post-event conditions (respectively corresponding to standing forest and windthrown forest conditions). The contribution of the rural road in altering terrain stability was hence taken into account. Results proposed in this last study attested the significant role played by windthrows in altering runoff regimes over time at sub-basin scale, therefore potentially promoting the activation of shallow landslides and terrain instabilities, specifically downstream of the road. Furthermore, the correlation between windthrows occurrence and runoff alterations was evinced. Starting from research outcomes, more studies could be conducted to further inspect the role of the road in the alteration of runoff flow paths respectively for standing forest and wind-disturbed forest conditions. In addition, multi-temporal ALS-based geomorphological analysis could be performed to detect the morphometrical changes characterizing wind-disturbed forested hillslope affected by landslides incidence. The investigated issue could be beyond detected by integrating ALS-data and plot-scale UAV-based photogrammetric surveys. Finally, sensitive analysis could be conducted in order to detect uncertainties related with models' parameters settings at the analysed scale. Results presented in this last work represents a solid starting point for planning specific interventions aiming to prevent the occurrence of similar issues, concurrently with the occurrence of analogous natural disturbances affecting forested ecosystems worldwide.

6.2 References (Introduction and Final remarks)

Abu Hammad, A., Tumeizi, A., 2012. Land degradation: Socioeconomic and environmental causes and consequences in the eastern mediterranean. L. Degrad. Dev. 23, 216–226. https://doi.org/10.1002/ldr.1069

Abushandi, E., Merkel, B., 2013. Modelling Rainfall Runoff Relations Using HEC-HMS and IHACRES for a Single Rain Event in an Arid Region of Jordan. Water Resources Management 27, 2391–2409. https://doi.org/10.1007/s11269-013-0293-4

Akay, A.E., Erdas, O., Reis, M., Yuksel, A., 2008. Estimating sediment yield from a forest road network by using a sediment prediction model and GIS techniques. Build. Environ. 43, 687-695. https://doi.org/10.1016/j.buildenv.2007.01.047

Akker, J.J.H. & Canarache, A., 2001. Two European concerted actions on subsoil compaction. Zeitschrift für Kulturtechnik und Landentwicklung 42 (1), 15-22.

Aksoy, H., Kavvas, M.L., 2005. A review of hillslope and watershed scale erosion and sediment transport models. Catena 64 (2-3), 247–271. https://doi.org/10.1016/j.catena.2005.08.008

Ali, M., Khan, S.J., Aslam, I., Khan, Z., 2011. Landscape and Urban Planning Simulation of the impacts of land-use change on surface runoff of Lai Nullah Basin in Islamabad, Pakistan. Landscape and Urban Planning 102 (4), 271–279. https://doi.org/10.1016/j.landurbplan.2011.05.006

American Society of Civil Engineers (ASCE), 2018. Design and Construction of Urban Stormwater Management Systems. https://doi.org/https://doi.org/10.1061/9780872628557.

Anderson, R.L., Rowntree, K.M., Le Roux, J.J., 2021. An interrogation of research on the influence of rainfall on gully erosion. CATENA 206, 105482. https://doi.org/10.1016/j.catena.2021.105482

Antrop, M., 2004. Landscape change and the urbanization process in Europe. Landsc. Urban Plan. 67, 9–26. https://doi.org/10.1016/S0169-2046(03)00026-4

Arnaez, J., Lasanta, T., Ruiz-Flaño, P., Ortigosa, L., 2007. Factors affecting runoff and erosion under simulated rainfall in Mediterranean vineyards. Soil Tillage Res. 93, 324–334. https://doi.org/10.1016/j.still.2006.05.013

Arnáez, J., Lasanta, T., Ruiz-Flaño, P., Ortigosa, L., 2007. Factors affecting runoff and erosion under simulated rainfall in Mediterranean vineyards. Soil Tillage Res. 93 (2), 324–334. https://doi.org/10.1016/j.still.2006.05.013

Asher, S., Novosad, P., 2020. Rural roads and local economic development†. Am. Econ. Rev. 110, 797–823. https://doi.org/10.1257/aer.20180268

Ashley, R., Blackwood, D., Butler, D., Jowitt, P., Davies, J., Smith, H., Gilmour, D., Oltean-Dumbrava, C., 2008. Making Asset Investment Decisions for Wastewater Systems That Include Sustainability. J. Environ. Eng. 134, 200–209. https://doi.org/10.1061/(asce)0733-9372(2008)134:3(200)

Bajocco, S., Analysis, A.E., Ferrara, A., 2012. The Impact of Land Use/Land Cover Changes on Land Degradation Dynamics: A Mediterranean Case Study. Environmental Management 49, 980-989. https://doi.org/10.1007/s00267-012-9831-8

Balbuena, R H.; Terminiello, A. M.; Claverie, J. A.; Casado, J. P.; Marlats, R., 2000. Soil compaction by forestry harvester operation. Evolution of physical properties. Rev. Bras. Eng. Agrícola e Ambient. 4, 453–459. https://doi.org/10.1590/S1415-43662000000300023

Bebi, P., Seidl, R., Motta, R., Fuhr, M., Firm, D., Krumm, F., Conedera, M., Ginzler, C., Wohlgemuth, T., Kulakowski, D., 2017. Forest Ecology and Management Changes of forest cover and disturbance regimes in the mountain forests of the Alps q. For. Ecol. Manage. 388, 43–56. https://doi.org/10.1016/j.foreco.2016.10.028

Berger, F., Rey, F., 2004. Mountain Protection Forests against Natural Hazards and Risks: New French Developments by Integrating Forests in Risk Zoning. Nat. Hazards 33, 395–404. https://doi.org/10.1023/B:NHAZ.0000048468.67886.e5

Berggren, K., Olofsson, M., Viklander, M., Svensson, G., Gustafsson, A.-M., 2012. Hydraulic Impacts on Urban Drainage Systems due to Changes in Rainfall Caused by Climatic Change. J. Hydrol. Eng. 17, 92–98. https://doi.org/10.1061/(asce)he.1943-5584.0000406

Bischetti, G.B., Chiaradia, E.A., Epis, T., Morlotti, E., 2009. Root cohesion of forest species in the Italian Alps. Plant Soil 324, 71–89. https://doi.org/10.1007/s11104-009-9941-0

Bodoque, J.M., M, J.A.B.-C.R.J., Perucha, M.Á., Nadal-Romero, E., Stoffel, M., 2017. Quantifying soil erosion from hiking trail in a protected natural area in the spanish Pyreneeis. L. Degrad. Dev. 28 (7), 2255–2267. https://doi.org/10.1002/ldr.2755

Bordoni, M., Galanti, Y., Bartelletti, C., Persichillo, M.G., Barsanti, M., Giannecchini, R., Avanzi, G.D., Cevasco, A., Brandolini, P., Galve, J.P., Meisina, C., 2020. The influence of the inventory on the determination of the rainfall-induced shallow landslides susceptibility using generalized additive models. Catena 193, 104630. https://doi.org/10.1016/j.catena.2020.104630

Borga, M., Dalla Fontana, G., Da Ros, D., Marchi, L., 1998. Shallow landslide hazard assessment using a physically based model and digital elevation data. Environ. Geol. 35, 81–88. https://doi.org/10.1007/s002540050295

Borga, M., Dalla Fontana, G., Gregoretti, C., Marchi, L., 2002a. Assessment of shallow landsliding by using a physically based model of hillslope stability. Hydrol. Process. 16, 2833–2851. https://doi.org/10.1002/hyp.1074

Borga, M., Dalla, G., Cazorzi, F., 2002b. Analysis of topographic and climatic control on rainfall-triggered shallow landsliding using a quasi-dynamic wetness index. Journal of Hydrology 268 (1-4), 56–71. https://doi.org/10.1016/S0022-1694(02)00118-X

Borga, M., Tonelli, F., Dalla Fontana, G., Cazorzi, F., 2005. Evaluating the influence of forest roads on shallow landsliding. Ecol. Modell. 187, 85–98. https://doi.org/10.1016/j.ecolmodel.2005.01.055

Borga, M., Tonelli, F., Selleroni, J., 2004. A physically based model of the effects of forest roads on slope stability. Water Resour. Res. 40 (12). https://doi.org/10.1029/2004WR003238

Bossi, G., Cavalli, M., Crema, S., Frigerio, S., Quan Luna, B., Mantovani, M., Marcato, G., Schenato, L., Pasuto, A., 2015. Multi-temporal LiDAR-DTMs as a tool for modelling a complex landslide: A case study in the Rotolon catchment (eastern Italian Alps). Nat. Hazards Earth Syst. Sci. 15, 715–722. https://doi.org/10.5194/nhess-15-715-2015

Bradbury, A., Hine, J., Njenga, P., Otto, A., Muhia, G., Willilo, S., 2017. Evaluation of the Effect of Road Condition on the Quality of Agricultural Produce. AfCAP, Phase 2 Report. ReCAP Project Management Unit, Cardno Emerging Market (UK) Ltd

Brown, K.R., Michael Aust, W., McGuire, K.J., 2013. Sediment delivery from bare and graveled forest road stream crossing approaches in the Virginia Piedmont. For. Ecol. Manage. 310, 836–846. https://doi.org/10.1016/j.foreco.2013.09.031

Bruen, M., Yang, J., 2006. Combined Hydraulic and Black-Box Models for Flood Forecasting in Urban Drainage Systems. J. Hydrol. Eng. 11, 589–596. https://doi.org/10.1061/(asce)1084-0699(2006)11:6(589)

Brunetti, M.T., Peruccacci, S., Rossi, M., Luciani, S., Valigi, D., Guzzetti, F., 2010. Rainfall thresholds for the possible occurrence of landslides in Italy. Nat. Hazards Earth Syst 10, 447–458. https://doi.org/10.5194/nhess-10-447-2010

Caine, N., 1980. The rainfall intensity duration control of shallow landslides and debris flows. Geografiska Annaler. Series A, Physical Geography 62 (1-2), 23-27. Taylor & Francis (Eds). https://doi.org/10.2307/520449

Camarero, J.J., Colangelo, M., Gazol, A., Pizarro, M., Valeriano, C., Igual, J.M., 2021. Effects of Windthrows on Forest Cover , Tree Growth and Soil Characteristics in Drought-Prone Pine Plantations. Forests 12 (7). https://doi.org/10.3390/f12070817

Cao, L., Zhang, K., Dai, H., Liang, Y., 2015. Modeling Interrill Erosion on Unpaved Roads in the Loess Plateau of China. L. Degrad. Dev. 26, 825–832. https://doi.org/10.1002/ldr.2253

Cao S. C., Chen L., Gao W., Chen Y., Y.M., 2006. Impact of planting grass on terrene roads to avoid soil erosion. Landsc. Urban Plan. 78, 205–216. DOI:10.1016/J.LANDURBPLAN.2005.07.007

Chalise, D., Kumar, L., Kristiansen, P., 2019. Land degradation by soil erosion in Nepal: A review. Soil Syst. 3, 1–18. https://doi.org/10.3390/soilsystems3010012

Chauhan, S., Sharma, M., Arora, M.K., 2010. Landslide susceptibility zonation of the Chamoli region, Garhwal Himalayas, using logistic regression model. Landslides 7, 411–423. https://doi.org/10.1007/s10346-010-0202-3

Chirici, G., Giannetti, F., Travaglini, D., Nocentini, S., Francini, S., D'Amico, G., Calvo, E., Fasolini, D., Broll, M., Maistrelli, F., Tonner, J., Pietrogiovanna, M., Oberlechner, K., Andriolo, A., Comino, R., Faidiga, A., Pasutto, I., Carraro, G., Zen, S., Contarin, F., Alfonsi, L., Wolynski, A., Zanin, M., Gagliano, C., Tonolli, S., Zoanetti, R., Tonetti, R., Cavalli, R., Lingua, E., Pirotti, F., Grigolato, S., Bellingeri, D., Zini, E., Gianelle, D., Dalponte, M., Pompei, E., Stefani, A., Motta, R., Morresi, D., Garbarino, M., Alberti, G., Valdevit, F., Tomelleri, E., Torresani, M., Tonon, G., Marchi, M., Corona, P., Marchetti, M., 2019. Forest damage inventory after the "Vaia" storm in Italy. Forest@, Journal of Silviculture and Forest Ecology 16, 3–9. https://doi.org/10.3832/efor3070-016

Clark, C.O., 1945. Storage and the unit hydrograph. Trans. Am. Soc. Civ. Eng. 110, 1419–1488.

Coker, R.J., Fahey, B.D. 1993. Road-related mass movement in weathered granite, Golden Downs and Motueka Forests, New Zealand: a note. Hydrol 31, 65–69.

Contreras-Hermosilla, A., 2000. The underlying causes of forest decline. Center for International Forestry Research (CIFOR Eds) https://doi.org/10.17528/cifor/000626

Corbane, C., Andrieux, P., Voltz, M., Chadaeuf, J., Albergel, J., Robbez-Masson, J. M., Zante, P., 2008. Assessing the variability of soil surface characteristics in row-cropped fields: the case of Mediterranean vineyards in Southern France. Catena 72 (1), 79–90. https://doi.org/10.1016/j.catena.2007.04.006

Corbari, C., Ravazzani, G., Galvagno, M., Cremonese, E., Mancini, M., 2017. Assessing crop coefficients for natural vegetated areas using satellite data and eddy covariance stations. Sensors 17 (11). https://doi.org/10.3390/s17112664

Cordoba, J.P., Mergili, M., Aristizábal, E., 2020. Probabilistic landslide susceptibility analysis in tropical mountainous terrain using the physically based r . slope . stability model. Nat. Hazards Earth Syst. Sci. 20, 815–829. https://doi.org/10.5194/nhess-20-815-2020

Corti, G., Cavallo, E., Cocco, S., Biddoccu, M., Brecciaroli, G., Agnelli, A., 2011. Evaluation of Erosion Intensity and Some of Its Consequences in Vineyards from Two Hilly Environments Under a Mediterranean Type of Climate, Italy. Soil Erosion Issues in Agriculture, Danilo Godone and Silvia Stanchi (Eds). DOI: 10.5772/25130

Costa, M., Marchi, N., Bettella, F., Bolzon, P., Lingua, E., 2021. Biological Legacies and Rockfall : The Protective Effect of a Windthrown Forest. Forests 12 (9), 1–17. https://doi.org/10.3390/f12091141

Coxhead, I., Shively, G., 1995. Measuring the Environmental Impacts of Economic Change: the Case of Land Degradation in Philippine Agriculture. University of Wisconsin-Madison, Department of Agricultural Economics, Staff Paper Series (384). https://doi.org/10.22004/ag.econ.12671

Croke, J., Mockler, S., Hairsine, P., Fogarty, P., 2006. Relative contributions of runoff and sediment from sources within a road prism and implications for total sediment delivery. Earth Surf. Process. Landforms 31 (4), 457–468. https://doi.org/10.1002/esp.1279

Cucchiaro, S., Maset, E., Cavalli, M., Crema, S., Marchi, L., Beinat, A., Cazorzi, F., 2020. How does co-registration affect geomorphic change estimates in multi-temporal surveys? GIScience & Remote Sens. 57, 611–632. https://doi.org/10.1080/15481603.2020.1763048

Čuchta, P., 2020. Natural disturbances (with a special reference to windthrow): a literature review, in: Advances in Environmental Research. pp. 153–172.

Da Silva, R.P., Lacerda, W.A., Coelho Netto, A.L., 2022. Relevant geological-geotechnical parameters to evaluate the terrain susceptibility for shallow landslides: Nova Friburgo, Rio de Janeiro, Brazil. Bull. Eng. Geol. Environ. 81, 57. https://doi.org/10.1007/s10064-021-02557-z

Dai, Z., Ma, C., Miao, L., Li, M., Wu, J., Wang, X., 2022. Initiation conditions of shallow landslides in two man-made forests and back estimation of the possible rainfall threshold. Landslides 19, 1031–1044. https://doi.org/10.1007/s10346-021-01823-1

Daigle, P., 2010. A summary of the environmental impacts of roads, management responses, and research gaps: A literature review. BC Journal of Ecosystems and Management 10(3):65–89. DOI:10.22230/jem.2010v10n3a38

Dalantai, S., Sumiya, E., Bao, Y., Otgonbayar, M., Mandakh, U., Batsaikhan, B., Natsagdorj, B., 2021. Spatial-temporal changes of land degradation caused by natural and human induced factors: Case study of bulgan province in central mongolia. Int. Arch. Photogramm. Remote Sens. Spat. Inf. Sci. - ISPRS Arch. 43, 79–85. https://doi.org/10.5194/isprs-archives-XLIII-B4-2021-79-2021

D'Amboise, C.J.L., Teich, M., Hormes, A., Steger, S., Berger, F., 2021. Modeling Protective Forests for Gravitational Natural Hazards and How It Relates to Risk-Based Decision Support Tools, in: Protective Forests as Ecosystem-Based Solution for Disaster Risk Reduction. https://doi.org/10.5772/intechopen.99510

David K. Keefer, Raymond C. Wilson, Robert K. Mark, Earl E. Brabb, William M.Brown, Stephen D. Ellen, Edwin L. Harp, Gerald F. Wieczorek, C.S.A. and Robert S.Z., 1987. Real-Time Landslide Warning during Heavy Rainfall. Science 238 (4829), 921–925. DOI: 10.1126/science.238.4829.92

Deluca, T.H., Freimund, W.A., Cole, D.N., 1998. Influence of Llamas, horses and hikers on soil erosion from established recreation trails in western Montana. Environ. Management 22 (2). 255–262. DOI: 10.1007/s002679900101

Demir, M., 2007. Impacts, management and functional planning criterion of forest road network system in Turkey. Transp. Res. Part A Policy Pract. 41, 56–68. https://doi.org/10.1016/j.tra.2006.05.006

Dhakal, A.S., Sidle, R.C., 2003. Long-term modelling of landslides for different forest management practices. Earth Surf. Process. Landforms 28, 853–868. https://doi.org/10.1002/esp.499

Dietrich, W.E., Wilson, C.J., Montgomery, D.R., McKean, J., Bauer, R., 1992. Erosion thresholds and land surface morphology. Geology 20, 675–679. https://doi.org/10.1130/0091-7613(1992)020<0675:ETALSM>2.3.CO;2

Dimitriou, E., 2011. Overland Flow, in: Encyclopedia of Earth Sciences Series. Springer, Dordrecht. pp. 536–536. https://doi.org/10.1007/978-90-481-3585-1_104

Donat, M.G., Lowry, A.L., Alexander, L. V, O'Gorman, P.A., Maher, N., 2017. More extreme precipitation in the world's dry and wet regions. Nature 6, 508–513. https://doi.org/10.1038/nclimate2941

Dougherty, M., Dymond, R.L., Grizzard, T.J., Godrej, A.N., Zipper, C.E., Randolph, J., 2007. Quantifying Long-Term Hydrologic Response in an Urbanizing Basin. J. Hydrol. Eng. 12, 33–41. https://doi.org/10.1061/(asce)1084-0699(2007)12:1(33)

Du, E., Link T.E., Wei, L., Marchall, J.D. 2016. Evaluating hydrologic effects of spatial and temporal patternsof forest canopy change using numerical modelling. Hydrological Processes 30, 217-231. https://doi.org/10.1002/hyp.10591

Dutton, A.L., Loague, K., Wemple, B.C., 2005. Simulated effect of a forest road on near-surface hydrologic response and slope stability. Earth Surf. Process. Landforms 30, 325–338. https://doi.org/10.1002/esp.1144

Ebodé, V.B., Mahé, G., Dzana, J.G., Amougou, J.A., 2020. Anthropization and Climate Change: Impact on the Discharges of Forest Watersheds in Central Africa. Water 12, 2718. https://doi.org/10.3390/w12102718

Eker, R., Aydin, A., 2014. Assessment of forest road conditions in terms of landslide susceptibility: a case study in Yığılca Forest Directorate (Turkey). Turkish J. Agric. For. 38, 281–290. https://doi.org/10.3906/tar-1303-12

Esri, 2021. Mosaic To New Raster (Data Management). Esri tool Ref. tools.

Fagnano, M., Diodato, N., Alberico, I., Fiorentino, N., 2012. An overview of soil erosion modelling compatible with RUSLE approach. Rend. Fis. Acc. Lincei 23, 69–80. https://doi.org/10.1007/s12210-011-0159-8

Fannin, R.J., Lorbach, J., 2007. Guide to forest road engineering in road engineering in mountainous terrain. Forest Harvesting and Engineering Working Paper 2, Food and Agriculture Organization Of The United Nations (Eds). https://www.fao.org/3/a1241e/a1241e00

FAO and ITPS, 2015. Status of the World's Soil Resources: Main Report. Food and Agriculture Organization Of The United Nations (Eds). https://www.fao.org/documents/card/en/c/c6814873-efc3-41db-b7d3-2081a10ede50/

Faouzi, E., Arioua, A., Hssaisoune, M., Boudhar, A., Elaloui, A., Karaoui, I., 2022. Sensitivity analysis of CN using SCS-CN approach, rain gauges and TRMM satellite data assessment into HEC-HMS hydrological model in the upper basin of Oum Er Rbia, Morocco. Model. Earth Syst. Environ. https://doi.org/10.1007/s40808-022-01404-8

Farrell, T.A., Marion, J.L., 2002. Trail impacts and trail impact management related to ecotourism visitation at Torres del Paine National Park, Chile. Leisure/Loisir 26 (1-2), 31–59. DOI:10.1080/14927713.2001.9649928

Filho, W.L., Mandel, M., Al-Amin, A.Q., Feher, A., Chiappetta Jabbour, C.J. 2017. An assessment of the causes and consequences of agricultural land abandonment in Europe. International Journal of Sustainable Development & World Ecology 24 (6). https://doi.org/10.1080/13504509.2016.1240113

Fleming, M.J., Doan, J.H., 2003. Geospatial hydrologic modeling extension, HEC-GeoHMS, user's manual.

Foltz, R.B., Copeland, N.S., Elliot, W.J., 2009. Reopening abandoned forest roads in northern Idaho, USA: Quantification of runoff, sediment concentration, infiltration, and interrill erosion parameters. J. Environ. Manage. 90, 2542–2550. https://doi.org/10.1016/j.jenvman.2009.01.014

Fox, D.M., Bryan, 5 R B.:, 2000. The relationship of soil loss by interrill erosion to slope gradient. Catena 38 (3), 211–222. https://doi.org/10.1016/S0341-8162(99)00072-7

Fu, B., Newham, L.T.H., Ramos-Scharrón, C.E., 2010. A review of surface erosion and sediment delivery models for unsealed roads. Environ. Model. Softw. 25, 1–14. https://doi.org/10.1016/j.envsoft.2009.07.013

Fungo, E., Krygsman, S., Nel, H., 2017. The role of road infrastructure in agricultural production. Southern African Transport Conference, Pretoria, South Africa 36. http://hdl.handle.net/2263/62769

Liu, G., Tian, F. X., Warrington, D. N., Zheng, S. Q., Zhang, Q. 2010. Efficacy of grass for mitigating runoff and erosion from an artificial loessial earthen road. American Society of Agricultural and Biological Engineers, Transactions of the ASABE. 53(1): 119-125. DOI: 10.13031/2013.29509)

Lopez-Vincente, M., Sun, X., Onda, Y., Kato, H., Gomi, T., Hiraoka, M. 2017. Effect of tree thinning and skidding trails on hydrological connectivity in two Japanese forest catchments. Geomorphology 292, 104-114. https://doi.org/10.1016/j.geomorph.2017.05.006

Galati, A., Gristina, L., Crescimanno, M., Barone, E., Novara, A., 2015. Towards more efficient incentives for agri-environment measures in degrade and eroded vineyards. L. Degrad. Dev. 26 (6), 557-564. https://doi.org/10.1002/ldr.2389

Getzner, M., Gutheil-Knopp-Kirchwald, G., Kreimer, E., Kirchmeir, H., Huber, M., 2017. Gravitational natural hazards: Valuing the protective function of Alpine forests. For. Policy Econ. 80, 150–159. https://doi.org/10.1016/j.forpol.2017.03.015

Ghafari, H., Gorjia, M., Arabkhedri, M., Roshani, G.A., Heidaria, A., Akhavand, S., 2017. Identification and prioritization of critical erosion areas based on onsite and offsite effects. Catena 156, 1-9. https://doi.org/10.1016/j.catena.2017.03.014

Giannetti, F., Pecchi, M., Travaglini, D., Francini, S., Amico, G.D., Vangi, E., Cocozza, C., Chirici, G., 2021. Estimating VAIA Windstorm Damaged Forest Area in Italy Using Time Series Sentinel-2 Imagery and Continuous Change Detection Algorithms. Forests 12 (6), 1–16. https://doi.org/10.3390/f12060680

Gollin, D., Rogerson, R., 2010. Agriculture, roads, and economic development in Uganda. NBER Working Paper 15863. DOI 10.3386/w15863

Grassini, P., Eskridge, K.M., Cassman, K.G., 2013. Distinguishing between yield advances and yield plateaus in historical crop production trends. Nat. Commun. 4, 2918. https://doi.org/10.1038/ncomms3918

Gruszowski, K.E., Foster, I.D.L., Lees, A., Charlesworth, S.M., 2003. Sediment sources and transport pathways in a rural catchment, Herefordshire, UK. Hydrol. Process. 17 (13), 2665–2681. https://doi.org/10.1002/hyp.1296

Gucinski, H., Furniss, M.J., Ziemer, R.R., Brookes, M.H., 2001. Forest roads: A synthesis of scientific information. General Technical Report PNW-GTR-509. Portland, Oregon: U.S. Dept. of Agriculture, Forest Service. 1, 103.

Guduru, J.U., Jilo, N.B., Rabba, Z.A., Namara, W.G., 2022. Rainfall-runoff modeling using HEC-HMS model for Meki River watershed, rift valley basin, Ethiopia. J. African Earth Sci. 104743. https://doi.org/10.1016/j.jafrearsci.2022.104743

Gumus, S., Acar, H.H., Toksoy, D., 2008. Functional forest road network planning by consideration of environmental impact assessment for wood harvesting. Environ. Monit. Assess. 142, 109–116. https://doi.org/10.1007/s10661-007-9912-y

Gunter, B., 2005. Rainfall-runoff Modeling of Ungauged. Encycl. Hydrol. Sci. 2274, 2267-2274. https://doi.org/10.1002/hyp

Gutiérrez-Martín, A., 2020. A GIS-physically-based emergency methodology for predicting rainfall-induced shallow landslide zonation. Geomorphology 359, 107121. https://doi.org/10.1016/j.geomorph.2020.107121

Guzzetti, F., Peruccacci, S., Rossi, M., Stark, C.P., 2007. Rainfall thresholds for the initiation of landslides in central and southern Europe. Meteorol Atmos Phys 98, 239–267. https://doi.org/10.1007/s00703-007-0262-7

Halsnas, K., Trarup, S., 2009. Development and climate change: A mainstreaming approach for assessing economic, social, and environmental impacts of adaptation measures. Environ. Manage. 43, 765–778. https://doi.org/10.1007/s00267-009-9273-0

Halwatura, D., Najim, M.M.M., 2013. Environmental Modelling & Software Application of the HEC-HMS model for runoff simulation in a tropical catchment. Environ. Model. Softw. 46, 155–162. https://doi.org/10.1016/j.envsoft.2013.03.006

Hamdan, A.N.A.., Almuktar, S.., Scholz, M., 2021. Rainfall-Runoff Modeling Using the HEC-HMS Model for the Al-Adhaim River Catchment, Northern Iraq. Hydrology 8 (2). https://doi.org/10.3390/hydrology8020058

Hamdy, A., Aly, A., 2014. Land Degradation , Agriculture Productivity And Food Security. V International Scientific Agricultural Symposium Agrosym 2014, Review Paper 10.7251/AGSY1404708H

Hanewinkel, M., Hummel, S., Albrecht, A., 2011. Assessing natural hazards in forestry for risk management: a review. Eur. J. For. Res. 130, 329–351. https://doi.org/10.1007/s10342-010-0392-1

Hein, L., 2007. Assessing the costs of land degradation: a case study for the Puentes catchment, southeast Spain. L. Degrad. Dev. 18 (6), 631–642. https://doi.org/10.1002/ldr.802

Huang, Y., Zhao, L., 2018. Review on landslide susceptibility mapping using support vector machines. Catena 165, 520–529. https://doi.org/10.1016/j.catena.2018.03.003

Jaafari, A., Janizadeh, S., Abdo, H.G., Mafi-Gholami, D., Adeli, B., 2022. Understanding land degradation induced by gully erosion from the perspective of different geoenvironmental factors. J. Environ. Manage. 315, 115181. https://doi.org/10.1016/j.jenvman.2022.115181

Jean-Matthieu, M., 2019. LiDARtRee: Forest Analysis with Airborne Laser Scanning (LiDAR) Data. https://gitlab.irstea.fr/jean-matthieu.monnet/LiDARtRee

Jebur, M.N., Pradhan, B., Tehrany, M.S., 2014. Optimization of landslide conditioning factors using very high-resolution airborne laser scanning (LiDAR) data at catchment scale. Remote Sens. Environ. 152, 150–165. https://doi.org/10.1016/j.rse.2014.05.013

Karki, K.B., Ojha, R. B., 2021. Land Degradation. In: Ojha, R.B., Panday, D. (eds) The Soils of Nepal. World Soils Book Series. Springer, Cham. https://doi.org/10.1007/978-3-030-80999-7_10

Kelly, C., Ferrara, A., Wilson, G.A., Ripullone, F., Nolè, A., Harmer, N., Salvati, L., 2015. Community resilience and land degradation in forest and shrubland socio-ecological systems: Evidence from Gorgoglione, Basilicata, Italy. Land use policy 46, 11–20. https://doi.org/10.1016/j.landusepol.2015.01.026

Keshavarzi, A., Kumar, V., Bottega, E.L., Rodrigo-Comino, J., 2019. Determining Land Management Zones Using Pedo-Geomorphological Factors in Potential Degraded Regions to Achieve Land Degradation Neutrality. Land 8 (6). https://doi.org/10.3390/land8060092

Kim, S.W., Chun, K.W., Kim, M., Catani, F., Choi, B., Seo, J. Il, 2021. Effect of antecedent rainfall conditions and their variations on shallow landslide-triggering rainfall thresholds in South Korea. Landslides 18, 569–582. https://doi.org/10.1007/s10346-020-01505-4

Kiprono, P., Matsumoto, T., 2018. Roads and farming: the effect of infrastructure improvement on agricultural intensification in South-Western Kenya. Agrekon 57, 198–220. https://doi.org/10.1080/03031853.2018.1518149

Knebl, M.R., Yang, Z., Hutchison, K., Maidment, D.R., 2005. Regional scale flood modeling using NEXRAD rainfall , GIS , and HEC-HMS / RAS: a case study for the San Antonio River Basin Summer 2002 storm event. J Environ Manage. 75 (4), 325–336. https://doi.org/10.1016/j.jenvman.2004.11.024

Koneti, S., Sunkara, S.L., Roy, P.S., 2018. Hydrological Modeling with Respect to Impact of Land-Use and Land-Cover Change on the Runoff Dynamics in Godavari River Basin Using the HEC-HMS Model. ISPRS Int. J. Geo-Inf. 7 (6). https://doi.org/10.3390/ijgi7060206

Krejci, L., Kolejka, J., Vozenilek, V., Machar, I., 2018. Application of GIS to Empirical Windthrow Risk Model in Mountain Forested Landscapes. Forests 9 (2), 1–18. https://doi.org/10.3390/f9020096

Kuriata-Potasznik, A.B., Szymczyk, S., 2016. Variability of the water availability in a river lake system - A case study of lake symsar. J. Water L. Dev. 31, 87–96. https://doi.org/10.1515/jwld-2016-0039

Lasanta, T., Arnàez, J., Pascual, N., Ruiz-Flaño, P., Errea, M.P., Lana-Renault, N. 2017. Space–time process and drivers of land abandonment in Europe. Catena 149 (3), 810-823. https://doi.org/10.1016/j.catena.2016.02.024

Laurance, W.F., Sayer, J., Cassman, K.G., 2014. Agricultural expansion and its impacts on tropical nature. Trends Ecol. Evol. 29, 107–116. https://doi.org/10.1016/j.tree.2013.12.001

Lennartz, T., 2013. Constructing Roads—Constructing Risks? Settlement Decisions in View of Landslide Risk and Economic Opportunities in Western Nepal. Mt. Res. Dev. 33, 364–371. https://doi.org/10.1659/mrd-journal-d-13-00048.1

Leung, Y-F., 1992. A Study of Trail Degradation along the Pat Sin Range, North New Territories, Hong Kong. M.Phil. Thesis., The Chinese University of Hong Kong

Leung, Y-F., Marion, L., 1996. Trail degradation as influenced by environmental factors: A state-of-knowledge review. Journal of Soil and Water Conservation 51 (2), 130-136. ISSN: 1941-3300

Levers, C., Schneider, M., Prishchepov, A.V., Estel, S., Kuemmerle, T. 2018. Spatial variation in determinants of agricultural land abandonment in Europe. Science of The Total Environment 644, 95-111. https://doi.org/10.1016/j.scitotenv.2018.06.326

Li, M., Maclean, D.A., Hennigar, C.R., Ogilvie, J., 2019. Spatial-Temporal Patterns of Spruce Budworm Defoliation within Plots in Québec. Forests 10 (3), 1–21. https://doi.org/10.3390/f10030232

Li, Q., Wei, X., Zhang, M., Liu, W., Giles-hansen, K., Wang, Y., 2018. The cumulative effects of forest disturbance and climate variability on streamflow components in a large forest-dominated watershed. J. Hydrol. 557, 448–459. https://doi.org/10.1016/j.jhydrol.2017.12.056

Lindblom, J., Lundstro, C., Jonsson, A., 2017. Promoting sustainable intensification in precision agriculture : review of decision support systems development and strategies. Precision Agriculture 18, 309–331. https://doi.org/10.1007/s11119-016-9491-4

Liu Y., Hu J., Wang T., Cai C., Li Z., Z.Y., 2016. Effects of vegetation cover and road-concentrated fl ow on hillslope erosion in rainfall and scouring simulation tests in the Three Gorges Reservoir Area, China. Catena 136, 108–117. https://doi.org/10.1016/j.catena.2015.06.006

Liu, Z., Jin, G., Qi, Y., 2012. Estimate of leaf area index in an old-growth mixed broadleaved-korean pine forest in northeastern China. PLoS One 7. https://doi.org/10.1371/journal.pone.0032155

Llanto, G.M., 2012. The Impact of Infrastructure on Agricultural Productivity. Philippine Institute for Development Studies (PIDS), Makati City. http://hdl.handle.net/10419/126883

Llorens, P., Gallart, F., 2000. A simplified method for forest water storage capacity measurement. J. Hydrol. 240, 131–144. https://doi.org/10.1016/S0022-1694(00)00339-5

Loeffler, D., Jones, G., Vonessen, N., Healey, S., Chung, W., 2009. Estimating diesel fuel consumption and carbon dioxide emissions from forest road construction. USDA Forest Service Proceedings. In: McWilliams, Will; Moisen, Gretchen; Czaplewski, Ray, comps. 2009. 2008

Lokesha, M.N., Mahesha, M., 2016. Impact of Road Infrastructure on Agricultural Development and Rural Road Infrastructure development programmes in India. International Journal of Humanities and Social Science Invention 5, 1–7. ISSN: 2319-7722

Louwagie, G., Gay, S.H., Sammeth, F., Ratinger, T., 2011. The potential of European Union policies to address soil degradation in agriculture. L. Degrad. Dev. 22, 5–17. https://doi.org/10.1002/ldr.1028

Luce, C.H., Black, T.A., 1999. Sediment production from forest roads in western Oregon. Water Resour. Res. 35, 2561–2570. https://doi.org/10.1029/1999WR900135

Lucieer, A., Jong, S.M. d., Turner, D., 2014. Mapping landslide displacements using Structure from Motion (SfM) and image correlation of multi-temporal UAV photography. Prog. Phys. Geogr. 38, 97–116. https://doi.org/10.1177/0309133313515293

Lugo, A.E., Gucinski, H., 2000. Function, effects, and management of forest roads. For. Ecol. Manage. 133, 249–262. https://doi.org/10.1016/S0378-1127(99)00237-6

MacDonald, L.H., Sampson, R.W., Anderson, D.M., 2001. Runoff and road erosion at the plot and road segment scales, St John, US Virgin Islands. Earth Surf. Process. Landforms 26, 251–272. https://doi.org/10.1002/1096-9837(200103)26:3<251::AID-ESP173>3.0.CO;2-X

Maedeh, P.A., Wu, W., Irdmoosa, K.G., Acharya, M.S., 2018. A new approach to estimate the factor of safety for rooted slopes with an emphasis on the soil property, geometry and vegetated coverage. Adv. Comput. Des. 3 (3), 269–288. https://doi.org/10.12989/acd.2018.3.3.269

Marion, J.L., Leung, Y.F., 2004. Environmentally sustainable trail management. Environmental Impacts of Ecotourism. https://doi.org/10.1079/9780851998107.0229

Märker, M., Angeli, L., Bottai, L., Costantini, R., Ferrari, R., Innocenti, L., Siciliano, G., 2008. Assessment of land degradation susceptibility by scenario analysis: A case study in Southern Tuscany, Italy. Geomorphology 93, 120–129. https://doi.org/10.1016/j.geomorph.2006.12.020

Martinec J., Rango A., Roberts R., 2008. Snowmelt Runoff Model (SRM) User's Manual. Agricultural Experiment Station, Special Report 100

Mauri, L., Sallustio, L., Tarolli, P., 2019. The geomorphologic forcing of wild boars. Earth Surf. Process. Landforms 44 (10), 2085-2094. https://doi.org/10.1002/esp.4623

Megahan, W.F., Ketcheson, G.L., 1996. Predicting downslope travel of granitic sediments from forest roads in Idaho. J. Am. Water Resour. Assoc. 32 (2), 371–382. https://doi.org/10.1111/j.1752-1688.1996.tb03459.x

Megahan, W.F., Kidd, W.J., 1972. Effect of logging roads on sediment production rates in the Idaho Batholith. USDA For. Serv. Res. Pap. INT-123, Intermt. Res. Station. Ogden, UT.

Mitasova, H., Barton, C.M., Ullah, I., Hofierka, J., Harmon, R.S., 2013. GIS-Based Soil Erosion Modeling. Treatise Geomorphol. Elsevier Inc. 3, 228–258. doi:10.1016/ B978-0-12-374739-6.00052-X

Montgomery, D.R., Dietrich, W.E., 1994. A physically based model for the topographic control on shallow landsliding. Water Resour. Res. 30 (4), 1153–1171. https://doi.org/10.1029/93WR02979

Motha, J.A., Wallbrinka, P.J., Hairsinea, P.B., Grayson, R.B., 2004. Unsealed roads as suspended sediment sources in an agricultural catchment in south-eastern Australia. J. Hydrol. 286, 1–18. https://doi.org/10.1016/j.jhydrol.2003.07.006

Navarro-Hevia, J., Lima-Farias, T.R., de Araújo, J.C., Osorio-Peláez, C., Pando, V., 2016. Soil Erosion in Steep Road Cut Slopes in Palencia (Spain). L. Degrad. Dev. 27, 190–199. https://doi.org/10.1002/ldr.2459

Nawaz, M.F., Bourrié, G., Trolard, F., 2013. Soil compaction impact and modelling. A review. Agron. Sustain. Dev. 33, 291–309. https://doi.org/10.1007/s13593-011-0071-8

Nazirah, A., Sabki, W.O.W.M., Zulkarnian, H., Afizah, A., 2021. Simulation of runoff using HEC-HMS for ungauged catchment. AIP Conf. Proc. 2347. https://doi.org/https://doi.org/10.1063/5.0051957

Nearing, M.A., Pruski, F.F., O'Neal, M.R., 2004. Expected climate change impacts on soil erosion rates: A review. J. Soil Water Conserv. 59 (1), 43–50. https://www.jswconline.org/content/59/1/43

Ngezahayo, E., Ghataora, G., Burrow, M., 2021. Modelling the Effects of Soil Properties, Rainfall and Road Geometry to Erosion in Unpaved Roads. Int. J. Civ. Infrastruct. 4. https://doi.org/10.11159/ijci.2021.015

Nguyen, H.., 2018. A Two-Sample Kolmogorov-Smirnov-Like Test for Big Data. In: Boo, Y., Stirling, D., Chi, L., Liu, L., Ong, KL., Williams, G. (eds) Data Mining. AusDM 2017. Communications in Computer and Information Science, vol 845. Springer, Singapore. https://doi.org/10.1007/978-981-13-0292-3_6

Panagos, P., Ballabio, C., Himics, M., Scarpa, S., Matthews, F., Bogonos, M., Poesen, J., Borrelli, P., 2021. Projections of soil loss by water erosion in Europe by 2050. Environ. Sci. Policy 124, 380–392. https://doi.org/10.1016/j.envsci.2021.07.012

Parsakhoo, A., Lotfalian, M., Kavian, A., Hosseini, S.A., 2014. Assessment of soil erodibility and aggregate stability for different parts of a forest road. J. For. Res. 25, 193–200. https://doi.org/10.1007/s11676-014-0445-2

Pašakarnis, G., Maliene, V., 2010. Towards sustainable rural development in Central and Eastern Europe: Applying land consolidation. Land use policy 27, 545–549. https://doi.org/10.1016/j.landusepol.2009.07.008

Pellegrini, G., Martini, L., Cavalli, M., Rainato, R., Cazorzi, A., Picco, L., 2021. The morphological response of the Tegnas alpine catchment (Northeast Italy) to a Large Infrequent Disturbance. Sci. Total Environ. 770, 145209. https://doi.org/10.1016/j.scitotenv.2021.145209

Pender, J., Nkonya, E., Jagger, P., Sserunkuuma, D., Ssali, H., 2004. Strategies to increase agricultural productivity and reduce land degradation: Evidence from Uganda. Agric. Econ. 31, 181–195. https://doi.org/10.1016/j.agecon.2004.09.006

Pendergrass, A.G., Hartmann, D.L., 2014. Changes in the Distribution of Rain Frequency and Intensity in Response to Global Warming. J. Clim. 27. https://doi.org/10.1175/JCLI-D-14-00183.1

Penna, D., Borga, M., Aronica, G.T., Brigandì, G., Tarolli, P., 2014. The influence of grid resolution on the prediction of natural and road-related shallow landslides. Hydrol. Earth Syst. Sci. 18, 2127–2139. https://doi.org/10.5194/hess-18-2127-2014

Perzl, F., Bono, A., Garbarino, M., Motta, R., 2021. Protective Effects of Forests against Gravitational Natural Hazards, in: Protective Forests as Ecosystem-Based Solution for Disaster Risk Reduction (ECO-DRR). IntechOpen, London. https://doi.org/10.5772/intechopen.99506

Pijl, A., Barneveld, P., Mauri, L., Borsato, E., Grigolato, S., Tarolli, P., 2019. Impact of mechanisation on soil loss in terraced vineyard landscapes. Geogr. Res. Lett. 45. https://doi.org/10.18172/cig.3774

Poesen J., Nachtergaele J., Verstraeten G., V.C., 2003. Gully erosion and environmental change : importance and research needs. Catena 50 (1-2), 91–133. https://doi.org/10.1016/S0341-8162(02)00143-1

Pokorný, R., Stojnič, S., 2012. Leaf area index of Norway spruce stands in relation to age and defoliation. Beskydy 5, 173–180. https://doi.org/10.11118/beskyd201205020173

Popescu, S., Wynne, R., 2004. Seeing the Trees in the Forest: Using LiDAR and Multispectral Data Fusion with Local Filtering and Variable Window Size for Estimating Tree Height. Photogramm. Eng. Remote Sensing 70, 589–604. DOI: 10.14358/PERS.70.5.589

Prosdocimi, M., Calligaro, S., Sofia, G., Fontana, G.D., Tarolli, P., 2015. Bank erosion in agricultural drainage networks: new challenges from structure-from-motion photogrammetry for post-event analysis. Earth Surf. Process. Landforms 40 (14), 1891-1906. https://doi.org/10.1002/esp.3767

Qiao, K., Zhu, W., Hu, D., Hao, M., Chen, S., Cao, S., 2017. Examining the distribution and dynamics of impervious surface in different functional zones of Beijing. Dili Xuebao/Acta Geogr. Sin. 72, 2018–2031. https://doi.org/10.11821/dlxb201711008

Rainato, R., Martini, L., Pellegrini, G., Picco, L., 2021. Catena Hydrological , geomorphic and sedimentological responses of an alpine basin to a severe weather event (Vaia storm). Catena 207, 105600. https://doi.org/10.1016/j.catena.2021.105600

Ramos-Scharròn, C.E. MacDonald, L.H., 2017. Measurement and prediction of natural and anthropogenic sediment sources, St. John, U.S. Virgin Islands. Catena 71 (2), 250–266. https://doi.org/10.1016/j.catena.2007.03.009

Ran, Q., Hong, Y., Li, W., Gao, J., 2018. A modelling study of rainfall-induced shallow landslide mechanisms under different rainfall characteristics. J. Hydrol. 563, 790–801. https://doi.org/10.1016/j.jhydrol.2018.06.040

Robinson, D.A., Philips, C.P., 2000. Crust development in relation to vegetation and agricultural pratice on erosion susceptible, dispersive clay soils from central and southern Italy. Soil and Tillage Research 60 (1-2), 1-9. https://doi.org/10.1016/S0167-1987(01)00166-0

Rodrigo Comino, J., Brings, C., Lassu, T., Iserloh, T., Senciales, J.M., Martínez Murillo, J.F., Ruiz Sinoga, J.D., Seeger, M., Ries, J.B., 2015. Rainfall and human activity impacts on soil losses and rill erosion in vineyards (Ruwer Valley, Germany). Solid Earth Discuss. 7, 259–299. https://doi.org/10.5194/sed-7-259-2015

Romm, J. 2011. Desertification: the next dust bowl. Nature 478, 450–451. https://doi.org/10.1038/478450a

Roussel, J.R., Auty, D., Coops, N.C., Tompalski, P., Goodbody, T.R.H., Meador, A.S., Bourdon, J.F., de Boissieu, F., Achim, A., 2020. lidR: An R package for analysis of Airborne Laser Scanning (ALS) data. Remote Sens. Environ. 251, 112061. https://doi.org/10.1016/j.rse.2020.112061

Ruel, J., 2000. Factors infuencing windthrow in balsam fir forests: from landscape studies to individual tree studies. For. Ecol. Manage. 135 (1-3), 169–178. https://doi.org/10.1016/S0378-1127(00)00308-X

Ruiz-Sinoga, J. D.; Martínez-Murillo, J.F., 2009. Effects of soil surface components on soil hy20 drological behavior in a dry Mediterranean environment (Southern Spain). Geomorphology 108, 234–245. DOI: 10.1016/j.geomorph.2009.01.012

Rull, V., Vegas-Vilarrúbia, T., 2021. A spatiotemporal gradient in the anthropization of Pyrenean landscapes. Preliminary report. Quat. Sci. Rev. 258, 106909. https://doi.org/10.1016/j.quascirev.2021.106909

Saikia, A., 2014. Over-Exploitation of Forests, A Case Study from North East India. In SpringerBriefs in Geography. Springer International Publishing, Cham. https://doi.org/10.1007/978-3-319-01408-1

Salesa, D., Terol, E., Cerdà, A., 2019. Soil erosion on the " El Portalet " mountain trails in the Eastern Iberian Peninsula. Sci. Total Environ. 661, 504–513. https://doi.org/10.1016/j.scitotenv.2019.01.192

Salvati, L., Mavrakis, A., Colantoni, A., Mancino, G., Ferrara, A. 2015. Complex Adaptive Systems, soil degradation and land sensitivity to desertification: a multivariate assessment of Italian agro-forest landscape. Sci. Total Environ. 521–522, 235–245. https://doi.org/10.1016/j.scitotenv.2015.03.094

Sakals, M.E., Sidle, R.C., 2004. A spatial and temporal model of root cohesion in forest soils. Can. J. For. Res. 34, 950–958. https://doi.org/10.1139/x03-268

Sarminingsih, A., Rezagama, A., Ridwan, 2019. Simulation of rainfall-runoff process using HEC-HMS model for Garang Watershed, Semarang, Indonesia. J. Phys. Conf. Ser. 1217. https://doi.org/10.1088/1742-6596/1217/1/012134

Sebald, J., Senf, C., Heiser, M., Scheidl, C., Pflugmacher, D., Seidl, R., 2019. The effects of forest cover and disturbance on torrential hazards: large-scale evidence from the Eastern Alps. Environ. Res. Lett. 14, 114032. https://doi.org/10.1088/1748-9326/ab4937

Semadeni-Davies, A., Hernebring, C., Svensson, G., Gustafsson, L.G., 2008. The impacts of climate change and urbanisation on drainage in Helsingborg, Sweden: Combined sewer system. J. Hydrol. 350, 100–113. https://doi.org/10.1016/j.jhydrol.2007.05.028

Shi, Z.H., Ai, L., Fang, N.F., Zhu, H.D., 2012. Modeling the impacts of integrated small watershed management on soil erosion and sediment delivery: A case study in the Three Gorges Area, China. J. Hydrol. 438–439, 156–167. https://doi.org/10.1016/j.jhydrol.2012.03.016

Shiferaw, B., Holden, S.T., 2001. Farm-level benefits to investments for mitigating land degradation: Empirical evidence from Ethiopia. Environ. Dev. Econ. 6, 335–358. https://doi.org/10.1017/S1355770X01000195

Shirvani, Z., Abdi, O., Buchroithner, M.F., 2020. A new analysis approach for long-term variations of forest loss, fragmentation, and degradation resulting from road-network expansion using Landsat time-series and object-based image analysis. L. Degrad. Dev. 31, 1462–1481. https://doi.org/10.1002/ldr.3530

Shukur, H.K., 2017. Estimation Curve Numbers using GIS and Hec-GeoHMS Model. J. Eng. 23 (5), 1–11. https://joe.uobaghdad.edu.iq/index.php/main/article/view/37

Sibanda, M., Mutanga, O., Dube, T., Vundla, T.S., 2019. Estimating LAI and mapping canopy storage capacity for hydrological applications in wattle infested ecosystems using Sentinel-2 MSI derived red edge bands. GIScience Remote Sens. 56, 68–86. https://doi.org/10.1080/15481603.2018.1492213

Sidle, R.C., 2020. Dark clouds over the silk road: Challenges facing mountain environments in Central Asia. Sustain. 12, 1–11. https://doi.org/10.3390/su12229467

Sidle, R.C., 2007. Using weather and climate information for landslide prevention and mitigation. In Environmental Science and Engineering, 285–307. https://doi.org/10.1007/978-3-540-72438-4_15

Sidle, R.C., Ghestem, M., Stokes, A., 2014. Epic landslide erosion from mountain roads in Yunnan, China-challenges for sustainable development. Nat. Hazards Earth Syst. Sci. 14, 3093–3104. https://doi.org/10.5194/nhess-14-3093-2014

Sidle, R.C., Ziegler, A.D., 2012. The dilemma of mountain roads. Nat. Publ. Gr. 5, 437–438. https://doi.org/10.1038/ngeo1512

Sidle RC, Ziegler AD, Negishi JN, Nik AR, Siew R, T.F., 2006. Erosion processes in steep terrain-Truths, myths, and uncertainties related to forest management in Southeast Asia. For. Ecol. Manage. 224 (1-2), 199–225. https://doi.org/10.1016/j.foreco.2005.12.019

Sikder, R., Xiaoying, J., 2014. Climate Change Impact and Agriculture of Bangladesh. J. Environ. Earth Sci. 4, 35–40. ISSN: 2225-0948

Silva, C.A., Hudak, A.T., Vierling, L.A., Loudermilk, E.L., O'Brien, J.J., Hiers, J.K., Khosravipour, A., 2016. Imputation of Individual Longleaf Pine (Pinus palustris Mill.) Tree Attributes from Field and LiDAR Data. Can. J. Remote Sens. 42, 554–573. https://doi.org/10.1080/07038992.2016.1196582

Smirnov, N.., 1939. Estimating the deviation between the empirical distribution functions of two independent samples. Bull. l'Universite Moscou 2, 3–16.

Soane, B.D., van C., Ouwerkerk, 1994. Chapter 1 - Soil Compaction Problems in World Agriculture. Dev. Agric. Eng. 11, 1–21. https://doi.org/10.1016/B978-0-444-88286-8.50009-X

Sosa-Pérez, G., MacDonald, L.H., 2017. Reductions in road sediment production and road-stream connectivity from two decommissioning treatments. For. Ecol. Manage. 398, 116–129. https://doi.org/10.1016/j.foreco.2017.04.031

Sridhar, V., 2017. Evapotranspiration Estimation and Scaling Effects Over The Nebraska Sandhills. Great Plains Research 17 (1), 35-45. https://www.jstor.org/stable/23779506

Steffen, M., Schipek, M., Anne-Farina Lohrengel Lennart Meine, 2021. Identification of windthrow-endangered infrastructure combining LiDAR-based tree extraction methods using GIS. J. Appl. Remote Sens. 15. https://doi.org/https://doi.org/10.1117/1.JRS.15.014522

Strzyżowski, D., Gorczyca, E., Krzemień, K., Żelazny, M., 2021. The intensity of slope and fluvial processes after a catastrophic windthrow event in small catchments in the Tatra Mountains. J. Mt. Sci. https://doi.org/10.1007/s11629-021-6726-2

Sun, D., Wen, H., Wang, D., Xu, J., 2020. Geomorphology A random forest model of landslide susceptibility mapping based on hyperparameter optimization using Bayes algorithm. Geomorphology 362, 107201. https://doi.org/10.1016/j.geomorph.2020.107201

Surfleet, C.G., Marks, S.J., 2021. Hydrologic and suspended sediment effects of forest roads using field and DHSVM modelling studies. For. Ecol. Manage. 499, 119632. https://doi.org/10.1016/j.foreco.2021.119632

Tarboron, D.G., 1997. A new method for the determination of flow directions and upslope areas in grid digital elevation models. Water Resour. Res. 33 (2), 309–319. https://doi.org/10.1029/96WR03137

Tarolli, P., Borga, M., Fontana, G.D., 2008. Analysing the influence of upslope bedrock outcrops on shallow landsliding. Geomorphology 93, 186–200. https://doi.org/10.1016/j.geomorph.2007.02.017

Tarolli, P., Borga, M., Chang, K.T., Chiang, S.H., 2011. Modeling shallow landsliding susceptibility by incorporating heavy rainfall statistical properties. Geomorphology 133, 199–211. https://doi.org/10.1016/j.geomorph.2011.02.033

Tarolli, P., Borga, M., Morin, E., Delrieu, G., 2012. Analysis of flash flood regimes in the North-Western and South-Eastern Mediterranean regions. Nat. Hazards Earth Syst. Sci 12, 1255-1265. https://doi.org/10.5194/nhess-12-1255-2012

Tarolli P., Calligaro S., Cazorzi F., Dalla Fontana G., 2013. Recognition of surface flow processes influenced by roads and trails in mountain areas using high resolution topography. Eur. J. Remote Sens., 46, 176-97

Taye, F.A., Folkersen, M.V., Fleming, C.M., Buckwell, A., Mackey, B., Diwakar, K.C., Le, D., Hasan, S., Ange, C. Saint, 2021. The economic values of global forest ecosystem services: A meta-analysis. Ecol. Econ. 189, 107145. https://doi.org/10.1016/j.ecolecon.2021.107145

Taylor, S.L., Maclean, D.A., 2007. Spatiotemporal patterns of mortality in declining balsam fir and spruce stands 253, 188–201. Forest Ecology and Management 253 (1-3), 188-201. https://doi.org/10.1016/j.foreco.2007.07.016

Thimonier, A., Sedivy, I., Schleppi, P., 2010. Estimating leaf area index in different types of mature forest stands in Switzerland : a comparison of methods 543–562. European Journal of Forest Research 129, 543-562. https://doi.org/10.1007/s10342-009-0353-8

Tomczyk, A.M., White, P.C.L., Ewertowski, M.W., 2016. Effects of extreme natural events on the provision of ecosystem services in a mountain environment: The importance of trail design in delivering system resilience and ecosystem service co-benefits. J. Environ. Manage. 166, 156–167. https://doi.org/10.1016/j.jenvman.2015.10.016

Tseng, C.M., Lin, C.W., Stark, C.P., Liu, J.K., Fei, L.Y., Hsieh, Y.C., 2013. Application of a multi-temporal, LiDAR-derived, digital terrain model in a landslide-volume estimation. Earth Surf. Process. Landforms 38, 1587–1601. https://doi.org/10.1002/esp.3454

Tunde, A.M., Adeniyi, E.E., 2012. Impact of Road Transport on Agricultural Development: A Nigerian Example. Ethiop. J. Environ. Stud. Manag. 5, 232–238. https://doi.org/10.4314/ejesm.v5i3.3

US Army Corps of Engineers (USACE), 2000. Hydrologic Modeling System (HEC-HMS) Technical Reference Manual.

USDA-SCS, 1972. National engineering handbook, USDA, Wash. ed.

Ustaoglu, E., Collier, M.J. Farmland abandonment in Europe: an overview of drivers, consequences, and assessment of the sustainability implications. Environmental Reviews 26 (4). https://doi.org/10.1139/er-2018-0001

Vergani, C., Schwarz, M., Soldati, M., Corda, A., Giadrossich, F., Chiaradia, E.A., Morando, P., Bassanelli, C., 2016. Root reinforcement dynamics in subalpine spruce forests following timber harvest: A case study in Canton Schwyz, Switzerland. Catena 143, 275–288. https://doi.org/10.1016/j.catena.2016.03.038

Vickerman, R., Spiekermann, K., Wegener, M., 1999. Accessibility and economic development in Europe. Reg. Stud. 33, 1–15. https://doi.org/10.1080/00343409950118878

Wale, A., Rientjes, T.H.M., Gieske, A.S.M., Getachew, H.A., 2009. Ungauged catchment contributions to Lake Tana's water balance. Hydrol. Process 23, 3682–3693. https://doi.org/10.1002/hyp.7284

Wallace, L., Lucieer, A., Turner, D., Watson, C., 2011. Error assessment and mitigation for hyper-temporal UAV-borne LiDAR surveys of forest inventory. Silvilaser, Hobart, Tasmania. Corpus ID: 73690287

Wang, Y., Fang, Z., Wang, M., Peng, L., Hong, H., 2020. Computers and Geosciences Comparative study of landslide susceptibility mapping with different recurrent neural networks. Comput. Geosci. 138, 104445. https://doi.org/10.1016/j.cageo.2020.104445

Webb, N.P., Marshall, N.A., Stringer, L.C., Reed, M.S., Chappell, A., Herrick, J.E., 2017. Land degradation and climate change: building climate resilience in agriculture. Front. Ecol. Environ. 15, 450–459. https://doi.org/10.1002/fee.1530

Wei, X., Zhang, M., 2010. Quantifying streamflow change caused by forest disturbance at a large spatial scale : A single watershed study. Water Resources Research 46 (12), 1–15. https://doi.org/10.1029/2010WR009250

Wemple, B.C., Swanson, F.J., Jones, J.A., 2001. Forest roads and geomorphic process interactions. Earth Surf Process Landf 26, 191–204. https://doi.org/10.1002/1096-9837(200102)26:2<191::AID-ESP175>3.0.CO;2-U

Xiao, Q., McPherson, E.G., 2016. Surface Water Storage Capacity of Twenty Tree Species in Davis, California. J. Environ. Qual. 45, 188–198. https://doi.org/10.2134/jeq2015.02.0092

Xiaoli Wua, Yonglu Tanga,∗, Chaosu Lia, A.D. McHughb, Zhuo Lia, C.W., 2017. Individual and combined effects of soil waterlogging and compaction on physiological characteristics of wheat in southwestern China. Field Crops Research 215, 163-172. https://doi.org/10.1016/j.fcr.2017.10.016

Yakubu, I., Gyimah, D.M., Duker, A.A., 2015. Review of methods for modelling forest fire risk and hazard. African J. Environ. Sci. Technol. 9, 155–165. https://doi.org/10.5897/ajest2014.182

Yakupoglu, T., Gundogan, R., Dindaroglu, T., Kusvuran, K., Gokmen, V., Rodrigo-Comino, J., Gyasi-Agyei, Y., Cerdà, A., 2021. Tillage Impacts on Initial Soil Erosion in Wheat and Sainfoin Fields under Simulated Extreme Rainfall Treatments. Sustainability 13, 789. https://doi.org/10.3390/su13020789

Yuan, W., Liu, M., Wan, F., 2019. Calculation of Critical Rainfall for Small-Watershed Flash Floods Based on the HEC-HMS Hydrological Model. Water Resour. Manag. 33, 2555–2575. https://doi.org/10.1007/s11269-019-02257-0

Zhang, W., Qi, J., Wan, P., Wang, H., Xie, D., Wang, X., Yan, G., 2016. An Easy-to-Use Airborne LiDAR Data Filtering Method Based on Cloth Simulation. Remote Sens. 8 (6), 501. https://doi.org/10.3390/rs8060501

Zhao, Q., Jing, Y., Wang, A., Yu, Z., Liu, Y., Yu, J., Liu, G., Ding, S., 2022. Response of Sediment Connectivity to Altered Convergence Processes Induced by Forest Roads in Mountainous Watershed. Remote Sens. 14, 3603. https://doi.org/10.3390/rs14153603

Zhou, Q., 2014. A review of sustainable urban drainage systems considering the climate change and urbanization impacts. Water 6, 976–992. https://doi.org/10.3390/w6040976

Ziegler, A.D., Giambelluca, T.W., 1997. Importance of rural roads as source areas for runoff in mountainous areas of northern Thailand. J. Hydrol. 196, 204–229. https://doi.org/10.1016/S0022-1694(96)03288-X

Ziegler AD, Sutherland RA, G.T.W., 2000. Runoff generation and sediment production on unpaved roads, footpaths and agricultural land surfaces in northern Thailand. Earth Surf. Process. Landforms 25, 519--534. https://doi.org/10.1002/(SICI)1096-9837(200005)25:5<519::AID-ESP80>3.0.CO;2-T

CHAPTER 7

7.1 Figure index

Figure 1.1 Landslide involving a slope under a section of a paved road located in a terraced vineyard in Trentino Alto-Adige region, northern Italy (photo by Luca Mauri) 11

Figure 1.2 Example of shallow landslide activated above a section of a paved road located in a mountain grassland environment (Trentino Alto-Adige region, northern Italy; photo by Luca Mauri) 14

Figure 1.3 Shallow landslide (black arrow) occurred in a wind-disturbed forested catchment (Veneto region, northern Italy; photo by Luca Mauri) 15

Figure 2.1. Overview of the entire study area (A) and focus on landslides detected during Uncrewed Aerial Vehicles-Structure from Motion surveys. In particular, this figure shows the paved road surface (B), the first observed landslide (L1, C), the second landslide (L2, D), and the third observed collapsed surface (L3, E). 24

Figure 2.2. Comparison between landslides detected during the first Uncrewed Aerial Vehicles (UAV) survey (A: 18 October 2019) and the second one (B: 17 December 2019). Both aerial photos were taken during field surveys with UAV 25

Figure 2.3. Detail of relative path impact index (RPII) underlining the flow alterations close to the paved section of the road, located upstream to the L1 (A) and L2 (C) zones and focus on L1 (B) and L2 (D) areas under the specific road section. Critical zones, identified by the higher σRPII values (reddish colours) represent the flow concentrations due to the presence of the road. In particular, the red circles highlight such alteration close to the road segment located upstream the L1 (A) and L2 zone (C). 34

Figure 2.4. Overview of the computed digital elevation models of difference (DoD) (95% confidence interval) (A) and focus on DoD elaborated for the L1 (B) and L2 zones (C). Erosion is shown in reddish colours, deposition in blue. The figure also shows the bar plot of elevation changes regarding volumetric erosion and deposition values derived from budget segregation results computed for the L1 (D) and L2 zones (E) respectively. 35

Figure 2.5. Multi-temporal comparison of profile curvature computed for L1-pre (A) and L1-post (C) and for L2 (D). Figure 2.5B shows the profile curvature elaborated for the zone affected by L2, before its occurrence. This figure also shows the multi-temporal comparison of the roughness index performed for L1-pre (E), L1-post (G) and L2 (H). Figure 2.5F shows the roughness index elaborated for the zone affected by L2, before its occurrence. 38

Figure 2.6. Multi-temporal comparison of Cmax computed for L1-pre (A), L1-post (B), L2 zones before (E) and after (F) its occurrence, and multi-temporal comparison between observed and extracted features for L1-pre (C), L1-post (D), L2 zones before (G) and after (H) the failure. The red arrows indicate the position of the extracted features as observed during the field surveys. 40

Figure 3.1. Overview of the study area (a) and focus on the landslides L1-pre (b), L1-post (c) and L2 (d) observed during each RPAS survey. The pictures in Fig. 3.1b–d were manually taken through the RPAS surveys. 52

Figure 3.2. Overview of shaded relief maps of each DEM obtained from the first RPAS survey (Fig. 3.2a), from the second one (Fig. 3.2b), and from the adopted smoothing procedure (Fig. 3.2c). The figure also shows details of each computed DEM, regarding L1-pre and the above paved road section (Fig. 3.2d), L1-post, L2 and the above unpaved road section (Fig. 3.2e) and the original location of the road in the smoothed DEM, which simulates its absence (Fig. 3.2f). 58

Figure 3.3. Water depth (m) computed for SIMWE simulations regarding L1-pre (YesRoad scenario). In particular, the figure shows water depth simulation in function of rainfall intensity peaks equal to 7.2 mmh−1 (a), 25.0 mmh−1 (b), 33.6 mmh−1 (c), 40.0 mmh−1 (d), 60.0 mmh−1 (e) and 80.0 mmh−1 (f). Fig. 3.3c refers to the highest rainfall intensity peak recorded by the weather station in the considered time range, while Fig. 3.3a, b, d-f refer to the simulated rainfall intensity peaks. Yellow arrows indicate the main road-induced water flows deviations in the direction of L1-pre. 62

Figure 3.4. Water depth (m) computed for SIMWE simulations regarding L1-post (YesRoad scenario). In particular, the figure shows water depth simulation in function of rainfall intensity peaks equal to 7.2 mmh−1 (a), 25.0 mmh−1 (b), 33.6 mmh−1 (c), 40.0 mmh−1 (d), 60.0 mmh−1 (e) and 80.0 mmh−1 (f). Fig. 3.4a refers to the highest rainfall intensity peak recorded by the weather station in the considered time range, while Fig. 3.4b–f refers to the simulated rainfall intensity peaks. Yellow arrows indicate main road induced water flows deviations in the direction of L1-post. 63

Figure 3.5. Water depth (m) computed for SIMWE simulations regarding L2 (YesRoad scenario). In particular, the figure shows water depth simulation in function of rainfall intensity peaks equal to 7.2 mmh−1 (a), 25.0 mmh−1 (b), 33.6 mmh−1 (c), 40.0 mmh−1 (d), 60.0 mmh−1 (e) and 80.0 mmh−1 (f). Fig. 3.5a refers to the highest rainfall intensity peak recorded by the weather station in the considered time range, while Fig. 3.5b–f refers to the simulated rainfall intensity peaks. Yellow arrows indicate the most relevant water flows deviated by the unpaved road section located above L2, crossing the terraces downstream and intercepting the collapsed hillslope. 64

Figure 3.6. Water depth (m) computed for SIMWE simulations regarding L1 (NoRoad scenario). In particular, the figure shows water depth simulation in function of rainfall peaks equal to 7.2 mmh−1 (a), 25.0 mmh−1 (b), 33.6 mmh−1 (c), 40.0 mmh−1 (d), 60.0 mmh−1 (e) and 80.0 mmh−1 (f). SIMWE simulations were computed adopting the same rainfall intensity peaks values previously set in the YesRoad scenarios. Yellow arrows indicate the highest water depth values involving an unaltered hillslope close to L1. 65

Figure 3.7. Water depth (m) computed for SIMWE simulations regarding L2 (NoRoad scenario). In particular, the figure shows water depth simulation in function of rainfall intensity peaks equal to 7.2 mmh−1 (a), 25.0 mmh−1 (b), 33.6 mmh−1 (c), 40.0 mmh−1 (d), 60.0 mmh−1 (e) and 80.0 mmh−1 (f). SIMWE simulations were computed adopting the same rainfall intensity peaks values previously set in the YesRoad scenarios. Yellow arrows indicate the highest water depth values, regarding assumed water overland flows crossing L2. 66

Figure 3.8. Boxplots of water depth values extracted from each control point located along the paved and the unpaved road sections above L1-pre (a), L1-post (b) and L2 (c). The figure shows the comparison between water depth values acquired from each control point for YesRoad and NoRoad scenarios regarding each computed SIMWE simulation. Outliers have been removed to propose a clearer visualization of the graphics. 68

Figure 3.9. Line plots showing water depth cross-sections computed for each simulation of the YesRoad and NoRoad scenarios. In particular, the figure shows water depth cross-sections elaborated both looking at the presence of the road and its assumed absence for L1-pre (a–b), L1-post (c–d) and L2 (e–f). 69

Figure 3.10. Barplots showing the trend of daily cumulative rainfall (mm day-1) and point-plots showing the trend of daily rainfall intensity peaks (mmh-1) recorded in September 2019 (a), October 2019 (b), November 2019 (c) and December 2019 (d). 74

Figure 3.11. Land types identified within the study area. 75

Figure 3.12. Overview of checkpoints location along the paved and the unpaved road section located above L1 and L2. The orthophoto was computed from the second RPAS-derived point cloud, so as to appreciate the presence of the two detected landslides within the study area. 75

Figure 4.1. ALS-derived shaded relief of the study area (a) and focus on the detected shallow landslide (b). The figure shows the watershed considered for soil stability analysis performed through the Road Erosion Steady-State (RESS) model (black area) and the sub-watershed considered for snowmelt simulations elaborated with the Snowmelt Runoff Model (SRM, red area). The figure also underlines the location of the respective outlets, as well as the road (orange polygon) and the observed shallow landslide (cyan polygon). Fig. 1b was obtained from high-resolution Uncrewed Aerial Vehicle (UAV)-derived aerial orthomosaic acquired during the post-event (2020) field survey. (For interpretation of the references to colour in this figure legend, the reader is referred to the web version of this article.) 90

Figure 4.2. Snowmelt runoff dynamics observed during field surveys conducted in 2020 (post-event conditions). The figure shows snowmelt runoff coming from the melting snow accumulations located on the grassy hillslope above the road (a-c), snowmelt overland flows along the roadway (d, e) and therefore snowmelt runoff falling toward the area involved in the observed shallow landslide (f). . 91

Figure 4.3. Research flowchart showing the ALS data post-processing (A), the interactive application of Snowmelt Runoff Model - SRM (B), Road Erosion Steady-State - RESS model (C) and SIMulated Water Erosion model - SIMWE (D), and the final statistical analysis (E). Respective model inputs and outputs are represented in rectangular boxes, while models are shown in cyan circles. The rhomboidal box represents data post-processing procedures used for DEM creation and road removal operations. (For interpretation of the references to colour in this figure legend, the reader is referred to the web version of this article.) 92

Figure 4.4. Details of landslide's features manually measured during the post-event field survey conducted in 2020. The 3D mesh was obtained through the UAV-derived point cloud data elaboration. 93

Figure 4.5. Overview of precipitation and average temperatures recorded by the Pordoi weather station during 2018 (a). The figure also shows the trend of both snow depth and Snowmelt Runoff Model (SRM)-derived daily snowmelt runoff values (Sr) for the 2018 melting season (b), as well as the rain contributing to runoff (Rr) during it (c). 103

Figure 4.6. Comparison of critical snowmelt runoff (Sr) calculated for the YesRoad (a) and NoRoad (b) scenarios. The figure also shows the calculated difference between NoRoad and YesRoad critical Sr (c). Fig. 4.6d-f represents a focus of critical Sr computed for the two scenarios and of critical Sr difference inside the landslide zone (black polygon). Reddish pixels stand for higher differences between NoRoad and YesRoad critical Sr, while bluish pixels stand for lower differences. No difference zones are represented in transparent coloring. In critical Sr computation, unconditionally unstable cells have values equal to −2. DEM-derived shaded relief is represented in the background. 105

Figure 4.7. Comparison of critical rainfall runoff (Rr) calculated for the YesRoad (a) and NoRoad (b) scenarios. The figure also shows the calculated difference between NoRoad and YesRoad critical Rr (c). Fig. 4.7d-f represents a focus of critical Rr computed for the two scenarios and of critical Rr difference inside the landslide zone (black polygon). Reddish pixels stand for higher differences between NoRoad and YesRoad critical Rr, while bluish pixels stand for lower differences. No difference zones are represented in transparent coloring. In critical Rr computation, unconditionally unstable cells have values equal to −2. DEM-derived shaded relief is represented in the background. 106

Figure 4.8. Pre-event RI index calculated from Snowmelt Runoff Model-derived critical snowmelt runoff (Sr) (a) and critical rainfall runoff (Rr) (b) for 2018. No change and unconditionally stable areas (i.e., grassland and road network) are represented with a transparent coloring to better appreciate the location of instabilities regions inside the landslide area. ALS-derived aerial orthophoto is reported in the background. 107

Figure 4.9. SIMWE outcomes. The figure shows snowmelt runoff (Sr) discharge computed for the YesRoad (a) and NoRoad (b) scenarios, and Sr flow depth for the YesRoad (c) and NoRoad (d) scenarios obtained using the pre-event DEM. For the YesRoad scenario, the white arrow indicates the point of critical convergence of Sr coming respectively from the road and the upper hillslope, in the direction of the manhole (yellow point) located on the top of the landslide's triggering area. (For interpretation of the references to colour in this figure legend, the reader is referred to the web version of this article.) 109

Figure 4.10. Cross-section line plots of snowmelt runoff (Sr) discharge and Sr flow depth extracted at each Control Point for the YesRoad and NoRoad scenarios. 110

Figure 4.11. Comparison of the shaded relief computed from the original (a) and the modified (b) pre-event ALS-derived DEM. The figure also shows the location of the observed shallow landslide (orange polygon) under the roadway (yellow arrow). 116

Figure 4.12. Detail of the location of cross section points inside the landslide zone. In particular, a focus on snowmelt overflows intercepting the manhole located above the unstable surface is appreciable in the figure b. Cross section points were placed at an equal distance of 10 cm along a line traced inside the landslide surface under the road. SIMWE-derived Sr overland flows are represented in the background. 117

Figure 5.1 Overview of the study area (a) and focus on the shallow landslide observed during filed surveys conducted in 2019 (b). 139

Figure 5.2 Overview of stand forest within the watershed (Fig. 5.2a) and focus on the distribution of standing trees at the hillslope (black box) involved in the occurrence of the shallow landslide (red dot; Fig. 5.2c). Fig. 5.2b shows the aerial orthophoto acquired during ALS-surveys in 2015, before the occurrence of the Vaia storm (pre-event scenario). 150

Figure 5.3 Overview of windthrows within the watershed (Fig. 5.3a) and focus on the windthrown trees located at the hillslope (black box) involved in the occurrence of the shallow landslide (red dot; Fig. 5.3c). Fig. 5.3b shows the aerial orthophoto acquired during ALS-surveys in 2019, after the occurrence of the Vaia storm (post-event scenario)..... 151

Figure 5.4 Sub-basins (brown polygons) delineated through the HEC-GeoHMS tool. The figure shows sub-basins outlets (black circles), watershed outlet (yellow circle), the main channel (cyan line) and D-inf water flow directions within the watershed (blue paths). Since the small extension and the closeness of sub-basins, their respective outlets partially overlap in the figure. ALS-derived DTM is reported in background for enhance the visualization of the map. 152

Figure 5.5 Bar plots showing daily average runoff values resulted by HEC-HMS simulations for the pre-event scenario. The figure shows daily runoff values for each sub-basin considered, as well as daily runoff values at the outlet of the catchment. 155

Figure 5.6 Bar plots showing daily average runoff values resulted by HEC-HMS simulations for the post-event scenario. The figure shows daily runoff values for each sub-basin considered, as well as daily runoff values at the outlet of the catchment 156

Figure 5.7 Boxplots showing the difference of daily average runoff values estimated by HEC-HMS model for the pre-event and post-event scenarios, for each sub-basin and looking at the outlet of the entire watershed. 158

Figure 5.8 Pre-event RI index computed for the pre-event scenario (standing forest; Fig. 5.8a) and post-event scenario (windthrown forest; Fig. 5.8c). Fig. 5.8b, d show a focus of the predictive instability susceptibility mapping at the landslide area respectively for the pre-event and post-event scenarios. No changes and unconditionally stable area are represented with a transparent coloring in order to better appreciate model outcomes. ALS-derived pre-event and post-event orthophoto are reported in the background 159

Figure 5.9 Scatter plot showing the correlation between relative runoff increment and percentage of windthrown trees resulted from HEC-HMS simulations and ALS-derived point cloud elaboration. The color palette represents lower (light green) to higher (dark green) percentage of fallen trees. Regression line is in black color, confidence interval (alpha equal to 0.05) is shown in light grey. 161

Figure 5.10 Shaded relief of the forested catchment computed starting from pre-event (a) and post-event (b) ALS-data acquisition and elaboration. The figure also shows a detail of the pre-event (c) and post-event (d) shaded relief at the hillslope affected by the shallow landslide activated under the unpaved road section. 177

Figure 5.11 Spatial discretization of CN values set for different land cover (i.e., stand forest, windthrows, terrain and road). The figure also shows a detail of CN values spatial distribution at the hillslope involved in the activation of the shallow landslide, occurred downstream a section of the unpaved road located in the catchment, looking at pre-event (c) and post-event (d) conditions..... 178

Figure 5.12 Spatial discretization of canopy water storage set for different land cover (i.e., stand forest and windthrows). The figure also shows a detail of canopy water storage spatial distribution at the hillslope involved in the activation of the shallow landslide, occurred downstream a section of the unpaved road located in the catchment, looking at pre-event (c) and post-event (d) conditions..... 179

Figure 5.13 Spatial discretization of surface water storage set for different land cover (i.e., standing forest, windthrows, terrain and road). The figure also shows a detail of surface water storage spatial distribution at the hillslope involved in the activation of the shallow landslide, occurred downstream a section of the unpaved road located in the catchment, looking at pre-event (c) and post-event (d) conditions. 180

Figure 5.14 Hydrograph computed starting from rainfall data collected by the Falzarego weather station in 2019 180

7.2 Table index

Table 2.1. Main errors in the Structure from Motion surveys point clouds. 33

Table 2.2. Detail of budget segregation results for the digital elevation models of difference (DoD) computed for L1 and L2. The table shows the results of thresholded DoD and their respective raw DoD results for each detected landslide. 36

Table 3.1. Overview of main parameters describing the SfM point clouds and the obtain DEMs for the first RPAS survey (18 October 2019) and the second one (17 December 2019). The table shows the point cloud accuracy (described by the absolute mean of CPs residuals), point cloud precision (described by the standard deviation of CPs residuals) for the two RPAS surveys, RMSE3D total value observed during point clouds' elaboration, respectively regarding GCPs and CPs, co-registration error and RMSE values of final DEMs. 56

Table 3.2. Overview of SIMWE input selected for each simulation of the YesRoad-pre and YesRoad-post scenarios. In particular, the table shows Manning, infiltration rate and excess rate values considered for each land type, i.e., vineyard (V), grassland (G), bare soil (i.e., landsides zones, BS), concrete road sections (CR) and unpaved road sections (UR). Simulations 1 and 3 were computed considering the highest rainfall intensity peaks recorded by the weather station in the time range referring to the first and the second RPAS survey respectively, while simulations 2, 4, 5 and 6 were computed considering hypothetical rainfall intensity peaks. 59

Table 3.3. Overview of SIMWE input selected for each simulation of the NoRoad scenario. In particular, the table shows Manning, infiltration rate and excess rate values considered for each land type, i.e., vineyard (V), grassland (G) and bare soil (i.e., landsides zones, BS). SIMWE simulations were computed adopting the same rainfall intensity peak values previously set in each YesRoad scenario. 60

Table 3.4. Overview of statistical parameters derived from t-test and p-value computation for water depth values extracted from control points placed along the paved road section above L1-pre 76

Table 3.5. Overview of statistical parameters derived from t-test and p-value computation for water depth values extracted from control points placed along the paved road section above L1-post 77

Table 3.6. Overview of statistical parameters derived from t-test and p-value computation for water depth values extracted from control points placed along the paved road section above L2 78

Table 4.1. Overview of ALS surveys parameters and characteristics 94

Table 4.2. Overview of Snowmelt Runoff Model (SRM) inputs.....95

Table 4.3. Overview of Road Erosion Steady-State (RESS) inputs necessary for soil stability investigations. 98

Table 4.4. Overview of SIMulated Water Erosion (SIMWE) inputs. G stands for grassland, Rd stands for road and Rk stands for rocky areas located on the top of the watershed. 100

Table 4.5. Confusion matrix for ROC analysis computation. The table shows the number of pixels for true positives (TP), true negatives (TN), false positives (FP) and false negatives (FN), and the respective percentage compared with the total number of pixels defining the section of the watershed below the road, considered for investigating predictive RESS performance. Stable and NoChange zones cover the remaining 64.08% and 77.07% of the considered RESS-watershed's section under the road, looking at RESS-derived Rr and Sr simulations respectively.....111

Table 4.6. Percentage of observed instabilities area and respective catchment area for each range of critical snowmelt runoff (Sr).....112

Table 4.7. Percentage of observed instabilities area and respective catchment area for each range of critical rainfall runoff (Rr). 112

Table 4.8. Overview of the computed SRM, RESS and SIMWE predictive simulations, looking at both YesRoad and NoRoad scenarios.....117

Table 4.9. Overview of symbols and abbreviations used in models application 118

Table 5.1 Geomorphological parameters of sub-basins computed for HEC-HMS simulations.....153

Table 5.2 Summary statistics of HEC-HMS derived runoff values estimated for each sub-basin looking at pre-event and post-event scenarios 154

Table 5.3 Overview of percentage of windthrown trees and relative percent runoff increment for each sub-basin 157

Table 5.4 Results of D2PC and TSS calculation. The table shows the number of pixels for true positives (TP), true negatives (TN), false positives (FP) and false negatives (FN), and the respective percentage compared to the total number of pixels for the section of the watershed considered in investigating predictive RESS performance. Table and NoChange areas cover the remaining 45.67% of the considered watershed section.....162

Table 5.5 Overview of ALS surveys parameters and main characteristics 181

Table 5.6 Overview of HEC-HMS components and respective inputs necessary for model simulations 182

Table 5.7 Overview of RESS inputs necessary for computing soil stability simulations. Pre and post terms stand for pre-event scenario (standing forest conditions) and post-event scenario (windthrows conditions)..... 182

Table 5.8 Statistical results of the Student t-test computed looking at daily average runoff values calculated by HEC-HMS model in function of windthrown-induced land use changes at sub-basin detail..... 184

Table 5.9 Outcomes of R-based linear regression analysis computed looking at HEC-HMS outcomes in function of windthrown-induced land use changes 185

ABBREVIATIONS AND TERMS CITATIONS

A

ALS

Airborne Laser Scanning · 1; 16; 18; 86; 88; 90; 91; 92; 94; 98; 107; 115; 116; 135; 137; 140; 141; 144; 148; 149; 150; 151; 158; 160; 162; 163; 164; 175; 179; 184; 185; 186; 209; 210; 211; 212; 214; 215

An

Degree-day factor · 28; 33; 86; 95; 96; 118; 119; 121; 138; 152

aT

Daily potential snowmelt depth · 122

AUC

Area Under the ROC Curve · *See AUC-ROC*

AUC-ROC

Area Under the Receiver Operating Characteristic curve · 86

C

c

Runoff coefficient · 120

CHM

Canopy Height Model · 140; 141; 148; 186

CI

Confidence Interval · 30; 35; 36

Cmax

Maximum curvature · 31; 39; 40

CN

Curve Number · 142; 143; 148; 150; 176; 180; 212

Coh_r

Root cohesion · 98; 99; 118; 145; 181

Coh_s

Soil cohesion · 98; 99; 118; 145; 181

CPs

Check Points · 26; 27; 28; 33; 55; 56; 110

Cr

Rain Runoff coefficient · 95; 97; 118; 122 · *See c*

$Crit_{Rr}$

Critical Rr · *See Rr*

$Crit_{Sr}$

Critical Sr · *See Sr*

$Crit_{SRr}$

Critical SRr · *See SRr, Sr, Rr*

Cs

Snow Runoff coefficient · 95; 97; 118; 122· *See c*

csf

Cloth Simulation Filter algorithm · 140

D

D2PC

Distance to Perfect Classification · 135; 146; 147; 160; 161; 215

DEM

Digital Elevation Model · 20; 22; 27; 28; 29; 30; 31; 32; 41; 47; 48; 50; 53; 55; 56; 57; 58; 62; 71; 73; 86; 88; 91; 92; 94; 95; 98; 99; 100; 105; 106; 108; 109; 113; 115; 116; 123; 163; 180; 181; 185; 186

DoD

Digital elevation model Of Difference · 29; 30; 35; 36; 41; 184

DTM

Digital Terrain Model · 137; 140; 141; 144; 148; 151; 164; 186; 211

F

FN

False Negatives · 32; 101; 111; 146; 161

FP

False Positives · 32; 101; 111; 146; 161

FPR

False Positive Rates · 101; 146; 161

FS

Factor of Safety · 119

G

GCD

Geomorphic Change Detection · 29; 30

GCPs

Ground Control Points · 26; 27; 33; 55; 56

GIS

Geographic Information Systems · 1; 3; 16; 17; 19; 28; 29; 31; 53; 56; 85; 98; 101; 119; 123; 130; 134; 136; 141; 142; 144; 151

GNSS

Global Navigation Satellite System · 26; 28; 55; 56

H

HEC-HMS

Hydrologic Engineering Center-Hydrologic Modelling System model · 134; 135; 137; 141; 142; 143; 144; 145; 146; 151; 152; 153; 154; 155; 157; 159; 160; 162; 163; 164; 180; 182; 183; 186; 195; 198; 211; 212; 215; 216

I

IQR

Interquartile Range · 31; 39

K

k

Cohen’s kappa-index · 86; 101; 102; 111

Recession coefficient · 95; 97; 118; 121

Saturated soil conductibility · 57; 100; 118

L

L

Time Lag · 95; 97; 118; 122

L8

Landsat 8 · 95; 96

LAI

Leaf Area Index · 142

LiDAR

Light Detection and Ranging · 1; 3; 21; 88; 94; 137; 179

M

M3C2

Multiscale Model to Model Cloud Comparison · 28; 29; 33

N

n

Manning's n · 53; 56; 59; 60; 100; 118; 123

NDSI

Normalized Index of Differences in Snow cover · 96

P

P

Precipitation · 95; 118; 121

PCL

Point Cloud Library · 55; 140

R

R

R studio · 54; 69; 94; 123; 140; 141; 143; 145; 146; 159; 183; 188; 189; 191; 192

RCA

Rainfall Contributing Area · 95; 96; 118; 121

RESS

Road Erosion Steady-State model · 10; 88; 89; 90; 91; 92; 97; 98; 99; 101; 102; 103; 104; 107; 111; 113; 115; 117; 118; 122; 135; 137; 144; 145; 146; 158; 160; 161; 162; 163; 164; 181; 185

RI

Relative Impact index · 107; 117; 118; 120; 122; 144; 158; 163

RI_{Rr}

Relative Impact index from Rr · *See RI, Rr*

RI_{SRr}

Relative Impact index from SRr · 118

RMSE

Root Mean Square Error · 27; 28; 33; 56; 148

ROC

Receiver Operating Characteristic analysis · *See AUC-ROC*

RPAS

Remotely Piloted Aircraft Systems · 50; 51; 52; 54; 55; 56; 57; 58; 59; 62; 63; 71; 73; 75· *See UAV*

RPII

Relative Path Impact Index · 28; 29; 33; 34; 41; 43; 184

Rr

Rainfall runoff · 99; 102; 103; 104; 106; 107; 112; 114; 115; 118; 121

r_{rc}

Relative road cut depth · 98; 118; 181

Rr_{max}

Max Rainfall runoff · *See Rr*

S

SCA

Snow Covered Area · 95; 118

SCS-CN

Soil Conservation Service Curve Number · *See CN*

SfM

Structure from Motion · 1; 3; 18; 19; 20; 21; 22; 26; 29; 33; 41; 48; 50; 55; 56; 71; 73; 214

SIMWE

SIMulated Water Erosion model · 48; 50; 53; 54; 56; 57; 58; 59; 60; 61; 62; 63; 64; 65; 66; 67; 68; 71; 72; 73; 76; 77; 78; 88; 91; 92; 100; 103; 108; 109; 110; 113; 115; 117; 118; 123; 185

SOR

Statistical Outlier Removal · 27; 55; 140

Sr

Snowmelt runoff · 99; 100; 101; 102; 103; 104; 105; 107; 108; 109; 110; 111; 112; 114; 115; 118; 121

SRM

Snowmelt Runoff Model · 88; 89; 90; 91; 92; 95; 96; 97; 99; 100; 103; 104; 113; 114; 115; 117; 118; 120; 121; 122; 125; 185

Sr_{max}

Max snowmelt runoff · *See Sr*

SRr

Combined Sr and Rr · *See Sr, Rr*

T

T

Temperature · 95; 118

T_{CRIT}

Critical Temperature · 95; 96; 118; 121

Td

Degree-days · 119

T_{MAX}

Daily maximum Temperature · *See T*

T_{MIN}

Daily minimum Temperature · *See T*

TN

True Negatives · 101; 111; 146; 161

TP

True Positives · 32; 101; 111; 146; 161

TPR

True Positive Rate · 101; 146; 161

Tr

Soil Transmissivity · 98; 99; 118; 122; 145; 181

TSS

True Skill Statistic · 135; 146; 147; 160; 161; 215

U

UAV

Uncrewed Aerial Vehicle · 1; 3; 16; 18; 19; 20; 21; 22; 25; 26; 28; 33; 36; 37; 39; 41; 42; 43; 90; 93; 101; 164; 184; 206; 209 · *See RPAS*

W

W

Vegetation surcharge · 98; 99; 118; 145; 181

Z

z

Soil depth · 98; 99; 118; 145; 181

Other symbols and abbreviations

γ

Temperature Lapse Rate · 95; 96; 118

ρ_s

Snow density · 96

Soil density · 98; 99; 118; 145; 181

ρ_w

Water density · 96; 98; 99; 118; 181

ϕ

Internal friction angle · 98; 99; 118; 145; 181